2014

Geochemical and geochronological constraints on Quaternary volcanism in southern Mendoza, Argentina

Venera Ruth Espanon
University of Wollongong

Geochemical and geochronological constraints on Quaternary volcanism in southern Mendoza, Argentina

Venera R. Espanon

University of Wollongong
NSW, Australia

GEOCHEMICAL AND GEOCHRONOLOGICAL CONSTRAINTS ON QUATERNARY VOLCANISM IN SOUTHERN MENDOZA, ARGENTINA

A thesis submitted in partial fulfilment of the
requirements for the award of the degree

DOCTOR OF PHILOSOPHY

from

UNIVERSITY OF WOLLONGONG

by

VENERA RUTH ESPANON,
Bachelor of Science Honours, Geology

SCHOOL OF EARTH AND ENVIRONMENTAL SCIENCES

2014

I, Venera R. Espanon, declare that this thesis, submitted in partial fulfilment of the requirements for the award of Doctor of Philosophy, in the School of Earth and Environmental Sciences, Faculty of Science, Medicine and Health, University of Wollongong, is wholly my own work unless otherwise referenced or acknowledged. The document has not been submitted for qualifications at any other academic institution.

Venera R. Espanon
November, 2014

“we shall be deeply impressed with the grandeur of the one motive power, which, causing the elevation of the continent, has produced, as secondary effects, mountain-chains and volcanos”

Charles Darwin, 1840

Abstract

The basaltic volcanism occurring on a continental plate behind a volcanic arc is not well studied, as this type of volcanic activity is neither common nor easily classified by conventional tectonic setting. In order to investigate the volcanism of this type, an area with abundant Quaternary monogenetic volcanism behind a volcanic arc was chosen, namely, the Payenia Basaltic Province (PBP), in central west Argentina. The PBP is subdivided into several volcanic fields; Nevado, Payún Matrú, Llancanelo and Rio Colorado. The Quaternary alkali volcanism produced in this region has been the focus of several studies since the 1960s, with the pioneering work of Llambías (1966), mainly dedicated to the polygenetic Payún Matrú caldera. More recently, several studies have dealt with the monogenetic volcanism in the PBP, classifying this setting as back-arc (Bermudez and Delpino, 1989; Bertotto et al., 2009; Gudnason et al., 2012; Jacques et al., 2013; Espanon et al., 2014b; among others), intraplate (Ramos and Folguera, 2011) or a transition between back-arc and intraplate (Søager et al., 2013; Hermando et al., 2014), highlighting the difficulty in assigning a setting. In the last few years, the understanding of this basaltic province has significantly increased; however, there are some aspects and approaches that have not been previously considered and applied. These are, for example; to integrate and compare the geochemical signatures of the volcanic fields composing the PBP, in order to obtain a general geochemical fingerprint. Furthermore, using a combined approach with geochemistry and geochronology, the evolution of the PBP can be reconstructed.

The focus of this investigation is the Llancanelo and the Payún Matrú volcanic fields as they represent the latest stages of activity in the PBP and are late Quaternary in age, according to the available chronology. The aims of the investigation are i) to determine the geochemical signatures that have controlled the volcanism during the Pleistocene and the Holocene, ii) to temporally and spatially determine the volcanic evolution and to comprehend the processes that shaped these two volcanic fields, and iii) to contribute broadly to the understanding of this type of volcanism and thereby relate the findings with similar locations around the globe. In the current investigation, new geochemical data from the Llancanelo Volcanic Field (LLVF) and Payún Matrú Volcanic Field (PMVF) are presented. In addition, new numerical ages from three different dating methods are provided. These ages are from basalts of the Pampas Onduladas flow which have not been previously dated and from the Santa Maria volcano which has been regarded as young (Espanon et al., 2014a), but for which no previous reliable numerical ages were available. Of special interest are the Holocene basalts from the Santa Maria volcano, as they constitute the most recent history of the PBP.

Even though the LLVF and the PMVF are located in close proximity and were both active in the last 500 ka the inferred geochemical signatures are different. The LLVF shows some arc-like compositional features. However, these signatures are relatively weak compared to the subduction signature present in the basalts of the Andean arc. The weak subduction signature inferred for the LLVF is not related to the dehydration of the subducting Nazca plate but,

possibly to sediments transported by the slab. It is less likely that the signature is related to slab partial melts as a residual garnet signature is not evident. By contrast, in the PMVF, no subduction-related signature has been inferred. Both volcanic fields have an ocean island basalt (OIB)-like source, modified by lower crustal assimilation.

The Pampas Onduladas long lava flow has provided the strongest evidence for lower crustal assimilation among the investigated locations. The Pampas Onduladas flow has an extreme length of 167 km making it one of the four longest Quaternary flows on Earth, all of which are associated with ocean island basalt sources. Therefore, the genesis of the Pampas Onduladas flow can be attributed to an intraplate classification. The first radiometric ages for this long flow is 373 ± 10 ka using $^{40}Ar/^{39}Ar$ and 398 ± 30 ka by surface exposure dating (SED) using ^{3}He and ^{21}Ne cosmogenic isotopes, showing very good agreement and highlighting the importance of using a multi-dating approach. With the exception of the 600 ka ages reported by Quidelleur et al. (2009) and Melchor and Casadío (1999), the ages determined for the Pampas Onduladas flow are among the oldest Quaternary ages documented for the PMVF.

By contrast, the Santa Maria volcano has been proposed as one of the most recent eruptions in the PMVF (Espanon et al., 2014). Therefore, this volcano was selected for U-series analysis in order to understand the recent magmatic history of the region. The ^{226}Ra-^{230}Th disequilibrium measured among basalts of this volcano reveals that the magma ascent occurred relatively rapidly within the last 8 ka in order to preserve the measured ^{226}Ra excess. In addition, the magmatic source for the Santa Maria volcano is at the stability boundary between garnet and spinel peridotite as inferred from an intermediate pressure where hydrous minerals are stable. Finally, this volcano also shows evidence for lower crustal assimilation in accord with other volcanic rocks within the PMVF.

Samples from the Santa Maria volcano represent the first successful attempt to date young basaltic rocks close to the analytical limit of the cosmogenic noble-gas method. These ages provide a new challenge to further refine the surface exposure dating technique using cosmogenic ^{3}He and ^{21}Ne. The young numerical ages determined agree with previous estimates and support the hypothesis that Santa Maria may be one of the latest eruptions in the PMVF.

In summary, the evolution of the Payenia Basaltic Province is not simple and it involved several magmatic source components (e.g. OIB, subducting slab and lower continental crust), making the process of classifying this Quaternary basaltic province into either continental back-arc and/or intraplate is problematic. The complexity of this type of setting emphasises the importance in understanding the interaction between the subducting plate and the mantle in areas where slab dehydration is not the driving force for volcanism.

Acknowledgments

I would probably need to write another thesis in order to thank all the people that have helped me through this journey and if I have forgotten someone please excuse me; as I generally say that, the two neurons left were consumed writing the thesis!

I would like thank my supervisor Allan R. Chivas, who talked to me about Payunia in September 2009 when I was finishing my undergraduate work. Payunia captivated me during Honours in 2010 but 9 months are not enough for such a vast volcanic area. So then in 2011 we conducted the first comprehensive field trip to this exquisite volcanic location in which we spent several very successful field trips. Thank you, for giving me the opportunity to do research in this volcanic area, in my native Mendoza, which attracted me since I was a kid. Very special thanks to my co-supervisor Anthony Dosseto, who helped me in developing critical thinking, with his thought-provoking questions and for being there every time I had a question or I needed his comments. Thanks to my associate supervisor, Masahiko Honda, for letting me use his laboratory, for his support with the cosmogenic analysis and for having the time to talk and explain things to me every time I went to Canberra.

The fieldwork component of this study was funded in part by a short-term mobility scholarship for field training in young geological processes from the then Department of Industry, Innovation, Science, Research and Tertiary Education of the Australian Government. Thanks to GeoQuEST, for providing the funding for some of the analysis.

This project would have not been possible without all the people that collaborated in the field trips and in the laboratory during sample preparation and analysis. Thanks to the Dirección de Recursos Naturales Renovables, part of the Mendoza government for providing the research permits and to the park rangers in Llancanelo and Payunia provincial reserves for being always helpful. Special thanks to all the people that participated in the field trips to Payunia, Adriana Garcia, Stephanie Kerr, Laura Pistrellini, Marcelino Azaguate, Daniel Espanon and especially to Paul Connolly, for walking long hours uphill to get to the Payún Matrú caldera and to Ryan Manton for his assistance during adverse weather conditions in Payún Matrú. My gratitude goes to Leandro Rojo for being my “field buddy” when visiting the lovely Santa Maria Volcano in which he learned how an a’a flow feels after several hours of walking on it; Gracias Leo! To my favourite field driver, Lucho (Luis) Lopez always so motivated and with a “mate” in his hand. Special thanks to Alberto Quesada and his family from Malacara homestead for letting me stay there and opening his house to me. My gratitude to Paul Carr, Brian Jones and José Abrantes for their help with XRF analysis and thin section preparation. Thanks to Colleen Bryant, for her help with the LA-ICP-MS, in Canberra. To Lily Yu and Helen Price for their very much appreciated help with the ICP-MS and in Tony’s Lab thanks very much ladies! Thanks to Norman Pearson from Macquarie University for his contribution with the TIMS, to Shane Paxton for his help and coaching with mineral separation. Many thanks to David Phillips, and especially

to Erin Matchan for her very detailed explanations and for taking the time to thoroughly reply to every single e-mail I sent her with questions. Thanks to Toshiyuki Fujioka for some very helpful discussions. To everyone in the School of Earth and Environmental Sciences at the University of Wollongong, thank you very much for always sharing a “Hi” or a smile or asking how things were going? As that made me feel-like a person.

To all PhD mates and friends, Omar Mohammad, Sarah Eccleshall, Ryan Manton, Lily Yu, Behrooz Karamiqucham, Amy Blakemore, Deirdre Ryan, Florian Dux, Ashley Martin, Nathan Jankowski, Davide Menozzi, Brent Koppel, Mika Rizki Puspaningrum, Rafael Carvalho, Martin Struck, Anna Habeck, Claire Perrette and Daniela Muller, thanks very much for always listening to me during my frustrated and happy days, thanks for being there with a chocolate or a coffee when I needed. To the coffee club and your “jocularity”, I enjoyed it so much and at times, made me laugh so much that I thought I was already in Illaroi! Well maybe that is the trick to start living in it before it is all over.

Finally thanks to my family. My parents Silvia Espanon and Oscar Espanon thanks, for always teaching me to appreciate life, to achieve my goals and to enjoy even the little precious moments. To my brother Daniel Espanon, thanks for believing in me always, for coming with me to Payunia for sharing the experience and for his love. To my very special other half Jan-Hendrik May, the word “thanks” is small to thank you for all the patience, support and strength you have given me, for believing in me more than anybody, for all the many scientific discussions over dinner and for your unconditional love, Te amo!

Table of Contents

List of Figures

Chapter 1

Chapter 2

Chapter 3

Chapter 4

Chapter 5

Chapter 6

List of Tables

Chapter 1

Chapter 2

Chapter 3

Chapter 4

Chapter 5

Introduction

Back-arc volcanism occurring on a continental plate is not a common setting; hence is not well understood. The majority of the literature concerned with back–arc volcanism deals with ocean-ocean collision and with extension and breakage in the back-arc region resulting in sea floor spreading such as in the western Pacific. The collision of an oceanic and a continental plate such as the Andean-type is different as it involves continental crust. The continental crust is older, thicker and tectonically more active than oceanic crust while it is less dense than the oceanic crust. Oceanic-continental collisions are associated with Andean-type volcanism with abundant intermediate to felsic magmatism on the western side of South America. This arc volcanism occurs in a belt approximately 100 km wide and on average 300 km from the trench axis and with geochemical signatures strictly of mantle metasomatism. In addition to the arc volcanism, parts of South America have alkali basaltic volcanism, occurring approximately 400 km from the trench on the continental plate, constituting the back-arc. However, the geochemical signatures of this volcanism occurring behind the Andean arc have not been thoroughly described and their evolution through time has not been examined; constituting one of the original aims of this investigation. The western margin of South America has a long history of back-arc volcanism since the Early Cretaceous (Mpodozis and Allmendinger, 1993), continues during the late Paleogene after a major tectonic reorganisation and is documented in the Quaternary. Considering the extended history of back-arc volcanism especially in the southern part of South America, an alkali volcanic field with tectonic extension and covering a long period of continuous volcanic activity was chosen for this investigation. The Payenia Basaltic Province has these characteristics therefore was utilised to investigate its magmatic genesis in relation to its location in the continental back-arc.

The objective of this work is to present geochemical evidence for processes that have controlled the evolution of the Quaternary back-arc in the Payenia Basaltic Province. Identifying, how the signatures in this back-arc have evolved during the past 2.6 Ma will help to comprehend and quantify the influence of the subducting Nazca Plate on the continental back-arc as well as recognising possible magmatic sources and/or magmatic types of contaminants. Furthermore, the Pleistocene history of this basaltic back-arc province has been partly documented whereas the Holocene volcanism has not been widely investigated. Accordingly, this investigation aims to produce new Pleistocene and Holocene numerical dates by a range of methods and finally to correlate the geochemical signatures with magmatic evolution

The first chapter provides a literature review and an overview of the geographical setting and previous geochemistry and geochronology of the study site. In addition, this first chapter contains a brief introduction to the field of igneous geochemistry with emphasis on isotopic systems and the geochronological methods used in subsequent chapters. The second chapter deals with the geochemistry of the Quaternary continental back-arc with particular attention given to the Llancanelo and the Payún Matrú volcanic fields. Furthermore, in this chapter, maps

of spatial geochemical distribution are presented to illustrate variations in geochemical signatures.

Chapter three is concerned with an example of a long basaltic flow, which poses a puzzling question as to how it flowed for more than 160 km. Generally, long basaltic flows occur in intraplate tectonic settings and are related with hotspots such as the long flows in Northern Queensland, Australia and in Iceland. Accordingly, this chapter analyses the chronology, geochemistry and morphology of the long Pampas Onduladas basaltic flow. The fourth chapter investigates a Holocene volcanic cone and corresponding basaltic flow (the Santa Maria volcano). For this chapter, U-series analysis was conducted in order to determine the magmatic origin of the most recent eruption in this continental back-arc. The final chapter (Chapter 5) brings together the Quaternary chronology and the geochemistry in order to explain the evolution of the continental back-arc. The chronology is derived using noble-gas surface exposure dating, $^{40}Ar/^{39}Ar$, and thermoluminescence. Finally the last pages present a major summary of the thesis and presents conclusions obtained from this investigation.

Thesis Outline

The thesis has a journal article style with only chapter one "Literature review" not having a manuscript format. Chapter 2 is published in *Lithos* (see also the published version, Appendix D) and Chapter 3 is in-press in the *Journal of Volcanology and Geothermal Research*. These two chapters have been re-formatted from the original published version in order to conform to thesis requirements, in addition within the thesis they are cited as Chapter 2 (Espanon et al., 2014b) and Chapter 3 (Espanon et al., in-press). Chapters 4 and 5 have a manuscript format; but have not yet been submitted for publication. Chapter 6 includes a synthesis of the findings and results. The supplementary material for the chapters is included at the end of each chapter. There are 4 appendices at the end of the thesis: Appendix A, contains a declaration of co-author contributions to each of the manuscripts; Appendix B, contains several geological maps of the northern and central Payenia Basaltic Province; Appendix C, is a published article from the author, from a previous investigation; Appendix D and E are published articles from the author from the current investigation (Chapter 2 and 3 of this thesis).

Chapter 1:

Literature Review

1.1. History of volcanoes and volcanology

Magmatic processes have been shaping the Earth since its beginning, modifying its interior, exterior and atmosphere. Nevertheless, it is difficult to obtain information regarding the earliest volcanic eruptions on Earth as there are very few places on Earth where Archaean (2.5 to 4.0 Ga) rocks are found (< 15% of present continental areas) (Bowring and Williams, 1999). The Earth's primary crust was basaltic in composition (Taylor, 1992), however, it has not been preserved in its original mafic composition. Additionally, many volcanic sequences from the Palaeozoic and Mesozoic have been identified and studied in different parts of the world along with the most recent and best constrained Cenozoic volcanism. The volcanism in the last 2.6 Ma (Quaternary) is better understood not only because the rocks are slightly altered but also because since humans started to inhabit the Earth, volcanic eruptions have been recorded by different means such as footprints, wall paintings and written reports. In fact the oldest *Australopithecus* footprints (3.7 Ma) are recorded in volcanic ash within the East African rift (Harris, 2000). Volcanic deposits have exclusive preservation characteristics and can also be dated readily. In addition, some volcanic rocks (obsidian, ignimbrite and basalts) have been widely used by ancient civilisations to make tools, ornaments and buildings. The evidence and the connection between ancient civilisations and volcanoes are quite close as early people were using these resources. The earliest known visual record of a volcanic eruption comes from a wall painting from a shrine at Catal Huyuk (central Anatolia, Turkey) dated to 6200 B.C. (Figure1.1; Mellaart, 1967). Other historic and prehistoric volcanic eruptions have been preserved by mud flows, pyroclastic deposits and lava flows that have been only recently discovered and studied.

Understanding the processes involved in producing magma or how volcanoes are formed was mainly associated with mythology in many early societies such as in Central and South America, Indonesia and Europe. In the 5th century BC Anaxagoras, a Greek philosopher, proposed the first scientific hypothesis concerning volcano: "volcanoes were caused by great winds inside the Earth". This first hypothesis was then acquired and modified by a Roman philosopher, Seneca whose original contribution to volcanism was that the heat produced from volcanoes was the result of ignitable substance inside the Earth. Scientific ideas to explain the origin of volcanoes were many times challenged by the growing Christian religion, which believed that volcanoes were the remainder of hellfire (see The History of Volcanology chapter of Sigurdsson, 2000). By the late 17th century, René Descartes established that volcanism was due to original or primordial heat in the Earth. During this time the Neptunist and the Plutonist theories were rising, the former claiming that columnar basalts were formed by precipitation from a primordial ocean and the later proposing that basalts owes its origin to solidification of

magma. During the late 18th century the Plutonist hypothesis was dominant as geologist made experiments and undertook field expeditions. Volcanology was established as one sub-discipline of Earth Sciences and Poulett Scrope wrote the first volcanology book in 1825. Many different aspects of volcanology were formulated during the 19th and 20th centuries including hypotheses of magmatic sources, the role of water and gases in magma and the physical properties of magma ascent. During the 20th century developments in analytical techniques have help volcanology in understanding the internal processes occurring inside volcanoes and with the development of accurate dating methods a better constraint on ancient volcanic eruptions has been possible.

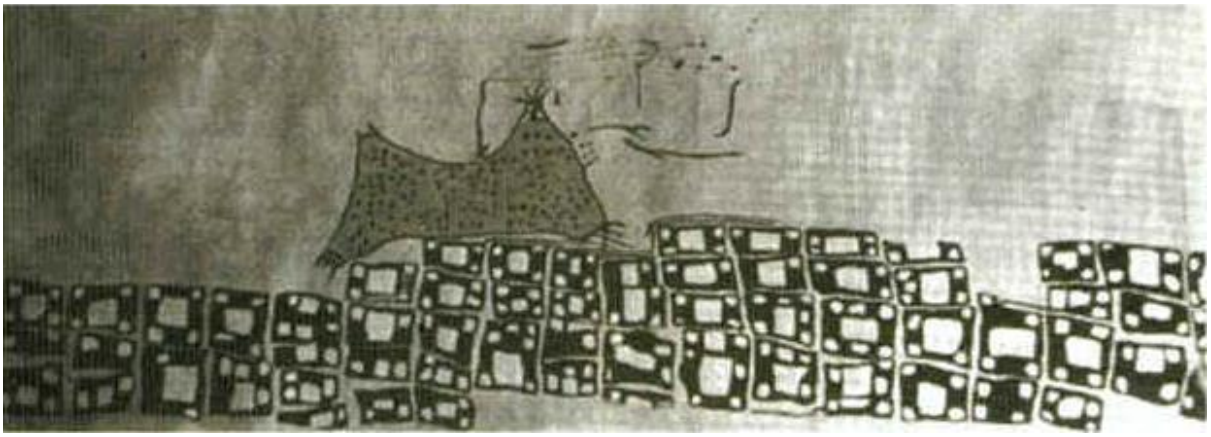

Figure 1.1 Representation of a wall painting from Anatolia, Turkey and which is the first known volcanic representation by ancient civilisations. (from Mellaart, 1967)

1.2. Continental back-arc volcanism

Back-arc volcanism occurring on convergent continent margins is not as common as on convergent oceanic margins and it has not been as thoroughly described. Therefore, describing the basaltic volcanism occurring behind the volcanic arc on a continental plate is restricted to particular examples. This type of volcanism is not commonly described, however, it is briefly described in a volcanology textbook by Schmincke as being dominated by sporadic scoria cones up to a 400 km inland from the continental convergence zone and having a chemical composition little disturbed by slab dehydration (Schmincke, 2006, Ch: 8, p: 119). This type of volcanism has been related to a low degree of partial melting as well as to a high K content and low SiO_2, hence a primitive magmatic composition (Walker, 1981).

Magmas associated with continental convergent margins are geochemically more variable than magmas erupted along an oceanic island arc. The variability of the magmas on a continental plate is related to the diverse composition of the continental crust compared to the oceanic crust and to the age of the continental lithosphere. Generally, the continental lithosphere is older than the oceanic and hence it becomes modified through time and by ascending magma. The

variability can be also associated with the thickness of the continental crust as thicker crust (less dense) would act as a barrier for ascending magma, which in time will modify its chemical composition. One of the ways of addressing the issue of assessing the characteristics of continental back-arc volcanism is to evaluate common characteristics among areas where back-arc continental volcanism is evident. Areas of continental back-arc are found in northern Argentina (see Kay et al., 1994), northern Patagonia such as the Crater Basalt volcanic field (see Haller, M., 2000 and Massaferro et al., 2006), in southern Patagonia such as the the Palei-Aike volcanic field (see Skewes and Stern, 1979) and other back-arc fields in Central and South America.

Continental back-arc volcanism has been evident in South America since the Miocene, developing as large areas of mafic volcanic flows. Back-arc volcanism is associated with extension in the overriding plate. In South America, the extension processes are not as strong as in oceanic back-arcs such as along the western Pacific, resulting from the continental nature of the South American plate. Generally, back-arc volcanism, whether continental or oceanic, is associated with crustal thinning and basaltic volcanism. Continental back-arc volcanism has been recognized along the western part of South America: in the southern part of the NVZ in Equator (Barragan et al., 1998), in the southern part of the CVZ in northern Argentina (Kay et al., 1994), in the SVZ several back-arc volcanic centers have been described such as Payenia Basaltic Province, Tromen, Laguna Blanca and Crater basalt volcanic field (Figure 1.3) and also in the AVZ such as, the Palei-Aike volcanic field (Figure 1.2) has been described by Skewes and Stern, (1979).

1.3. South American volcanism

Evidence for old Precambrian magmatic activity in South America is found among the eastern stable margin of the continent (part of the Brazilian craton), as terrains were accreted by previous subduction resulting in magmatic arcs and orogenic belts. During the Palaeozoic (540 to 250 Ma), Gondwana was the southern continent after Pangea broke up, consisting of South America, Africa, Antarctica, Australia and India. During the Palaeozoic, several terrains were incorporated to the northern and to the southern part of the South American portion of Gondwana, one of the latest being the Patagonian terrain which was obliquely accreted in the middle to late Palaeozoic (Ramos, 1988). During the late Permian, rapid convergence and subduction were taking place along the western margin of Gondwana, followed by a period of extension, leading to silicic magmatic activity (see summary in Kay et al., 1989).

Later volcanism in South America has been associated with the subduction zone on its western margin since the mid-Jurassic until present resulting from the western migration of South America as the southern Atlantic Ocean was opening (see summary in Kay et al., 1989). In the Early Cretaceous (~140 Ma) subduction was established along the western margin and the western cordillera started to form. Up to the Paleogene, the volcanic front migrated eastward resulting from tectonic erosion of the continent margin by subduction. The Cenozoic volcanism

of South America has been strongly influenced by changes in subduction geometry. Approximately 27 Ma ago, a major change occurred in the convergence between the Nazca and South American Plates (Figure 1.2), changing from oblique to almost perpendicular as the Farallon plate broke into the Cocos Plate and Nazca Plate (Cande and Leslie, 1986). The change in subduction geometry also increases the convergence rate producing an increase in magmatism. Furthermore, along the northern Andes, the change in subduction rate resulted in mountain building (Barberi et al., 1988). In the central Andes, the change in subduction geometry and rate resulted in compression followed by crustal shortening, uplift of the plateau (~10 Ma) and crustal thickening (see review of Stern, 2004 for references). In the southern Andes, extensional processes were occurring simultaneously with fore-arc, intra-arc and back-arc volcanism (see review of Stern, 2004 for references). Volcanism has occurred in the main Andean arc since the Miocene, except for some areas where subduction occurs at a very low angle (Figure 1.2).

The volcanic areas in South America are grouped following the regional classification: the Northern Volcanic Zone (NVZ), the Central Volcanic Zone (CVZ), the Southern Volcanic Zone (SVZ) and the Austral Volcanic Zone (AVZ) (Figure 1.2). The flat subduction areas are located between the NVZ and the CVZ and the CVZ and the SVZ. The boundary between the SVZ and the AVZ is delimited by the subduction of the Chile Rise (Figure 1.2). The Chile Rise constitutes the plate boundary between the Nazca Plate and the Antarctic Plate; hence the AVZ is different to the other volcanic zones especially in the subduction rate. The Nazca Plate subducts faster at a rate of 6 to 7 cm/a (Kendrick at al., 2003), while the Antarctic Plate subducts at a rate of 2 cm/a (DeMets et al., 1990). Each of the four volcanic zones has particular characteristics and has been further sub-divided according to specific internal features. General characteristics among the four volcanic areas are summarised in Table 1.1.

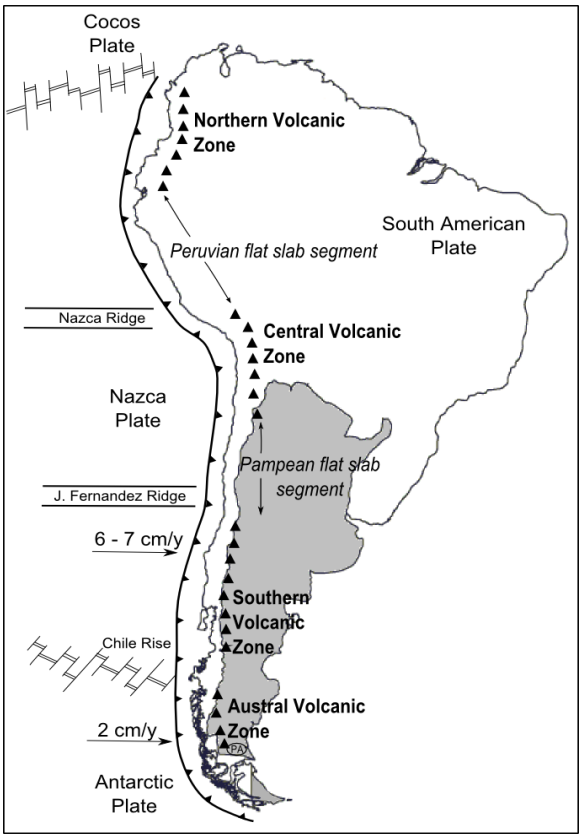

Figure 1.2. Distribution of South American volcanic zones with general tectonic features. PA; Pali-Aike volcanic field.

Table 1.1. Characteristics of the four main volcanic zones of South America. Note: [1] denotes decreases southwards and [2] denotes increases southward. Modified from Stern 2004.

	Northern Volcanic Zone	Central Volcanic Zone	Southern Volcanic Zone	Austral Volcanic Zone
Subducting Plate	Nazca	Nazca	Nazca	Antarctic
Distance from trench	~380 - 300 km [1]	240-300 km	290 – 270 km [1]	~260 – 200 km
Age of subducted ocean floor	12 – 20 Ma [2]	~60 Ma	45 – 0 Ma [1]	12 – 24 Ma
Subduction rate	6 - 8 cm/a	~6 cm/a	6 – 8 cm/a	2 cm/a
Angle of subduction	25° – 30°	25°	20° - 25° [2]	(Benioff zone not determined)
Depth below the arc to subducting slab	~150 – 90 km [1]	~ 120 km	120 – 90 km [1]	(Benioff zone not determined)
Crustal thickness	40 – 55 km	70 km	50 km to 30 – 35 km [1]	35 km

1.3.1. The Southern Volcanic Zone (SVZ) and its evolution

The Southern Volcanic Zone comprises the area between 33°S and 46°S along the main Andes. The northern end is delimited by the flat subduction segment from 27°S to 33°S while the southern end is bounded by the Chile rise, which also constitutes the southern limit of the Nazca plate (Figures 1.2 and 1.3; see review of Stern, 2004 for references). The SVZ has been subdivided into the northern (NSVZ), transitional (TSVZ), central (CSVZ) and southern (SSVZ) southern volcanic zones (Figure 1.3). The NSVZ is the zone with least volcanoes; they are aligned north-south and are located 290 km from the trench. The TSVZ is relatively wide ~200 km and includes the continental back-arc. In this zone, the arc front is ~ 270km east of the trench. Pleistocene and Holocene continental back-arc volcanism is most abundant in this region. The CSVZ is wider in its northern part, decreasing southwards from 120 km to 80 km. The age of oceanic crust subducting also decreases southwards, in particular south of the Valdivia Fracture Zone it is <18 Ma (Herron et al., 1981). The SSVZ is the region where the youngest oceanic crust subducts. This region is located ~270 km east of the trench and back-arc volcanism includes the Crater Basalt volcanic field.

Subduction along the Central Southern Volcanic Zone began in the late Carboniferous (~305 Ma; Willner et al., 2004) along the western margin of Gondwana. Prior to which, the area was part of a passive margin. Evidence for this comes from turbiditic Palaeozoic sedimentary sequences found along the margin, which were later metamorphosed due to magmatic activity and activation of the western margin (Hervé, 1988). After the onset of subduction deformation, magmatic activity and metamorphism increased considerably. One of the main faults that developed in this area during this time was the Lanalhue Fault (~38°S), which developed oblique to the collision zone (Ernst, 1975). During the Permian and Triassic, the area north of the Lanalhue Fault was mainly subjected to extension and rifting related to the westward rollback of the slab (see summary by Kay et al., 1989) and dominated by metamorphic sequences. South of the fault, the dominant process was accretion (see review of Glodny et al., 2006 for references). In the Jurassic, the Andes started emerging on the western side of the margin while on the eastern side the African continent was separating from South America. The magmatic activity in the Jurassic was mainly confined to the Andes and the back-arc, while part of the fore arc basin was submerged (see review of Glodny et al. 2006 for references). During the Cretaceous, abundant magmatism was occurring along the southern Andes. In the late Paleocene to Eocene, part of the Andes was still submerged, despite its evident uplift (Vergani et al., 1995). During the Miocene, the angle of subduction changed (Section 1.3) and the Liquiñe-Ofqui Fault Zone (Figure 1.3) developed (Cembrano et al., 1996), which is a major tectonic feature controlling the Pleistocene to Holocene volcanism in the SVZ. This strike-slip fault dextral displacement is almost parallel to the main volcanic arc (Cembrano et al., 1996). In addition, there are many other relatively small faults that have also contributed to control the location and orientation of volcanoes in this area. The volcanic front moved ~ 500 km eastward in the Miocene north of the Cortaderas lineament (Figure 1.4). This shift in volcanism has been

interpreted to be caused by a period of shalower subduction than the current subducting angle (Kay et al. 2006a), which was segmented at approximately 33°S. To the north, is the present day Pampean flat slab segment (Figure 1.2), while south of 33°S the subducting slab steepened in the Pliocene producing the extension processes and facilitating the back-arc volcanism.

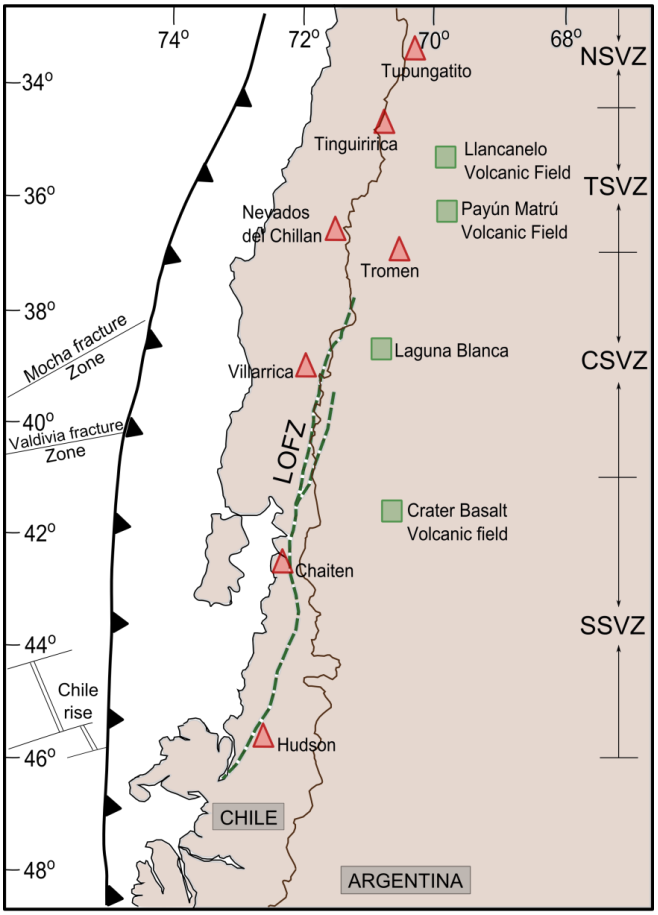

Figure 1.3. Segmentation of the Southern Volcanic Zone showing selected volcanic cones from the the arc and some back-arc volcanic fields for reference. The segments are: Northern Southern Volcanic Zone (NSVZ), Transitional Southern Volcanic Zone (TSVZ), Central Southern Volcanic Zone (CSVZ) and Southern Southern Volcanic Zone (SSVZ). Note the position of the Liquiñe-Ofqui Fault Zone. (green dashed line, LOFZ). Red triangles represent selected volcanoes from the arc and green squares represent some of the the continental back-arc volcanic fields.

1.3.2. Evolution of the continental back-arc in southern Mendoza

The volcanism in the southern Mendoza continental back-arc is part of the Payenia Basaltic Province (PBP) (Polanski, 1954) later called the Andino-Cuyana Basaltic Province (ACBP), by Bermudez and Delpino (1989). The PBP has an area of approximately 16,000 km^2 with more than 800 volcanic cones; the majority being monogenetic (Llambias, 2010). Nevertheless, there are some polygenetic volcanoes such as Nevado, Payún Matrú, Payún Liso and Chachahuén (Figure 1.4), characterised by explosive eruptions, with only Payún Matrú presenting a collapse caldera.

Magmatic activity has occurred since the early Miocene in southern Mendoza and northern Neuquén provinces (Kay et al., 2006a, b, Kay et al., 2013). This early volcanism had an ocean island basalt (OIB)-like composition which changed to arc–like in the late Miocene associated with a period of shallow subduction (Kay et al. 2006a). The shallow subduction is mainly characterised by the Chachahuén volcanic complex (Figure 1.4) located ~ 500km from the trench, while during this period contractional deformation occurred producing the uplift of the San Rafael Block (Figure 1.4; Kay et al. 2006a). During the latest Miocene and Pliocene, the southern part of this shallow subduction was separated from the northern part at ~33°S (Folguera et al., 2011), resulting from the subduction of the Juan Fernandez Ridge (Figure 1.2). At present, the northern part is subducting at a very shallow angle producing the Pampean flat slab which extends from 27° to 33°S (Figure 1.2). In the southern part, the separation at ~33°S resulted in a steepening of the subducting slab, inducing magmatism south of this latitude. Due to this steepening, back-arc volcanism was triggered by injection of hot asthenosphere under the South American Plate (Folguera et al., 2011). Since the Pliocene and with the increase in the angle of subduction, the deformation of the back-arc has been extensional. The extensional regime is linked with slab roll back (Folguera et al., 2009), therefore facilitating magma ascent as the lithosphere thins. The Quaternary continental back-arc province in southern Mendoza has been divided into several volcanic fields, the Nevado, Llancanelo, Payunia and Río Colorado volcanic fields (Figure 1.4; See Appendix B for a general overview).

- The Nevado volcanic field (Figure 1.4) is dominated by monogenetic basaltic volcanism with a main stratovolcano, the Nevado volcano, which is also the highest point in the region at 3980 MASL. The Nevado volcanic field was active in the late Pliocene to middle Pleistocene (from 2.83 ± 0.04 Ma to 0.79 ± 0.06 Ma; Gudnason et al., 2012; Appendix B, Figure 4). According to geochemical studies, the lavas erupted in the Nevado volcanic field were highly influenced by lower continental crustal contamination (Søager et al., 2013).
- The Río Colorado volcanic field is composed of two distinct types of volcanism. One described by the Chachahuén volcano having an arc-like geochemical signature suggesting that it was active during the flat slab subduction period, in the late Miocene (Kay et al., 2006a, b). The second defined by younger basaltic flows erupted in the Pleistocene showing a high enrichment in incompatible elements which has been interpreted as been associated with an enriched mantle similar to an Ocean Island Basalt-type.
- The Llancanelo volcanic field is dominated by basaltic volcanism and was active during most of the Pleistocene. There were two phreatomagmatic eruptions in this volcanic field corresponding to the Carapacho and Malacara volcanoes (Figure 1.4, Appendix B, Figure 2) producing large tuff deposits (Risso et al., 2008).
- The Payún Matrú volcanic field has been active during much of the Quaternary with some flows being less than 2 ka old (Marchetti et al., 2014; Appendix B, Figure 3). Most of the volcanism in the Payún Matrú Volcanic field is alkali basaltic with only sporadic

felsic volcanism associated with the Payún Matrú caldera. The oldest part of this volcanic field is located on the eastern side of the Payún Matrú caldera and it is also where the longest Quaternary flow on Earth is found (181 km from its basal point; Pasquaré et al., 2008).

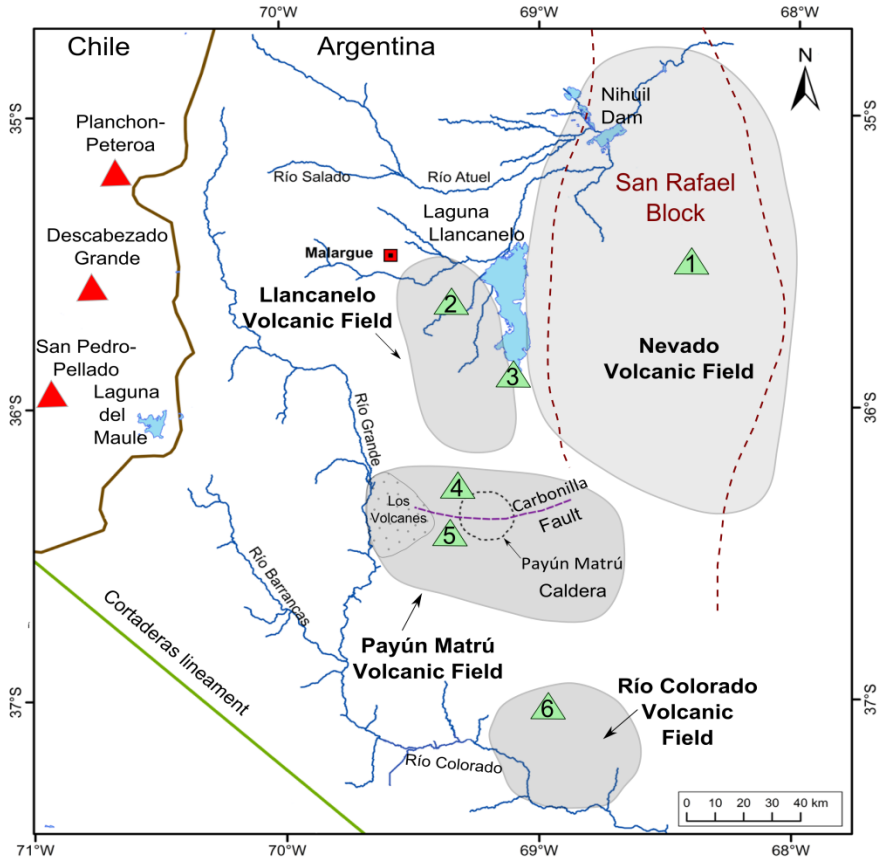

Figure 1.4. Location of the volcanic fields in the Payenia Basaltic Province. Green triangles are some of the main volcanic cones in the continental back-arc: 1: Nevado volcano, 2: Malacara volcano, 3: Carapacho volcano, 4: Santa Maria volcano, 5: Payún Liso volcano and 6: Chachahuén volcano. The dark brown dashed line represents the eastern and western limits of the San Rafael Block. The grey dotted area in Payún Matrú volcanic field corresponds to the area of Los Volcanes.

1.3.2.1. Geochemistry of the continental back-arc in southern Mendoza

The Payenia Basaltic Province (PBP) covers a vast area where most of the volcanic products are alkali basalts (Bermudez and Delpino, 1989; Germa et al., 2010; Llambías et al., 2010; Søager et al., 2013). These basalts have diverse geochemical signatures, for instance the Nevado volcanic field has been described by Søager et al. (2013) as having up to 70% lower crustal contamination. While the area of Llancanelo volcanic field, has been modified at some extent by processes associated with the subducting Nazca Plate (Bermudez and Delpino, 1989; Søager et al., 2013, Jacques et al., 2013). Llancanelo volcanic Field has been described as having high Mg# and a relatively low concentration of high field strength elements (HFSE) (Bermudez and Delpino, 1989). This field has also been defined as transitional by Søager, et al.

(2013) as it contains geochemical signatures associated with the strictly back-arc volcanism north of Llancanelo volcanic field and the intraplate volcanism of the southern Payún Matrú volcanic field.

In the case of the Payún Matrú volcanic field, the geochemistry indicates an increase in HFSE related to an enriched mantle (Jacques et al., 2013). Typical geochemical signatures associated with arc magmatism are absent, as diagnostic trace elemental ratios such as La/Ta and Ba/Ta are low (Kay et al., 2004; Germa et al., 2010; Jacques et al., 2013; Søager et al., 2013; Søager and Holm, 2013;). The geochemical signatures of the Payún Matrú volcanic field have been interpreted as typical of an intraplate setting (Bermudez and Delpino, 1989; Kay et al., 2004; Germa et al., 2010; Søager et al., 2013; Søager and Holm, 2013; Jacques et al., 2013). In addition, it has been proposed that the mantle source for the Payún Matrú volcanic field lavas is a plume-like upwelling mantle based on geochemical (Germa et al., 2010; Hernando et al., 2012) and geophysical studies (Burd et al., 2008).The chemical composition of the basalts erupted in the Payún Matrú volcanic field is associated with an enriched mantle (Ocean Island Basalt-like composition) related with peridotite melts at low pressure (Søager and Holm, 2013).

1.3.2.2. Geochronology of the continental back-arc in southern Mendoza

The volcanic activity in Southern Mendoza commenced in the early Miocene with intraplate volcanism and without influence from the subducting slab (Kay et al., 2006a). During this period the magmas erupted were derived from an OIB-like mantle (Dyhr et al., 2013a). In the late Miocene an inversion took place as the volcanic arc migrated to the east approximately 500 km from the trench. The arc migration resulted in volcanism with an arc-like composition approximately 8-5 Ma as in the Chachahuén volcano (Figure 1.4) (Kay et al., 2006b). Due to the low angle of subduction, the volcanic arc during the late Miocene migrated towards the east close to the Chachahuén area; hence the rocks from this period have an arc-like geochemistry (Kay et al., 2006b). During the Pliocene, the subducting Nazca Plate increased its angle of subduction returning the volcanic arc to its current location and back-arc volcanism was produced (Kay et al., 2006a).

In the late Pliocene and early Pleistocene the Nevado volcanic field (Figure 1.4; Appendix B) was active. This field has subduction-related geochemical signatures and ranges in age from 2.83 ± 0.04 Ma to 0.79 ± 0.06 Ma ($^{39}Ar/^{40}Ar$ dating technique at 2σ confidence level; Gudnason et al., 2012). The Llancanelo volcanic field was active from 0.39 ± 0.07 Ma ($^{39}Ar/^{40}Ar$ dating technique at 2σ confidence level; Espanon, 2010) to 73.7 ± 1.1 ka (using cosmogenic ^{3}He from Espanon et al., 2014a; Appendix B). In addition, Gudnason et al. (2012) produced two ages 0.28 ± 0.02 Ma and 0.16 ± 0.07 Ma from this volcanic field using $^{39}Ar/^{40}Ar$ dating method. The ages for the Llancanelo volcanic field suggest that it was active during the mid and late Pleistocene.

The oldest eruptions dated from the Payún Matrú volcanic field come from basalts from the Fortunoso area and are Miocene in age. Some of these rocks have been dated to 20.7 ± 0.30 Ma, 8.62 ± 0.17 Ma ($^{39}Ar/^{40}Ar$ method at 2σ confidence level; Dyhr et al., 2013a) and 6.80 ±0.03 Ma (Gudnason et al., 2012). The early Miocene lavas have geochemical signatures similar to an OIB-type while the late Miocene rocks are transitional between an OIB-like and arc-like composition (Dyhr et al., 2013b), similar to the Chachahuén volcano. The Quaternary volcanic activity in the Payún Matrú volcanic field possibly started on the eastern side of the Payún Matrú caldera, as this area is dominated by early to middle Pleistocene basalts (see review of Ramos and Folguera, 2011 for references), although there are no radiometric ages from this area. Most of the dating from the Payún Matrú volcanic field comes from the Payún Matrú caldera (Figure 1.4) and from the area to the west of the caldera (Appendix B). The Payún Matrú caldera was described by Hernando et al. (2012) as, being the result of mingling and mixing in the crust from an original mafic magma. Recently the activity in the Payún Matrú caldera has been extended to 701 ± 11 ka based on $^{40}Ar/^{39}Ar$ dating (Hernando et al., 2014a). Furthermore, the caldera-forming event occurred between 168 ± 4 ka and 82 ± 2 ka, (K/Ar dating method at 1σ confidence level; Germa et al., 2010) while the youngest flow after the caldera collapse is 7 ± 1 ka obtained from a trachyte flow inside the caldera (Germa et al., 2010).

The Quaternary basaltic volcanism in the Payún Matrú volcanic field has been dated to 0.32 ± 0.05 Ma ($^{39}Ar/^{40}Ar$ method; Gudnason et al., 2012) and 0.23 ± 0.01 Ma (K/Ar method; Germa et al., 2010) from the Río Grande and from Payún Liso volcano, respectively (Figure 1.4). The youngest volcanism in the Payún Matrú volcanic field is found in the area of Los Volcanes (Figure 1.4; Appendix B). Marchetti et al. (2014) produced an age of <2 ka (surface exposure date using cosmogenic ^{3}He) from a flow west of the Payún Matrú caldera. In addition, Espanon et al. (2014a) produced two surface exposure ages of 6.6 ± 1 ka and 4.0 ± 1.4 ka using cosmogenic ^{3}He and ^{21}Ne respectively, from the same area. Two samples analysed for surface exposure dating using cosmogenic ^{3}He and ^{21}Ne from Santa Maria volcano (Figure 1.4) have cosmogenic nuclide concentrations below the detection limit and suggesting that this volcano is very young (Espanon et al., 2014a). Furthermore, aboriginal oral tradition from the region suggests that the area was active during historic times (Groeber, 1946).

1.4. Geochemistry and its applications to volcanology

1.4.1. Introduction to igneous geochemistry

The term geochemistry was first used in 1838 by the Swiss-German chemist Christian Schönbein. The first publication on the distribution of major elements distribution in the Earth's continental crust was published by Frank Wigglesworth Clarke (1888). The purpose of geochemistry was established by Goldschmidt (1933) as the principle to determine the composition of the Earth and its parts as well as to discover the laws that control the distribution of individual elements. In the 1930s Goldschmidt contributed to understand the distribution of

elements in the Earth and also classified different elements according to their affinity to oxygen, iron, sulfur or elements that are gases or rare gases concentrated in the atmosphere.
A routine geochemical analysis of an igneous rock gathers information from major elements, which are the main constituents of rocks, and from trace elements, which are the elements in low concentration generally less than 0.1%. These analyses generally result in trends such as for example that potassium content of subduction related rocks increases in a systematic manner with distance from the trench. The trace elements provide information regarding the amount of melting, residual minerals present during melting and the elemental abundance of the original source rock. Furthermore, due to their low concentration they are highly susceptible to changes in pressure, temperature, degree of fractionation and fluid interaction.

1.4.2. The use of isotopes in igneous geochemistry

Information concerning magma genesis and evolution can be obtained from radiogenic and stable isotopes. Radiogenic isotopes are generated by radioactive decay while the stable isotopes do not decay over time. The most common radiogenic isotopic systems in igneous geochemistry are $^{87}Sr/^{86}Sr$, $^{143}Nd/^{144}Nd$ and $^{207}Pb/^{204}Pb$. Radiogenic ^{87}Sr is produced by natural decay of ^{87}Rb; which has a half-life of 48.8×10^9 years (Neumann and Huster, 1974). This decay rate is very slow and hence produces very low concentrations of ^{87}Sr over time; however, as the ^{87}Sr isotope abundance increases over geologic time the $^{87}Sr/^{86}Sr$ ratio also increases. In addition, the ^{87}Sr production will be proportional to the concentration of Rb which is one of the most incompatible elements in the mantle hence primitive magmas show low Rb/Sr ratios compared with intermediate to silicic magmas derived from the crust or magmas that have been contaminated by crustal material. Furthermore, older crust will also have higher $^{87}Sr/^{86}Sr$ ratio as a consequence of the longer time on which ^{87}Rb has decayed. In the case of the $^{143}Nd/^{144}Nd$ isotopic system, ^{143}Nd is produced by radioactive decay of ^{147}Sm which has a half-life of 1.06×10^{11} years (Lugmair and Marti, 1978). The ^{147}Sm decay rate is even slower than the ^{87}Rb hence the production of ^{143}Nd is slow, resulting in small variations over geologic time scales. In older and potentially altered rocks, $^{143}Nd/^{144}Nd$ does have advantages over $^{87}Sr/^{86}Sr$ in that the former is less vulnerable to modification by hydrothermal alteration and weathering. In the case of the $^{207}Pb/^{204}Pb$ system, ^{207}Pb is the last product of the radioactive ^{235}U decay chain; therefore it is stable (Bourdon et al., 2003). These isotopic systems provide information regarding the origin of the magma, as well as mantle and crustal evolution. The three commonly applied isotopic systems may also be used as geochronometers as the concentration of daughter product is proportional to the original concentration of parent isotope and its decay rate during time.

The most commonly analysed stable isotope in volcanic rocks is oxygen. Oxygen has 3 isotopes ^{16}O, ^{17}O and ^{18}O; the most abundant is ^{16}O. The heavier ^{18}O can constrain crustal contamination, alteration reservoir conditions and magma mixing of volcanic rocks. Magmatic rocks and magmas derived from the mantle typically have $\delta^{18}O$ values (a measure of $^{18}O/^{16}O$) between +5.4 and +5.8‰, whereas rocks from the continental crust have average $\delta^{18}O$ values

+8‰ (when not altered by meteoric water) (James, 1981), while sedimentary rocks it is much higher. Therefore, crustal contamination of an unaltered (not altered by meteoric water) crust results in higher $\delta^{18}O$. Meteoric water and seawater have low $\delta^{18}O$ values. Hydrothermal alteration above 300°C is recorded as a reduction in the oxygen isotopic composition in the rock whereas weathering (i.e. lower temperature alteration) produces higher than initial $\delta^{18}O$ values in such rocks.

1.4.3. Introduction to uranium-series and their applications to magmatism

The beginnings of U-series analysis can be traced to the end of the 19th century when Marie and Pierre Curie discovered the element radium and radioactivity. Uranium and thorium decay at a constant rate, producing daughter elements that are also decaying at lower but constant rates until they reach the stable isotope of Pb. The three commonly used decay chains are ^{238}U, ^{235}U and ^{232}Th (Figure 1.5) the daughter products of these decay chains have different half-lives which provide a wide spectrum of usages in several fields (Bourdon et al., 2003). U-series have two decay chains starting with ^{238}U and ^{235}U, while the Th-series start with ^{232}Th and ending with stable Pb isotopes ^{205}Pb, ^{207}Pb and ^{208}Pb respectively (Figure 1.5). However, the ^{238}U and ^{235}U chains are the most widely used for magmatic processes. Parent-daughter radioactive systems record fractionation over timescales of approximately 300 ka (^{238}U-^{230}Th system) ,~8 ka (^{230}Th-^{226}Ra system) and 100's of thousand years such as (^{235}U-^{231}Pa system) (based on half-lives from Cheng et al., 2000; Holden, 1990; Robert et al., 1969, respectively). The fundamentals of this method are based in the concept that the parent isotope decays into the daughter isotope at a known rate, defined as the "half-life"; this decay is produced by alpha or beta emission. After approximately 5 half-lives, in a closed system, the rate of decay of daughter being produced by decay of its parent, would be the same as the rate of decay of the daughter decaying into the next daughter down the chain; this is termed "secular equilibrium". In addition, all the isotopic systems of a chain would reach equilibrium after 1 Ma, provided that the system is closed (based on the half life of ^{234}U from Cheng et al., 2000).

To assess the different time scales associated with melting and magma transport rates as well as residence time the ^{238}U and the ^{235}U decay chains are commonly used. In the case of the ^{232}Th decay chain (Figure 1.5) the daughter products have relative short half-lives hence they can only be applied to investigate volcanic eruptions that occurred >29 years ago, after this time ^{228}Ra (the first daughter in ^{232}Th decay chain with $t_{1/2}$ = 5.75 a) will reach secular equilibrium (Bourdon and Sims, 2003). Magmatic processes are diverse and the time required for the magma to form, ascend and finally extrude, range from 1000 years to more than 100,000 years depending on the geological setting, pressure, temperature, porosity and chemical composition (Dosseto et al., 2011). Therefore the preferred isotopes covering this time range are the daughter products of the ^{238}U and ^{235}U decay chains, such as ^{234}U, ^{230}Th, ^{226}Ra and ^{231}Pa respectively, which are of particular interest, as they provide information regarding melt transport time scales and crustal residence time (Condomines et al., 2003). In this sense, during

magma ascent, in the case of the parent isotope ^{230}Th, the daughter ^{226}Ra is produced. Since the half-live of ^{226}Ra is 1600 years, secular equilibrium is attained after 5 half-lives or ~8000 years (Gill and Condomines, 1992). Therefore, if a basaltic rock sample has excess ^{226}Ra over ^{230}Th it can be directly inferred that this particular sample is less than 8000 years old and possibly that the ascent rate was relatively fast, in order to preserve the high ^{226}Ra excess from the reservoir.

One of the assumptions in using some of the isotopic systems provided by the U-series decay is that in the mantle all the systems are in secular equilibrium. This corresponds, to an activity ratio of 1 prior to melting. However, during partial melting, radioactive disequilibrium between the parent and daughter nuclides is produced as elements have different partitions coefficients. In addition, processes such as fluid addition (Turner et al., 2003), hydrothermal alteration (Villemant et al., 1996) and fractional crystallization among others, can create radioactive disequilibrium. By quantifying the disequilibrium between isotopes of the same decay chain, inferences can be drawn regarding the type of perturbation the system received in order to produce the observed disequilibrium. Furthermore, timescales for magmatic processes can be inferred from modelling radioactive disequilibria.

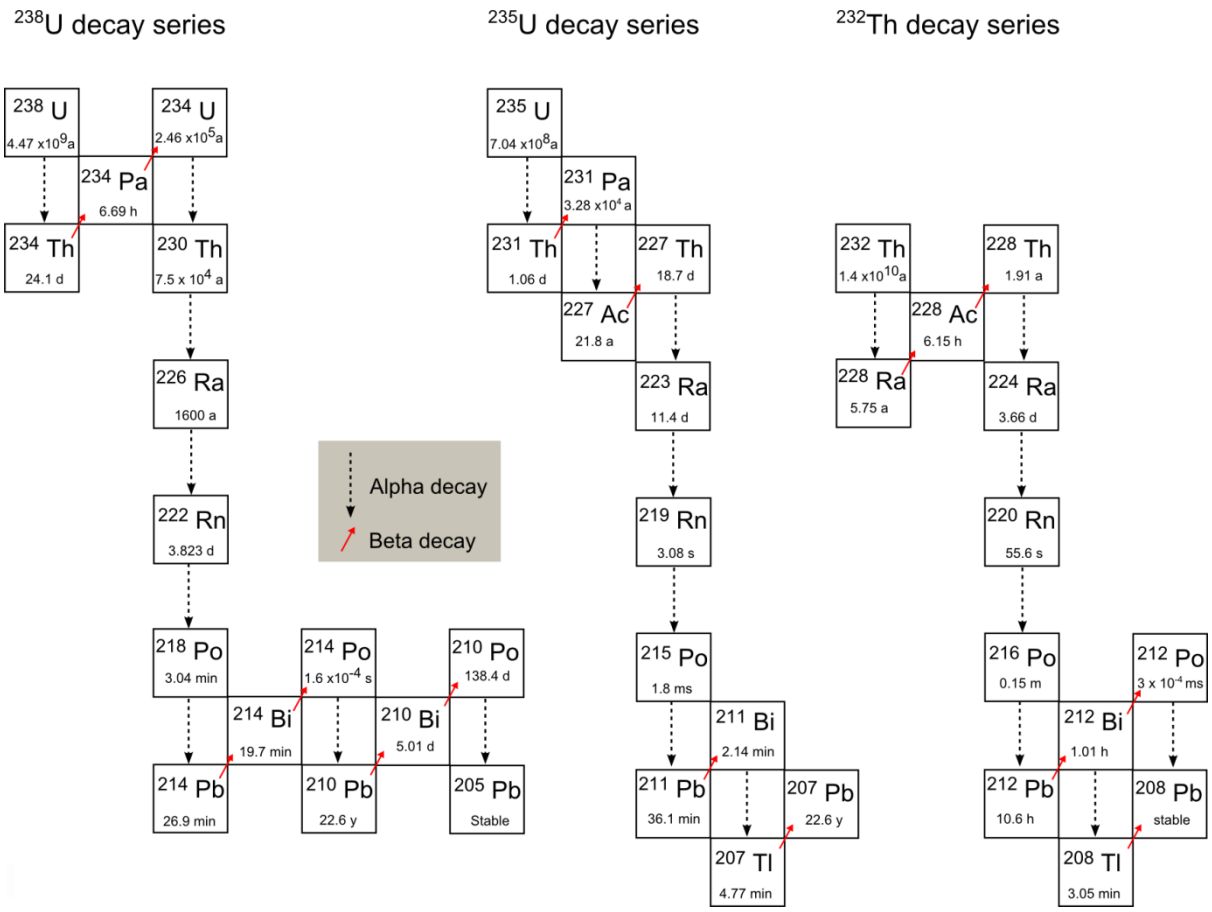

Figure 1.5. Uranium and thorium decay chain

Nevertheless, the concept is not that simple as there are many processes that need to be considered

that could produce an excess of the daughter isotope. In one of the most common volcanic settings, oceanic-continental convergent margins, fluid-mobile elements such as U and Ra are enriched over Th (Turner et al., 2000). Hence, one of the many uses of U-series is to provide timescales for fluid addition in volcanic arc settings as well as to provide times scales for magma residence time in the crust and subsequent fractionation. Furthermore, one of the most characteristic features of U-series is that the isotopic systems behave differently; in this sense, the activity ratios (^{230}Th/^{232}Th) and (^{238}U/^{232}Th) increase with increasing partial melting, while ^{226}Ra does not depend on the degree of partial melting degree (Gill and Condomines, 1992). Once the magma starts to differentiate the activity ratios between the whole rock and the phenocryst will generally change due to different partition coefficients. By analysing U-series from phenocrysts, the timescales for differentiation can be inferred as well as insights into magma chamber zonation can be obtained (Gill and Condomines, 1992; Condomines et al., 2003; Dosseto and Turner, 2011). After differentiation in the magma chamber, magmas ascend resulting from depresuration; the ascent rate can be determined using isotopes of the U-series decay chain such as, ^{238}U - ^{232}Th - ^{226}Ra and ^{235}U – ^{231}Pa systems (Turner and Bourdon, 2011). In applying this approach, porosity plays a dominant role as highly porous melts will ascend at low velocity as there is more friction imposed, while those with low porosity will have the opposite effect. Nevertheless, high velocity ascent rates require channel flow in order to create a rapid pathway (Turner and Bourdon, 2011). Some of the minimum inferred ascent rates are 1-20 m/a, for mid-ocean ridge basalts, ocean island basalts and island arc basalts (IAB), using long half-life isotopes (U, Th and Pa). A maximum of 70 m/a, has been inferred for an IAB, using ^{226}Ra (Turner and Bourdon, 2011).

1.5. Geochronological methods

1.5.1. History and introduction to cosmogenic dating

In 1912 cosmic radiation was discovered by Victor Hess and its study was initially aimed to understand fundamental particle physics. Throughout the 1930s and until the 1950s, before man-made particle accelerators reached very high energies, cosmic rays served as a unique source of particles for studies in high-energy physics and led to the discovery of various subatomic particles, including the positron and the muon (Powell et al. 1959). The term “cosmic ray” was proposed by Grosse (1934) who suggested that cosmic radiation could produce radioactive nuclides at the Earth’s surface. In 1946, Libby, detected the presence of cosmogenically produced ^{14}C and ^{3}He. Three years later Libby and colleagues used ^{14}C to date carbonates and especially organic matter such as wood form Egyptian tombs (Libby et al., 1949). Six years later, Davis and Schaeffer (1955) observed that cosmogenic nuclides could be produced in minerals from rocks on the surface of the Earth, constituting the first approach to use terrestrial cosmogenic nuclides (TCN) for determining surface exposure ages. These

authors used radiogenic ^{36}Cl to determine the age of a rock from Cripple Creek, Colorado (Davis and Schaeffer, 1955). During the 1950s and 1960s most of the cosmogenic work was relegated to meteorites due to their high concentration of cosmogenic nuclides which were able to be detected by counting techniques (Lal, 1988).

Rocks on the surface of the Earth have low production rates of cosmogenic isotopes compared to meteorites therefore it was not until the development of accelerator mass spectrometry (AMS) in the 1980s that analysis of very low concentrations of cosmogenic nuclides become feasible. The interaction between cosmic radiations, Earth's complex geomagnetic field and the atmosphere were fundamental observations made in the 1950s and the 1960s, to determine in-situ production rates and to understand that cosmogenic nuclides production increases with altitude (Gosse and Phillips, 2001). Since then production rates for different cosmogenic isotopes have been proposed based on physical principles, irradiation experiments and geological calibration (Dunai, 2010).

A production rate generally is calculated and calibrated to the conditions of a particular site. Nevertheless, in order to use a production rate in different geographical localities other than the calibration site, it has to be adjusted to the particular parameters of the sampling location which is defined as the scaling factor. Up until the year 2000, the most used and widely accepted scaling factor was the one proposed by Lal (1991), while in the last decade this scaling factor has been criticised and other scaling factors have emerged (reviewed below, Section 1.5.1.3). The use of TCN in Earth sciences has increased exponentially in the last decade. The possibility of using a wide range of cosmogenic nuclides according to the sediment or rock analysed gives this method its particular versatility. The most commonly used TCN are ^{10}Be, ^{26}Al, ^{36}Cl, ^{3}He, ^{21}Ne and ^{14}C as they have been extensively studied and their production rates are well constrained. Furthermore, these cosmogenic nuclides are generally produced within major rock-forming minerals. Using surface exposure dating, Quaternary geological events can be inferred such as, glacial erosion records, ages for volcanic events, surface uplift rates, incision and denudation rates.

1.5.1.1. Production of cosmogenic nuclides

Highly charged particles composing galactic cosmic rays originate in the Milky Way. When these highly charged particles, mainly composed of protons, and α-particles, interact with the atmosphere they decrease their energy and produce a secondary radiation, including neutrons, protons, electrons, α-particles, muons, pions and neutrinos (Simpson and Fagot, 1953; Lal and Peters, 1967) (Figure 1.6). According to the type of secondary particles produced and their energy they can be divided into three main components electromagenetic, mesonic and nucleogenic (Simpson and Fagot, 1953; Lal and Peters, 1967; Allkofer and Grieder, 1984). The electromagnetic component is composed of positrons and electrons as well as some γ-rays, these particles are not very effective in penetrating rocks, therefore do not contribute to TCN (see review of Dunai, 2010 for references) (Figure 1.6). The mesonic component is mainly

composed of pions which decay into muons and other particles. Muons interact only weakly with matter and they have a much longer range than nucleons and therefore are the most abundant cosmic-ray particles at sea level (Lal, 1988). The nucleogenic component is composed of neutrons and protons which are high energy particles able to penetrate the surface of the Earth and are responsible for the majority of the TCN produced. Protons and α-particles are positively charged particles that are affected by the Earth's magnetic field; the least energetic particles will be highly deflected at low latitudes. Therefore cosmic ray intensity and nuclide production is higher at the poles than at the equator (Ivy-Ochs and Kober, 2008). The atmospheric depth through which incoming cosmic rays must pass is thinnest for rays arriving from a perpendicular trajectory and increases in a diagonal to horizontal trajectory. A similar effect is observed for particles arriving at the Earth's surface, as the production of TCN decreases exponentially with increasing depth from the surface. Due to the high energies involved, which are far above the binding energies of atomic nuclei, the main type of nuclear reaction taking place is spallation, in which a few neutrons are sputtered off the target nucleus resulting in a lighter nucleus (Niedermann, 2002). Most of the cosmogenic nuclides are produced by spallation reactions between primary and secondary highly energetic particles and target elements encountered in the atmosphere and at the surface of the Earth (Table 1.2). However, the composition of the particle flux changes as the reactions develop from proton-dominated to neutron dominated, due to a higher probability of neutrons escaping from a nucleus, as they do not have to overcome the Coulomb barrier neither do they lose energy by electromagnetic interactions (see review of Gosse and Phillips, 2001; Niedermann, 2002; Dunai, 2010).

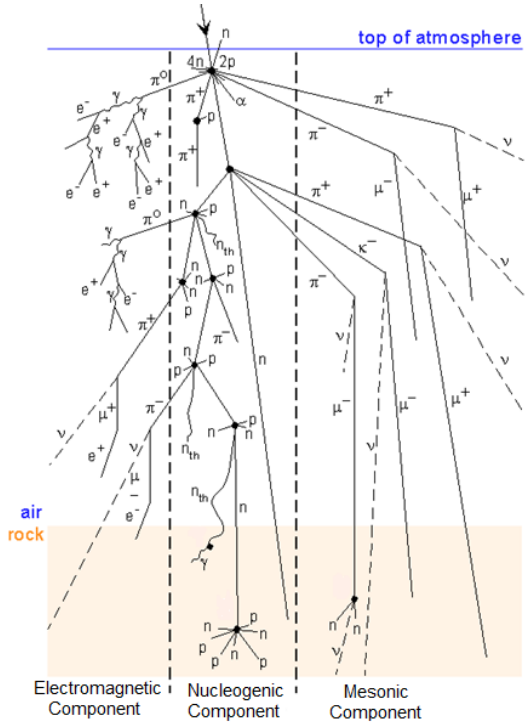

Figure 1.6. Components of the cosmogenic cascade as cosmic rays interact with the atmosphere. Modified figure after Gosse and Phillips (2001).

The target nuclei generally have a larger mass than the cosmogenic nuclide produced. Nevertheless, ^{3}He is an exception as it could be produced by spallogenic reactions of all heavier masses. Apart from spallogenic reactions there are also thermal neutron capture and negative muon reactions (Niedermann, 2002; see review of Dunai, 2010 for references). Thermal neutrons are produced by multiple collisions between fast secondary neutrons with atoms from the atmosphere and rocks, resulting in large energy losses of energy (see review of Gosse and Phillips, 2001). Thermal neutron capture reactions are only important in the top few metres of the Earth and they are responsible for the production of several cosmogenic isotopes such as ^{3}He and ^{36}Cl (Table 1.2) (Niedermann, 2002; see revirews of Ivy-Ochs and Kober, 2008; and Dunai, 2010). Negative muon reactions, are important below a depth of about 2 m (depending on rock density) as muons have low mass and only interact weakly with matter, via ionisation hence they have a much longer penetration range than nucleons. Negative muon reactions on various target nuclei can produce ^{10}Be, ^{26}Al, ^{36}Cl, ^{21}Ne, ^{53}Mn and ^{14}C (Niedermann, 2002).

Table 1.2. Commonly used terrestrial cosmogenic nuclides with their principal target mineral and element and contribution from different reaction pathways according to the 3 components of secondary particles. Modified after Dunai (2010).

Isotope	Target Mineral	Target element	Reaction Pathway (at sea level and high latitude)		
			Spallation	Thermal Neutron	Negative Muon capture
^{3}He	olivine, pyroxene	All major elements and Li	100%	From Li	-
^{21}Ne	olivine, pyroxene, quartz, sanidine	Mg, Al, Si, Na	>96.4%	-	<3.6%
^{10}Be	quartz	O, Si	96.4%	-	3.6%
^{14}C	quartz	O, Si	82%	-	18%
^{26}Al	quartz	Si	95.4%	-	4.6%
^{36}Cl	carbonate, feldspar, whole rock	K, Ca, Cl,	K = 95.4% Ca = 86.6%	From Cl and K	K= 4.6% Ca = 13.4%

1.5.1.2 Cosmogenic Nuclides

The cosmogenic nuclides produced by spallation reactions can be stable such as those resulting in noble gases or radiogenic such as ^{10}Be, ^{14}C, ^{26}Al, ^{36}Cl, ^{41}Ca and ^{53}Mn. The following description is focused on stable cosmogenic nuclides with especial interest in helium and neon.

1.5.1.2.1. Stable cosmogenic nuclides

Helium- 3

Helium is a stable element and it is the lightest of the noble gases. Cosmogenic ^{3}He can be produced by spallation reactions in basically all major elements present in minerals from rocks at the Earth's surface (Table 1.2). However, because ^{3}He is a gas it is not retained in all minerals, consequently its application is limited by its retentive properties. Olivine and pyroxene phenocrysts are some of the preferred minerals to determine surface exposure ages applying cosmogenic ^{3}He, as they typically have low concentrations of U and Th and good ^{3}He retentivity (Kurz et al., 1990; Licciardi at al., 1999; Niedermann, 2002). As a consequence of intensive research in the last 25 years improvements in understanding the production of ^{3}He provide evidence regarding the dependence of production rates on chemical composition and additional helium-retentive minerals have been proposed. One of the main advantages of using cosmogenic ^{3}He is that this isotope is stable and therefore does not decay over time and can be used to date surfaces that are more than 10 million years old (Niedermann, 2002). Furthermore, cosmogenic ^{3}He can be used to date young (few thousand years) porphyritic basalts as it has the highest production rate of all TCN and a low limit of detection (Cerling and Creig, 1994).

^{3}He can also be produced by a thermal-neutron capture reaction, ^{6}Li (n,α)^{3}H (β^{-})^{3}He (see review of Dunai, 2010 for references). In this reaction, one α-particle and one ^{3}He are produced. This ^{3}He is a nucleogenic component which has to be determined as its origin is non-cosmogenic and contributes to the total ^{3}He concentration, resulting in an older apparent age. In addition, the radiogenic ^{4}He, another non-cosmogenic isotope must also be determined as it is produced in-situ by α-particles produced by radioactive decay of U and Th (Niedermann, 2002; Blard and Farley, 2008). Radiogenic ^{4}He becomes critical in minerals with high concentrations of U and Th and especially in old samples. The nucleogenic and radiogenic component are critical when determining cosmogenic ^{3}He; however, a third source of non-cosmogenic ^{3}He, the trapped component, needs also to be determined. This third component constitutes the gases residing in the crystal lattice or fluid inclusions and can be atmospheric, magmatic or crustal in origin (Niedermann, 2002).

Neon-21

Cosmogenic ^{21}Ne is the second most studied noble gas cosmogenic isotope. It has a larger ionic radius than ^{3}He and is more readily retained in minerals. Cosmogenic ^{21}Ne is mainly produced in rocks by spallation reactions (>96.4%) while negative muon capture reactions produce a small contribution (<3.6%; Table 1.2) (see review of Dunai, 2010 for references).

Neon has three naturally occurring isotopes ^{20}Ne (most abundant in the atmosphere), ^{21}Ne and ^{22}Ne, all three neon isotopes are produced at similar rates by spallation reactions in rocks (Niedermann, 2002). Consequently it is important to specifically determine and discriminate the contribution from other neon isotopes. The trapped component is similar to that of helium, from atmospheric, crustal or magmatic origin. The atmospheric source is present in all exposed samples. Crustal fluid inclusions are typically enriched in ^{21}Ne and ^{22}Ne derived from (α,n)-reactions in oxygen which produces ^{21}Ne and (α,n)-reactions on fluorine which produce ^{22}Ne (Niedermann et al., 1993). Another possible source of the trapped component is from the mantle which is enriched in ^{20}Ne and ^{21}Ne relative to air (Graham, 2002). However, mantle neon is usually not a concern for cosmogenic applications as its concentration is minimal compared with the absorbed or trapped atmospheric component. The trapped component can be determined by performing a vacuum crushing experiment in which the fluid inclusions are ruptured and the gases are released under vacuum conditions and subsequently analysed. In many instances the trapped component is similar to the atmospheric isotopic composition (^{21}Ne/^{20}Ne= 0.002959, ^{22}Ne/^{20}Ne= 0.1020) in which case the atmospheric values can be assumed. In addition, another source of non-cosmogenic ^{21}Ne is nucleogenic neon, produced by nuclear reactions; this component is mainly released during step heating of the sample. Nucleogenic ^{21}Ne can be produced by nuclear reactions from α-particles produced by U and Th decay which may contribute significantly over long timescales (Niedermann et al., 1993). Some of the possible nuclear reactions are ^{18}O(α,n)^{21}Ne, ^{19}F(α,n)^{22}Na(β^-)^{22}Ne and ^{24,25}Mg (n,α) ^{21,22}Ne (Niedermann, 2002).

Non-cosmogenic interferences can be identified using a neon three-isotope diagram (Figure 1.7) (^{22}Ne/^{20}Ne vs ^{21}Ne/^{20}Ne) (Niedermann et al., 1993; Niedermann, 2002). By using gas concentrations obtained from extractions at different step-heating temperatures and using the neon three-isotope diagram which contain different end-members, air, crustal, nucleogenic, cosmogenic and mantle (Mid-ocaean ridge basalt, MORB), compositions and trends of the various Ne components can be determined. The mixing line between cosmogenic and air is well defined and determines the spallation line. Any deviation from the cosmogenic or spallation line is interpreted as contributions from other neon components (nucleogenic Ne or non-atmospheric trapped Ne such as mantle neon) (Niedermann, 2002). Nevertheless, the slope of the spallation line is different for various minerals as it is dependent on the production ratios of the three isotopes (Niedermann, 2002).

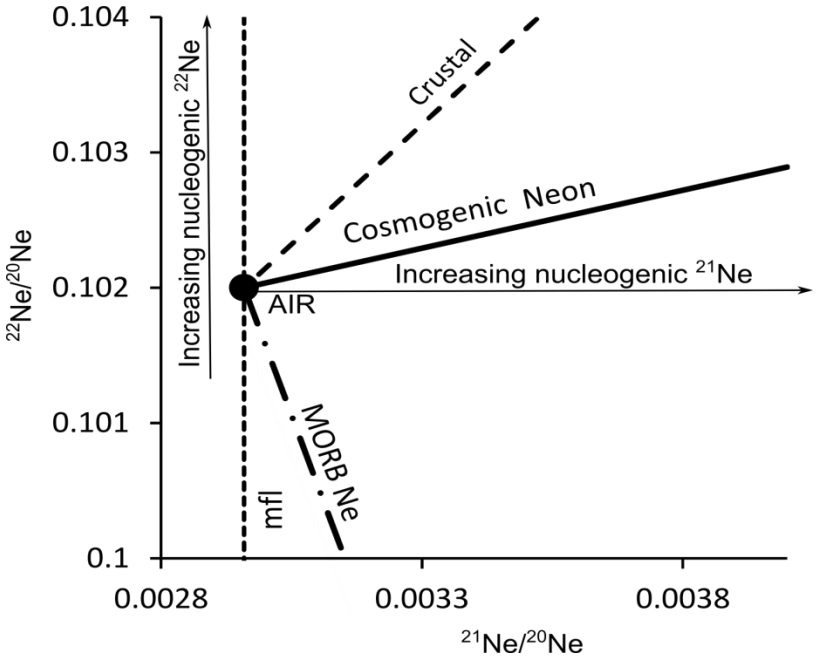

Figure 1.7. Neon three-isotope diagram. The atmospheric neon composition is shown as AIR. The cosmogenic or spallogenic line corresponds to Schäfer (1999) and indicates a mixing composition between cosmogenic ^{21}Ne and air neon. The crustal neon composition corresponds to Kennedy et al. (1990) and MORB corresponds to Sarda et al. (1988). Modified after Niedermann (2002) with the spallogenic line determined for quartz.

The majority of the investigations using ^{21}Ne has been performed on minerals from basaltic rocks, therefore production rates for these minerals, especially for olivine has been well constrained. Apart from basalts and their rock-forming minerals, most experimental determinations of cosmogenic nuclide production rates have dealt with quartz (Niedermann, 2002). (Production rates will be further discussed in Section 1.5.5). The possibility of measuring ^{21}Ne in quartz offers an important advantage over ^{3}He as the latter is not retained in quartz. Cosmogenic ^{21}Ne is produced by spallation of Si, Al, Mg and Na in quartz, olivine, pyroxene and sanidine (Ivy-Ochs et al., 2007). However, there are few investigations using ^{21}Ne, along with other cosmogenic nuclides, in sanidine separates (Kober et al., 2005; Ivy-Ochs et al., 2007). Sanidine is a common feldspar occurring mainly in silicic to intermediate volcanic rocks (such as rhyolites, dacites and andesites) and alkaline volcanic rocks (such as trachytes and phonolites) (Ivy-Ochs et al., 2007). The successful application of ^{21}Ne to sanidine expands the possible uses of ^{21}Ne as the whole volcanic suite technically can be dated with ^{21}Ne. Additionally, other basaltic rock forming-minerals have been investigated for cosmogenic ^{21}Ne retention such as plagioclase while others such as amphibole have been suggested as possible minerals for ^{21}Ne retention (Niedermann, 2002). Poreda and Cerling (1992) determined that volcanic plagioclase may be a suitable mineral for cosmogenic ^{21}Ne dating surfaces. Nevertheless Bruno et al. (1997) claimed possible cosmogenic neon loss from dolerite whole-rock analysed from Antarctica, since this rock contains 50% to 60% plagioclase which is a mineral prone to diffusive

loss of cosmogenic Ne. Consequently the retentivity of plagioclase is unproven at the moment and further analysis is needed to clarify this issue.

Similarly to ^{3}He, cosmogenic ^{21}Ne can be used to investigate extremely long exposures; this is possible because the two isotopes are stable (see summary by Gosse and Phillips, 2001 for references). However, it is important to consider that dealing with old samples also implies significant nucleogenic ^{21}Ne correction as it accumulates over periods of millions of years from U and Th decay. This complication may restrict the use of cosmogenic ^{21}Ne to young rocks unless appropriate corrections can be made for nucleogenic ^{21}Ne (Poreda and Cerling 1992). No estimate for the younger cosmogenic ^{21}Ne limit has been proposed; however, it can be estimated to be a few thousand years.

Other stable cosmogenic nuclides: argon, krypton and xenon

The most abundant noble gas in the atmosphere is argon, which is problematic to measure as the low concentration of cosmogenic ^{36}Ar and ^{38}Ar is largely overwhelmed by common atmospheric argon and its isotopes. ^{36}Ar and ^{38}Ar are the two isotopes of argon that are produced by spallation reactions on K, Ca and to a lesser extent from Ti and Fe (see review of Dunai, 2010 for references). Furthermore, ^{38}Ar can be also produced by negative muon capture reactions with K and Ca, while ^{36}Ar is also produced indirectly by thermal neutron capture reactions with ^{39}K or ^{35}Cl which produces ^{36}Cl and its decay produces ^{36}Ar (Niedermann, 2002). In addition, thermal neutron capture reactions are important in producing heavy noble gases such as Kr and Xe (Niedermann, 2002). Spallation reaction from Rb, Sr, Y, and Zr and heavier elements produce cosmogenic Kr while spallation reactions from Cs, Ba, La, Ce, and all heavier rare earth elements produce cosmogenic Xe (see review of Dunai, 2010 for references). Nevertheless, the main process for the production of Kr and Xe isotopes in the crust is by spontaneous fission of U (Ballentine and Burnard, 2002).

The three heavy noble gases have larger ionic radii and tend to be better retained in minerals than the lighter helium or neon isotopes. The use of cosmogenic argon is mainly limited by its considerable background levels resulting from its high concentration in the atmosphere as well as from the capability of producing ^{36}Ar from ^{36}Cl decay which will be much more difficult to account for especially in old surfaces. Nevertheless, cosmogenic ^{38}Ar could potentially be used in conjunction with other stable cosmogenic isotopes (i.e. ^{3}He and ^{21}Ne) in rocks which are depleted of olivine, pyroxene or quartz but have abundant feldspar (see review of Dunai, 2010 for reference). The application of cosmogenic krypton and xenon to geochronology is not fully tested.

1.5.1.2.2. Radiogenic cosmogenic nuclides

Several useful radiogenic isotopes are produced by nuclear reactions between cosmic rays and target nuclei in minerals. However, radiogenic isotopes decay over time at varying rates depending on the isotope produced, until they reach secular equilibrium. The most commonly used and best understood radiogenic isotopes are ^{10}Be, ^{14}C, ^{26}Al and ^{36}Cl, with less attention

being given to ^{41}Ca and ^{53}Mn. In the current review these radiogenic isotopes are mentioned but not described.

1.5.1.3. Scaling factors

Scaling factors are used to translate the production rate from a calibration site to the particular location from where an individual sample was extracted (Niedermann, 2002). To determine the scaling factor parameters, effective means of detecting highly energetic cosmic rays at and above sea level are essential. The basic parameter of sea level is standard, as at this elevation the production rate is lowest. Highly energetic fast neutrons have to travel further through the troposphere to reach target elements at sea level; therefore, the absorption mean free path length decreases with increasing altitude (Dunai, 2000). Currently there are five proposed scaling factors from Lal (1991), Dunai (2000 and 2001), Stone (200), Desilets and Zreda (2003) and Lifton et al. (2005). However, all use available neutron flux information from the same sources (from photographic emulsion or neutron monitor or combination of the two at sea level and higher altitudes) therefore the differences among scaling factors reside in the amount of data from monitoring devices but not in the type of data (Dunai, 2010).

Table 1.3. Comparison between different scaling factors. [a] types of neutron detectors PE (photographic emulsion) NM (neutron monitor), [b] Attenuation length based on: λ geomagnetic latitude or R_c cut-off rigidity value, R_{ce} is the trajectory-tracing derived cut-off rigidity. Modified from Dunai (2010).

Scaling factor	Coordinate system	Atmospheric pressure	Magnetic variations	Solar modulation	Neutron detector [a]	Attenuation length [b] (Λ)	Polarity component
Lal (1991)	geographic	altitude			PE +NM	λ	Dipole field
Stone (2000)	geographic	X			PE +NM	λ	Dipole field
Dunai (2000 and 2001)	geomagnetic	X	X[c]		NM	R_c	Non-dipole field
Desilets & Zreda (2003)	geomagnetic	X	X	X	NM	R_{ce}	Non-dipole field
Lifton (2005)	geomagnetic	X	X	X	NM	R_{ce}	Non-dipole field

The main difference between Lal (1991) and Stone (2000) and the other three scaling factors resides in the attenuation coefficients used by the former two approaches which are mainly based on geographic latitude while Dunai (2000), Desilets and Zreda (2003) and Lifton et al. (2005) use geomagnetic latitude. Another major difference between Lal's and the later scaling

factors is that they use atmospheric pressure rather than altitude. In Lal's approach, atmospheric pressure anomalies are not considered (Table 1.3). In addition Desilets and Zreda (2003) and Lifton et al. (2005) also incorporate changes in solar modulation, as it affects the production rates of cosmogenic nuclides especially at high geomagnetic latitudes.

The most commonly used scaling factor is that one proposed by Lal (1991), as it was the first and has a simple approach to convert production rates from calibration site to individual locations. Nevertheless, the use of Stone (2000) and Dunai (2001) scaling factors have increased considerably. Additionally, it is recommended that the user apply the same scaling factor for their sampling location as for the calibration site (Niedermann, 2002; Dunai, 2010).

1.5.1.4. Production rates

The production rates of fast neutrons are directly related to the effects of Earth's magnetic field and atmospheric pressure at a particular location.

Production rates can be determined by:

- Geological calibration, by measuring the concentration of cosmogenic nuclides from an exposed un-weathered surfaced and normalising the isotopic concentration against an independently determined age such as from $^{40}Ar/^{39}Ar$.
- Experimentally, by placing a rock or mineral of known composition into a particle accelerator that simulates secondary. After a known period of exposure, the concentration of cosmogenic nuclides can be determined, hence a production rate derived.
- Numerical simulation, by using a physical model of nuclear processes involved in the production of cosmogenic nuclides (Masarik, 2002).

Independently of the method used to calculate the production rate, it is recommended to be consistent with the type of scaling factor used (Gosse and Phillips, 2001; Niedermann, 2002). Furthermore, for the purpose of the current review, only the production rates of the stable isotopes ^{3}He and ^{21}Ne will be considered, regardless of the method used to determine the production rate.

1.5.1.4.1. Helium-3 and neon-21

The production rates of cosmogenic ^{3}He and ^{21}Ne have been determined on mineral separates such as olivine, pyroxene, and to a less extent in plagioclase from basaltic rocks. Volcanic rocks are well suited for calibration, as simple exposure histories can be easily inferred from careful field observation. Moreover, volcanic eruptions can be dated by any of the well-established dating methods such as ^{14}C, $^{40}Ar/^{39}Ar$ or K-Ar. The production rate of cosmogenic ^{3}He is the most studied among the noble gases. One of the first attempts to determine the production rate of ^{3}He was by Kurz (1986), who measured cosmogenic ^{3}He from olivine phenocrysts on a dated basaltic flow from Hawaii, calculating a production rate at sea level and 37°N latitude of 97 at/g/a. The ^{3}He production rate was later calculated on 26 samples from Hawaii obtaining production rates normalised at sea level ranging from 47 to 150 at/g/a (Kurz et al., 1990). Subsequently other production rates have been determined (Poreda and Cerling, 1992; Cerling

and Craig, 1994; Licciardi et al., 1999; Dunai, 2001; Fenton et al., 2009) by geological calibration or by a combination of methods such as in the case of Fenton et al. (2009) who also used the numerical simulation proposed by Masarik (2002) to calculate production rates for cosmogenic ^{3}He and ^{21}Ne. The cosmogenic ^{3}He production rate in olivine ranges between 103 ± 4 at/g/a (Dunai, 2001) to 120 at/g/a (Fenton et al., 2009) (Table 1.4). The cosmogenic ^{21}Ne production rate in olivine phenocrysts, has not been as widely studied as that for cosmogenic ^{3}He. Nevertheless, the two production rates currently available agree between them (45± 4 at/g/a, Poreda and Cerling, 1992 and 48-51 at/g/a; Fenton et al., 2009) (Table 1.4). In addition, the production rates of cosmogenic ^{3}He and ^{21}Ne have also been analysed in other basaltic mineral separates such as clinopyroxene with a production rate of 114 at/g/a and 23 at/g/a, respectively (Fenton et al., 2009). For plagioclase, the production rate of cosmogenic ^{21}Ne is 16.8 ± 1.7 at/g/a (Poreda and Cerling, 1992). Furthermore, cosmogenic ^{21}Ne is quantitatively retained in quartz. The production rate of cosmogenic ^{21}Ne in quartz was determined by Niedermann (2000), and subsequently by Balco and Shuster (2009) and Goethals et al. (2009). The cosmogenic ^{21}Ne production rate in quartz ranges from 18.3 at/g/a to 20.1 at/g/a (Table 1.4). Due to the high retentivity of cosmogenic ^{21}Ne in a range of minerals, it has been also investigated in minerals typical of intermediate and felsic volcanic rocks such as sanidine. The production rate of ^{21}Ne in sanidine is 30.4 ± 5.4 at/g/a (Kober et al., 2005).

Table 1.4. The production rate of several stable and radiogenic isotopes determined from mineral separates.

Cosmogenic isotope	**Mineral**	**Production rate at SLHL (at/g/a)**	**Reference**
^{3}He	olivine	109	Poreda and Cerling, 1992
^{3}He	olivine	115	Cerling and Craig, 1994
^{3}He	olivine	116	Licciardi et al., 1999
^{3}He	olivine	103	Dunai, 2001
^{3}He	olivine	117-120	Fenton et al., 2009
^{3}He	clinopyroxene	114	Fenton et al., 2009
^{21}Ne	plagioclase	17	Poreda and Cerling, 1992
^{21}Ne	olivine	45	Poreda and Cerling, 1992
^{21}Ne	olivine	48-51	Fenton et al., 2009
^{21}Ne	clinopyroxene	23	Fenton et al., 2009
^{21}Ne	sanidine	30	Kober et al., 2005
^{21}Ne	quartz	19	Niedermann, 2000
^{21}Ne	quartz	18	Balco and Shuster, 2009
^{21}Ne	quartz	20	Goethals et al., 2009

1.5.2. History and introduction to $^{40}Ar/^{39}Ar$ dating

In 1940 the decay of ^{40}K to stable ^{40}Ar was first utilised for chronological purposes (Aldrich and Nier, 1948), constituting the beginning of the K-Ar dating method which has been used since then and the basis for the later developed $^{40}Ar/^{39}Ar$ dating. In the 1960s Merrihue (1965) and Merrihue and Turner (1966) proposed a variation of the well-known K-Ar method based on the conversion of ^{39}K to ^{39}Ar by neutron bombardment. Using this new approach the different isotopes of argon could be measured simultaneously, such as ^{40}Ar (produced from ^{40}K decay), ^{39}Ar (produced from ^{39}K by neutron interaction) and ^{36}Ar (atmospheric isotope). By measuring these isotopes the ratio between radiogenic ^{40}Ar (designated $^{40}Ar^*$) and ^{39}Ar produced by neutron irradiation ($^{39}Ar_K$) can be calculated, which is proportional to the $^{40}Ar^*/^{40}K$ ($^{40}K/^{39}K$ is constant in nature) and is related to the K-Ar age of the rock (McDougall and Harrison, 1999). The age is calculated by comparing the $^{40}Ar^*/^{39}Ar_k$ of the unknown sample with a standard of well-known age, which is irradiated with the unknown in order to determine the neutron flux received by the sample. The standard is called the neutron flux monitor which then is used to calculate the J-parameter that is dependent on the duration of radiation, neutron flux and the neutron cross-section (Mitchell, 1968).

Early $^{40}Ar/^{39}Ar$ dating, utilised total fusion whose results correlated relatively well with K-Ar ages. However, in the 1970s Turner proposed to determine the age by step heating, producing a major breakthrough in identifying samples that had been thermally disturbed after crystallisation (McDougall and Harrison, 1999). Accordingly, a well-behaved sample has the same age (within error) during all the heating steps constituting what is known as a "plateau age". A good example of a well-behaved sample can be found in Chapter 5, supplementary Figure 2A, while the rest of the age spectrum diagrams in the same figure did not produce a plateau age and the heating steps do not have the same age, representing a sample disturbed after crystallisation.

1.5.2.1. Assumptions, problems and usage of $^{40}Ar/^{39}Ar$ dating

One of the main assumptions in $^{40}Ar/^{39}Ar$ dating as well as in many other dating methods is that the system has remained closed since eruption; meaning negligible weathering and the absence of xenoliths. This assumption can be easily confirmed by conducting petrographic observation of the sample. Another important assumption is that all the measured ^{40}Ar is derived from ^{40}K decay (McDougall and Harrison, 1999). However, ^{40}Ar is the most abundant isotope of argon and is also abundant in the atmosphere. Therefore the total ^{40}Ar measured in a rock or mineral can have a radiogenic and an atmospheric component. In order to overcome this problem; ^{36}Ar is measured and the atmospheric $^{40}Ar/^{36}Ar$ composition is derived which is compared with the present-day $^{40}Ar/^{36}Ar$ value of 295.5 ± 0.5 (Nier, 1950). However, during the irradiation process argon isotopes such as ^{36}Ar can be produced from Ca, hence the $^{40}Ar/^{36}Ar$ ratio is not a reliable solution and another isotope ^{37}Ar (non-naturally occurring isotope and produced from Ca as well) has to be also measured in order to account for the ^{36}Ar produced by irradiation from Ca (Aitken, 1990).

In addition, after measuring the argon isotopes and applying the corrections to ^{40}Ar and ^{36}Ar, several argon isotopic ratios can be derived such as $^{36}Ar/^{40}Ar$ and $^{39}Ar/^{40}Ar$, from which an isochron plot can be constructed. The isochron diagram plots the isotopic ratios from the individual heating steps in a binary plot (Figure 1.8). A regression line is created where the y-intercept constitutes the air composition, which ideally should be within error of the reciprocal of $^{40}Ar/^{36}Ar = 295.5 \pm 0.5$ (Nier, 1950). The x-intercept value is related to the amount of radiogenic argon, which is proportional to the age of the sample.

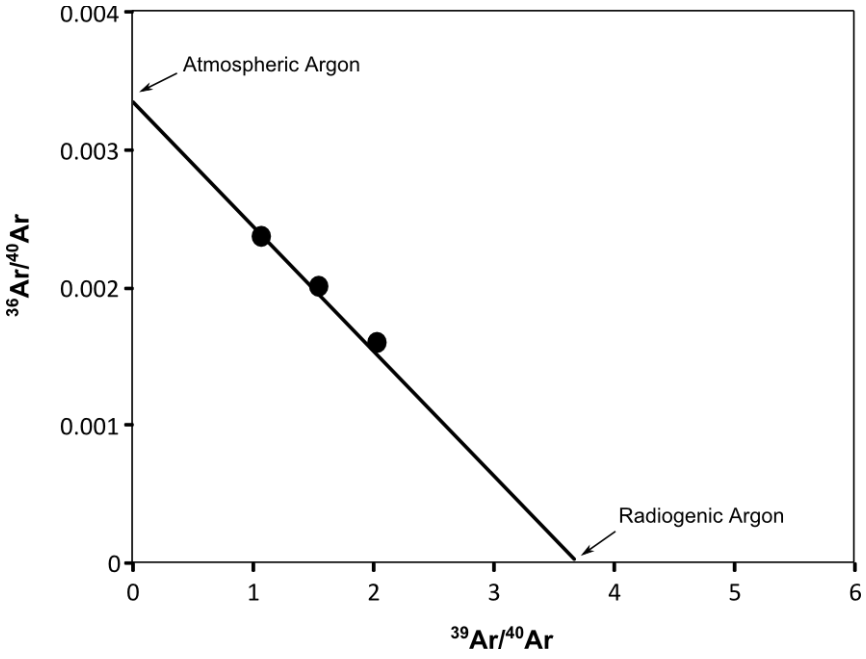

Figure 1.8. Argon isochron diagram. Modified from McDougal and Harrison (1999)

The $^{40}Ar/^{39}Ar$ step-heating dating technique is mostly applied to volcanic rocks and is a reliable tool to date basic and acid volcanic products. However, the younger limit of the method is determined by the presence of atmospheric argon and the possibility of measuring very low concentrations of radiogenic argon with high precision. Accordingly, rocks with a higher concentration of K will be more suitable as the amount of $^{40}Ar^*$ produced per unit time is higher (McDougall and Harrison, 1999). Consecuently, sanidine, which is an alkali feldspar with a high K content, has been used to date volcanic deposits (79 AD) in Pompeii with a precision of 5% and a late Holocene age of 1925 ± 94 years (Renne, 1997). In the case basaltic samples, the concentration of K is much lower, therefore the younger limit is probably 10 ka for mafic whole rocks (McDougall and Harrison, 1999).

Chapter 2:

*Geochemical variations in the Quaternary Andean back-arc volcanism, southern Mendoza, Argentina**

Venera R. Espanon [a,b], Allan R. Chivas[a], Leslie P.J. Kinsley[c] and Anthony Dosseto[a,b]

[a] *GeoQuEST Research Centre, School of Earth & Environmental Sciences, University of Wollongong, NSW 2522, Australia.*

[b] *Wollongong Isotope Geochronology Laboratory, School of Earth & Environmental Sciences, University of Wollongong, NSW 2522, Australia*.

[c] *Research School of Earth Sciences, The Australian National University, Canberra, ACT 0200, Australia.*

Allan R. Chivas: toschi@uow.edu.au

Leslie J. Kinsley: leslie.kinsley@anu.edu.au

Anthony Dosseto: tonyd@uow.edu.au

*Manuscript published (2014) in *Lithos*, volume 208–209, pages 251-264
DOI:10.1016/j.lithos.2014.09.010

Abstract

The Payenia Basaltic Province (PBP) is located 450 km east of the Chile-Peru trench in central west Argentina, behind the Andean arc front, constituting the back-arc. In order to evaluate the influence of the subducting slab as well as the magmatic source of this region, two volcanic fields located at comparable distance to the trench, having abundant basaltic products and similar eruptive timeframes were chosen. The Llancanelo (LLVF) and the Payún Matrú (PMVF) volcanic fields are part of the Payenia Basaltic Province and exhibit abundant basaltic activity during the Pleistocene. The geochemical data suggest that the LLVF has some arc signatures which have been described as weak as they are not as pronounced as in the Andean arc. The weak arc signature is not derived from slab dehydration as high Th enrichment relative to U cannot be explained by this process. We relate the Th enrichment as well as the lack of large residual garnet signatures, to slab sediments in the source. In the case of the Payún Matrú volcanic field, no arc signature has been inferred despite being only 30 km south of the LLVF. However the PMVF has a composition similar to that of the local intraplate end-member, represented by the Río Colorado volcanic field. The two volcanic fields, LLVF and PMVF, show indications of lower crustal assimilation as they trend towards the lower continental crust end-member in Nb/U vs Ce/Pb and Nb/Yb vs Th/Yb diagrams.

The geochemical differences between the LLVF and the PMVF as well as between several volcanic fields are illustrated using spatial distribution maps of geochemical ratios. Using this new approach, the decrease in arc signature can be traced in the back- arc and the higher enrichment in high field strength elements (HFSE) relative to large ion lithophile elements (LILE) in the PMVF compared to the LLVF is explicitly shown. These geospatial maps provide a graphical manner to illustrate the presence of two distinct types of volcanism (OIB-like and arc-like) occurring in the same Quaternary basaltic province.

2.1. Introduction

The Patagonian basaltic provinces extend from 35° to 52°S and have been widely studied providing several explanations for occurrence of the continental back-arc volcanism. For instance, the back-arc volcanism of the late Oligocene to early Miocene Somuncura Plateau, part of the Patagonian Massif (PM, Figure 2.1), has been considered the result of asthenospheric upwelling (De Ignacio et al., 2001; Kay et al., 2007). In contrast, the late Miocene back-arc volcanism was associated with a period of shallow slab subduction in a compressional tectonic regime (Kay et al 2004; Kay et al., 2006 a, b; Kay and Copeland, 2006). In the same area, the angle of subduction increased during the Pliocene, producing extensional processes which facilitated the generation of the Quaternary basaltic volcanism present in the Payenia Basaltic Province (PBP, Figure 2.1; Kay et al., 2006a).

The basaltic melts erupted in the Payenia Basaltic Province continental back-arc are described as heterogeneous, as they have been variably influenced by slab components, lower crustal contamination and intraplate melts, associated with an ocean island basalt (OIB)-like mantle source (Germa et al., 2010; Hernando et al., 2012; Jacques et al., 2013; Kay et al., 2004; Søager et al., 2013; Søager and Holm, 2013). In the northern part of the PBP, the basalts have been associated with mixing between a south Atlantic MORB-like source and slab components (Jacques et al., 2013, Søager et al., 2013). The southern PBP presents geochemical signatures related to mantle upwelling and an OIB-like source with little or no influence from the subduction zone to the west, as best exemplified by the basalts from the Río Colorado volcanic field (Jacques et al., 2013; Kay et al 2004; Søager et al., 2013; Søager and Holm, 2013). The PBP has been the focus of several geochemical investigations (Bermudez and Delpino, 1989; Bertotto et al., 2009; Germa et al., 2010; Hernando et al., 2012; Paquaré et al., 2008; Søager et al., 2013) as it provides an optimum framework to investigate the magmatic processes related to a continental back-arc setting. Accordingly, the purpose of this investigation is (i) to determine the contribution of arc-type magmatism in the continental back-arc, (ii) to understand the spatial geochemical variation in this area and (iii) to describe and comprehend the processes responsible for the geochemical characteristics observed in the continental back-arc.

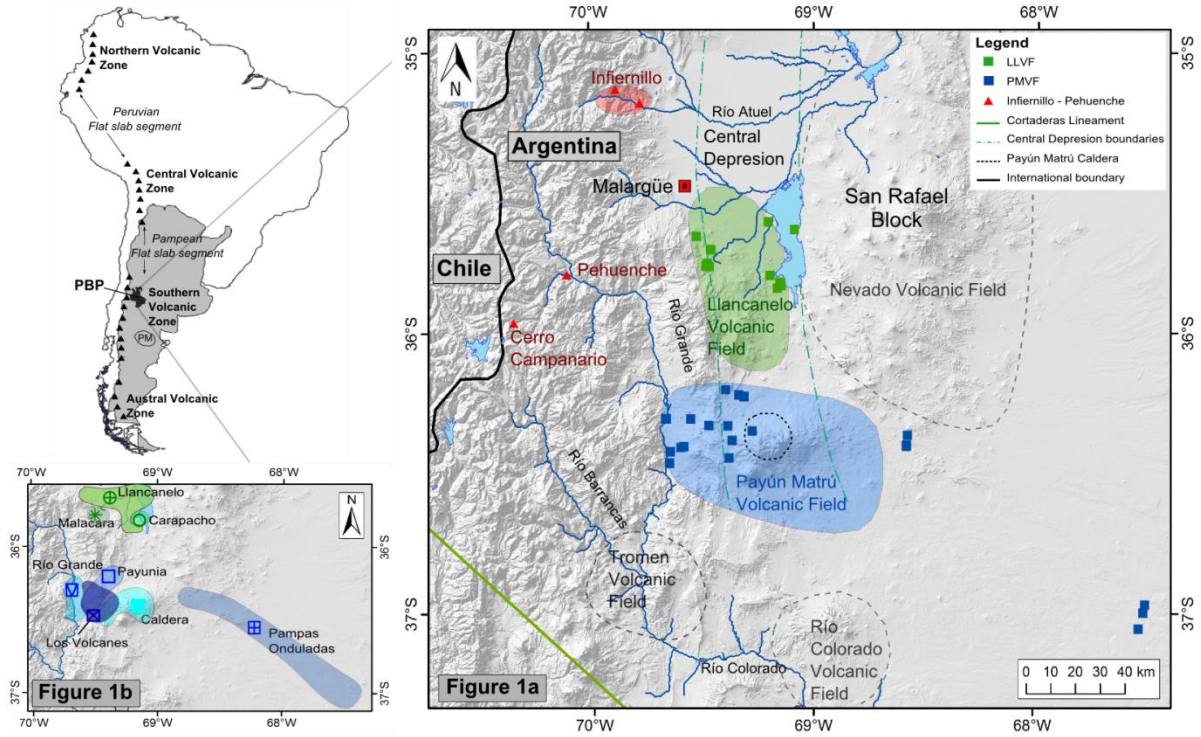

Figure 2.1. Geographical setting of the Payenia Basaltic Province (PBP). PM represents the Patagonian Massif. Figure 2.1a shows the geographic location of the volcanic fields. Green and blue fields represent the volcanic fields here investigated, while other volcanic fields are outlined in grey dashed lines. The green field is the Llancanelo volcanic field (LLVF) and the blue field is the Payún Matrú volcanic field (PMVF). Note that the blue squares located outside the PMVF correspond to Pampas Onduladas, a long flow (<160 km) that has its effusion point within the PMVF. The red field corresponds to the Infiernillo volcanic field. Red triangles correspond to felsic samples from Cerro Campanario and Pehuenche. The green dashed-point lines indicate the east and west boundaries of the Central Depression. The dashed circle delimits the Payún Matrú caldera. The black line indicates the international boundary and the green line indicates the Cortaderas lineament. Figure 2.1b shows the groups in which the Llancanelo volcanic field and the PMVF have been divided, with the corresponding symbol used in the following diagrams.

2.2. Geological Setting

Volcanism in the Andes extends from Colombia to the southern tip of South America and is related to the subduction of the Nazca Plate (from ~7.3°N to 45.6°S) and the Antarctic Plate (south of ~45.6°S) under the South American Plate. The Nazca Plate subducts beneath the Nazca Plate at an angle of 25 – 35°. Most volcanic activity in South America is restricted to the Andean volcanic arc, with the dominant volcanic product being intermediate to silicic (mainly andesite) and large amounts of pyroclastic material while areas of continental back-arc volcanism are evident to the east of the Andean volcanic arc.

The study area is located between 35°S and 37°S and 67°W and 70°W, in central-west Argentina (Figure 2.1) and is part of the northernmost Patagonian basaltic province named Payenia (Polanski, 1954; also called the Andino-Cuyana Basaltic Province by Bermudez and

Delpino, 1989). The Payenia Basaltic Province (PBP) was initially divided into the Llancanelo volcanic field to the north and the Payún Matrú volcanic field to the south (Bermudez and Delpino, 1989). Recently this initial division was reviewed by Gudnason et al. (2012) who redefined the original Llancanelo volcanic field from Bermudez and Delpino, (1989) into the Llancanelo and Nevado volcanic fields while the Payún Matrú volcanic field was divided into the Payún Matrú and Río Colorado volcanic fields (Figure 2.1a). The PBP encompasses an area of 15,900 km2 with more than 800 volcanic cones. This basaltic province is bounded on its western side by the Malargüe Fault and thrust belt, the central part is defined by a tectonic depression named the Central Depression (Llambías et al., 2010) and the eastern part is positioned on the uplifted San Rafael Block (Figure 2.1). The Central Depression was formed in the late Miocene during a period of shallow subduction that lasted until the early Quaternary in the northern PBP. North of 36°S, the Central Depression has been filled by approximately 1000 m of Cenozoic sediments (Ostera and Dalpeña, 2003) while south of 36°S, Cenozoic sedimentation was almost absent. Mesozoic sedimentary rocks of the Neuquén Basin underlie the sediments of the Central Depression. The southern limit of the Central Depression is not well defined as it vanishes south of the Payún Matrú caldera (Llambías et al., 2010).

The southern limit of the PBP is marked by the Cortaderas lineament (Ramos, 1978) south of which there is an absence of Cenozoic back-arc volcanism (Llambías et al., 2010). Volcanic activity has been evident in this continental back-arc since the earliest Miocene (Dyhr et al., 2013a; Gudnanson, et al., 2012; Kay and Coperland, 2006, Kay et al., 2006a; Kay et al., 2006b). However, Holocene volcanic activity is only known from the Payún Matrú volcanic field (Espanon et al., 2014a; Germa et al., 2010; Marchetti et al., 2014).

The current study is focused on the central part of the PBP, the Llancanelo volcanic field and the Payún Matrú volcanic field with the addition of some Andean arc samples from the areas of Cerro Campanario-Pehuenche and some retroarc samples from Infiernillo (Figure 2.1). Alkaline basalts are the dominant lithology in the PBP with minor silicic flows around the Payún Matrú caldera and the Cerro Nevado volcano (Llambías et al., 2010). The Llancanelo volcanic field has high cone density dominated by monogenetic scoria cones with some tuff rings (Risso et al., 2008). The two distinct phreatomagmatic volcanoes in this volcanic field are Carapacho and Malacara. Within the Llancanelo volcanic field, the volcanic cones are oriented along ENE-WSW trending fissures (Risso et al., 2008). The chronology of the Llancanelo volcanic field is not well constrained, however recent $^{40}Ar/^{39}Ar$ determinations suggest that it was active 1.1 Ma ago (Dyhr et al., 2013a) and the volcanic activity probably lasted until the late Pleistocene (Espanon et al., 2014a).

Most of the volcanism in the Payún Matrú volcanic field is monogenetic with only two polygenetic centres corresponding to the Payún Matrú caldera and the Payún Liso stratovolcano. The Payún Matrú caldera-forming event occurred approximately between 168 ka and 82 ka (Germa, et al., 2010), accompanied by an ignimbrite eruption which covered a vast

area up to 40 km (Hernando et al., 2012) from the caldera. This volcanic field has more than 220 scoria cones (Hernando et al., 2014b), many aligned along a major east-west fissure called La Carbonilla which is only exposed on the eastern side of the Payún Matrú caldera. The oldest part of this volcanic field is located on the eastern side of the Payún Matrú caldera and is also where the longest Quaternary basaltic flow is found, Pampas Onduladas (Pasquaré et al., 2008). The Payún Matrú volcanic field has been active during much of the Quaternary with some flows being less than 2 ka old (Marchetti et al., 2014).

The two volcanic fields investigated, Llancanelo and Payún Matrú volcanic fields are here sub-divided in order to assess their diversity. The criteria used to divide the volcanic fields are based on geographic and geochemical characteristics. The samples from Llancanelo volcanic field were divided into the Carapacho, Malacara and Llancanelo groups (Table 2.1). The Carapacho volcano resulted from explosive eruptions with direct magma-groundwater interaction. This volcano is characterised by abundant accidental lithic fragments (Llambías et al., 2010) and is therefore associated with a deeper water-magma interaction. The Malacara volcano has well defined basaltic flows to the north and it is composed of abundant scoria deposits with interbedded basaltic bombs. This volcano is a tuff cone and it was formed by dry and wet tephra fallout (Risso et al., 2008). It does not contain many accidental lithic fragments and is therefore considered to have formed by explosions close to the surface from an open vent. These two phreatomagmatic volcanoes have been analysed separately (Carapacho and Malacara groups), based on their geographical location and their distinct erupted products associated with differences in water-magma interaction. The remaining samples from the Llancanelo volcanic field that do not contain phreatomagmatic components have been placed in one group here designated the Llancanelo group.

The Payún Matrú volcanic field was divided into Los Volcanes, Río Grande, Payunia, Pampas Onduladas and Caldera groups. Los Volcanes group corresponds to young samples (~<10 ka, Espanon et al., 2014a; Marchetti et al., 2014) on the western side of the Payún Matrú caldera. This group is dominated by scoria cones and basaltic flows with a`a texture. The Río Grande group is characterised by pahoehoe basaltic flows that flow towards the Río Grande and are older than 10 ka (Germa et al., 2010; Marchetti et al., 2014). The Payunia group is composed of the remaining samples from the north-western side of the Payún Matrú caldera. The Pampas Onduladas group constitutes the basaltic samples from a compound long pahoehoe flow on the eastern side of the caldera and younger than 400 ka (Melchor and Casadio 1999; Pasquarè et al., 2008). The Caldera group, within the Payún Matrú volcanic field, is the only silicic group analysed from the continental back-arc and it includes samples from the Payún Matrú caldera.

2.3. Methods

Whole-rock samples were washed, dried and crushed in a Cr-Ni TEMA ring grinder (hence those elements were not used for the geochemical analysis). Samples with secondary mineralisation (SM16, VRE21, VRE46a, CP4, VRE27, VRE11 and VRE43) were soaked in 10% HCl for several hours to remove carbonate-filled vesicles followed by washing and drying prior to crushing. The leaching of these samples does not show a systematic shift with the samples that were not leached; nevertheless, trace-element duplicates were done for each of the leached samples using X-ray fluorescence analysis (Supplementary Table 2.1). The major-element analysis was by X-ray fluorescence on glass discs using a Spectro Xepos energy-dispersive polarisation X-ray spectrometer at the School of Earth and Environmental Sciences, University of Wollongong (Supplementary Table 2.1). Glass discs for the mafic samples were prepared by fusion of ~0.4g of ground sample and ~2.4 g of flux, which is a mixture of lithium tetraborate (35.3%), and lithium metaborate (64.7%). For the silicic samples, the flux used was 100% lithium metaborate. W-2 dolerite standard (n=4), was used during the period from October 2012 to November 2013 with a relative percentage standard deviation of <3 % for all the major elements.

Loss on ignition was measured using ~1 g of ground sample in a furnace at 1050°C. The glass discs prepared for major-element analysis were also analysed for 36 trace elements by LA-ICP-MS (Agilent 7200) at the Research School of Earth Sciences, Australian National University. The laser used was an Excimer laser (ArF 193 nm) 50 mJ, 5 Hz at a scan rate of 10 µm per second and a spot diameter of 105 µm. The data were calibrated using the international standard NIST612 (GEoReM reference material, Jochum et al., 2011) which was analysed under the same conditions as the samples. Reproducibility was monitored using the international rock standard BCR-2 (n=12) (USGS rock standard, Wilson, 1997) treated as an unknown and analysed under the same conditions as the samples. The relative standard deviation of BCR-2 ranges from 1.6 % to 5.7 % (2σ) for all elements (Supplementary Table 2.2). The major- and trace-element data obtained were plotted using the GeoChemical Data toolkit (GCDkit) developed by Janoušek et al. (2006).

Sr isotopic analysis was conducted on 9 samples (Table 2.2). Approximately 0.1 g of powdered sample was dissolved (only samples SM16 and VRE27 were previously leached with 10% HCl) in 1.5 mL 30% HCl, 2mL 70% $HClO_4$, 0.5 mL 65% HNO_3 and 2 mL 48% HF, at 130ºC for 12 hours. The samples were dried, re-dissolved in 2M HNO3 then loaded on a cation exchange column packed first with 0.1 mL Eichrom pre-filter® resin overlain by 0.2 mL Eichrom Sr-spec® resin (Moffat, 2013). Sr was eluted in 0.02M HNO_3 (Moffat, 2013). Sample preparation was performed in the Wollongong Isotope Geochronology Laboratory at the University of Wollongong while the Sr isotopic analysis was conducted using a Thermo Scientific Neptune multi-collector ICP-MS at the Research School of Earth Sciences, Australian National University. The precision of the Sr isotopic measurements was monitored by the SRM987

standard. The $^{87}Sr/^{86}Sr$ value obtained for SRM987 is 0.710342 ± 0.000007 (2σ) which is within the recommended value ($^{87}Sr/^{86}Sr$ = 0.71034 ± 0.00026, National institute of Standards and Technology, standard reference material 987). Total procedural blank for Sr is 52.4 pg which represents <0.003% of the total Sr analysed and was measured on an Agilent 7500cs quadrupole ICP-MS, at the School of Earth and Environmental Sciences, University of Wollongong.

Trace-element data (this study; Bertotto et al., 2009; Germa et al., 2010; Jacques et al., 2013; Pasquarè et al., 2008; Søager et al., 2013) were used to create several spatial distribution geochemical maps. The data from the current investigation and from previous publications were carefully examined and only samples with less than 53% SiO_2 were considered, in order to avoid geochemical modification of parent magma, by fractional crystallisation. A total of 255 and 230 data points were used and converted to a shapefile using the natural neighbourhood interpolation tool from ArcMap 10®. This tool was selected as it is the most appropriate method where sample data points are distributed with uneven density. Geospatial distribution maps were made at a broader scale (with 230 to 255 data points) including the back-arc fields and the Andean arc as well as on a more detailed scale (with ~112 data points) including the Llancanelo and the Payún Matrú volcanic field.

2.4. Results

2.4.1. Mineralogy

The basaltic rocks analysed have mainly a porphyritic texture, while some samples exhibit a glomeroporphyritic texture. The most abundant phenocrysts are olivine and plagioclase, with scarce pyroxene, opaque minerals and interstitial glass. The basaltic groundmass is composed of plagioclase and olivine with scattered pyroxene microcrysts. The olivine phenocrysts have a euhedral to subhedral shape, with some showing alteration to iddingsite especially for the samples from the Pampas Onduladas group. Opaque mineral phenocrysts were observed in most of the basalts. Euhedral plagioclase phenocrysts are abundant and are also the main component of crystal clots. The compositional zoning in plagioclase is normal with rare oscillatory zoning. The silicic samples from Payún Matrú caldera (here termed Caldera group) have been petrographically described by Germa et al. (2010) and Hernando et al. (2012). The Caldera group samples, have a porphyritic texture with abundant sanidine phenocrysts. The Infiernillo and Cerro Campanario-Pehuenche group samples have a glomeroporphyritic texture and are rich in feldspar phenocrysts.

Table 2.1. List of samples analysed including their area of origin and the group classification for each volcanic field. PMVF is the Payún Matrú volcanic field and LLVF is the Llancanelo volcanic field.

Area	Group classification	Sample	sample location	Latitude	Longitude	Material
PMVF	Los Volcanes	LV1	Los Volcanes	-36.33761	-69.47198	Basalt
PMVF	Los Volcanes	LV3	Los Volcanes	-36.31385	-69.55395	Basalt
PMVF	Los Volcanes	LV6	Los Volcanes	-36.45405	-69.38122	Basalt
PMVF	Los Volcanes	LV8	Los Volcanes	-36.41360	-69.58483	Basalt
PMVF	Los Volcanes	PN1	Pampas Negras	-36.39170	-69.36699	Basalt
PMVF	Río Grande	RG1	Río Grande	-36.47188	-69.64996	Basalt
PMVF	Río Grande	RG2	Río Grande	-36.47218	-69.65015	Basalt
PMVF	Río Grande	RG5	Río Grande	-36.31321	-69.66588	Basalt
PMVF	Río Grande	RG11	Río Grande	-36.43145	-69.64609	Basalt
PMVF	Río Grande	LV9	Los Volcanes	-36.41650	-69.59911	Basalt
PMVF	Río Grande	VRE12	La pasarela	-36.31422	-69.66344	Basalt
PMVF	Río Grande	VRE13	La pasarela	-36.31269	-69.66558	Basalt
PMVF	Payunia	VRE37	Payunia	-36.35861	-69.27650	Basalt
PMVF	Payunia	VRE38	Payunia	-36.33972	-69.38658	Basalt
PMVF	Payunia	VRE40	Payunia	-36.21031	-69.39516	Basalt
PMVF	Payunia	SM16	W side of Santa Maria	-36.22966	-69.33609	Basalt
PMVF	Payunia	SM17	W side of Santa Maria	-36.23573	-69.31216	Basalt
PMVF	Payunia	SM18	W side of Santa Maria	-36.23532	-69.31325	Basalt
PMVF	Pampas Onduladas	VRE19	Pampas Onduladas	-36.41244	-68.57889	Basalt
PMVF	Pampas Onduladas	VRE20	Pampas Onduladas	-36.40847	-68.58000	Basalt
PMVF	Pampas Onduladas	VRE21	Pampas Onduladas	-36.37317	-68.57544	Basalt
PMVF	Pampas Onduladas	VRE46 (A)	Pampas Onduladas	-36.97117	-67.49233	Basalt
PMVF	Pampas Onduladas	VRE47	Pampas Onduladas	-36.99872	-67.49917	Basalt
PMVF	Pampas Onduladas	VRE49	Pampas Onduladas	-37.05717	-67.52031	Basalt
PMVF	Caldera	VRE31	Payún Matrú	-36.37697	-69.25739	Trachytes
PMVF	Caldera	VRE33	Payún Matrú	-36.37667	-69.25872	Trachytes
PMVF	Caldera	VRE34	Payún Matrú	-36.37664	-69.25908	Trachytes
PMVF	Caldera	VRE35	Payún Matrú	-36.37672	-69.26119	Trachytes
PMVF	Caldera	VRE36	Payún Matrú	-36.35665	-69.27699	Trachytes

Table 1 (cont)

Area	Group classification	Sample	sample location	Latitude	Longitude	Material
PMVF	Caldera	VRE39	Payún Matrú	-36.25514	-69.40653	Trachytes
PMVF	Caldera	LV5	Los volcanes	-36.49188	-69.36781	Ignimbrite
PMVF	Caldera	LC1	La Calle	-36.45584	-69.38641	Ignimbrite
PMVF	Caldera	LC2	La Calle	-36.45621	-69.38509	Ignimbrite
LLVF	Carapacho	VRE25	Carapacho	-35.83594	-69.14550	Basalt
LLVF	Carapacho	VRE26 (A)	Carapacho	-35.83972	-69.14394	Basalt
LLVF	Carapacho	CP1	Carapacho	-35.82869	-69.15128	Tuff
LLVF	Carapacho	CP3	Carapacho	-35.82869	-69.15128	Basalt
LLVF	Carapacho	CP4	Carapacho	-35.82869	-69.15128	Tuff
LLVF	Malacara	VRE9	Malacara	-35.77222	-69.46592	Basalt
LLVF	Malacara	MC3	Malacara	-35.76870	-69.48225	Basalt
LLVF	Malacara	MC5	Malacara	-35.75967	-69.47816	Basalt
LLVF	Malacara	MC6	Malacara	-35.76090	-69.47373	Basalt
LLVF	Malacara	VRE27	Llancanelo	-35.71181	-69.45694	Basalt
LLVF	Llancanelo	VRE8	Llancanelo	-35.61292	-69.20192	Basalt
LLVF	Llancanelo	VRE11	Llancanelo	-35.63997	-69.08389	Basalt
LLVF	Llancanelo	VRE42	Llancanelo	-35.84869	-69.16200	Basalt
LLVF	Llancanelo	VRE43	Llancanelo	-35.80328	-69.19545	Basalt
LLVF	Llancanelo	VRE44	Llancanelo	-35.71044	-69.46106	Basalt
LLVF	Llancanelo	VRE45	Llancanelo	-35.66356	-69.52397	Basalt
retroarc	Infiernillo	VRE1	Infiernillo	-35.18650	-69.77327	basaltic-andesite
retroarc	Infiernillo	VRE4	Infiernillo	-35.13675	-69.88212	basaltic-andesite
retroarc	Infiernillo	VRE6	Infiernillo	-35.13689	-69.88161	basaltic-andesite
arc	Cerro Campanario-Pehuenche	VRE16A	Pehuenche	-35.79714	-70.10533	Rhyolite
arc	Cerro Campanario-Pehuenche	VRE16B	Pehuenche	-35.79714	-70.10533	Ignimbrite
arc	Cerro Campanario-Pehuenche	VRE17	Cerro Campanario	-35.96706	-70.34622	basaltic-andesite

2.4.2. Geochemistry

2.4.2.1. Major elements

The total alkali vs SiO_2 content diagram (Figure 2.2; Le Bas et al., 1986) shows that most samples from Llancanelo and Payún Matrú volcanic fields are alkaline basalts with the exception of samples from the caldera group which are silicic (trachytes and trachydacites). Samples from the Infiernillo group are basaltic andesites and have a composition similar to the Andean volcanic arc (Figures 2.2 and 2.3). The basalts from the Llancanelo and the Payún Matrú volcanic fields show similar variations among major-element oxide concentrations, while the Payún Matrú volcanic field basalts have higher TiO_2 and K_2O at a given MgO content than the Llancanelo volcanic field (Figure 2.3). The Caldera and Cerro Campanario-Pehuenche groups show very low MgO, TiO_2, CaO, P_2O_5, FeO_t and high SiO_2, Na_2O, K_2O contents (Figure 2.3) typical of their silicic nature. Infiernillo samples show an intermediate composition between the basalts and the silicic groups (Figure 2.3).

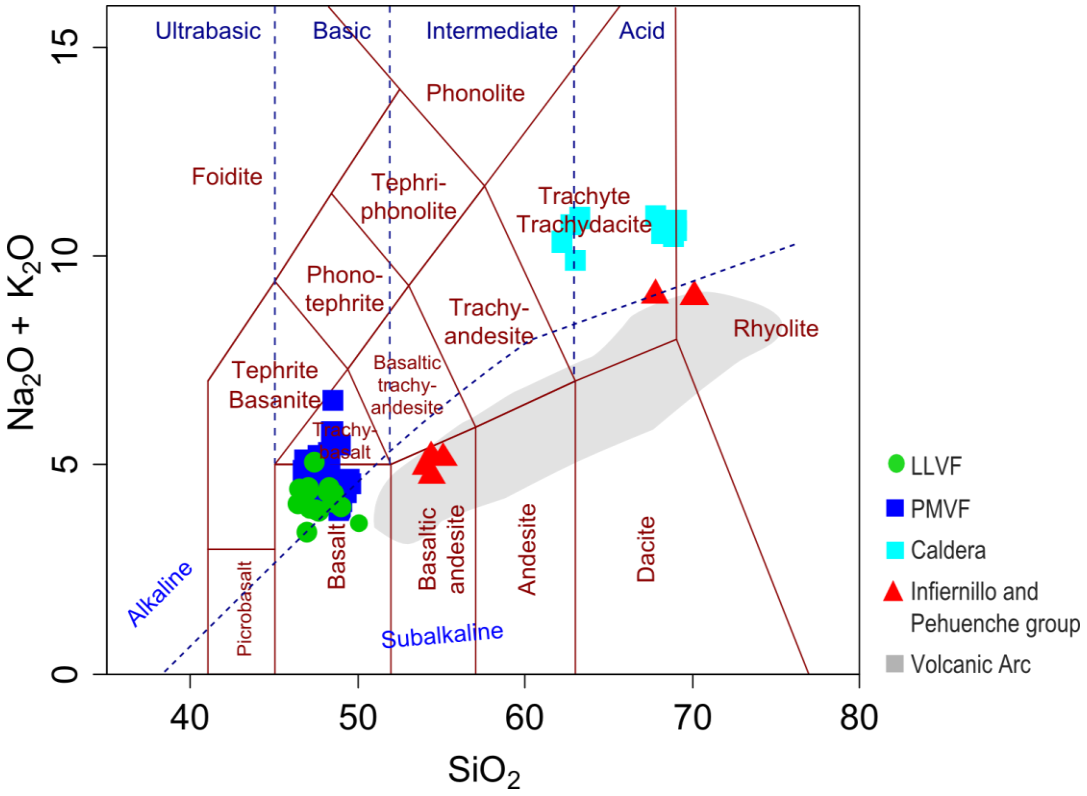

Figure 2.2. Total alkalies versus silica diagram (Le Bas et al., 1986). Most of the basalts and trachydacites from the back-arc are alkaline while the samples from the arc are sub-alkaline. The grey field corresponds to the Andean volcanic arc from the Mainz geochemical database (http://georoc.mpch-mainz.gwdg.de/georoc/Entry.html); only data from the region near our study area were included (34-39°S, 69-72°W).

The MgO content ranges from 4.5 to 12.2 wt % in basalts, from 4.6 to 5.7 wt % in intermediate samples and is <1% in the silicic samples (Figure 2.3). The average MgO content for basalts from Llancanelo volcanic field is 8.5 wt % while for the Payún Matrú volcanic field it is 6.8 wt %. The low MgO content in Los Volcanes group (LV1= 4.5 wt % and PN1= 5.4 wt %) from the Payún Matrú volcanic field are in agreement with the MgO content presented by Jacques et al. (2013) and Søager et al. (2013). The MgO content decreases in the Payún Matrú volcanic field from the Pampas Onduladas group with the highest MgO content (average 7.5 wt %); to the Río Grande, Payunia and Los Volcanes groups (average 6.1 wt %). In the case of the Llancanelo volcanic field, the MgO content decreases from the Carapacho group with the highest average MgO (9.9 wt %), to Malacara and Llancanelo groups (average 7.9 wt %) (Suplementary Table 2.1).

2.4.2.2 Trace elements

Rare earth element (REE) concentrations normalised to chondrites (Boynton, 1984) show a consistent pattern for the basalts from Llancanelo volcanic field and Payún Matrú volcanic field (Supplementary Table 2.1; Figure 2.4). All samples show enrichment in light rare earth elements (LREE) relative to heavy rare earth elements (HREE) as indicated by the La/Yb ratios (average Llancanelo volcanic field La/Yb = 9.14, Payún Matrú volcanic field La/Yb = 8.48). However, the Payún Matrú volcanic field has a steeper HREE pattern than the Llancanelo volcanic field as indicated by higher Dy/Yb (average Payún Matrú volcanic field Dy/Yb=2.25, Llancanelo volcanic field Dy/Yb = 2.18). Negative Eu anomalies, diagnostic of plagioclase crystallisation, are evident for the caldera group (Figure 2.4), as previously observed by Germa et al. (2010).

The majority of the basalts from the Llancanelo and Payún Matrú volcanic fields show enrichment in most of the incompatible elements compared to basalts from the Andean arc (Figure 2.5). The samples from the Llancanelo volcanic field compared to the Payún Matrú volcanic field present higher enrichment in the fluid-mobile elements Cs, Rb, Ba, U and Pb (Large Ion Lithophile Elements, LILE) and depletion in fluid-immobile elements Nb, Ta (High Field Strength Elements, HFSE) relative to LREE such as La, which are typical signatures of the volcanic arc (Jacques et al., 2013). Accordingly, Ba/Ta, La/Ta, Ba/Nb, La/Nb, and Th/Nb are higher in the arc and Infiernillo and Cerro Campanario-Pehuence groups than in the back-arc, and are slightly higher in the Llancanelo than in the Payún Matrú volcanic field (Figure 6a, b, f, g). On the Ba/Ta and La/Nb geospatial distribution maps, the lowest ratios are in the Payún Matrú and the Río Colorado volcanic fields, while these ratios increase towards the Llancanelo volcanic field and the arc (Figure 2.7a, b and 2.8a).

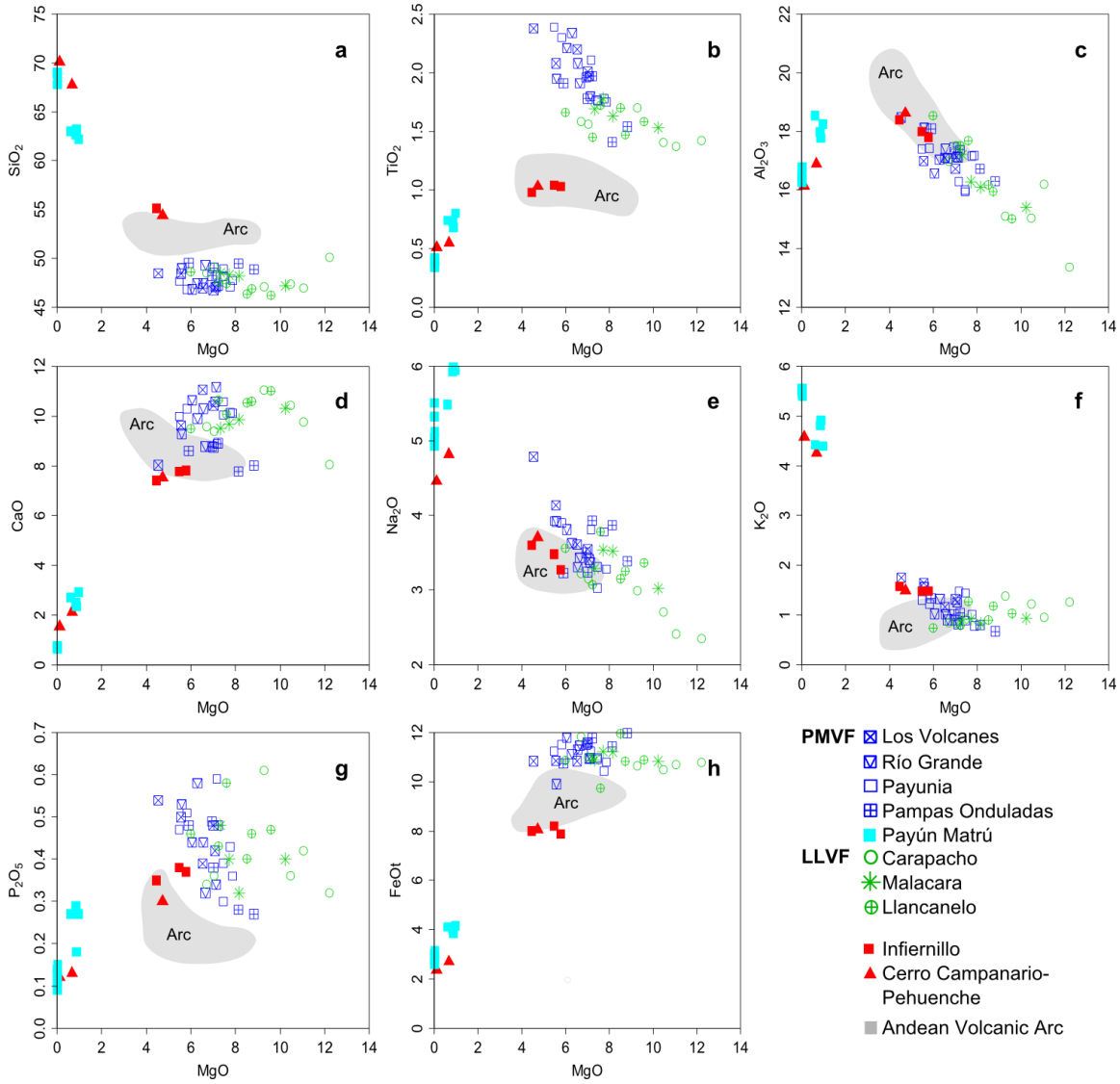

Figure 2.3. Major oxides versus MgO concentration (all in wt %). The Andean volcanic arc field corresponds to data from samples with SiO_2 ranging from 50.9 to 53.0 wt % from the Andean arc between 35°S and 38°S (Costa and Singer, 2002; Ferguson et al., 1992; Jacques et al., 2013; Lopez-Escobar et al., 1977; Tormey et al., 1991; 1995).

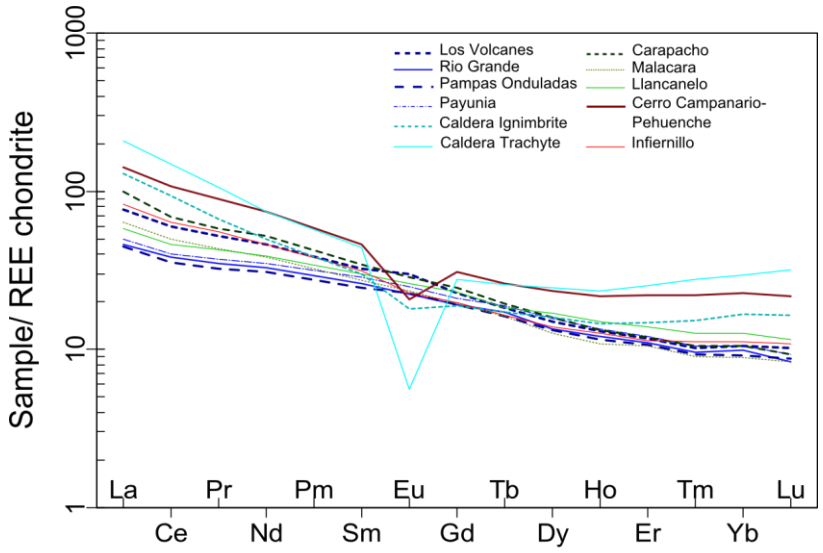

Figure 2.4. Rare earth element concentrations normalised to the chondrite values of Boynton (1984).

The basalts from the Payún Matrú volcanic field have higher Ta/Hf, Nb/Zr ,Ce/Pb, Nb/ Yb and Nb/Y, than the Llancanelo volcanic field; these ratios are highest in the Río Colorado volcanic field which is used in the present study as the local intraplate end-member with ocean island basalt (OIB)-like composition (Figure 2.6f) and may be associated with mantle upwelling (Søager et al., 2013). Basalts from the Llancanelo volcanic field show an intermediate composition between the arc and the OIB-like end-member (Figure 2.5 and 2.6a, c, d, e, f, g). Ce/Pb and Nb/Zr decrease in a westerly direction from the back-arc to the arc and from the Río Colorado northwards (Figure 2.7c, d). The Zr, Nb, and Ta contents increase southward, from Llancanelo to Payún Matrú volcanic fields (Figure 2.8 b, c, d). The Caldera group displays the lowest Ba/Ta and La/Ta ratios (Figure 2.6a) while this group shows the highest Ta/Hf and Nb/Yb (Figure 2.6 e, f) as a result of fractionation.

2.4.2.3. Sr isotopic ratios

The $^{87}Sr/^{86}Sr$ ratios show a restricted range of values, between 0.703747 and 0.704089 (Table 2.2). These values are similar to previous Sr-isotopic measurements reported in the same area (Hernando et al., 2012; Jacques et al., 2013; Muñoz et al., 1989; Pasquarè et al., 2008; Søager and Holm, 2013; Stern et al., 1990). These low Sr isotopic values are indicative of a mantle origin with little to no sialic crustal contamination.

Table 2.2. Sr isotope results for selected samples from the LLVF and the PMVF

Area	Group	Samples	$^{87}Sr/^{86}Sr$
PMVF	Los Volcanes	LV1	0.703858
PMVF	Río Grande	VRE12	0.704083
PMVF	Payunia	SM16	0.704027
PMVF	Payunia	SM18	0.704063
PMVF	Pampas Onduladas	VRE20	0.703747
LLVF	Carapacho	CP3	0.703846
LLVF	Malacara	MC5	0.704050
LLVF	Malacara	VRE27	0.703981
Retroarc	Infiernillo	VRE4	0.704089

2.5. Discussion

2.5.1. Arc influence in the Payenia Basaltic Province

The volcanic arc is characterised by enrichment in LILE relative to HFSE and LREE and enrichment in LREE relative to HFSE, therefore ratios such as Ba/Ta, La/Ta, Ba/Nb, La/Nb, and Th/Nb are high in the arc compared to the back-arc. The geospatial distribution maps illustrate an easterly decrease from the arc to the back-arc in these ratios (Figure 2.7a, b). This trend of decreasing arc signatures in an easterly direction away from the volcanic front is related to a decrease in the amount of slab-derived fluids or melts in the magmas (Jacques et al., 2013; Rivalenti et al., 2004; Stern et al., 1990). Furthermore, a N-S trend is also illustrated, as the Llancanelo volcanic field has higher enrichment in Ba and La relative to Ta and Nb than the

Payún Matrú volcanic field (Figure 2.7a and 2.8a). The Llancanelo volcanic field has a more pronounced arc signature than the Payún Matrú volcanic field as suggested by higher ratios of fluid-mobile to fluid-immobile elements and depletion in Nb and Ta. The Llancanelo volcanic field is interpreted to have a weak arc signature as shown by moderate Ba/Ta (>500), high La/Ta (>24), La/Nb (>1.5), Th/Nb (>0.25) and low Nb/U (<20), Ta/Hf (<0.21), Nb/Yb ratios (< 6.5), in addition to negative Nb, Ta and Ti anomalies.

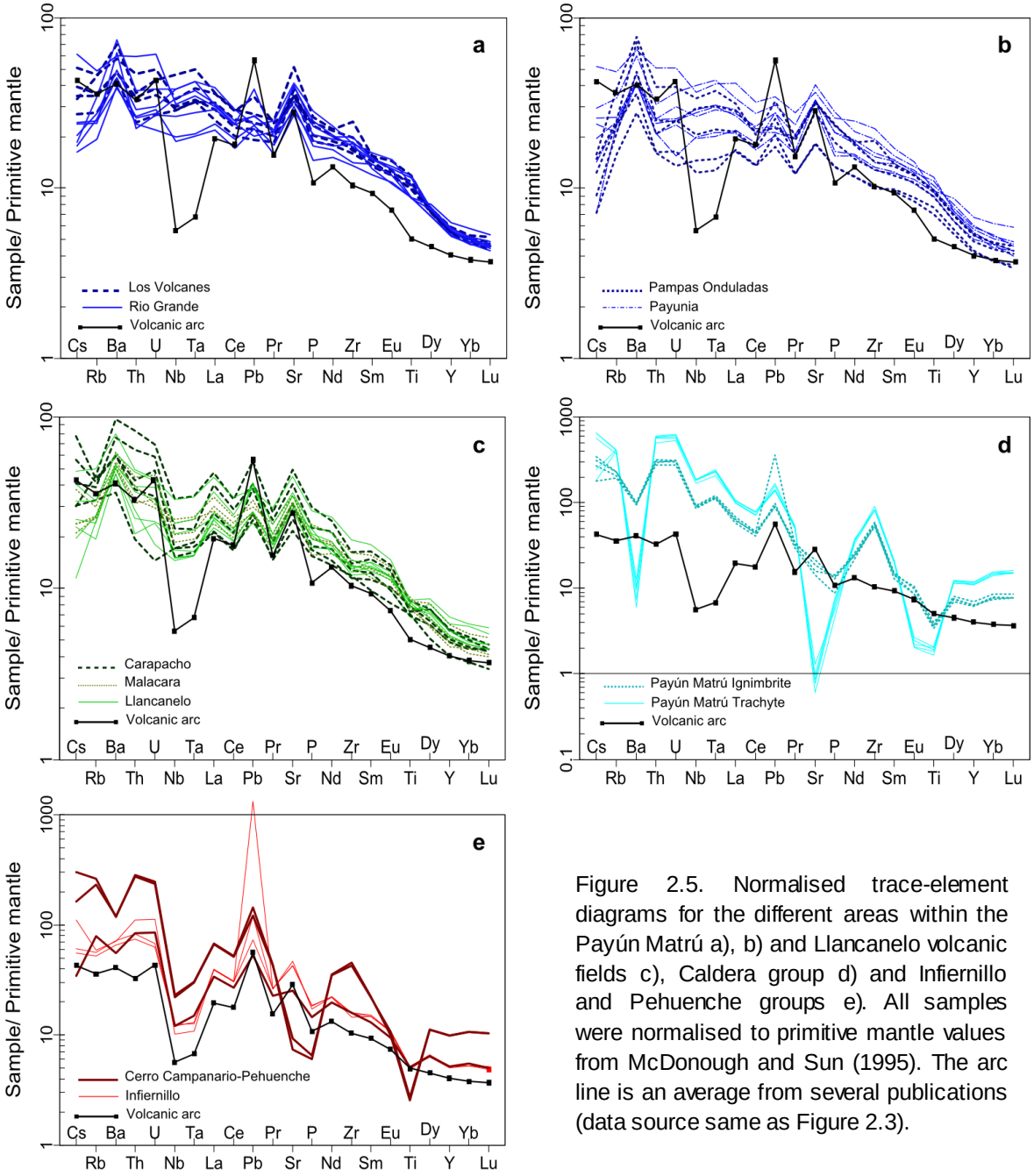

Figure 2.5. Normalised trace-element diagrams for the different areas within the Payún Matrú a), b) and Llancanelo volcanic fields c), Caldera group d) and Infiernillo and Pehuenche groups e). All samples were normalised to primitive mantle values from McDonough and Sun (1995). The arc line is an average from several publications (data source same as Figure 2.3).

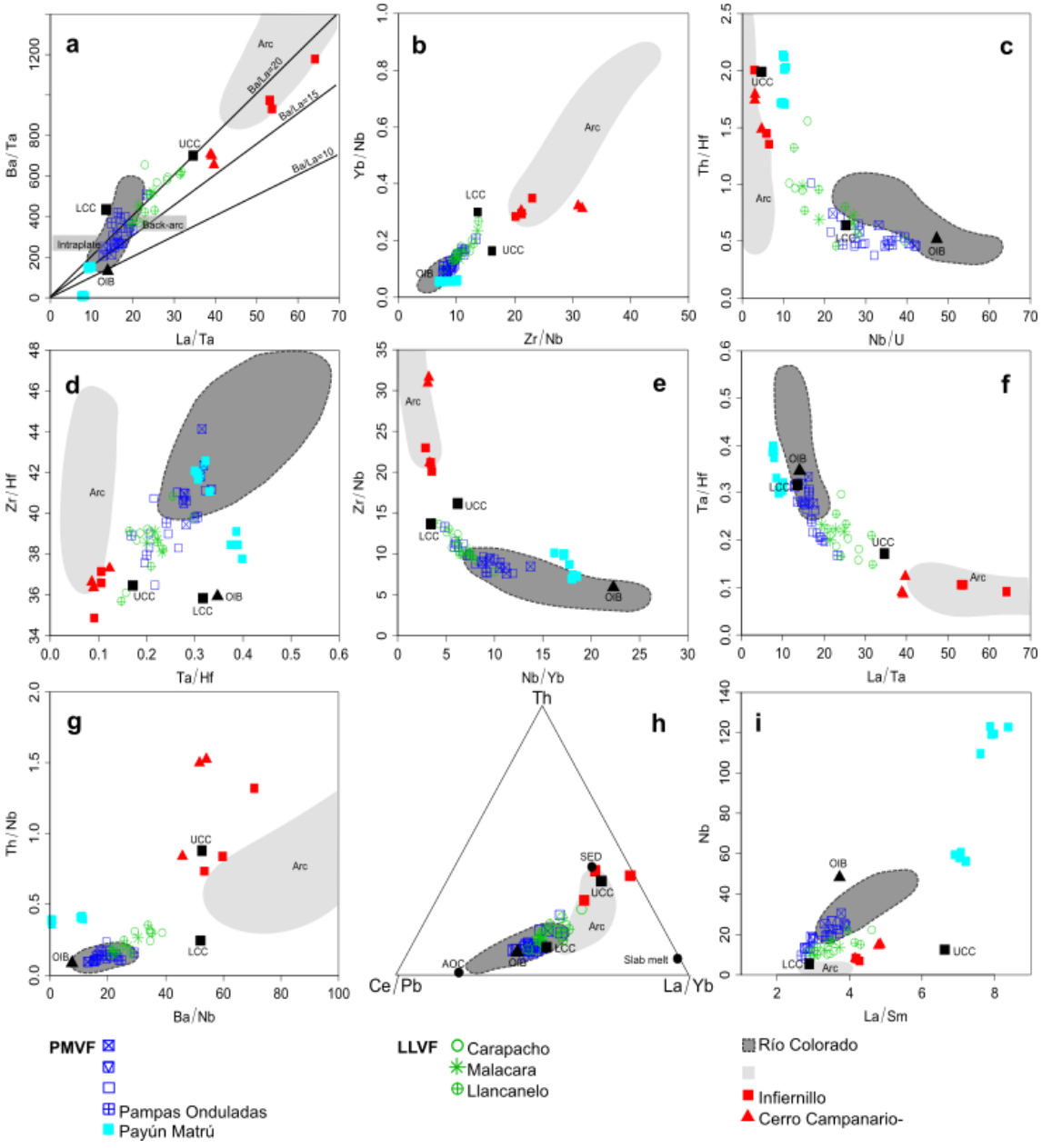

Figure 2.6. Trace-element ratio diagrams, a) La/Ta vs Ba/Ta, b) Zr/Nb vs Yb/Nb, c) Nb/U vs Th/Hf, d) Ta/Hf vs Zr/Hf, e) Nb/Yb vs Zr/Nb, f) La/Ta vs Ta/Hf, g) Ba/Nb vs Th/Nb, h) ternary diagram of Ce/Pb, Th concentration and La/Yb, i) La/Sm vs Nb. The symbols are as in Figure 2.3. The arc field is compiled from several publications (data source same as Figure 2.3). The dark grey field corresponds to the Río Colorado volcanic field (data from Søager et al., 2013) and represents the local intraplate end-member. Compositions for the upper continental crust (UCC) and the lower continental crust (LCC) are from Rudnick and Gao (2003). Composition for the OIB is from Sun and McDonough (1989). Values for slab melt, sediment from the subducting Nazca plate (SED) and altered oceanic crust (AOC) are from Jacques et al. (2013). Note that differentiated samples from the Payún Matrú caldera have been included therefore Ba/Ta, La/Ta, Th/Hf and Ba/Nb ratios are especially modified by fractional crystallisation.

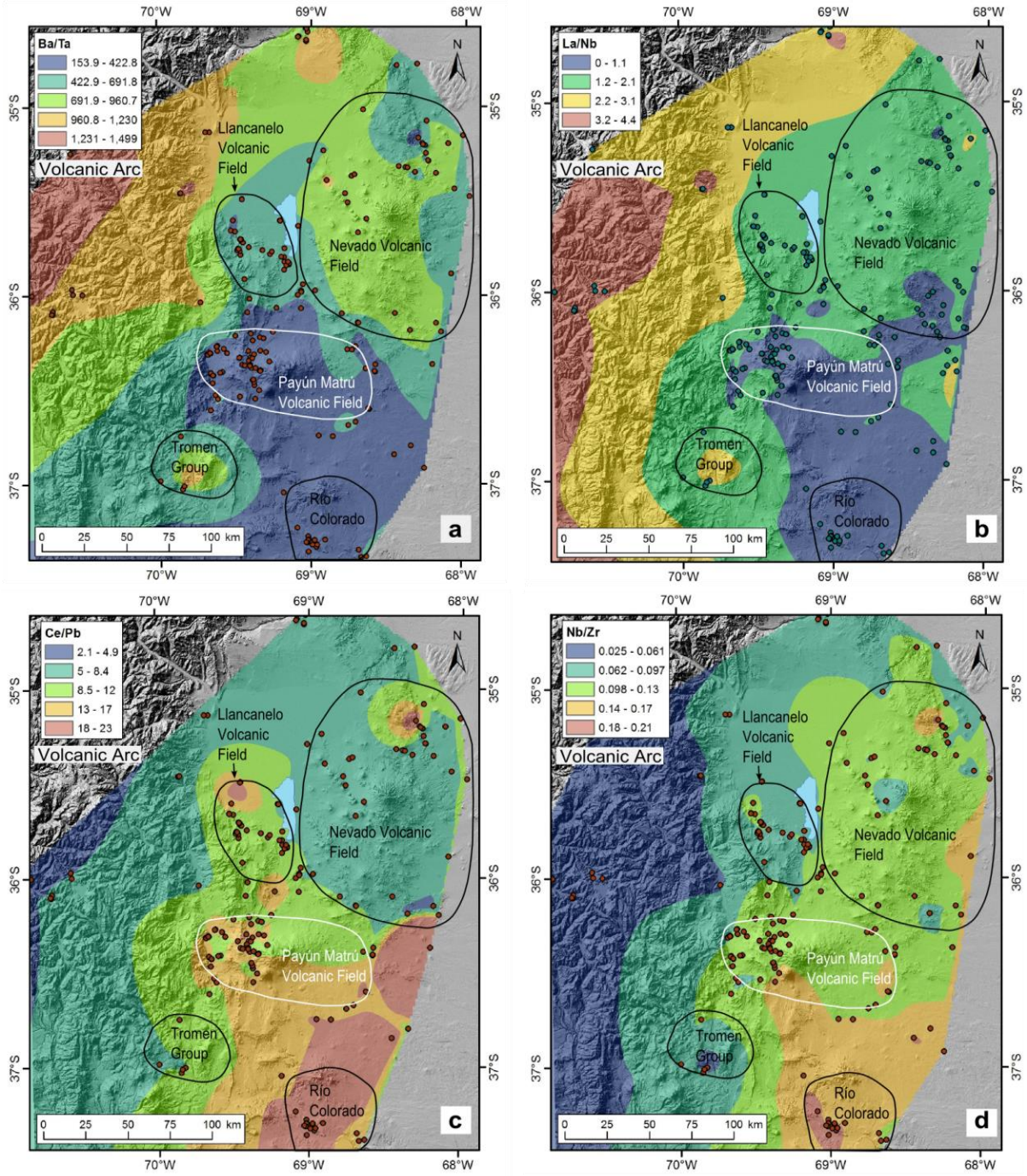

Figure 2.7. Geospatial distribution of trace-element ratios. a) Ba/Ta, b) La/Nb, c) Ce/Pb, and f) Nb/Zr. The trace-element spatial distribution ratios were created using a natural neighbourhood, interpolation tool from ArcMap10. The data points used for these maps were obtained from this investigation as well as from Bertotto et al. (2009), Costa and Singer (2002), Ferguson et al. (1992), Germa et al. (2010), Jacques et al. (2013), Pasquarè et al. (2008), Søager et al. (2013) and Tormey et al. (1991; 1995) and were selected to have SiO_2 <53 wt %. For all the maps, approximately 255 data points were used except for Ce/Pb for which 230 data points were used. The background image used for all of the maps is a hill-shaded SRTM (Shuttle Radar Topography Mission).

In a Ba/Ta vs La/Ta diagram (Figure 2.6a), used among Patagonian back-arc basalts to discriminate between arc, back-arc and intraplate basalts (Kay et al., 2006a), the groups from the Llancanelo volcanic field show a broad distribution and are closer to the arc end-member than the Payún Matrú volcanic field groups. On the same diagram, the Payún Matrú volcanic field groups overlap with the composition of the local intraplate basalts, suggesting no association with the arc (Figure 2.6a). In a Ba/Nb vs Th/Nb diagram (Figure 2.6g), the samples from the Llancanelo volcanic field display a positive trend towards the arc composition, showing higher Ba and Th relative to Nb. Furthermore, the high Th content is demonstrated by the displacement of all the Llancanelo volcanic field groups to a higher Th content (Figure 2.6h and 2.9d). In addition, the Llancanelo volcanic field groups are above the mid ocean ridge-ocean island basalt array (MORB-OIB array; Figure 2.9b) as Th is incorporated from slab components. The Carapacho and Llancanelo groups have the highest Th content of all basaltic groups (averages 3.6 and 3.8 ppm respectively). The high Th concentration among these groups does not result from enrichment during crystallisation because these samples have high MgO contents. The high Th concentration is not likely to be linked to slab dehydration as Th is highly immobile in hydrous fluids (Turner et al., 2003). The location of the subducting slab in the back-arc at this latitude is not well defined, however it has been inferred to be approximately 200 km deep (Tassara et al., 2006), it is improbable that dehydration of the slab will still be occurring (Turner et al., 2003) at such depth. Moreover, a fluid-sensitive ratio such as Sr/Th (Dosseto et al., 2003) is relatively lower for the Llancanelo volcanic field (average Sr/Th= 195, 244, 251 for Carapacho, Llancanelo and Malacara groups, respectively) compared to the Andean arc (average Sr/Th = 283) suggesting that the weak arc signature observed is not likely to be related to fluids released from the slab.

The basalts from the Llancanelo volcanic field trend towards a higher La/Yb at higher Th and lower Ce/Pb than the basalts from the Payún Matrú volcanic field, locating the Llancanelo volcanic field close to the arc-like composition and between the slab melts and the slab sediments end-members (Figure 2.6h). Slab partial melts can fractionate and transport Th and LREE (Kessel et al., 2005) and are characterised by their high residual garnet signature which is reflected in high La/Yb, Sm/Yb and Dy/Yb as HREE are compatible in garnet (La/Yb=100, Sm/Yb=25, Dy/Yb= 6.8, based on slab melt values from Jacques et al., 2013). A strong depletion in HREE associated with slab-derived partial melts is not characteristic of the basalts from the Llancanelo volcanic field. Slab partial melts have previously been suggested for some volcanic segments of South America such as the Austral Volcanic Zone (Figure 2.1; Sigmarsson et al., 1998) and the Southern Volcanic Zone (Figure 2.1; Jacques et al., 2013), where lavas are characterised by high Th concentrations, La/Yb and Sr/Y ratios and low Ce/Pb ratios. It is unclear if slab partial melting is a valid hypothesis for the Llancanelo volcanic field as lavas in this region have low La/Yb and Sr/Y ratios, while the Th content is relatively high (average Th in Llancanelo volcanic field = 3.22 ppm). The Ce/Pb ratio is not a good discriminatory parameter for slab melting in our study area, because of evidence for lower crustal contamination which affects this ratio (Søager et al., 2013) (see Section 2.5.2). The slab

melt influence can also be determined by using U-series radioactive disequilibrium, which can be employed as a tracer for magma generation processes such as in the Austral Volcanic Zone (Sigmarsson et al., 1998). In this study, U-series analyses were not carried out. However, it will be desirable in future investigations, in order to fully assess the hypothesis of partial melting of the subducting slab.

The sediment component has high Ba/Ta, Ba/La, Th/Ta and Th/La than the altered oceanic crust (AOC values from Jacques et al., 2013) and has lower Nb/Yb, Sr/Th and Dy/Yb than any other slab component. The groups from the Llancanelo volcanic field follow this trend possibly indicating that the arc signature could be related to source input of sediment melts from the slab (Figures 2.6, 2.7, 2.9) while Payún Matrú volcanic field dies not. In addition, the groups from Llancanelo volcanic field are displaced to a higher Th/Nb at a higher Th content than the Payún Matrú volcanic field, also suggesting that the slab component observed in the Llancanelo volcanic field can be associated to sediment melting in order to transport Th (Figure 2.9d).

2.5.2. Geochemical variations in the continental back-arc and possible causes

The Llancanelo and Payún Matrú volcanic fields have some geochemical similarities such as having alkaline basalts and trachybasalts with a restricted SiO_2 content (46.2 – 50.0 wt %; Figure 2.2). However, the two volcanic fields have distinct geochemical features suggesting different magmatic sources. In the previous section, it was established that the Llancanelo volcanic field has a weak arc signature possibly attributed to sediment melts transported from the slab, while the Payún Matrú volcanic field does not show such signatures.

The Llancanelo volcanic field shows little to no overlap with the local intraplate composition (Río Colorado volcanic field; Søager et al., 2013), situating this volcanic field at an intermediate composition between the arc and the local intraplate end-members. Geochemical signatures such as low Sm/Yb, Sr/Y and Ce/Pb observed especially in the Carapacho and Llancanelo groups from the Llancanelo volcanic field compared to the local OIB-like can be the result not only of slab sediment melts but also of lower continental crust assimilation. The lower continental crust (LCC, Rudnick and Gao, 2003) is depleted in K, Rb, Ba, Zr, Hf, Th, U and LREE relative to the average arc, the OIB and slab components such as sediments and slab melts. The Llancanelo volcanic field samples have Zr and Hf depletion (Figure 2.5, only Zr shown) while the remaining elements (Rb, Ba, Pb, Th, U) are enriched in relation to the Payún Matrú volcanic field. They are best explained by the contribution of slab-derived sediments as previously discussed. Intermediate Th/Nb and La/Nb ratios can be diagnostic of lower crustal assimilation, as these ratios initially low in the mantle-derived magmas, increase during crustal assimilation. In a diagram of Nb/U vs Ce/Pb (Figure 2.9a) the arc and the local intraplate end-members are well differentiated and form a linear trend. Samples from the Llancanelo volcanic field also show a linear trend but they are shifted towards the LCC end-member. This shift to a higher Nb/U values is interpreted as an indication of lower crustal assimilation, taking place possibly in both volcanic fields. The Ba/Th vs Sr/Th diagram also shows a similar shift towards

higher Ba/Th, supporting a crustal assimilation hypothesis, in particular for the Pampas Onduladas group (Figure 2.9c). The Llancanelo volcanic field groups are shifted towards the LCC and with an intermediate composition between the MORB-OIB array and the average Andean arc composition (Figure 2.9b). Lower continental crust contamination was previously suggested by Søager et al. (2013) for this volcanic field where they suggested up to 70% of lower continental crust assimilation in the Nevado volcanic field (Figure 2.1).

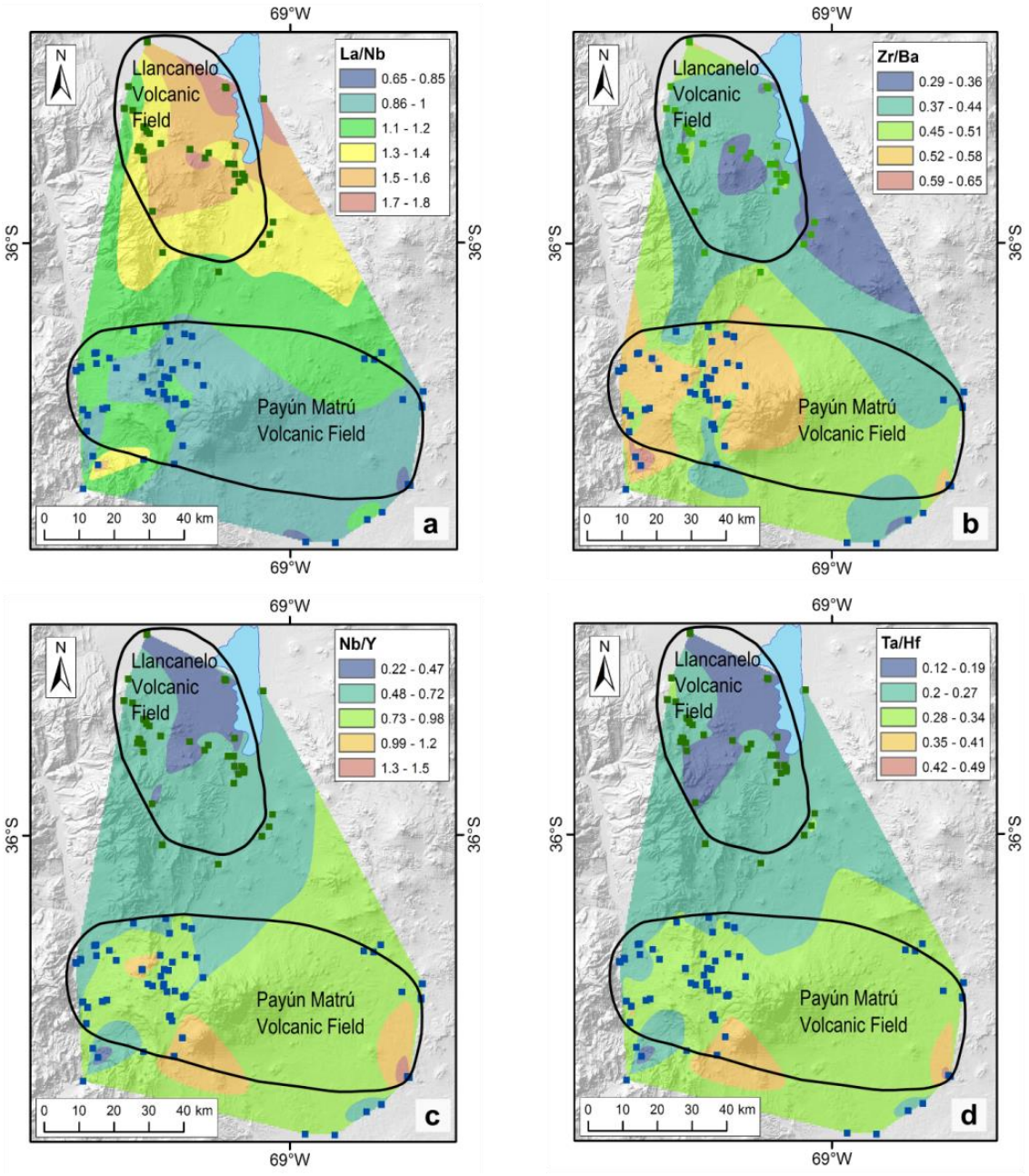

Figure 2.8. Localised geospatial distribution maps of trace-element ratios. a) La/Nb, b) Zr/Ba, c) Nb/Y, and d) Ta/Hf. The data points used are from this study as well as Germa et al. (2010), Jacques et al. (2013) and Søager et al. (2013). These maps are based on 112 data points.

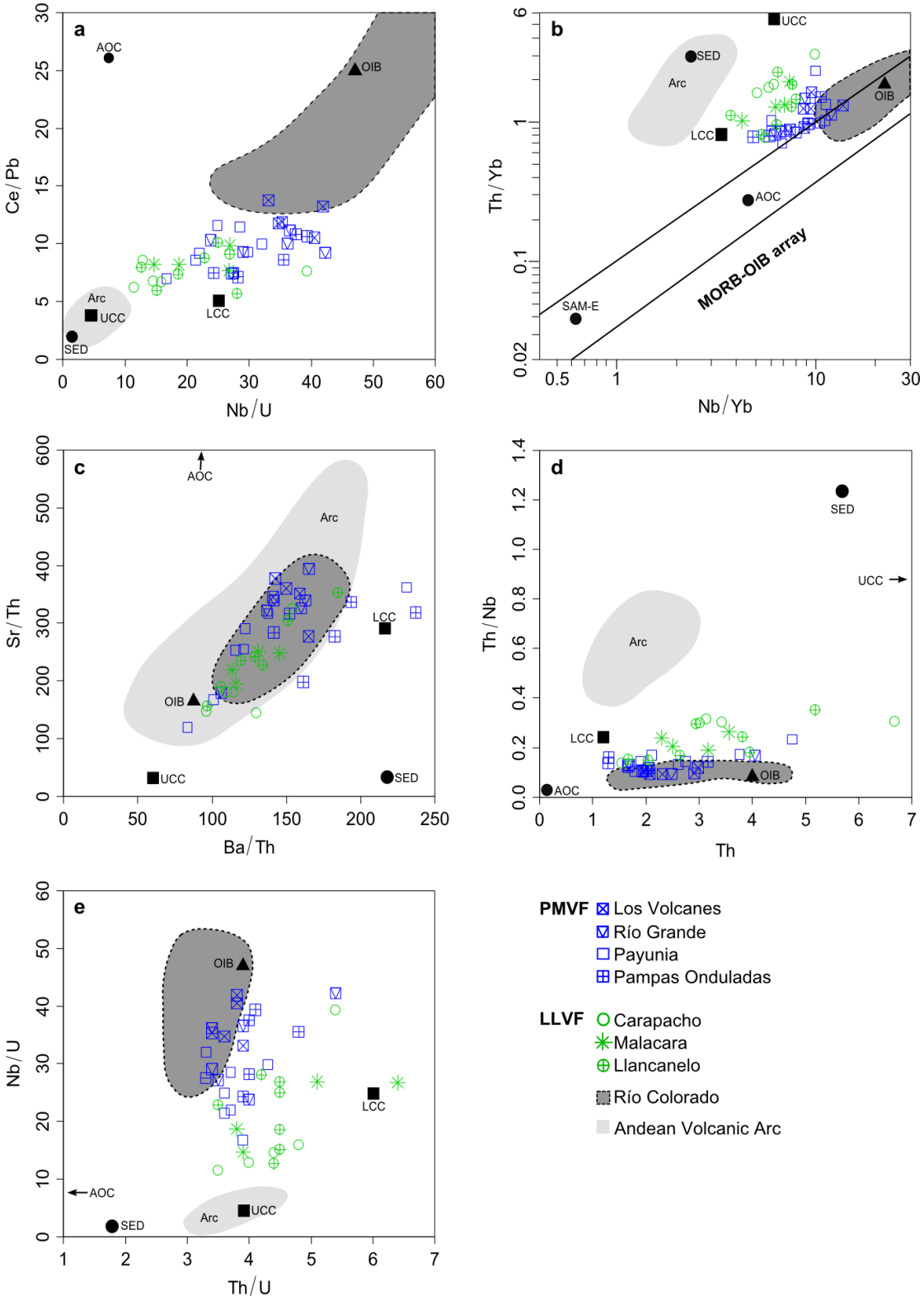

Figure 2.9. Trace-element diagrams. a) Nb/U vs Ce/Pb (modified from Jacques et al., 2013) wherein a shift to the right towards a higher Nb/U is interpreted as lower continental crust assimilation. b) Nb/Yb vs Th/Yb (modified from Pearce, 2008), c) Ba/Th vs Sr/Th, d) Th vs Th/Nb and e)Th/U vs Nb/U. Reference as in Figure 2.3 (Arc field) and Figure 2.6.

In addition, it is important to consider that geochemical signatures from the LCC and melts related to the lithospheric mantle can be similar. The contribution from the sub-continental lithospheric mantle has been inferred in the back–arc of southern Mendoza based on O, Nd and Hf isotopes (Jacques et al., 2013). However, Søager et al. (2013) attributed the feldspar signature, indicated by positive Ba, K, Sr and Eu anomalies in the affected basalts, to the lower continental crust, as feldspars are not stable in the lithospheric mantle. Melting of the lithospheric mantle would result in a weaker garnet signature than deeper asthenospheric melts and high Th/U ratios up to 7.5 (Bourdon and Sims, 2003). The Th/U ratios in the Llancanelo and the Carapacho groups are in many cases high and range up to 6.4. However, high Th/U ratios could also be generated by lower crustal assimilation since the lower crust commonly has a Th/U value of 6. Overall, the data suggest that the geochemical signatures observed in the Llancanelo volcanic field magmatic source were modified by several processes such as a slab component (sediment melts from the slab) and lower crustal contamination. Lithospheric mantle melts may have also contributed to the Llancanelo volcanic field magmas, however further investigation is required to test this hypothesis.

The basalts from the Payún Matrú volcanic field are enriched in most of the immobile elements, such as Nb, relative to the Llancanelo volcanic field and the Andean arc basalts (Figures 2.6i). Nevertheless, the strongest Nb enrichment is shown among the Río Colorado basalts. This was previously interpreted by Jacques et al. (2013), Kay et al. (2006a) and Søager et al. (2013) as due to derivation from an enriched mantle. Thus, here we used the composition of the Río Colorado volcanic field, as the local intraplate end-member. The basalts from the Payún Matrú volcanic field have a similar composition to that of the Río Colorado field (Figure 2.6) suggesting that the general magmatic source for this volcanic field could also be the same enriched mantle (Jacques et al., 2013; Søager and Holm, 2013). The samples from Los Volcanes group show the greatest Zr, Nb, Hf and Ta enrichment among groups of the Payún Matrú volcanic field as indicated by high Ta/Hf (0.29) resembling the values observed in the local intraplate end-member (Río Colorado basalts, Ta/Hf = 0.41). Most of the samples from Los Volcanes group are placed within the Río Colorado field (Figure 2.6), and are within the MORB-OIB array (Figure 2.9b; Pearce, 2008).

Our Sr isotope data show a restricted range and are in agreement with previous data reported for basalts in the Payenia basaltic province (Bertotto et al., 2009; Hernando et al., 2012; Jacques et al., 2013; Kay et al., 2004; Paquarè et al., 2008; Søager and Holm, 2013; Stern et al., 1990). The low Sr isotope ratios suggest little scope for sialic crustal contamination. Accordingly, Hernando et al. (2012) concluded that any crustal contamination in the Payún Matrú caldera would have been small as it is not reflecting an increase in radiogenic ^{87}Sr among the basalts. Furthermore, Eby (1990) determined that A-type (intraplate setting) granitoids derived from an OIB source result in constant Y/Nb and Yb/Ta <1.2 and low Sr isotopic ratios. The silicic Caldera group presents Y/Nb and Yb/Ta ratios <1.2, further supporting the association of these volcanic rocks with an initial intraplate mantle source. In order to determine

the possibility of upper crustal contamination in this volcanic field it is recommended to use another isotopic system with a shorter time-scale such as Th and U or stable isotopes such as $\delta^{18}O$.

2.5.3. Slab geometry and Payenia Basaltic Province volcanism

The variable geochemical signatures observed in the continental back-arc can be related to geometrical changes in the subducting slab. This area of the continental back-arc experienced an episode of shallow subduction peaking in the late Miocene associated with compressional deformation of the overriding plate and an eastward migration of the volcanic arc (Kay and Copeland, 2006; Kay et al., 2006a, b). During the Pliocene and Quaternary, the angle of subduction increased producing the retreat of the volcanic arc to its current location and resulting in mild extension of the overriding plate (Kay et al., 2006a). This mild extension has been linked to slab roll-back as inferred from the migration of back-arc volcanism in the Nevado Volcanic field towards the N-W from ~2.8 Ma to 0.5 Ma (Gudnason et al., 2012). This is also shown by the geospatial distribution maps where the Nevado volcanic field has higher Ba/Ta and lower Ce/Pb than Llancanelo and Payún Matrú volcanic fields (Figure 2.7a, c). The slab roll-back results in extension and provides the necessary space for mantle up-welling. However, it is unclear why the Llancanelo volcanic field does not show high enrichment in HFSE such as in the Payún Matrú volcanic field when they are located only ~30 km apart. One of the possible explanations is that the strong intraplate signature has been overprinted by the components present in the Llancanelo volcanic field such as lower continental crust assimilation and slab components. Another possibility is that because the Llancanelo volcanic field is located closer to the present Pampean flat slab (~270 km north of the Llancanelo volcanic field; Figure 2.1) than the Payún Matrú volcanic field, this colder area could act as a barrier for an ascending enriched mantle. This is supported by the geospatial distribution maps showing a N-S trend in the continental back-arc with an increase in Nb and Zr content from north to south (Figure 2.8). This N-S trend observed in the geochemical distribution maps correlates with a decrease in lithospheric thickness as the lithosphere-athenosphere boundary (LAB) depth decreases from the north-east cold dense flat slab portion (~120 km) to the south-west (~60 km), therefore having a shallower asthenosphere (Tassara et al., 2006). By decreasing the lithospheric mantle thickness, heat flow convection is induced therefore increasing the temperature in the back-arc.

2.6. Conclusions

Continental back-arc magmas of the Payenia Basaltic Province are influenced by several constituents such as (i) slab component (such as: slab fluids and/or sediment melts), (ii) lower crustal contamination, and (iii) an enriched intraplate mantle source (Jacques et al., 2013; Søager et al., 2013). Nevertheless, the influences of these constituents vary across the several volcanic fields of this region. The Llancanelo volcanic field shows evidence of a weak arc signature. This arc signature in the Llancanelo volcanic field is not likely to be related to slab dehydration, as inferred from the slab location and the enrichment in less fluid-mobile Th

relative to U (Figure 2.9e). Instead, the influence from subduction components in the Llancanelo volcanic field lavas can be dominated by the contribution of subducted sediments. The absence of HREE depletion argues against the involvement of slab partial melts which is another possible slab component. On the geospatial distribution maps, the Ba/Ta and La/Nb ratios decrease from the Andean arc in an easterly direction. These ratios also decrease from north to south, reflecting the absence of a slab influence in the Payún Matrú volcanic field lavas, while high Nb/U values at a given Ce/Pb could suggest the occurrence of lower crustal assimilation. However, the Sr isotope data do not suggest sialic crustal contamination. In particular, Los Volcanes group shows high Zr/Ba, Nb/Y, Ce/Pb, Nb/Yb and Ta/Hf ratios similar to the local intraplate end-member. Geochemical maps show that while an enriched mantle signature is observed for the Payún Matrú volcanic field, it is diminished in the Llancanelo volcanic field. Thus, geochemical mapping could be used to help identify areas of elevated concentration of high field strength element coinciding with areas of mantle upwelling.

Supplementary Table 2.1. Major- and trace-element results from samples analysed. Major-elements in wt % and trace-elements in ppm

Sample	LV6	LV1	LV3	LV8	PN1	RG1	RG2	RG5	RG11	LV9	VRE12
SiO_2	46.83	48.34	46.95	46.06	47.33	49.02	47.76	48.39	46.95	46.92	46.77
TiO_2	2.20	2.38	1.97	1.98	2.02	2.15	2.40	1.75	2.28	1.72	1.76
Al_2O_3	17.06	18.42	17.09	16.49	16.57	16.55	17.44	15.83	17.49	15.49	17.03
FeO_t	10.81	10.81	10.92	11.45	10.45	11.43	11.27	10.82	11.30	10.78	10.37
MnO	0.15	0.15	0.15	0.16	0.15	0.16	0.15	0.15	0.15	0.16	0.16
MgO	6.52	4.53	7.06	6.91	5.36	7.27	5.48	7.39	5.85	7.33	7.70
CaO	11.04	8.01	10.55	10.28	9.35	9.02	10.02	10.49	10.24	9.77	10.08
Na_2O	3.60	4.78	3.40	3.50	4.01	3.87	3.94	3.00	4.00	3.21	3.75
K_2O	1.15	1.74	1.24	1.30	1.60	1.49	1.30	0.87	1.21	1.40	1.00
P_2O_5	0.38	0.54	0.42	0.48	0.49	0.60	0.48	0.30	0.51	0.38	0.42
Total	99.52	99.49	99.42	98.23	97.09	101.5	100.2	99.08	99.94	98.56	99.93
V	298	238	259	262	252	222	272	239	262	232	251
Cu	49	29	46	48	42	40	37	60	56	55	74
Zn	55	56	55	54	54	62	58	59	56	53	69
Ga	19.9	20.8	18.9	19.2	20.1	19.8	21.0	19.7	20.4	18.9	19.6
Rb	16.7	27.1	20.8	21.4	27.9	20.6	16.5	14.9	15.3	29.4	14.5
Sr	701	1023	753	694	631	826	797	537	782	565	647
Y	23.6	23.8	23.1	23.7	25.4	25.0	24.9	22.4	24.2	22.8	26.8
Zr	168	258	181	174	208	192	209	142	184	191	196
Nb	18.8	30.4	19.8	19.1	22.0	25.2	25.2	12.4	22.3	20.4	17.3
Cs	0.57	0.70	0.73	0.83	1.07	0.39	0.43	0.51	0.37	1.29	0.50
Ba	292	462	317	317	379	491	325	256	295	396	413
Sc	36.5	21.1	33.4	31.3	27.5	25.7	30.3	33.0	28.6	30.4	33.3
La	16.3	23.6	18.8	20.5	23.2	25.2	20.0	14.2	20.4	19.5	18.8
Ce	33.7	48.2	38.0	42.4	47.3	48.4	40.0	28.8	41.4	39.7	39.6
Pr	4.73	6.34	5.13	5.64	6.13	6.27	5.48	4.00	5.55	5.06	5.41
Nd	22.4	27.7	23.4	25.2	27.2	28.8	25.0	18.9	25.4	22.0	24.2
Sm	5.55	6.28	5.46	5.86	6.30	6.56	6.04	4.86	5.94	5.27	6.01
Eu	1.87	2.21	1.83	1.82	1.93	2.27	2.06	1.66	2.00	1.62	1.98
Gd	5.59	5.85	5.33	5.81	5.91	6.39	5.97	5.25	5.91	5.07	6.29
Tb	0.92	0.87	0.88	0.90	0.94	0.96	0.92	0.80	0.89	0.81	0.92
Dy	4.83	4.85	4.84	4.87	5.09	5.16	5.06	4.56	5.07	4.59	5.38
Ho	0.95	0.93	0.91	0.93	0.99	0.99	0.97	0.92	0.96	0.90	1.06
Er	2.54	2.46	2.44	2.50	2.73	2.58	2.57	2.38	2.52	2.47	2.95
Tm	0.33	0.33	0.32	0.33	0.37	0.33	0.33	0.30	0.33	0.34	0.41
Yb	2.15	2.21	2.09	2.20	2.32	2.24	2.26	2.07	2.12	2.05	2.55
Lu	0.29	0.33	0.32	0.31	0.35	0.31	0.33	0.29	0.32	0.31	0.36
Hf	4.25	5.84	4.42	4.29	5.08	4.67	4.99	3.63	4.34	4.70	4.80
Ta	1.20	1.84	1.22	1.19	1.42	1.56	1.56	0.75	1.39	1.29	1.03
Pb	2.87	4.06	3.31	3.66	5.16	3.52	3.03	3.37	3.94	5.71	3.98
Th	1.95	2.91	2.60	2.74	3.76	2.98	2.31	2.11	2.07	4.75	1.79
U	0.54	0.86	0.70	0.77	1.00	0.76	0.60	0.58	0.55	1.22	0.54

Major-element oxide analysis: School of Earth and Environmental Sciences, University of Wollongong, Australia

Trace-element analysis: Research School of Earth Sciences, Australian National University, Canberra , Australia

Note: The average MgO in wt % for each group classification is, Los Volcanes = 6.08, Río Grande = 7.02, Payunia = 7.47, Pampas Onduladas = 7.47, Caldera = 0.66, Carapacho = 9.86, Malacara = 8.39, Llancanelo = 7.87, Infiernillo = 5.26, Cerro Campanario-Infienillo = 1.90.

Supplementary Table 2.1. (cont)

Sample	VRE13	VRE37	VRE38	VRE40	SM16	SM17	SM18	VRE19	VRE20	VRE21	VRE46a
SiO_2	49.15	48.45	49.82	49.20	46.26	46.27	46.94	48.31	49.71	49.34	50.05
TiO_2	1.80	2.13	1.98	1.91	2.28	2.19	1.79	2.01	2.02	1.90	1.82
Al_2O_3	17.70	17.78	18.45	17.04	16.62	16.37	17.07	17.78	17.99	18.03	17.59
FeO_t	11.13	11.56	10.09	11.45	10.86	11.65	10.94	12.07	11.84	10.71	11.79
MnO	0.15	0.15	0.15	0.15	0.15	0.16	0.15	0.16	0.15	0.14	0.15
MgO	8.11	6.70	5.69	6.64	6.14	5.98	7.12	7.39	7.15	5.88	7.16
CaO	10.42	10.53	9.45	8.76	9.66	10.52	11.16	9.13	9.06	8.59	8.93
Na_2O	3.38	3.38	3.99	3.43	3.54	3.77	3.37	4.03	3.61	3.22	3.31
K_2O	0.80	1.04	1.59	0.90	1.29	1.01	0.82	1.06	1.04	1.33	0.91
P_2O_5	0.37	0.45	0.54	0.32	0.56	0.43	0.34	0.49	0.51	0.48	0.39
Total	102.8	101.7	101.5	99.37	98.97	99.03	100.2	102.0	103.1	102.0	102.3
V	255	264	257	214	251	278	270	221	225	242	221
Cu	61	59	47	47	46	50	51	47	46	57	53
Zn	61	62	59	67	57	60	56	64	66	65	69
Ga	20.4	20.9	21.1	20.2	20.8	20.1	20.1	20.5	20.0	20.8	20.0
Rb	11.7	14.7	29.0	14.2	20.2	15.7	12.8	14.5	14.8	22.8	12.7
Sr	600	653	727	570	808	660	653	642	638	626	557
Y	24.2	25.7	28.8	22.7	24.5	25.2	21.6	23.5	23.1	22.6	20.8
Zr	148	160	234	134	202	170	139	148	149	199	135
Nb	13.2	18.2	24.2	13.1	26.6	17.4	12.8	19.0	19.3	22.3	13.6
Cs	0.34	0.41	1.09	0.15	0.62	0.54	0.50	0.30	0.31	0.33	0.19
Ba	261	272	430	273	396	280	273	308	475	510	320
Sc	34.6	34.3	30.9	25.1	27.9	32.6	34.8	25.0	25.8	28.2	25.4
La	15.5	17.3	27.0	13.6	21.9	17.9	14.2	18.7	18.4	20.4	14.0
Ce	32.5	35.7	53.4	28.1	46.1	38.8	30.9	37.6	36.0	34.4	28.6
Pr	4.53	4.93	7.06	4.05	5.97	5.24	4.23	4.99	4.88	5.12	3.93
Nd	20.9	22.7	30.9	19.2	26.8	23.9	19.8	23.2	22.4	23.3	18.5
Sm	5.61	5.84	6.93	4.95	6.27	5.99	5.05	5.64	5.45	5.61	4.80
Eu	1.82	1.96	2.20	1.73	2.06	1.89	1.63	1.86	1.83	1.84	1.66
Gd	5.44	6.00	6.80	5.38	6.03	5.87	4.96	5.53	5.42	5.29	4.95
Tb	0.89	0.95	1.06	0.85	6.87	0.97	0.82	0.89	0.85	0.86	0.77
Dy	5.03	5.42	5.84	4.78	4.91	5.13	4.30	4.93	4.66	4.61	4.29
Ho	0.96	1.03	1.14	0.90	1.00	1.03	0.86	0.91	0.91	0.86	0.83
Er	2.54	2.77	3.06	2.39	2.50	2.63	2.30	2.53	2.43	2.35	2.23
Tm	0.34	0.37	0.41	0.31	0.34	0.35	0.31	0.33	0.31	0.33	0.30
Yb	2.20	2.30	2.74	1.97	2.22	2.34	2.05	2.08	2.09	2.11	1.92
Lu	0.30	0.33	0.40	0.29	0.32	0.31	0.27	0.29	0.29	0.31	0.28
Hf	3.95	4.18	5.71	3.66	4.92	4.36	3.63	3.73	3.75	4.90	3.40
Ta	0.77	1.11	1.51	0.79	1.59	1.07	0.75	1.14	1.13	1.38	0.82
Pb	3.50	3.20	5.19	3.05	4.61	4.18	4.17	3.47	3.39	4.84	3.83
Th	1.90	1.92	4.05	1.68	2.48	2.05	1.66	2.03	2.00	3.16	1.66
U	0.44	0.50	1.02	0.31	0.73	0.60	0.47	0.51	0.49	0.79	0.50

Supplementary Table 2.1. (cont)

Sample	VRE47	VRE49	VRE31	VRE33	VRE34	VRE35	VRE36	VRE39	LV5	LC1	LC2
SiO_2	50.70	49.34	68.46	69.62	69.83	70.07	67.87	63.21	61.48	62.34	62.01
TiO_2	1.60	1.41	0.42	0.39	0.37	0.34	0.40	0.74	0.79	0.67	0.72
Al_2O_3	16.91	16.68	16.94	16.69	16.44	16.65	16.71	18.60	18.04	17.51	17.79
FeO_t	12.43	11.40	3.07	2.86	2.80	2.62	3.12	4.12	4.10	3.78	3.96
MnO	0.15	0.15	0.12	0.11	0.11	0.11	0.14	0.10	0.10	0.10	0.10
MgO	9.15	8.11	0.008	0.008	0.008	0.008	0.02	0.61	0.96	0.86	0.84
CaO	8.31	7.75	0.76	0.74	0.70	0.64	0.68	2.71	2.89	2.31	2.48
Na_2O	3.52	3.87	5.56	4.99	5.11	5.41	5.11	5.51	5.88	5.91	5.87
K_2O	0.70	0.80	5.51	5.61	5.63	5.62	5.39	4.44	4.35	4.85	4.77
P_2O_5	0.28	0.28	0.14	0.11	0.13	0.09	0.15	0.28	0.27	0.18	0.29
Total	103.1	99.3	101.6	101.5	101.5	102.0	101.5	100.6	99.11	99.81	99.73
V	186	179	24	18	20	19	23	57	42	39	42
Cu	52	60	31	47	39	18	26	23	9	22	276
Zn	69	66	64	52	60	53	59	45	34	49	532
Ga	19.8	19.4	24.9	24.6	24.6	23.6	25.1	21.3	20.5	20.4	21.4
Rb	9.5	14.1	223.5	237.4	247.1	249.5	242.8	137.7	123.0	136.2	117.5
Sr	367	360	17	26	15	12	19	373	432	284	316
Y	18.4	17.8	46.7	48.1	50.8	49.6	48.5	29.8	27.5	26.2	26.8
Zr	104	108	956	865	859	852	886	615	553	579	590
Nb	9.5	8.1	109.6	119.1	123.2	122.9	119.4	60.7	56.2	58.0	59.4
Cs	0.15	0.26	11.83	3.81	5.12	13.76	13.60	7.22	5.61	6.58	3.75
Ba	183	237	64	70	49	40	84	667	643	624	619
Sc	23.0	21.5	5.7	4.5	4.5	4.5	5.7	7.6	6.4	6.1	5.5
La	10.7	10.8	64.8	63.5	68.2	69.0	67.9	44.0	41.7	37.2	39.9
Ce	22.6	23.0	120.4	118.0	128.3	128.1	130.9	77.9	72.8	68.8	75.0
Pr	3.06	3.11	12.84	12.40	13.61	13.58	13.38	8.74	8.21	7.47	8.13
Nd	14.7	14.4	44.5	41.9	46.9	45.3	45.5	32.4	30.5	27.5	30.0
Sm	4.01	3.88	8.52	8.03	8.66	8.24	8.50	6.23	5.80	5.29	5.79
Eu	1.36	1.29	0.41	0.38	0.32	0.31	0.34	1.53	1.63	1.31	1.33
Gd	4.09	3.94	7.20	6.71	7.28	7.14	7.13	5.40	5.16	4.64	4.89
Tb	0.67	0.63	1.22	1.23	1.24	1.26	1.32	0.87	0.84	0.76	0.82
Dy	3.83	3.62	7.91	7.69	8.27	8.26	8.25	5.39	5.03	4.72	5.12
Ho	0.72	0.69	1.69	1.68	1.75	1.76	1.77	1.14	1.05	0.99	1.04
Er	1.96	1.88	5.33	5.35	5.79	5.61	5.58	3.37	3.05	3.02	3.11
Tm	0.26	0.26	0.90	0.87	0.97	0.95	0.90	0.55	0.49	0.49	0.49
Yb	1.63	1.67	6.18	6.42	6.86	6.80	6.59	3.75	3.28	3.37	3.47
Lu	0.24	0.23	1.03	1.02	1.10	1.04	1.04	0.58	0.53	0.53	0.53
Hf	2.74	2.77	23.27	22.10	22.34	22.57	23.04	14.65	12.98	13.77	14.16
Ta	0.55	0.47	7.71	8.54	8.72	9.01	8.63	4.47	4.18	4.13	4.34
Pb	2.62	3.08	21.09	23.62	25.11	20.65	21.23	13.50	13.38	14.81	53.73
Th	1.29	1.30	39.66	44.78	47.37	48.20	46.39	25.18	22.18	23.61	24.23
U	0.27	0.33	10.66	11.29	12.16	12.44	11.77	6.18	5.54	6.22	6.02

Supplementary Table 2.1. (cont)

Sample	VRE25	VRE26a	CP1	CP3	CP4	VRE9	MC3	MC5	MC6	VRE27	VRE8
SiO_2	47.99	47.78	44.70	46.91	44.50	49.66	48.07	47.01	48.17	49.93	48.48
TiO_2	1.57	1.40	1.32	1.70	1.27	1.73	1.63	1.52	1.78	1.71	1.48
Al_2O_3	16.80	16.48	14.18	15.05	11.88	17.61	16.06	15.35	16.24	19.03	17.82
FeO_t	11.71	10.89	9.91	10.60	9.58	11.14	11.19	10.80	11.20	11.16	11.17
MnO	0.16	0.17	0.15	0.16	0.13	0.16	0.16	0.16	0.16	0.15	0.16
MgO	6.67	11.26	9.90	9.26	12.23	7.51	8.14	10.20	7.70	6.16	7.37
CaO	9.49	9.94	9.84	11.00	7.16	9.75	9.84	10.29	9.66	9.76	10.84
Na_2O	3.19	2.46	2.55	2.98	2.08	3.37	3.51	3.01	3.53	3.66	3.13
K_2O	0.84	0.97	1.14	1.37	1.11	0.94	0.81	0.93	0.92	0.75	0.81
P_2O_5	0.34	0.43	0.34	0.61	0.28	0.50	0.32	0.40	0.40	0.47	0.44
Total	100.5	102.1	100.1	100.6	99.80	102.3	100.4	100.0	99.53	103.1	102.5
V	203	270	247	269	242	235	231	249	231	237	283
Cu	55	69	61	70	46	47	52	54	40	47	61
Zn	65	60	51	64	46	53	63	55	64	68	54
Ga	19.4	17.8	16.4	19.1	14.6	20.4	19.6	18.4	19.8	21.6	20.1
Rb	19.5	19.4	25.1	27.4	26.0	15.9	15.3	17.8	15.4	11.7	14.4
Sr	502	566	616	980	434	693	627	693	637	590	691
Y	21.6	21.1	20.9	24.4	17.2	26.4	19.6	20.7	22.5	22.2	26.6
Zr	121	126	134	171	124	169	140	142	154	143	136
Nb	11.3	10.0	11.3	21.9	10.1	16.7	12.3	13.6	15.8	11.0	9.9
Cs	0.64	0.85	1.18	0.63	1.62	0.50	0.50	0.79	0.44	0.48	0.53
Ba	238	345	393	643	391	360	328	413	341	309	351
Sc	25.5	35.1	31.2	32.0	29.2	31.9	30.6	32.7	29.8	28.7	37.6
La	13.9	16.6	17.9	30.8	13.7	22.2	15.5	19.6	18.3	14.6	18.1
Ce	28.7	36.0	35.2	55.2	27.9	43.9	33.2	40.3	37.9	31.6	37.2
Pr	3.85	4.64	4.76	7.04	3.72	6.02	4.32	5.28	4.99	4.29	5.21
Nd	18.1	20.9	21.3	31.1	17.1	26.3	19.9	23.1	22.6	19.9	23.4
Sm	4.58	4.93	4.99	6.68	3.96	6.32	4.69	5.28	5.31	5.09	5.80
Eu	1.57	1.50	1.50	2.10	1.26	2.05	1.55	1.71	1.85	1.73	1.91
Gd	4.74	4.62	4.77	6.37	3.77	6.15	4.51	5.00	5.25	4.94	5.99
Tb	0.79	0.70	0.76	0.92	0.63	0.96	0.76	0.77	0.81	1.46	0.86
Dy	4.33	4.14	4.15	5.11	3.43	5.50	4.02	4.09	4.55	4.47	5.43
Ho	0.84	0.81	0.79	0.95	0.65	1.06	0.79	0.78	0.90	0.88	1.08
Er	2.32	2.25	2.14	2.50	1.82	2.84	2.14	2.19	2.35	2.34	2.93
Tm	0.32	0.32	0.31	0.34	0.25	0.39	0.30	0.29	0.32	0.32	0.41
Yb	2.01	1.96	1.94	2.20	1.63	2.40	1.96	1.84	2.08	2.07	2.65
Lu	0.29	0.30	0.30	0.30	0.23	0.35	0.28	0.27	0.30	0.30	0.37
Hf	3.09	3.26	3.41	4.30	3.19	4.37	3.63	3.63	4.04	3.66	3.82
Ta	0.65	0.58	0.69	1.28	0.60	0.97	0.72	0.79	0.94	0.61	0.57
Pb	3.77	4.21	5.71	8.31	4.13	4.47	4.06	4.92	4.17	3.62	6.24
Th	1.55	3.14	3.43	6.68	3.01	3.17	2.50	3.56	2.64	1.67	2.94
U	0.29	0.78	0.98	1.38	0.69	0.62	0.66	0.92	0.59	0.48	0.66

Supplementary Table 2.1. (cont)

Sample	VRE11	VRE42	VRE43	VRE44	VRE45	VRE1	VRE4	VRE6	VRE16a	VRE16b	VRE17
SiO_2	47.23	49.45	48.21	45.69	45.96	56.32	54.21	54.09	68.93	66.57	56.74
TiO_2	1.49	1.58	1.75	1.56	1.70	1.00	1.05	1.03	0.50	0.54	1.07
Al_2O_3	16.07	17.64	17.98	14.85	16.06	18.79	18.04	17.72	15.87	16.59	19.42
FeO_t	10.91	11.07	9.91	10.76	11.83	8.17	8.23	7.85	2.32	2.66	8.42
MnO	0.16	0.15	0.15	0.16	0.17	0.13	0.13	0.12	0.07	0.08	0.13
MgO	8.81	7.11	7.74	9.49	8.45	4.55	5.49	5.74	0.10	0.65	4.93
CaO	10.67	9.45	10.27	10.89	10.50	7.58	7.80	7.78	1.50	2.10	7.84
Na_2O	3.28	3.17	3.84	3.33	3.10	3.68	3.49	3.25	4.39	4.74	3.87
K_2O	1.18	0.84	1.29	1.01	0.88	1.60	1.48	1.48	4.51	4.19	1.56
P_2O_5	0.47	0.36	0.59	0.47	0.39	0.36	0.38	0.37	0.12	0.13	0.31
Total	102.0	100.7	101.5	100.2	98.89	102.6	100.7	100.3	101.1	103.1	103.9
V	265	234	259	243	265	205	212	215	32	43	206
Cu	58	43	55	80	107	71	49	50	31	49	38
Zn	53	65	57	69	73	59	53	46	46	50	55
Ga	19.1	20.5	20.2	18.1	19.6	19.9	19.6	19.2	16.5	16.9	18.9
Rb	23.4	14.8	29.8	19.4	15.9	35.5	31.3	33.5	158.7	138.6	47.1
Sr	807	568	897	724	619	929	842	851	147	184	499
Y	24.8	24.2	29.3	22.8	24.3	22.1	21.5	22.4	42.5	42.5	22.4
Zr	147	131	202	153	140	153	164	167	478	449	168
Nb	14.8	9.6	21.8	15.8	13.6	6.7	8.1	7.9	15.1	14.5	7.9
Cs	0.86	0.24	1.02	0.68	0.41	2.32	1.16	1.28	6.34	3.42	0.72
Ba	502	333	529	405	307	472	434	472	782	785	363
Sc	33.2	30.3	32.6	31.5	33.2	25.2	28.2	29.1	9.3	10.4	26.7
La	26.0	16.3	28.9	23.8	17.0	25.7	25.0	25.8	43.7	43.0	21.9
Ce	48.5	31.9	56.8	45.2	34.5	50.8	50.9	51.4	87.2	85.4	44.7
Pr	6.33	4.54	7.52	6.01	4.75	6.64	6.74	6.76	10.94	10.79	5.79
Nd	26.8	21.1	32.8	26.5	22.1	27.5	27.4	27.8	44.2	43.3	24.8
Sm	6.04	5.37	7.30	5.75	5.48	6.00	6.02	6.15	9.02	8.97	5.28
Eu	1.96	1.79	2.26	1.79	1.80	1.63	1.67	1.66	1.51	1.64	1.44
Gd	5.79	5.53	7.03	5.72	5.42	5.01	5.17	5.08	7.96	7.84	4.75
Tb	0.87	0.89	1.12	0.86	0.87	0.75	0.76	0.78	1.23	1.24	0.77
Dy	5.07	5.00	5.84	4.78	4.85	4.31	4.23	4.45	7.53	7.58	4.31
Ho	0.99	0.97	1.14	0.91	0.96	0.84	0.86	0.90	1.56	1.57	0.88
Er	2.61	2.50	3.12	2.43	2.54	2.38	2.32	2.37	4.61	4.50	2.48
Tm	0.37	0.33	0.41	0.31	0.35	0.35	0.34	0.36	0.71	0.70	0.34
Yb	2.30	2.25	2.73	2.07	2.14	2.33	2.32	2.33	4.72	4.67	2.41
Lu	0.32	0.32	0.40	0.30	0.32	0.34	0.33	0.35	0.70	0.70	0.34
Hf	3.92	3.63	4.94	4.01	3.64	4.40	4.41	4.58	13.05	12.35	4.49
Ta	0.82	0.57	1.26	0.94	0.81	0.40	0.47	0.48	1.12	1.11	0.55
Pb	6.11	4.16	5.65	6.15	6.06	17.90	10.97	198.44	21.59	18.19	7.95
Th	5.18	2.29	3.95	3.82	2.04	8.81	5.97	6.63	22.69	22.13	6.67
U	1.17	0.36	0.87	0.85	0.49	2.26	1.25	1.36	4.97	4.71	1.70

Supplementary Table 2.1. (cont)

Duplicates of 10% HCl leached samples

Sample	Ga	Rb	Sr	Y	Zr	Nb	Hf	Pb
	ppm	ppm	ppm	ppm	ppm	ppm	ppm	ppm
SM16	18.8	20.4	802.0	27.5	188.2	25.7	4.2	3.4
VRE21	19.9	24.8	631.6	28.9	173.3	20.3	4.0	3.7
VRE46a	20.2	14.5	566.8	23.0	119.1	12.4	3.2	3.4
VRE43	20.3	30.3	808.3	27.7	166.7	18.5	3.0	5.9
CP4	12.7	32.4	486.7	19.1	107.8	9.0	4.2	4.2
VRE27	19.1	14.9	580.4	27.0	129.5	9.8	3.1	6.5
VRE11	19.0	25.1	726.9	24.1	124.2	12.4	2.9	7.4
VRE27R	18.8	15.0	575.4	27.1	129.2	9.5	4.1	6.2
BCR-2	21.6	49.3	342.5	37.2	184.3	12.6	4.7	12.5
BCR-2 recommended value	23±2	48±2	346±14	37±2	188±16	12.6±0.4	4.8±0.2	11±2

Trace-element analysis performed by XRF at the School of Earth and Environmental Sciences, University of Wollongong, Wollongong, Australia

Supplementary Table 2.2. Reproducibility of LA-ICP-MS data for BCR-2 rock standard.

All values are in ppm

Standard: BCR-2	^{45}Sc	^{51}V	^{65}Cu	^{66}Zn	^{71}Ga	^{85}Rb	^{88}Sr	^{89}Y	^{91}Zr	^{93}Nb	^{133}Cs	^{137}Ba	^{139}La	^{140}Ce	^{141}Pr	^{146}Nd
BCR-2	37.0	427	20	109	22.4	46.5	349	35.2	190	13.0	1.14	695	26.2	52.9	6.85	29.4
BCR-2	38.2	424	20	105	22.0	46.6	358	36.1	197	13.3	1.15	706	26.8	52.9	6.97	29.7
BCR-2	35.5	425	19	117	21.5	45.0	334	33.8	181	12.3	1.14	664	24.8	50.3	6.48	28.0
BCR-2	36.1	424	21	116	21.9	45.5	339	34.4	186	12.4	1.15	663	25.5	50.9	6.61	28.2
BCR-2	37.0	426	21	113	22.0	46.0	340	34.6	189	12.5	1.13	678	25.4	51.1	6.56	28.5
BCR-2	34.5	416	19	114	21.5	43.3	312	30.7	176	11.6	1.06	625	22.6	46.4	5.96	25.8
BCR-2	36.1	434	19	114	22.0	47.0	343	34.4	185	12.5	1.14	676	25.0	51.7	6.62	28.3
BCR-2	35.6	441	19	118	22.7	48.2	346	33.6	182	12.5	1.20	685	24.9	52.7	6.64	28.3
BCR-2	36.7	431	20	125	22.0	46.7	346	34.9	187	12.7	1.15	683	25.8	51.8	6.69	28.7
BCR-2	35.2	426	19	116	21.7	45.5	334	33.4	182	12.3	1.12	665	24.6	50.6	6.44	27.8
BCR-2	35.3	438	21	122	22.4	47.0	334	32.9	183	12.4	1.13	667	24.4	51.2	6.46	27.5
BCR-2	35.0	431	20	118	21.7	46.7	332	32.9	180	12.2	1.11	665	24.5	50.9	6.40	27.4
Average	36.0	429	20	116	22.0	46.2	339	33.9	185	12.5	1.14	673	25.0	51.1	6.56	28.1
Std dev	1.0	6.7	0.7	5.3	0.4	1.2	11.3	1.4	5.32	0.4	0.03	20.1	1.1	1.7	0.25	1.0
Std dev relative %	2.9	1.6	3.7	4.6	1.6	2.7	3.3	4.1	2.88	3.3	2.92	3.0	4.2	3.4	3.85	3.5
Reference value (certificate)	33±2	416±14	19±2	127±9	23±2	48±2	346±14	37±2	188±16		1.1±0.1	683±28	25±1	53±2	6.8±0.3	28±2
Difference in ppm (reference-average)	3.00	12.58	0.83	11.37	1.00	1.83	7.06	3.10	3.09		0.04	10.23	0.04	1.89	0.24	0.13
Error % to recommended value	9.09	3.02	4.39	8.95	4.34	3.82	2.04	8.38	1.64		3.22	1.50	0.14	3.57	3.57	0.48

Supplementary Table 2.2. (cont)

^{147}Sm	^{153}Eu	^{157}Gd	^{159}Tb	^{163}Dy	^{165}Ho	^{166}Er	^{169}Tm	^{172}Yb	^{175}Lu	^{178}Hf	^{181}Ta	^{205}Tl	^{208}Pb	^{232}Th	^{238}U
6.94	2.04	6.76	1.07	6.64	1.35	3.84	0.53	3.64	0.52	5.24	0.80	0.26	10.62	6.33	1.66
6.98	2.09	6.98	1.09	6.86	1.40	4.00	0.55	3.80	0.53	5.47	0.81	0.24	10.40	6.44	1.66
6.62	1.95	6.48	1.03	6.26	1.29	3.63	0.51	3.48	0.51	4.97	0.77	0.26	10.58	6.01	1.65
6.69	1.97	6.59	1.02	6.36	1.30	3.67	0.52	3.44	0.50	5.05	0.77	0.24	10.76	6.01	1.63
6.83	1.95	6.68	1.02	6.54	1.33	3.70	0.52	3.61	0.51	5.10	0.78	0.25	10.61	6.12	1.65
6.13	1.77	5.97	0.92	5.76	1.17	3.29	0.47	3.14	0.46	4.51	0.70	0.21	10.12	5.43	1.53
6.90	1.98	6.61	1.03	6.33	1.31	3.64	0.51	3.51	0.49	4.97	0.77	0.25	10.87	6.00	1.70
6.58	1.97	6.51	1.01	6.34	1.29	3.59	0.50	3.46	0.50	4.89	0.75	0.24	11.14	5.94	1.74
6.82	2.01	6.78	1.05	6.51	1.33	3.76	0.52	3.51	0.52	5.03	0.79	0.24	11.17	6.19	1.69
6.45	1.92	6.42	1.01	6.26	1.26	3.58	0.51	3.44	0.49	4.87	0.76	0.24	10.59	5.94	1.63
6.40	1.96	6.37	1.01	6.28	1.27	3.58	0.50	3.43	0.49	4.80	0.74	0.25	11.14	5.89	1.65
6.39	1.95	6.35	1.00	6.22	1.27	3.61	0.51	3.35	0.49	4.70	0.76	0.25	10.72	5.92	1.64
6.64	1.96	6.54	1.02	6.36	1.30	3.66	0.51	3.48	0.50	4.97	0.77	0.24	10.73	6.02	1.65
0.26	0.08	0.26	0.04	0.27	0.06	0.17	0.02	0.16	0.02	0.25	0.03	0.01	0.32	0.25	0.05
3.99	3.89	3.94	4.11	4.22	4.27	4.66	3.81	4.64	3.63	5.02	3.73	5.68	2.95	4.19	2.94
6.7±0.3	2.0±0.2	6.8±0.3	1.07±0.04		1.33±0.06		0.54	3.5±0.2	0.51±0.02	4.8±0.2			11±2	6.2±0.7	1.69±0.19
0.06	0.04	0.21	0.05		0.03		0.03	0.02	0.01	0.17			0.27	0.18	0.04
0.85	1.80	3.09	4.60		2.47		5.01	0.45	2.23	3.48			2.48	2.94	2.25

Chapter 3:

*Geochronological, morphometric and geochemical constraints on the Pampas Onduladas long basaltic flow (Payún Matrú volcanic field, Mendoza, Argentina)**

Venera R. Espanon [a,b], Allan R. Chivas[a], David Phillips[c], Erin L. Matchan[c] and Anthony Dosseto[a,b]

[a] *GeoQuEST Research Centre, School of Earth & Environmental Sciences, University of Wollongong, NSW 2522, Australia.*

[b] *Wollongong Isotope Geochronology Laboratory, School of Earth & Environmental Sciences, University of Wollongong, NSW 2522, Australia*.

[c]*School of Earth Sciences, The University of Melbourne, Parkville, VIC 3010, Australia.*

Allan R. Chivas: toschi@uow.edu.au

David Phillips: dphillip@unimelb.edu.au

Erin L. Matchan: ematchan@unimelb.edu.au

Anthony Dosseto: tony_dosseto@uow.edu.au

*Manuscript published (2014) in the *Journal of Volcanology and Geothermal Research,* volume 289, pages 114-129. DOI: 10.1016/j.jvolgeores.2014.10.018

Abstract

The Pampas Onduladas flow in southern Mendoza, Argentina, is one of the four longest Quaternary basaltic flows on Earth. Such flows (>100 km) are relatively rare on Earth as they require special conditions in order to travel long distances and there are no recent analogues. Favourable conditions include: a gentle topographic slope, an insulation process to preserve the melt at high temperature, and a large volume of lava with relatively low viscosity. This study investigates the rheological and geochemical characteristics of the ~170 km long Pampas Onduladas flow, assessing conditions that facilitated its exceptional length. This study also reports the first geochronological results for the Pampas Onduladas flow. $^{40}Ar/^{39}Ar$ step-heating analyses of groundmass reveal an eruption age of 373 ± 10 ka (2σ), making the Pampas Onduladas flow the oldest Quaternary long flow.

The methods used to assess the rheological properties include the application of several GIS tools to a digital elevation model (DEM) to determine the length, width, thickness, volume and topographic slope of the flow as well as algorithms to determine its density, viscosity and temperature. The slope of the Pampas Onduladas flow determined from the initial part of the flow on the eastern side of La Carbonilla fracture to its end point in the province of La Pampa is 0.84% (0.29°), the steepest substrate amongst long Quaternary flows. The rheological properties, such as density viscosity and temperature from the Pampas Onduladas flow are similar to values reported for other long Quaternary flows. However, the minimum volume calculated is relatively low for its length compared with other long Quaternary flows. Therefore, the extension of the Pampas Onduladas flow was probably controlled by a steep slope, combined with an insulating mechanism, which helped in providing optimal conditions for a travel length of almost 170 km.

3.1. Introduction

Long basaltic flows (>100 km) produced in a single volcanic eruption are unusual on Earth (but common on Mars), as they require relatively large lava volumes and steep slopes (Keszthely and Self, 1998; Keszthely et al., 2004). For the Quaternary (<2.6 Ma), only four flows have been reported to be longer than 100 km, and there are no historic analogues of long flows. The four long Quaternary flows recognised are: the Toomba and Undara flows in Queensland, Australia (Stephenson et al., 1998); the Thjorsa flow in Iceland (Vilmundardottir, 1977); and the Pampas Onduladas flow in Mendoza, Argentina (Pasquarè et al., 2005). These have reported volumes greater than 12 km^3 and a pahoehoe character. Some of the basic requirements for long basaltic flows are: i) an insulating mechanism to maintain the lava at high temperature; and ii) a large volume of erupted lava (Pikerton and Wilson, 1994). The four long Quaternary basaltic flows exhibit inflation structures such as lava rises and/or tumuli and in some cases lava tubes such as in the Toomba and Undara flows (Stephenson et al., 1998) that insulate the lava, thereby reducing its cooling by <50°C/100 km according to the models of Keszthely and Self (1998). Of special interest is the Pampas Onduladas flow as it has been described as the longest on Earth during the Quaternary (Pasquarè et al., 2008). It has a relatively narrow (~5 km) tongue-like structure that dominates for more than 70% of its length and lacks lava tube structures.

Despite the significance of the Pampas Onduladas flow, rheological, geochemical and geochronological analyses are lacking. Previous investigations mainly dealt with recognising and describing this flow from a morphological view point (Pasquarè et al., 2005; Pasquarè et al., 2008). The purpose of this investigation is to assess some of the physical parameters and geochemical characteristics of this flow, in order to comprehend the factors that have facilitated its length, and to also determine the eruption age.

3.2. Background (This section is a reduced version of the publication, see thesis appendix D)

3.2.1. Regional geological setting

Most of the volcanism in South America is characterised by Andean arc volcanism resulting from the dehydration of the subducting Nazca plate. In general, the subduction signature decreases in the back-arc in an easterly direction (Stern et al., 1990; Rivalenti et al., 2004; Jacques et al., 2013). In some basaltic volcanic fields, such as Llancanelo and Payún Matrú (Figure 3.1), the arc signature among basalts of the continental back-arc is variable to negligible (Espanon et al., 2014b corresponding to Chapter 2). The Pampas Onduladas flow is part of the Payún Matrú volcanic field (PMVF) in the central western region of Argentina (Figure 3.1). The Payún Matrú volcanic field is one of four volcanic fields that constitute the Payenia Basaltic Province (PBP), defined by Polanski (1954) (also described as the Andino-Cuyana Basaltic Province by Bermudez and Delpino, 1989). The Quaternary volcanic fields in this region have

been re-grouped recently into the Nevado, Llancanelo, Payún Matrú and Río Colorado volcanic fields (see review by Ramos and Folguera, 2011; Gudnason et al., 2012).

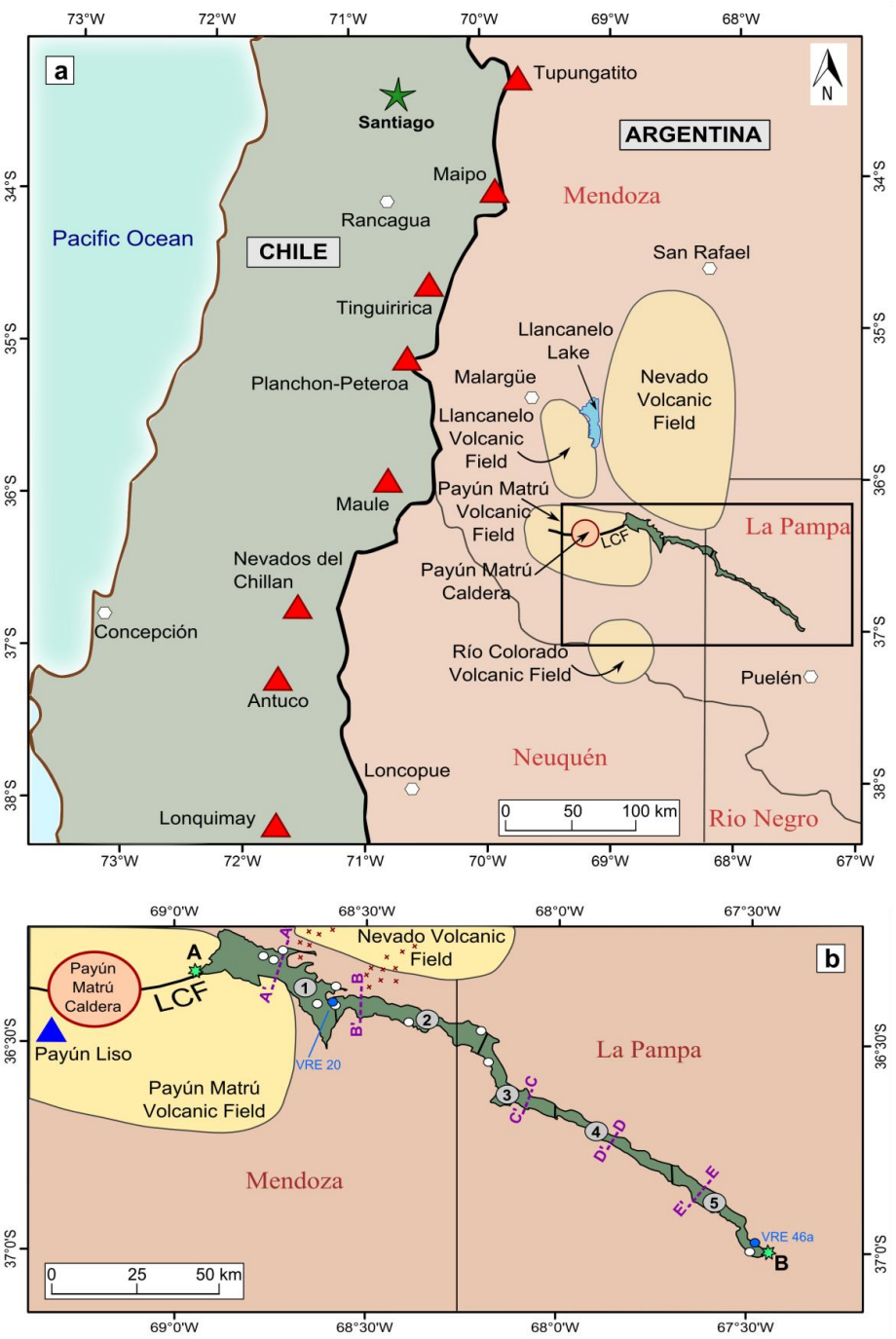

Figure 3.1. a) Geographical setting of the Pampas Onduladas flow. LCF indicates La Carbonilla Fracture in the Payún Matrú volcanic field. The hexagons are towns. Red triangles are volcanoes from the Andean arc. b) Map of the southern Mendoza region with the Pampas Onduladas flow in green. The numbers on the Pampas Onduladas flow indicate sections 1 to 5 into which it has been divided. Dashed purple lines indicate the location of each of the cross sections (refer to Figure 3.5). The red crosses indicate exposures of the San Rafael Block. The white circles within the flow are samples from Pasquarè et al. (2008) and from Chapter 2, while the two blue circles are the samples used for $^{40}Ar/^{39}Ar$ dating. The two green stars (A and B) represent the initial and final points of the flow; between which the length was calculated.

3.2.2. Payún Matrú volcanic field (PMVF) and Pampas Onduladas flow

The back-arc volcanism in the PMVF is associated with an enriched mantle similar to an ocean island basalt-type (Kay et al., 2004; Germa et al., 2010; Søager et al., 2013) associated with an intraplate tectonic setting. The volcanic cones in the PMVF are mainly aligned in an E-W direction corresponding to La Carbonilla Fracture (Figure 3.1; Llambías et al., 2010). This fracture was formed by crustal relaxation after a period of compression associated with flat subduction during the Miocene (Kay et al., 2006a). La Carbonilla Fracture is exposed in its eastern part, interrupted by the Payún Matrú caldera in its central part (Figure 3.1) and completely covered along its western part (inferred to underlie a field of aligned scoria cones; Hernando et al., 2014b). The Pampas Onduladas flow is located on the eastern side of the PMVF (Figure 3.1) and its eruption point is associated with the far eastern end of La Carbonilla Fracture. However, tracking the actual eruption point is challenging, as the area is covered by several younger basaltic flows. The basement beneath the Pampas Onduladas flow is composed of older basaltic flows.

The volcanism in the PMVF is understood to be older on its eastern side; however, the geochronology is poorly constrained. Flows from the eastern side of the PMVF have reported K-Ar ages ranging from 600 ± 100 ka (Bertotto, 1997) to 950 ± 500 ka (Núñez, 1976). A single age estimate comes from a basaltic flow located stratigraphically below the Pampas Onduladas flow dated to 400 ± 100 ka by K-Ar (Melchor and Casadío, 1999). Furthermore, the Pampas Onduladas flow pre-dates the Payún Matrú caldera (Figure 3.1) as the Portezuelo Ignimbrite stratigraphically overlies the Pampas Onduladas flow. The caldera-forming event is recognised to have occurred between 168 ± 4 ka and 82 ± 2 ka based on K-Ar dating (Germa et al., 2010), providing a minimum age constraint for the Pampas Onduladas flow. Therefore, its the age is possibly younger than 400 ka and older than 168 ka([*]).

The Pampas Onduladas flow as well as most of the older flows in the PMVF, has a pahoehoe character, in contrast to the younger flows (<10 ka), which are dominated by a'a morphology (Inbar and Risso, 2001; Figure 3.2). The Pampas Onduladas flow has been described by Pasquarè et al. (2005; 2008) as a compound flow, having an external morphology dominated by tumuli and lava rises, which are typical of an internally inflated flow. The tumuli are elongated in the medial area, while in the distal areas elongated lava rises are abundant (Figure 3.3). The appearance of the tumuli (~40km from the initial part) is similar to those described in the Llancanelo volcanic field (Nemeth et al., 2008) as they are flow-lobe tumuli generally less than 9 metres in height with relatively steep angles and a central crack from which lava outpour was not recognised (Figure 3.3). The lava rises are randomly oriented long the flow and with a range of dimensions and they generally have a central cleft (Figure 3.3). Lava rises are recognised on the side of the kipukas (Figure 3.3) in the proximal to medial section of the flow where higher pre-existing topography was engulfed by the flowing lava. The internal structure is composed of a thin, highly vesicular crust, which is on average less than 1 metre thick and the vesicles are

([1]) this long flow has been dated in the current investigation to 373 ± 10 ka.

rounded to subrounded with a maximum diameter of 2 cm. This upper zone is underlain by a dense layer in some parts heavily jointed which is approximately 2-3 m thick (Pasquarè et al., 2008). Below this layer, the jointing diminishes and the lava is more vesicular (elongated aligned vesicles), gradually changing to a massive layer formed by co-mingling of the elongated vesicles (Pasquarè et al., 2008). The flow has a hawaiite composition with low phenocryst content (Figure 3.4; Pasquarè et al., 2008).

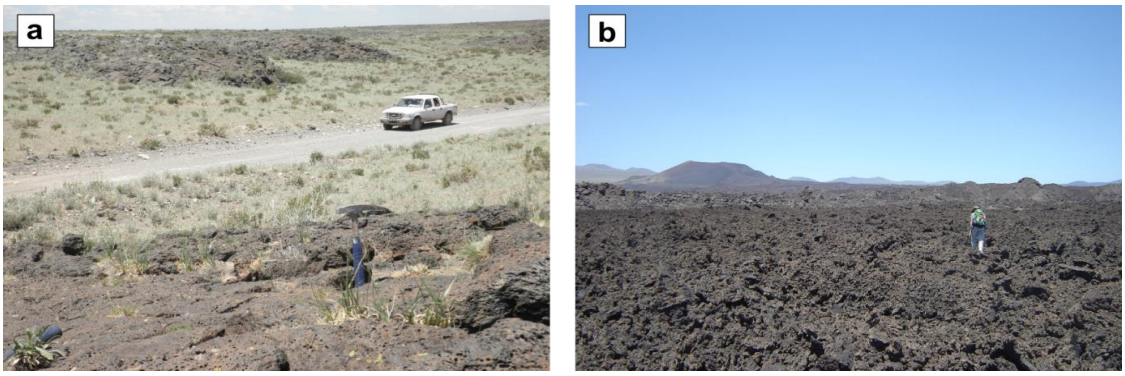

Figure 3.2. Examples of basaltic morphotypes from the Payún Matrú volcanic field. a) Proximal to central part of Pampas Onduladas flow, showing a pahoehoe morphology; b) Proximal to central part of Santa Maria flow, showing an a'a morphology. Note the smooth surface of the pahoehoe Pampas Onduladas flow in contrast to the rough surface of the Santa Maria flow.

The magmatic source region for this extensive flow has been inferred to be affected by metasomatism associated with the subduction of the Nazca plate (Pasquarè et al., 2008), although recent studies suggest that the Payún Matrú volcanic field (PMVF, Figure 3.1) shows minimal (Jacques et al., 2013; Søager et al., 2013) to negligible (Chapter 2) evidence for subduction signatures. The basalts in the PMVF have geochemical characteristics similar to the local ocean island basalt (OIB) source (Chapter 2), taken as the Río Colorado volcanic field previously described by Søager et al. (2013) as OIB-type. In addition, lower crustal assimilation has been suggested (Chapter 2) for the Pampas Onduladas flow.

3.3. Methods

Available geochemical data from the Pampas Onduladas flow are summarised in Table 3.1 (Pasquarè et al., 2008; Chapter 2). The extent of the Pampas Onduladas flow was determined using existing maps (Pasquarè et al., 2008) as well as a digital elevation model and surface maps. The length was calculated along the medial axis of the mapped flow from the inferred eruption and terminal points (Cashman et al., 2013). The eruption point is inferred to be close to the eastern limit of La Carbonilla fracture (point A; Figure 3.1) while the inferred terminal point is located in the province of La Pampa (point B; Figure 3.1) with the following geographical coordinates: 36.33778°S, 68.93918°W, 1852 MASL (Point A); and 37.00509°S, 67.45564°W, 445 MASL (Point B).

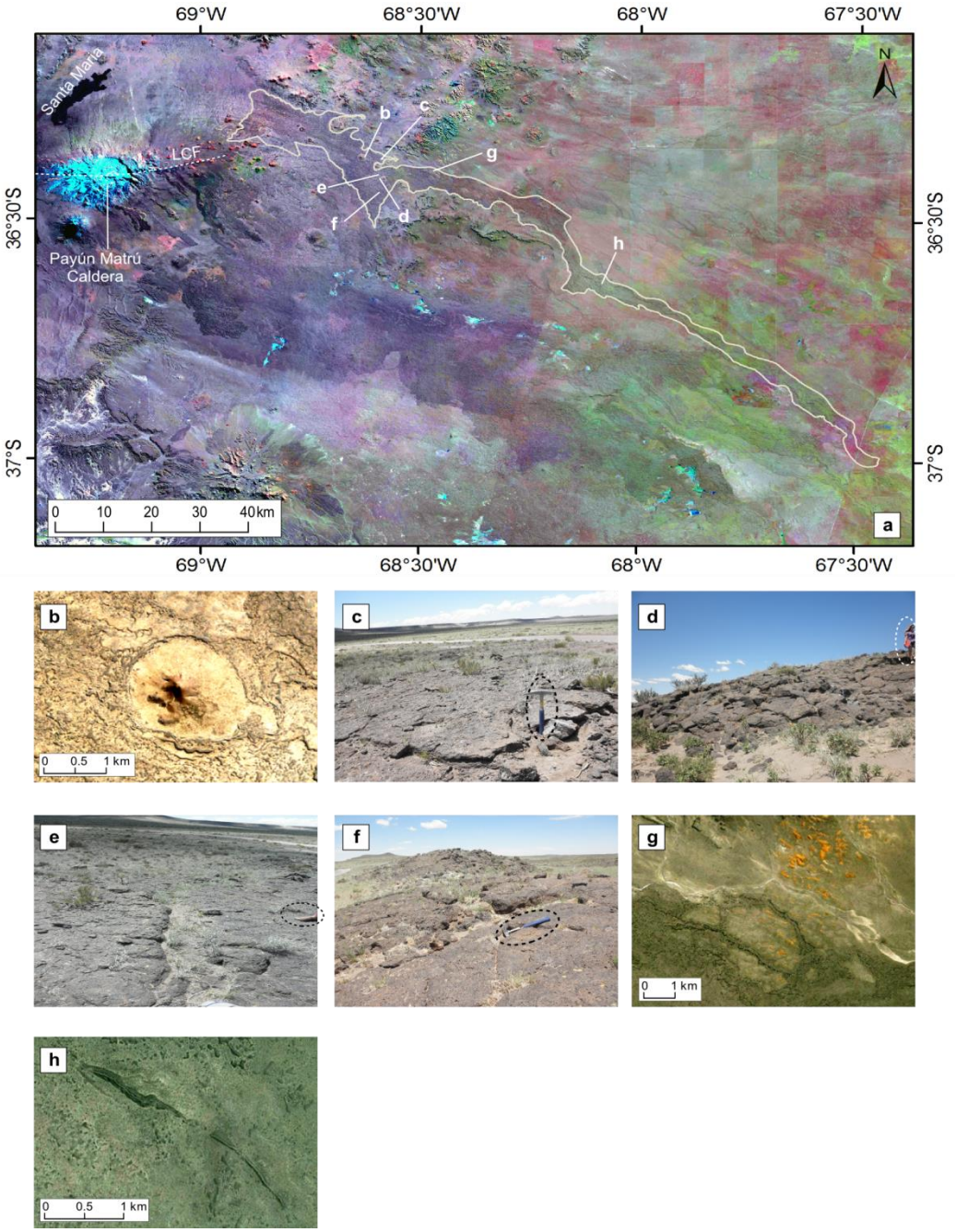

Figure 3.3. Morphological structures along the Pampas Onduladas flow. a) Outline of Pampas Onduladas flow showing the location for images b) to h). b) One of several kipukas located in the proximal-medial part of the flow. Note how the basaltic flow engulfed the pre-existing volcanic cone forming lava rises. c) Slabby pahoehoe flow; note the highly vesicular top layer. Geological hammer for scale is 32 cm long. d) Side view of a basaltic tumulus. Person on the right for scale. e) Groove on the surface of Pampas Onduladas flow. Note circled shoe for scale ~ 28 cm. f) view of a Pampas Onduladas surface and a tumulus in the background. Note the central crack in the tumulus. g) View of several kipukas in the northern margin of Pampas Onduladas. The pre-existing topography is part of the San Rafael block and the flow has formed lava rises in the margins of the kipukas. h) longitudinal lava rise with a central groove. The base satellite photo for a) is a mosaic contrast sharpening from preview images LC82300862013145LGN00, LC82310852013168LGN00, LC82310862013136LGN01 and LC82300852013145LGN00 from Landsat 8.

3.3.1. $^{40}Ar/^{39}Ar$ geochronology

Two samples were collected for $^{40}Ar/^{39}Ar$ geochronological analysis; sample VRE20 from the initial to medial part of the flow (36.40847°S, 68.58000°W), and sample VRE46a from the lower end of the flow (36.97117°S, 67.49233°W) (Figure 3.1). These samples are fine-grained, hypocrystalline alkali basalts with 1.0 wt % K_2O (VRE20) and 0.9 wt % K_2O (VRE46a), respectively (petrographic descriptions are provided in Section 3.4.1 and Figure 3.4). Following procedures described in Matchan and Phillips (2014), sample preparation involved crushing approximately 300 g of whole-rock to a grain-size of 180-250 µm followed by magnetic separation and hand picking to isolate unaltered groundmass from the phenocrysts. The groundmass separate and the neutron flux monitor Alder Creek Rhyolite (ACR) sanidine (1.186 ± 0.012 Ma (1σ); Turrin et al., 1994) were irradiated at the USGS TRIGA reactor for 0.5 MWH in the Cd-lined facility. Irradiated samples and the ACR flux monitor were analysed in the School of Earth Sciences at the University of Melbourne using a multi-collector Thermo Fisher Scientific ARGUSVI mass spectrometer linked to a gas extraction/purification line and Photon Machines Fusions 10.6 µm CO_2 laser system (Phillips and Matchan, 2013), following procedures described by Matchan and Phillips (2014). Blanks were measured after every third analysis and yielded <2.9 fA for ^{40}Ar, corresponding to 0.21% of the measured ^{40}Ar in the experiments. Mass discrimination was determined by automated air pipette aliquots before analysis assuming an atmospheric $^{40}Ar/^{36}Ar$ of 295.5 ± 0.5 (Nier, 1950). The ages were calculated relative to the ACR flux monitor, which determines the production of ^{39}Ar from ^{39}K during the radiation process and the ^{40}K decay constant of 4.962×10^{-10} yr^{-1} (Steiger and Jäger, 1977).

3.3.2. Rheological characterisation

The rheological parameters were calculated using the Magma® program from K. Wohletz (www.ees1.lanl.gov/Wohletz/Magma.htm). This program uses the major-element composition, crystal volume and crystal or vesicle size to calculate the density, liquidus temperature and viscosity of lava flows. The following values are used based on petrographic observations: phenocryst volume = 15 %; and crystal or vesicle maximum average size = 5 mm. The phenocrysts volume is based on hand specimens and photomicrograph observations (Figure 3.4) showing low phenocryst content as also noted by Pasquarè et al. (2008). The vesicle size is based on an average from field observations (Figure 3.3b, e) and hand specimens (Figure 3.4). Magma® calculates the liquidus temperature based on the method of Sisson and Grove (1993) and the density based on the method described by Bottinga and Weil (1972). A 20% vesicle volume correction (average vesicle volume of Pampas Onduladas flow) was applied to the density calculation which also correlated with observations from other large basaltic flows (Keszthelyi and Pieri 1993).

Table 3.1. Major- and trace-element analysis of the Pampas Onduladas flow. The major-elements are in wt % and the trace elements are in ppm. The major-elements are recalculated to an anhydrous basis (original data Pasquarè et al., 2008; Chapter 2).

Sample	**VRE19**	**VRE20**	**VRE21**	**VRE46 (A)**	**VRE47**	**PY16**	**PY20**
Latitude(°)	-36.4124	-36.4085	-36.3732	-36.9712	-36.9987	-36.3939	-36.2919
Longitude(°)	-68.5789	-68.5800	-68.5754	-67.4923	-67.4992	-68.6413	-68.7628
SiO_2	47.16	48.22	49.51	49.01	48.86	47.82	47.73
TiO_2	1.97	1.96	1.91	1.78	1.54	1.63	1.65
Al_2O_3	17.36	17.45	18.09	17.23	16.30	17.88	18.28
FeO_t	11.78	11.49	10.75	11.55	11.98	10.86	10.03
MnO	0.15	0.15	0.15	0.15	0.15	0.14	0.16
MgO	7.21	6.94	5.90	7.01	8.82	7.91	7.61
CaO	8.91	8.79	8.61	8.75	8.01	8.36	9.53
Na_2O	3.93	3.50	3.23	3.24	3.39	3.82	3.27
K_2O	1.04	1.01	1.33	0.89	0.67	1.04	0.84
P_2O_5	0.48	0.49	0.48	0.38	0.27	0.39	0.32
V	221	225	242	221	186	133	192
Cr	197	190	244	247	293	298	196
Ni	81	77	105	144	216	109	73
Rb	14.5	14.8	22.8	12.7	9.5	18.0	15.0
Sr	642	638	626	557	367	600	587
Y	23.5	23.1	22.6	20.8	18.4	16.0	16.0
Zr	148	149	199	135	104	123	123
Nb	19.0	19.3	22.3	13.6	9.5	15.0	14.0
Cs	0.3	0.3	0.3	0.2	0.2	0.3	0.5
Ba	308	475	510	320	183	305	356
La	18.7	18.4	20.4	14.0	10.7	14.9	16.0
Ce	37.6	36.0	34.4	28.6	22.6	31.5	34.7
Pr	5.0	4.9	5.1	3.9	3.1	3.9	4.5
Nd	23.2	22.4	23.3	18.5	14.7	17.3	20.1
Sm	5.6	5.5	5.6	4.8	4.0	4.3	5.0
Eu	1.9	1.8	1.8	1.7	1.4	1.6	1.8
Gd	5.5	5.4	5.3	5.0	4.1	4.3	4.9
Tb	0.9	0.8	0.9	0.8	0.7	0.7	0.8
Dy	4.9	4.7	4.6	4.3	3.8	3.9	4.4
Ho	0.9	0.9	0.9	0.8	0.7	0.7	0.9
Er	2.5	2.4	2.4	2.2	2.0	1.9	2.3
Tm	0.3	0.3	0.3	0.3	0.3	0.3	0.3
Yb	2.1	2.1	2.1	1.9	1.6	1.5	1.8
Lu	0.3	0.3	0.3	0.3	0.2	0.2	0.3
Hf	3.7	3.7	4.9	3.4	2.7	2.5	3.3
Ta	1.1	1.1	1.4	0.8	0.5	0.7	0.7
Pb	3.5	3.4	4.8	3.8	2.6	3.0	
Th	2.0	2.0	3.2	1.7	1.3	1.5	1.6
U	0.5	0.5	0.8	0.5	0.3		0.5

Table 3.1. cont

Sample	PY23	PY24	PY25	PY34a	PY34b	SAL1	SAL4
Latitude(°)	-36.4597	-36.4721	-36.5541	-36.9702	-36.9702	-36.2764	-36.2944
Longitude(°)	-68.3886	-68.1894	-68.1754	-67.4913	-67.4913	-68.7088	-68.7316
SiO_2	47.56	47.25	47.86	48.75	47.25	48.86	47.86
TiO_2	1.9	1.83	1.77	1.73	1.49	1.85	1.78
Al_2O_3	17.53	17.2	17.56	17.49	16.83	16.48	16.2
FeO_t	10.74	10.65	11.15	10.65	10.81	11.21	11.1
MnO	0.16	0.16	0.16	0.16	0.18	0.17	0.16
MgO	6.87	7.35	7.3	7.62	9.14	6.96	7.05
CaO	9.5	9.39	8.96	8.75	9.32	9.78	10.17
Na_2O	3.47	3.5	3.46	3.5	3.43	3.74	3.61
K_2O	1.01	0.91	0.93	0.86	0.82	1.28	1.22
P_2O_5	0.37	0.35	0.35	0.29	0.26	0.44	0.44
V	179	187	188	152	197	210	217
Cr	221	256	256	247	417	240	220
Ni	82	97	103	115	190	110	110
Rb	15.0	15.0	15.0	14.0	18.0	23.0	26.0
Sr	583	571	564	553	518	627	621
Y	16.0	16.0	18.0	15.0	16.0	21.6	23.5
Zr	130	124	125	119	118	151	144
Nb	18.0	17.0	17.0	14.0	11.0	16.2	15.1
Cs	0.3	0.3	0.4	0.3	0.7	0.7	0.8
Ba	293	257	251	238	298	303	443
La	17.7	16.9	16.6	14.4	16.2	19.0	19.1
Ce	37.8	36.2	36.1	30.9	35.0	40.2	40.8
Pr	4.6	4.5	4.4	3.9	4.4	5.1	5.4
Nd	20.9	20.0	20.5	17.5	19.5	20.9	21.6
Sm	5.0	4.9	5.1	4.5	4.8	5.1	5.4
Eu	1.8	1.8	1.9	1.6	1.7	1.8	1.9
Gd	4.9	4.8	5.0	4.4	4.5	4.8	5.1
Tb	0.8	0.8	0.8	0.7	0.8	0.8	0.8
Dy	4.4	4.4	4.5	4.0	4.2	4.5	4.5
Ho	0.8	0.8	0.8	0.7	0.8	0.8	0.8
Er	2.2	2.2	2.2	2.0	2.1	2.2	2.3
Tm	0.3	0.3	0.3	0.3	0.3	0.3	0.3
Yb	1.8	1.7	1.8	1.6	1.8	2.0	2.0
Lu	0.3	0.3	0.3	0.2	0.3	0.3	0.3
Hf	3.4	3.2	3.3	3.0	3.1	3.6	3.6
Ta	1.0	1.0	0.9	0.7	0.6	1.3	1.1
Pb	2.0	2.0	1.0		6.0		
Th	1.7	1.6	1.6	1.4	2.3	3.0	2.7
U	0.5	0.5	0.5	0.4	0.7	0.7	0.7

The parameters here used to calculate the viscosity (15% phenocryst volume, 5mm phenocryst or vesicle size and 20% vesicle volume) are based on field observations. It is important to consider that the exposed part of the Pampas Onduladas flow is the uppermost highly vesicular layer (Figure 3.4a) which does not fully represent the characteristic of the long flow, therefore the values used were also correlated with those presented by Pasquarè et al. (2008) and other estimates on long lava flows (Keszthelyi and Self, 1998). The viscosity was calculated using Magma® and the algorithms proposed by Bottinga and Weil (1972). Furthermore, the flow velocity was calculated using Jeffrey's Law equation:

$$v = \frac{\rho\, g\, \theta\, H^2}{8\eta}$$

where ρ is the density of the flow (in kg/m^3), g is the gravitational acceleration (9.8 m/s^2), θ is the slope (0.0084), H is the thickness (variables used: 20m, 15m, 10m and 5m) and η is the viscosity (in Pa.s). The 20m thick variable used is based on, the preserved Pampas Onduladas thickness above the surrounding topography (Figure 3.5) which also corresponds to the minimum thickness proposed by Pasquarè et al. (2008). However, the 20m thick variable is the preserved thickness of the flow after inflation and cooling, therefore it does not represent the original thickness. In order to account for the velocity several hypothetical thickness values of less than 20m, were chosen at regular set intervals.

3.3.3. Volume Calculation

The topographic slope was calculated using the difference in elevation from the initial point A (1852 MASL) to the final point B (445 MASL) divided by the total calculated length of the flow. The elevation of points A and B and volume calculation were based on the digital elevation model (DEM), Shuttle Radar Topography Mission (SRTM) 90 m (30m x 30 m) with an absolute vertical error of less than 9 m and a relative vertical error of less than 10 m (Rodriguez et al., 2006). Five cross-sections (Figure 3.1) were made along the flow in order to assess the topographic correlation between the flow and the adjacent pre-existing surfaces, as well as to estimate its thickness. The volume was calculated using the procedure described by Smith et al. (2009) based on the SRTM digital elevation model and employing the ArcGIS® software. To calculate the volume, the Pampas Onduladas flow was divided into 5 segments (Figure 3.1) in order to account for the changes in slope and adjacent topography. The volume was calculated for each individual segment and then summed to provide the total. There are areas of the flow, especially in its proximal part, where it is interrupted by the pre-existing topography (kipukas) such as scoria cones and elevated landscapes (i.e. parts of the flow where the underlying substrate has not been covered; Figure 3.3a, f). The volumes of each of the kipukas was calculated and later subtracted from the total (see following section for further details). The errors associated with the volume calculations have not been determined as this is a first-order estimate of the volume (see Smith et al., 2009) and there are several potential sources of error that are difficult to quantify. The possible sources of error include: (i) the SRTM has an absolute

height error of less than 9 m in a global scale and 6.2 m for South America (Rodriguez et al., 2006); (ii) digitalisation is based on user interpretation; (iii) topographic highs on the sides of the flow may give inaccurate base surfaces; and (iv) data point interpolation. The interpolation algorithm uses the values from the sides of the flow to create a planar estimate of the underlying surface; however the interpolation does not consider topographic lows that may have existed before the lava emplacement.

3.3.3.1. Detailed volume calculation method

The volume was calculated by modifying the approach of Smith et al. (2009). The procedure used is described in several steps.

1- The Pampas Onduladas flow was digitised using Landsat7 imagery Google Earth® and then divided into 5 segments. In addition, features such as kipukas, were also digitised.

2- The files created where exported to ArcGIS10® and the remaining analyses were performed using this software. The volume was calculated individually for each sector and kipuka. The total volume was determined by summing all the sector volumes. The same principle was applied to all the kipukas. Finally, the total volume of the kipukas was subtracted from the total volume.

3- The SRTM 90m (30 m x 30 m) digital elevation model covering the area of interest was uploaded to ArcGIS10®. Using the Windows tool, selecting the sector shapefile and employing the create-a-void command a cavity covering the area of the sector was created in the DEM. Basically, in this step, the sector of the flow being calculated was removed from the DEM. The same principle was applied for the kipukas.

4- After removing the sectors, the surrounding topography was interpolated to create an approximate base surface. In order to do this, all the values of each cell in the SRTM were converted to point values using the conversion tool. Once the new point layer was created, interpolation between point values was carried out. The interpolation tool used is the spline (Smith et al., 2009) and the output cell size was set with the default value for sector 1. The default value used for sector 1 was then used for all sectors from 2 to 5.

5- The hypothetical basal surface created, was isolated from the rest of the DEM. This was done using the Windows tool and employing the clip option. The resulting layer should only contain the interpolated base area of the sector. The same principle was applied to the original DEM so that the top surface of the sector was isolated from the rest of the DEM.

6- Once the base and top part of a particular section were isolated, the volume and area of the top and the base surface were calculated separately using the Area and Volume statistics option. In the calculation, the plane height differed from sector to sector as they have different elevations; therefore the default value for each particular sector was used. The calculated volume and area from the top and base of the sector were exported into Excel.

7- The final volume of each sector was calculated using Excel by subtracting the base volume from the top volume. The volume from the 5 sectors was summed and the volume from the kipukas that interrupted the Pampas Onduladas flow was subtracted.

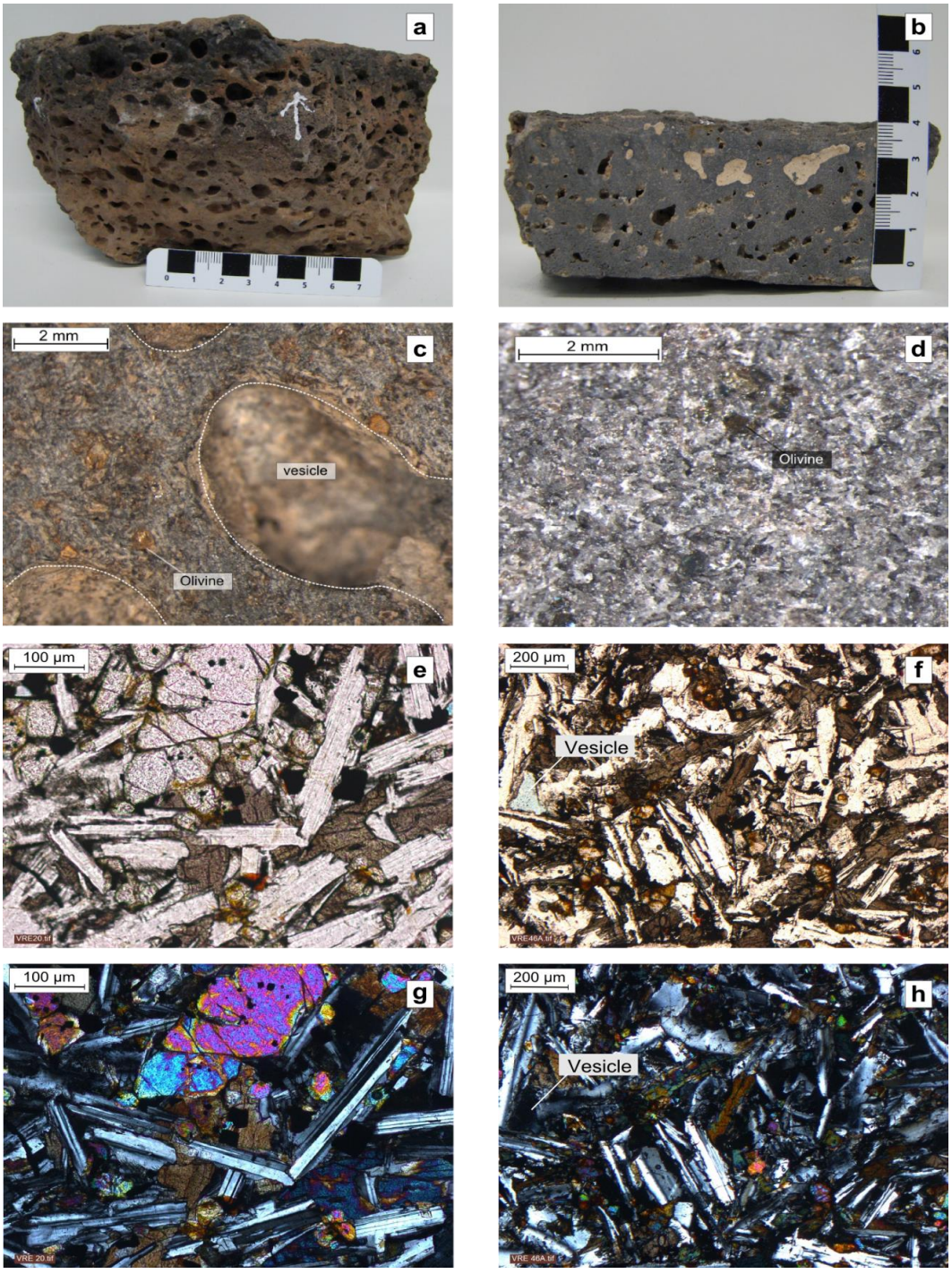

Figure 3.4. Images of samples from the Pampas Onduladas flow. a) Sample VRE20 uppermost layer. White arrow indicates way up, note the roundness of the vesicles (scale in cm and mm). b) Sample VRE46a uppermost layer. Note the vesicles are not rounded and some are filled by carbonates. c) photomicrograph of a cut surface of sample VRE21. d) photomicrograph of the surface of sample VRE46a showing the high crystal content of the rock. e) and f) polarised photomicrographs of samples VRE20 and VRE46a, respectively. g) and h) cross-polarised photomicrographs of samples VRE20 and VRE46a, respectively.

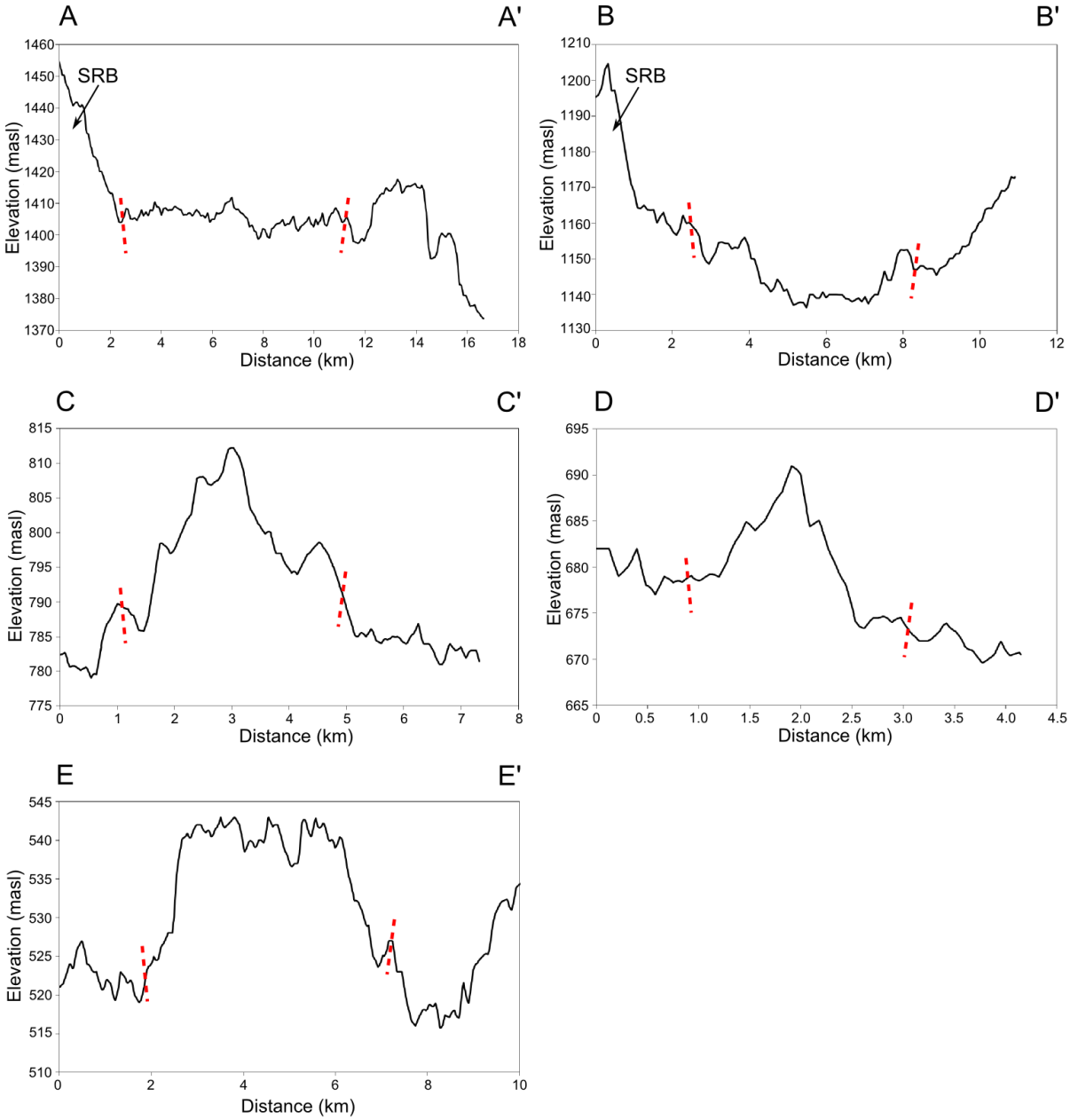

Figure 3.5. Cross sections of the Pampas Onduladas flow. North is to the left in each case and the vertical scale is exaggerated. Cross sections a) to e) correspond to sections 1 to 5 of the flow. Red dashed lines in each of the cross sections delimit the margins of the Pampas Onduladas flow. The San Rafael block (SRB) outcrops on the northern side of cross sections A-A' and B-B'.

3.4. Results

3.4.1. Petrographic description of the Pampas Onduladas Flow

The Pampas Onduladas samples are highly vesicular in the uppermost layer (Figure 3.4) with well developed roundness in the proximal-middle part of the flow (Figure 3.4a) while the vesicles are longitudinally deformed in the distal part (Figure 3.4b). Nevertheless, a sub-angular vesicle can be observed in sample VRE46a (Figure 3.4f and h). The rocks from the flow are fine

grained and hypocrystalline (Figure 3.4c and d) with sparse phenocrysts; the groundmass is composed of microliths. The photomicrographs show a subophitic texture for sample VRE20 (Figure 3.4e and g), which is generally found in the central part of basaltic flows (Llambías, 2008). Sample VRE46a has an interstitial texture (Figure 3.4f and h). The rocks are mainly composed of plagioclase, olivine, and orthopyroxene with some clinopyroxene (Figure 3.4g, h). Olivine phenocrysts are euhedral to subhedral, and some show alteration on the margins to iddingsite. All the samples contain opaque minerals.

3.4.2. $^{40}Ar/^{39}Ar$ results

A summary of the results from the $^{40}Ar/^{39}Ar$ analysis is shown in Table 3.2 (including plateau, inverse isochron and total gas ages) and Figure 3.6, while the full data set is presented in Supplementary Data 3.1. Plateau age plots (Figure 3.6a), step heating spectra (Figure 3.6b) and inverse isochron graphs were produced using the Isoplot 3.75 add-in for Microsoft Excel (Ludwig, 2012).

The age spectrum for VRE20 comprises an essentially flat profile followed by successively older apparent ages for high-temperature steps. A plateau age of 373 ± 10 ka (2σ) was calculated for sample VRE20 (Table 3.2), using the plateau criteria of Singer and Pringle (1996). The slightly higher apparent age calculated for the initial step most likely reflects release of excess ^{40}Ar from fluid inclusions at low temperature. The older apparent ages calculated for the high temperature steps most likely reflect outgassing of incompletely removed plagioclase and clinopyroxene phenocrysts, consistent with elevated Ca/K ratios and observations in other whole-rock basalt $^{40}Ar/^{39}Ar$ studies (e.g. Cassata et al., 2008). An inverse isochron generated for all data, excluding the anomalous result from the final fusion step, suggests a trapped argon component ($^{40}Ar/^{36}Ar_i$) with a near-atmospheric composition of 299.2 ± 2.9 (95% CI; MSWD = 5.5). However, the high MSWD of this fit reflects the discordance of the data, indicating the presence of at least two trapped argon components. A well-constrained atmospheric $^{40}Ar/^{36}Ar_i$ ratio of 296.6 ± 1.7 (2σ; MSWD=1.2) is revealed by data from the plateau-forming steps (2-6), supporting the interpretation of the plateau age as an eruption/cooling age. Owing to the extremely low radiogenic $^{40}Ar^*$ concentration in this sample ($^{40}Ar^*$ comprises ~3% of total ^{40}Ar), the corresponding inverse isochron age has a poorly constrained value of 349 ± 68 ka (2σ), within error of the plateau age. The significantly older total-gas age of 434 ± 10 (2σ) reflects the extraneous $^{40}Ar^*$ released in the initial and high-temperature heating steps.

In contrast to VRE20, the age spectrum for VRE46a is highly discordant and a plateau age could not be resolved (Figure 3.6b). The monotonic decrease in apparent ages implicates recoil loss/redistribution of ^{39}Ar and ^{37}Ar from secondary phases and/or fine-grained magmatic phases during irradiation (e.g. Koppers et al., 2000). The older apparent ages calculated for the high-temperature steps likely reflect release of extraneous ^{40}Ar during degassing of plagioclase and clinopyroxene phenocrysts, as for sample VRE20. Due to the recoil issue apparent in this sample, inverse isochron analysis is of limited value in constraining the trapped argon

composition (Koppers et al, 2000). The data are highly discordant in three-isotope space (Figure 3.6), but suggest a atmospheric $^{40}Ar/^{36}Ar_i$ ratio of 295.6 ± 3.0 (95% CI; MSWD=35). Therefore, assuming negligible loss of ^{39}Ar from the sample, the total gas age of 370 ± 8 ka (2σ) can be regarded as a maximum age estimate for sample VRE46a.

Table 3.2. $^{40}Ar/^{39}Ar$ results for groundmass samples from the Pampas Onduladas basaltic flow

Sample		**VRE20**	**VRE46a**
Flow sector		2	5
Plateau age	age (ka) MSWD cum ^{39}Ar (%)	373 ± 10 (2σ) 1.4 68.2	N/A N/A N/A
Inverse Isochron age	age (ka) MSWD steps included	349 ± 68 (2σ) 1.2 5 of 9	374 ± 76 (95% CI) 35 9 of 9
Total-gas age	age (ka)	434 ± 10 (2σ)	370 ± 8 (2σ)

N/A not applicable

3.4.3. Geochemistry of Pampas Onduladas

Major-element concentrations of the Pampas Onduladas flow suggest a primitive composition with low and restricted SiO_2 content (Table 1). The MgO content ranges from 9.1 wt % (Sample PY34b, Pasquarè et al., 2008) to 6.0 wt % (Chapter 2). The MgO concentration is negatively correlated with TiO_2, P_2O_5 and K_2O concentrations (not shown), while no correlation was established with Al_2O_3, CaO, Na_2O and FeO_t contents. A positive correlation is apparent between TiO_2 and K_2O contents (Figure 3.7a). Rare Earth Element (REE) concentrations normalised to the primitive mantle (values from McDonough and Sun, 1995) show enrichment in light REEs over heavy REEs (Figure 3.7e). This pattern is generally associated with the presence of residual garnet in the magmatic source. Trace-element concentrations, normalised to the primitive mantle (values from McDonough and Sun 1995; Figure 3.7f), display enrichment for Ba and Sr while some samples have a positive Pb anomaly. Positive Pb spikes are generally associated with crustal contamination (Kay et al., 2013). The negative Nb-Ta anomaly typical of arc volcanism is not apparent (except for sample PY34b, from Pasquarè et al., 2008) among samples of the Pampas Onduladas flow (Figure 3.7f). Sr isotope values are low, ranging from 0.703747 (Chapter 2) to 0.704151 (Pasquarè et al., 2008), which are comparable with $^{87}Sr/^{86}Sr$ values reported by Hernando et al. (2012) for pre-caldera basalts (0.703766 to 0.703906).

3.4.4. Rheology

The average calculated viscosity is 96 Pa.s at a mean temperature of 1170°C and with a 15% phenocryst content correction, corresponding to a typical olivine basalt melt (Williams and McBirney, 1979). The value for viscosity and temperature inferred for the Pampas Onduladas are slightly higher than the range suggested by Pasquarè et al. (2008) of 3-73 Pa.s for viscosity

and 1130 - 1160°C for temperature. However, the viscosity values are within the range of those calculated for the Undara and Toomba flows in Queensland, Australia, which have a similar composition to the Pampas Onduladas flow (Stephenson et al., 1998). The calculated bulk density ranges from 2120 to 2466 kg/m^3 after correction for 20% vesicle volume.

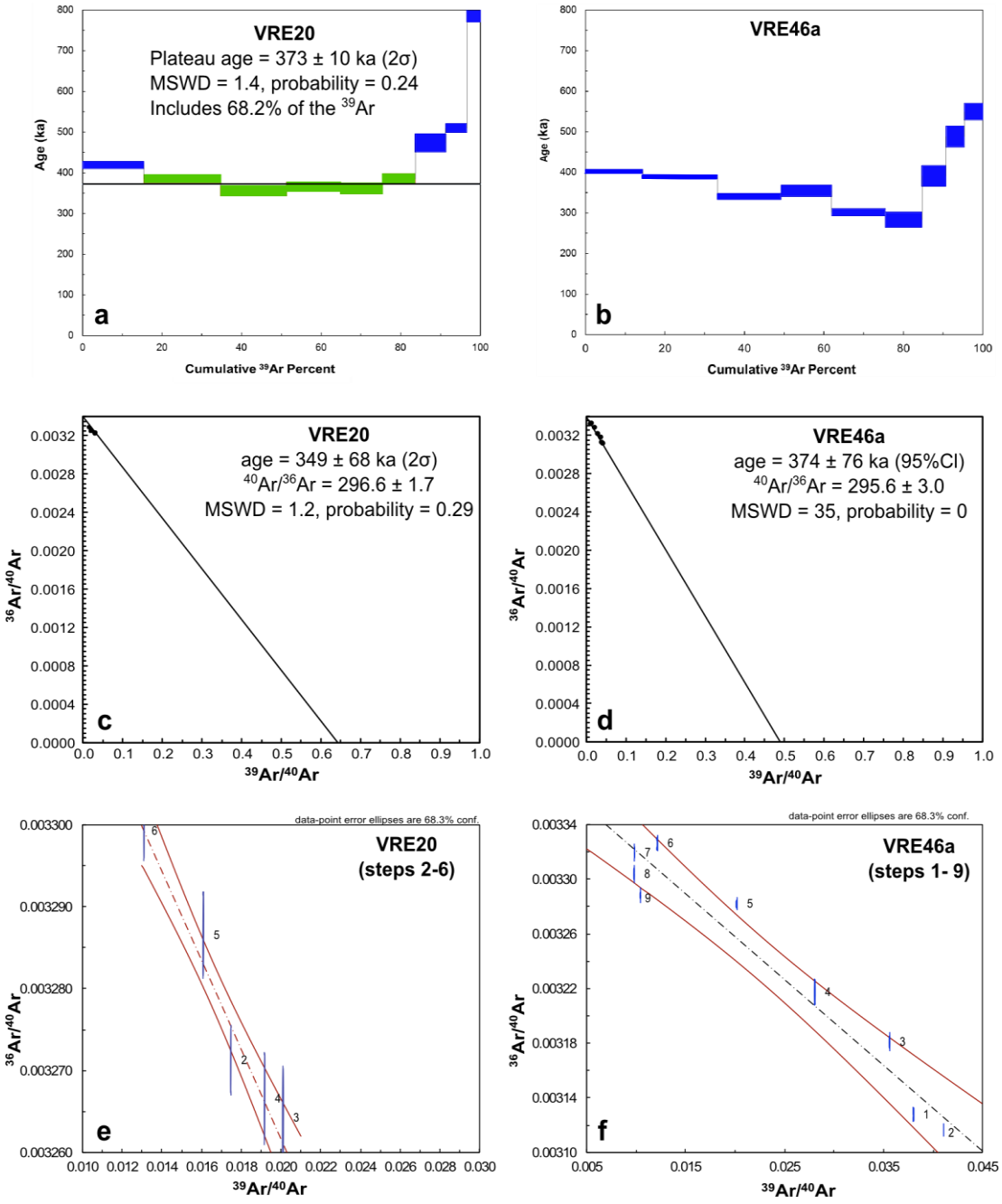

Figure 3.6 (previous page). $^{40}Ar/^{39}Ar$ results for samples of the Pampas Onduladas basaltic flow. a) Plateau diagram for sample VRE20. b) Spectrum diagram for sample VRE46a. c) and d) Inverse isochron diagrams for samples VRE20 and VRE46a, respectively. e) and f) large-scale inverse isochron diagrams for samples VRE20 and VRE46a, respectively. The heating steps in green are those which were accepted while those in blue were rejected. Error symbols in e) and f) are 1σ.

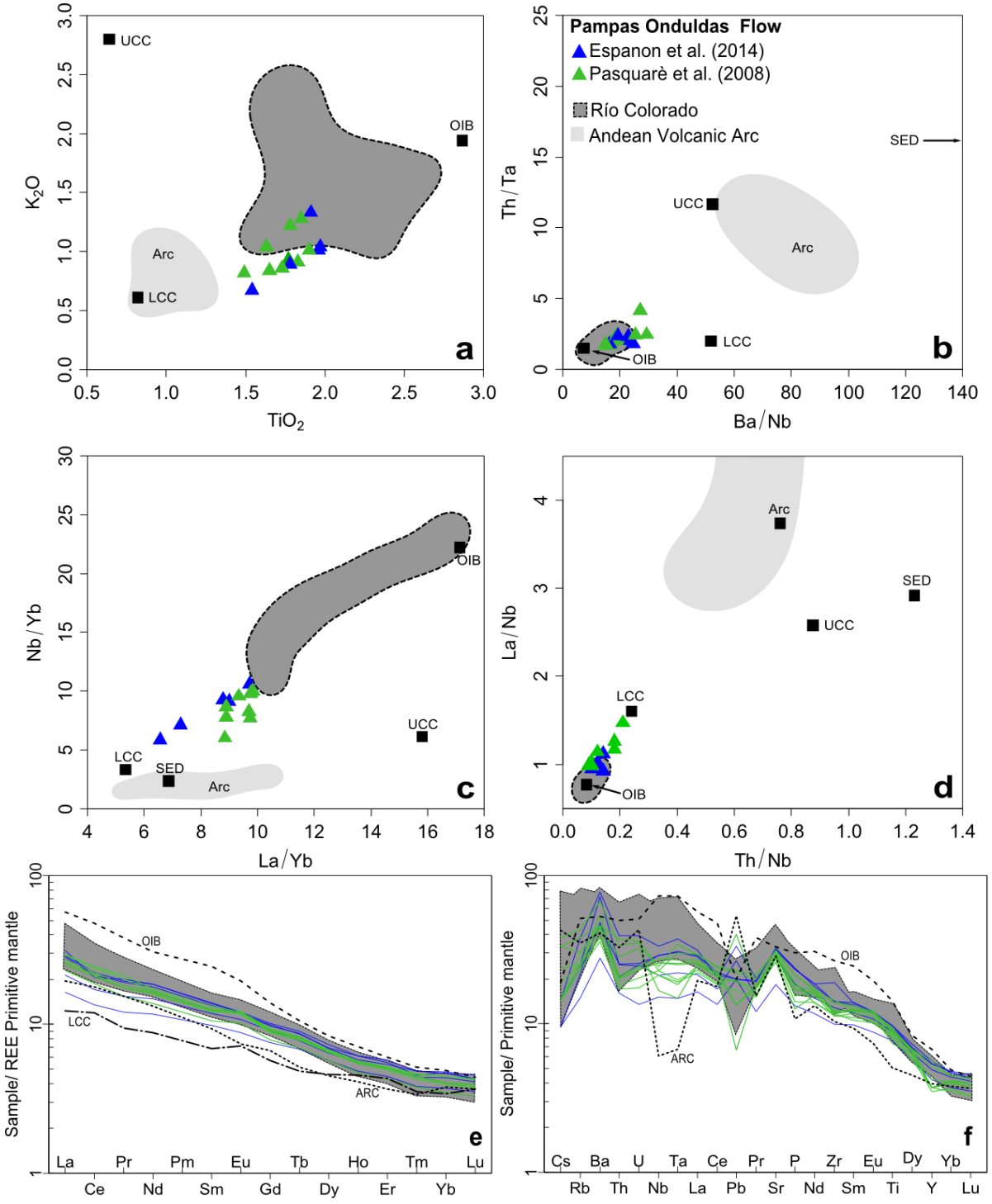

Figure 3.7. Geochemical data for Pampas Onduladas lavas. a) TiO_2 vs K_2O concentrations in wt %, b) Ba/Nb vs Th/Ta, c) La/Yb vs Nb/Yb, d) La/Nb vs Th/Nb, e) Rare earth element (REE) concentrations normalised to primitive mantle values (McDonough and Sun, 1995) and f) trace-element concentrations, normalised to primordial mantle values (McDonough and Sun 1995). The green triangles and lines are from Pasquarè et al. (2008), and the blue triangles and lines are from Chapter 2. The upper continental crust (UCC) and the lower continental crust (LCC) compositions are from Rudnick and Gao (2003). The ocean island basalt (OIB) composition is from Sun and McDonough, (1989). The Río Colorado volcanic field is taken as the local intraplate composition similar to an OIB endmember from Søager et al. (2013). Data from the basaltic Andean volcanic arc (ARC) are from Lopez-Escobar et al. (1977), Tormey et al. (1991) Ferguson et al. (1992), Tormey et al. (1995), Costa and Singer (2002) and Jacques et al. (2013).

The calculated velocity of the Pampas Onduladas flow (assuming a mean density value of 2300 kg/m^3) is 99 (~355 km.h^{-1}), 55, 25 and 6 m.s^{-1} for flow thicknesses of 20, 15, 10 and 5 m, respectively (Table 3.3). These flow velocities were calculated assuming a laminar flow behaviour. The average velocities appear excessive in comparison to the fastest velocity recorded for basaltic lava flows such as for Mt. Nyiragongo (ultramafic flow) in 1977 with speeds of approximately 17 m.s^{-1} (60 km.h^{-1}; Tazieff, 1977) or some of the Mauna Loa flows with speeds of up to 15 m.s^{-1} (55 km.h^{-1}; Lipman and Banks, 1987). Because the average velocities calculated are excessive, Reynolds numbers *(Re)* (Reynolds, 1974) were calculated to determine whether the flow was turbulent (density = 2300 kg/m^3 and viscosity = 96 Pa.s). Using velocities calculated above, *Re* values do suggest a turbulent flow (*Re* values of 47000, 20000 and 6000 at 20 m, 15 m and 10 m flow thickness; Table 3.3). For a 5 m thick flow, the *Re* number is 700, which is regarded as laminar. In order to calculate the velocity of a turbulent flow, a different equation must be applied that incorporates the friction coefficient (C_f) in the Chezy equation (Jeffreys, 1925) (see Appendix A for equations). Using the calculated *Re* numbers and employing the Gonacharov (1964) equation for turbulent sheet flow, a C_f value of 0.0021, 0.0025 and 0.0033 for a 20 m, 15 m and 10 m thick flow respectively were calculated. These values were incorporated into the Chezy equation to calculate the velocity of a turbulent flow: 28 (~101 km.h^{-1}), 22 (~ 79 km.h^{-1}) and 16 (58 km.h^{-1}) m.s^{-1} for a 20, 15 and 10 m thick flow, respectively (Table 3). The calculated average flow velocities are high even for a turbulent flow compared with observations from Mt Nyiragongo (Tazieff, 1977) and Mauna Loa (Lipman and Banks, 1987). Consequently some parameters were modified in order to examine the velocity change by increasing the maximum phenocryst and/or vesicle size and the vesicle volume proportion. By increasing the maximum phenocryst or vesicle size the velocity did not incur in much change (~1%) while increasing the vesicle volume to 30% the average viscosity increased to 133 Pa.s and the average bulk density decreased to 1924 kg/m^3, therefore reducing the velocity by an average of 11% which is still elevated.

Table 3.3. Velocity calculated at liquidus temperature for a laminar and turbulent flow, for the Pampas Onduladas flow.

Thickness (m)	*Re* number	Velocity @1170°C for laminar flow (m.s^{-1})	Velocity @1170°C for turbulent flow (m.s^{-1})
20	47000	99	28
15	20000	55	22
10	6000	25	16
5	700	6	9

3.4.5. Length and Volume

The length of the Pampas Onduladas flow was measured from the far eastern end of La Carbonilla fracture to 35 km north of Puelén (Figure 3.1) in the province of La Pampa. The length is estimated to be 167 km (following the method by Cashman et al., 2013; see Section 3.3 Methods). This value is slightly less than previous measurements of 174 km and 181 km (Pasquarè et al., 2005; Pasquarè et al., 2008, respectively). This variation is attributed to the uncertainty in assessing the initial eruption point and the final point of the Pampas Onduladas flow as the eruption point for the Pampas Onduladas flow has not been identified. In this sense Pasquarè et al. (2005 and 2008) provided some general description of the initial and terminal point of the flow determining that its proximal part belongs to the eastern end of the Payún fissure system (also referred to as La Carbonilla fracture) while the end point was located in the Salado river valley in the province of La Pampa (Pasquarè et al., 2008). The length of La Carbonilla fracture on its eastern side is ~ 14 km (Llambías et al., 2010) therefore, providing a wide area from which the Pampas Onduladas eruption point might be.

The flow volume was calculated to be 7.2 km^3, while the surface area was calculated as 739 km^2 (Table 3.4). The calculated volume should be regarded as a minimum as the base of the flow was extrapolated from the adjacent topography, which may not represent its true basal surface. The topographic slope from the initial to the final part of the flow is 0.84% or 0.24°; however, the slope is not constant along the length. The slope is much steeper in the initial part than in most of its length (Figure 3.8) as it changes from 1.6% in section 1, to 0.9% in section 2 and then to 0.6, 0.5 and 0.4% in sections 3, 4, and 5, respectively. The mean width of the flow decreases downhill from 9.4 km in section 1, to 5.1 km in section 2, then to 3.8, 2.6 and 3.5 km in sections 3, 4 and 5, respectively.

Table 3.4. Area and volume calculated for the 5 sections of the Pampas Onduladas flow, as well as for the volcanic cones and the void areas that interrupted the flow.

Sector	Area (km^2)	Volume (km^3)
1	303	3.9
2	166	1.3
3	100	1.1
4	81	0.8
5	102	0.3
volcanic cones	4	0.1
voids	8	0.1
total for flow	739	7.2

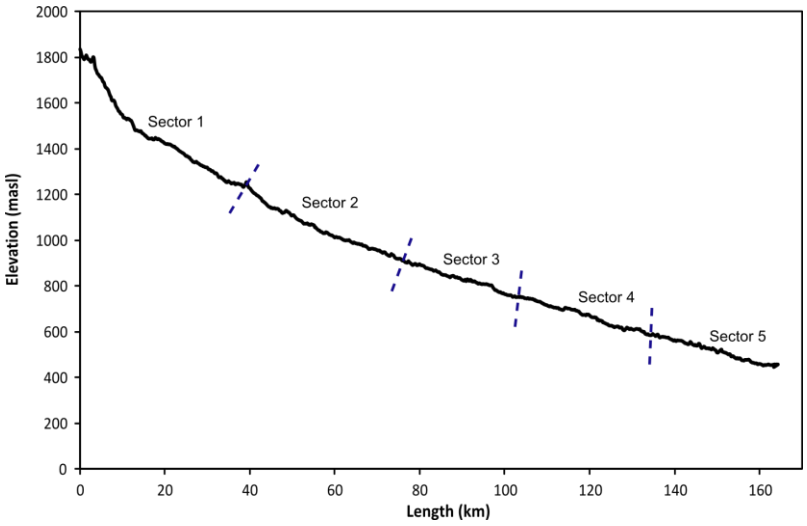

Figure 3.8. Elevation profile of the Pampas Onduladas flow from its initial (proximal) part to its final (distal) part. Dashed lines separate the five sectors into which the Pampas Onduladas flow was divided.

3.5. Discussion

3.5.1. Geochonology

The $^{40}Ar/^{39}Ar$ dating results for the Pampas Onduladas flow, provide the first direct radiometric age for this long flow. The highly precise plateau age of 373 ± 10 ka (3%; 2σ) determined for sample VRE20 is considered to represent the eruption age of the basalt, supported by inverse isochron analysis. The argon isotopic ratios measured for VRE46a appear disturbed, and the decrease in apparent age with increasing temperature is attributed to significant recoil loss/redistribution in this sample. This is consistent with petrographic studies revealing minor alteration (Figure 3.4f and h) mainly of the interstitial microcrystalline to cryptocrystalline material in this sample. Therefore determination of an eruption age is not possible for this sample, as total gas ages for samples affected by recoil only can be good approximations for eruption age (although these are not so reliable as we cannot be sure that the trapped component is atmospheric, therefore they may overestimate the eruption age), as looks to be the case in this instance, due to consistency with VRE20 results. An eruption age of 373 ± 10 ka (3%; 2s) determined from the Pampas Onduladas flow is stratigraphically consistent with a K-Ar age of 400 ± 100 ka (2σ) previously reported for an underlying basalt flow (see Section 3.2.2).

3.5.2 Petrogenesis of the Pampas Onduladas Flow

The origin of magma for the Pampas Onduladas flow has been regarded previously as having been affected by metasomatism of the subducting slab (Pasquarè et al., 2008). Trace-element compositions lack typical arc-related signatures such as negative Nb, Ta and Ti anomalies, high Ba/Ta and La/Ta, and enrichment in Th (inferred from slab sediments and slab partial melts, Jacques et al., 2013) or strong depletion in heavy rare earth elements (relative to slab partial melts; Figure 3.3 b, e). Therefore, the geochemical data suggest that the Pampas Onduladas flow does not exhibit signatures typical of the Andean arc (Figure 3.7).

The volcanism in the Payún Matrú volcanic field is intraplate with a geochemical composition resembling that of ocean island basalts (Germa et al., 2010, Jacques et al., 2013; Søager et al.,

2013; Chapter 2). The composition of the Pampas Onduladas flow also suggests some association with a local intraplate source (Figure 3.7b; local intraplate source is here taken as the Río Colorado field). The trace-element ratios show values intermediate to those of the local intraplate (Río Colorado field, Figure 3.7) and the lower continental crust (LCC) (Figure 3.7b, c, d). They also define a linear trend following the local intraplate-LCC regression line (Figure 3.7c and d), suggesting that some lower crustal assimilation has taken place. Furthermore, the the positive Pb spikes (Figure 3.7f) (Kay et al., 2013) are generally considered an indicator of crustal contamination. Typical LCC signatures include depletion in Th, K, Rb, Zr, Ba, LREE, Hf, and U relative to the local intraplate, slab components (sediments and partial melts) and Andean arc. The samples from the Pampas Onduladas flow show depletion in all of these elements and have high Th/U ratios (LCC = 6). Furthermore, Pasquarè et al. (2008) proposed sialic crustal assimilation for the Pampas Onduladas flow, based on Sr isotopic analyses. The issue of crustal contamination in the Payún Matrú volcanic field is not clear as there are no crustal Sr-isotopic values for this area (Chapter 2). The Sr isotope values for the Pampas Onduladas flow are in agreement with those previously presented for the Payún Matrú volcanic field (Pasquarè et al., 2008; Bertotto et al., 2009; Hernando et al., 2012; Jacques et al., 2013; Søager et al., 2013; Chapter 2).

As discussed above, geochemical data for the Pampas Onduladas flow are consistent with an intraplate volcanic signature of OIB affinity. It is noted that an intraplate signature is typical of other long (>100 km) basaltic flows such as the Toomba and Undara flows that are associated with mantle upwelling (Stephenson et al., 1998). This is intuitively predictable, as a magmatic body rising from the mantle, would be possessed of the high temperatures, low viscosity and high lava volumes expected to yield long lava flows. However, these magmatic characteristics are common to many volcanic settings, and yet long flows (>100 km) are not common. Rheological and topographical factors that may permit emplacement of a long flow are discussed in the following section

3.5.3. Rheology of the Pampas Onduladas flow

Formerly, it was generally accepted that long flows (>100 km, Keszthelyi and Self, 1998) require low viscosity, rapid emplacement (Walker, 1973) and large volumes (Pinkerton and Wilson, 1994). However, it has been proposed that effective insulation, in combination with a favourable topographic slope, can also contribute to form long basaltic flows (Keszthelyi and Self, 1998). Based on rheological characteristics, Keszthelyi and Self, (1998), modelled two types of emplacement for long lava flows (>100km); “rapid” and “insulated” models. “Rapid” emplacement requires less than 0.5°C/km of cooling at high velocities of 2 - 15 $m.s^{-1}$ for a channel 2 - 19 m deep and high effusion rates 200 – 17000 m^3/s (Keszthelyi and Self, 1998). On the contrary, “insulated” emplacement requires much lower velocities (0.1 - 1.4 $m.s^{-1}$), slightly thicker flows 2 - 23 m and lower effusion rates 8 – 7100 m^3/s (Keszthelyi and Self, 1998). The calculated viscosity for the Pampas Onduladas flow is in agreement with previous

viscosity calculations for long basaltic flows (Stephenson et al., 1998; Pasquarè et al., 2008). The viscosity of a flow increases with concentrations of solids, water and dissolved gases. Pinkerton and Stevenson (1992) suggested that for solid concentrations below 30%, the viscosity remains relatively constant and flow behaviour is approximately that of a Newtonian fluid. In the case of the Pampas Onduladas flow, the viscosity was calculated based on a 15% solid concentration, while Pasquarè et al. (2008) assumed a phenocryst-free magma in their calculation. In both cases the calculated average viscosity is similar (2- 73 Pa.s Pasquarè et al., 2008 and 96 Pa.s current study); therefore, provided the concentration of solids is less than 30%, viscosity values remain low. The vesicle volume proportion affects the average viscosity of the Pampas Onduladas flow as it increases from 20 to 30%. Nevertheless, and in agreement with the internal morphology of a basaltic flow, the vesicles can be associated with a viscosity reduction, as the pressure imposed by spherical bubbles is not absorbed by the system, but released as the vesicles deform and collapse (Llambías 2008). In Section 3.2.2, the internal structure of the Pampas Onduladas flow is described as having disrupted and elongated vesicles forming the lower massive layer, agreeing with the previous statement. Despite, the possibility of keeping the flow at low viscosity by vesicle deformation and collapse as previously mentioned, the sub-angular vesicle in Figure 3.4f and h suggest a transition to a more viscous character in the distal part. This constitutes the only evidence of a change in flow regime; therefore further studies along the flow are needed in order to fully assess the hypothesis of a viscosity change.

The calculated velocity for the Pampas Onduladas flow (Table 3.3) is higher than previous open channel basaltic flow velocity estimates (4-12 $m.s^{-1}$, Keszthelyi and Self, 1998). The high velocities determined here are regarded as maxima, as the velocity is dependent on thickness, slope and viscosity. The thickness of the flow is one of the largest sources of error. This is because inflation can take place after emplacement and cooling, hence resulting in an apparent thicker flow. In Hawaii, Hon et al. (1994) observed that a flow initially 30 cm thick was inflated to a thickness of 3-7 m in a period of over a week. In the current study several thicknesses (20, 15, 10 and 5 m) were considered in order to estimate the flow velocity, showing that it becomes turbulent at thicknesses greater than 5 m (Table 3.3). The velocity calculated for a 5 m thick flow (6 $m.s^{-1}$, Table 3.3) can be regarded as an appropriate value, as it is within the range of open-channel basaltic flows (see Keszthelyi and Self, 1998). Velocities calculated here are higher than the estimate of 1.4 $m.s^{-1}$ from Keszthelyi and Self (1998) for a sheet flow with a slope of 0.1%, an upper lava crust 1 m thick and a total thickness of 23 m. Furthermore, the same authors proposed that faster flows (>5 $m.s^{-1}$) would tend to have a thinner upper crust (<1 m thick), which agrees with the average <1 m thin Pampas Onduladas crust (Pasquarè et al., 2008).

In relation to other long basaltic flows on Earth, the calculated volume for the Pampas Onduladas flow is 7.2 km^3, which is lower than the volume calculated for the Toomba (12 km^3) and for the Undara flow (approximately 25 km^3; Stephenson et al., 1998). Furthermore, in their

model Keszthelyi and Self, (1998) proposed that the minimum volume for a 10 m thick long flow (>100 km in length) is 10 km^3. The calculated volume is much lower than previous calculated volumes for long flows on Earth, mostly resulting from the flat pre-flow topography assumption, therefore regarded as minimum.

The rheology of the Pampas Onduladas flow has been investigated in the current study, nevertheless there are some volcanic aspects that have not been addressed and require attention in order to fully constrain the evolution of this long basaltic flow. Some of these issues refer to the mechanism that caused abundant magma to accumulate in a short time, or what time lapse was requied for the flow to develop. According to the satellite images, the initial part of the flow (sector 1) was not channelized. Moreover, this sector has the largest area and volume of the entire flow (Table 3.4). In addition, and according to the cross section of sector 1 (Figure 3.5 A), the flow is widely spread and has been constrained by the surrounding higher topography. This possibly indicates that sector 1 may have acted as a lava reservoir, hence it can be suggested that the development of the flow did not require a short time frame. However, in order to provide a more definitive answer, further studies need to be made in sector 1 especially.

3.5.4 Aspects of the Pampas Onduladas pre-flow topography

The average slope of the Pampas Onduladas flow (0.84%) is greater than the slope of the Toomba, Undara and Thjotsa flows (0.4%, 0.5% and ~0.7% respectively, Keszthelyi and Self, 1998). Other Quaternary flows in the Pampas Onduladas region have been emplaced over an Andean piedmont topography that created a gradual and lengthy declining slope towards the east. The pre-existing topography is covered mainly by basaltic flows with some exposures of the uplifted San Rafael Block, characterised by Permian-Triassic volcanic and plutonic assemblages (Figure 3.1b and Figure 3.5a, b). The SRB acted as a wall on the northern part of sector 1 and 2, as is evident in cross section A-A' and B-B' (Figure 3.5). The eruption point for this flow has been associated with the activity in La Carbonilla Fracture (LCF in Figure 3.1; Pasquarè et al. 2008). Here, the topography is characterised by a high elevation resulting from uplift of the Payún Matrú eastern shield when it was magmatically active.

The Pampas Onduladas basalt flowed from its initial point over an irregular topography following its steepest course down-slope. The high slope suggests that the flow followed an unencumbered path, inferred from the long profile (Figure 3.8), while the irregular topography can be partly inferred from the cross sections. Accordingly, the Pampas Onduladas flow has a positive relief in relation to the surrounding topography in the middle and distal sectors (Figure 3.5 cross sections C-C', D-D' and E-E'). Interestingly, the cross-section from sector 1, shows a rough surface corresponding to the flow, which has been confined on its northern side by the San Rafael Block and by a topographic high on its southern part (Figure 3.5, cross section A-A'). Furthermore, in the cross-section from sector 2 (Figure 3.5, cross-section B-B') the topography adjacent to the flow shows higher elevation, suggesting that the flow has followed a

pre-existing topographic depression at least in some areas. This observation is critical in the volume calculation which can lead to underestimation assuming a flat base. Furthermore by following a topographic depression, the flow is insulated possibly resembling the type of effective insulation observed in lava tubes. The Pampas Onduladas has inflation structures such as tumuli and lava rises which are generally associated with pahoehoe sheet flow. No lava tubes have been identified for this basaltic flow. However, it is likely that at least in the proximal part, the flow was confined enhancing the insulation process.

The geochemical, rheological and topographical constraints presented here suggest that the Pampas Onduladas flow shows a combination of characteristics that assisted in the development of its great length. The extent of the Pampas Onduladas flow cannot be explained by its geochemical characteristics as it shares these with other basalts of the Payún Matrú volcanic field. Thus, it is likely that its exceptional length is related to a steep slope, aided by low viscosity and a good insulating system derived from its inflating nature and topographic confinement.

3.6. Conclusions

The Pampas Onduladas flow in southern Mendoza constitutes one of the four longest Quaternary lava flows on Earth. It was erupted during the pre-caldera basaltic volcanism of the Payún Matrú volcanic field (Hernando et al., 2012) as confirmed by the geochronological data. The $^{40}Ar/^{39}Ar$ analysis suggests an eruption age of 373 ± 10 ka (2σ), constituting the first direct age constraint for this flow. Geochemical characteristics are consistent with an intraplate setting. This corresponds to a negligible arc signature, an enriched mantle source similar to local ocean island basalts (Río Colorado volcanic field; Søager et al., 2013) and possible lower continental crust assimilation (Germa et al., 2010; Jacques et al., 2013; Søager et al., 2013; Chapter 2)

Rheological characteristics indicate that the viscosity was low and the average eruption temperature was 1170°C. An important feature is the topographic slope which is higher (0.84%) than that determined for the Undara (0.5%), Toomba (0.4%) (Stephenson et al., 1998) and Thjorsa (~0.7) (Vilmundardottir, 1977) flows. The slope is likely to be the most important feature affecting the length (Keszthelyi and Self, 1998) and velocity. The calculated velocity varies depending on thickness, from 30 $m.s^{-1}$ (>110 $km.h^{-1}$) to 17 $m.s^{-1}$ (~60 $km.h^{-1}$) for 20 m and 10 m thickness, respectively (turbulent velocities for flow thickness values >5 m). The proposed thickness is at least 20 m (Pasquarè et al., 2008), after the flow inflated and cooled. The original thickness however, could have been ten times smaller than that preserved, using the inflation ratios from Hon et al. (1994) for Hawaiian basalts. The volume calculated here (7.2 km^3) is regarded as a minimum estimate, based on the method used, which assumes a flat surface below the flow. The length of the Pampas Onduladas flow is not governed by its geochemical characteristics, but by the steep and constant topographic slope supported by an effective insulating system and low viscosity.

Appendix 3.A. (equations used for turbulent flow calculations)

1- Reynolds number (*Re*)

$$Re = \frac{\rho\, H\, v}{\eta}$$

Where ρ is density, H is the thickness, v is the velocity and η is the viscosity

2- Chezy equation

$$v^2 = \frac{g\, H\, \theta}{C_f}$$

Where v is the velocity for a turbulent flow, g is the gravitational acceleration, H is the thickness, θ is the slope and C_f is the friction coefficient

3- Goncharov equation (Goncharov, 1964) to determine the friction coefficient for a turbulent flow with *Re* < 10^5

$$C_{f} = \frac{\lambda}{2}$$

$$\lambda = \{4\ \log_{10}[6.15((Re' + \ 800)/41)^{0.92}]\}^{-2}$$

$$Re' = \ 2Re$$

Supplementary Tables 3.1A to 1D

Table 1A: $^{40}Ar/^{39}Ar$ analytical data

Sample ID	Step No	Laser Power	^{40}Ar (fA)	±1σ	^{39}Ar (fA)	±1σ	^{38}Ar (fA)	±1σ	^{37}Ar (fA)	±1σ	^{36}Ar (fA)	±1σ	^{39}Ar (x10^{-14}mol)	Ca/K	±1σ	%^{40}Ar*	^{40}Ar*/^{39}Ar	±1σ	Cum.% ^{39}Ar	Age (ka)	±1σ
VRE20																					
1a	1	3%	3541.609	1.240	55.157	0.038	2.179	0.001	61.685	2.724	11.598	0.007	0.196	1.957	0.086	3.229	2.073	0.044	15.38	418.621	8.936
1b	2	4%	3976.307	1.710	69.465	0.014	2.444	0.002	69.783	2.534	13.008	0.010	0.247	1.758	0.064	3.334	1.908	0.048	34.74	385.332	9.740
1c	3	5%	2959.609	1.539	59.480	0.044	1.815	0.002	69.292	2.996	9.661	0.011	0.211	2.039	0.088	3.542	1.762	0.061	51.32	355.832	12.378
1d	4	6%	2529.128	1.366	48.488	0.013	1.552	0.002	69.881	3.047	8.262	0.008	0.172	2.522	0.110	3.472	1.811	0.058	64.84	365.718	11.707
1e	5	7%	2370.201	1.446	38.126	0.025	1.463	0.001	75.342	2.733	7.790	0.007	0.135	3.458	0.125	2.883	1.792	0.065	75.47	361.918	13.151
1f	6	8%	2225.363	0.668	29.149	0.016	1.380	0.001	73.315	1.516	7.343	0.006	0.103	4.401	0.091	2.496	1.906	0.060	83.59	384.794	12.195
1g	7	10%	2223.890	0.734	27.652	0.016	1.373	0.002	111.362	2.491	7.306	0.010	0.098	7.048	0.158	2.916	2.345	0.112	91.30	473.467	22.582
1h	8	12%	1802.622	0.631	19.138	0.022	1.115	0.001	104.119	1.360	5.937	0.003	0.068	9.520	0.125	2.680	2.524	0.055	96.64	509.716	11.202
1i	9	14%	1357.506	0.407	12.059	0.031	0.833	0.001	95.918	2.182	4.434	0.004	0.043	13.920	0.319	3.490	3.929	0.110	100.00	793.197	22.293
VRE46A																					
1a	1	3%	1021.009	0.276	38.836	0.016	0.600	0.001	73.890	5.529	3.193	0.003	0.138	3.330	0.249	7.575	1.992	0.026	14.44	402.380	5.351
1b	2	4%	1228.006	0.430	50.438	0.027	0.719	0.001	81.167	3.899	3.827	0.003	0.179	2.816	0.135	7.908	1.925	0.022	33.20	389.013	4.471
1c	3	5%	1212.858	0.352	43.186	0.024	0.725	0.001	67.844	6.098	3.858	0.005	0.153	2.749	0.247	6.000	1.685	0.037	49.27	340.494	7.515
1d	4	6%	1215.970	0.353	34.118	0.029	0.735	0.001	61.036	5.797	3.912	0.008	0.121	3.131	0.297	4.927	1.756	0.068	61.95	354.784	13.833
1e	5	8%	1792.107	0.556	36.171	0.040	1.105	0.001	104.041	6.361	5.882	0.005	0.128	5.034	0.308	3.015	1.494	0.043	75.41	301.805	8.779
1f	6	10%	2046.050	0.757	24.868	0.034	1.279	0.001	110.753	4.468	6.806	0.007	0.088	7.794	0.315	1.705	1.403	0.092	84.66	283.501	18.572
1g	7	1%2	1645.830	0.494	16.213	0.019	1.026	0.001	102.247	5.660	5.463	0.007	0.058	11.037	0.611	1.907	1.936	0.126	90.69	391.162	25.402
1h	8	14%	1274.596	0.357	12.492	0.028	0.791	0.001	91.609	6.307	4.211	0.005	0.044	12.833	0.884	2.369	2.417	0.129	95.33	488.355	26.040
1i	9	18%	1203.026	0.421	12.547	0.026	0.743	0.001	111.268	6.038	3.956	0.004	0.045	15.519	0.843	2.834	2.717	0.102	100.00	548.890	20.513

Weight of sample VRE20 = 73.5 mg, J-value = (111.934 ± 0.117) x 10^{-6}

Weight of sample VRE46a = 75.3 mg, J-value = (112.005 ± 0.103) x 10^{-6}

Suplementary Table 3.1B. Blanks results

Blank Data	Sample ID	^{40}Ar (fA)	±1σ	^{39}Ar (fA)	±1σ	^{38}Ar (fA)	±1σ	^{37}Ar (fA)	±1σ	^{36}Ar (fA)	±1σ
EXB#2	VRE20-1a	0.6665	0.02	-0.0069	0.01	0.0178	0.0164	-0.0043	0.0254	0.0038	0.0001
EXB#2	VRE20-1b	0.6665	0.02	-0.0069	0.01	0.0178	0.0164	-0.0043	0.0254	0.0038	0.0001
EXB#3	VRE20-1c	2.0322	0.04	0.1065	0.01	-0.0182	0.0259	-0.0489	0.0275	0.0081	0.0004
EXB#3	VRE20-1d	2.0322	0.04	0.1065	0.01	-0.0182	0.0259	-0.0489	0.0275	0.0081	0.0004
EXB#3	VRE20-1e	2.0322	0.04	0.1065	0.01	-0.0182	0.0259	-0.0489	0.0275	0.0081	0.0004
EXB#5	VRE20-1f	2.8567	0.08	0.1133	0.01	0.0187	0.0125	-0.0273	0.0146	0.0105	0.0003
EXB#5	VRE20-1g	2.8567	0.08	0.1133	0.01	0.0187	0.0125	-0.0273	0.0146	0.0105	0.0003
EXB#5	VRE20-1h	2.8567	0.08	0.1133	0.01	0.0187	0.0125	-0.0273	0.0146	0.0105	0.0003
EXB#7	VRE20-1i	0.6341	0.03	-0.0060	0.03	0.0024	0.0159	-0.0426	0.0097	0.0037	0.0002
EXB#8	VRE46A-1a	1.7018	0.02	0.0031	0.01	-0.0388	0.0275	-0.0151	0.0206	0.0073	0.0001
EXB#8	VRE46A-1b	1.7018	0.02	0.0031	0.01	-0.0388	0.0275	-0.0151	0.0206	0.0073	0.0001
EXB#9	VRE46A-1c	1.9544	0.03	-0.0364	0.02	-0.0178	0.0275	-0.0049	0.0251	0.0087	0.0001
EXB#9	VRE46A-1d	1.9544	0.03	-0.0364	0.02	-0.0178	0.0275	-0.0049	0.0251	0.0087	0.0001
EXB#10	VRE46A-1e	2.0426	0.03	0.0109	0.03	-0.0610	0.0355	0.0008	0.0183	0.0084	0.0003
EXB#10	VRE46A-1f	2.0426	0.03	0.0109	0.03	-0.0610	0.0355	0.0008	0.0183	0.0084	0.0003
EXB#12	VRE46A-1g	2.0086	0.05	-0.0039	0.01	-0.0390	0.0383	-0.0102	0.0251	0.0081	0.0002
EXB#12	VRE46A-1h	2.0086	0.05	-0.0039	0.01	-0.0390	0.0383	-0.0102	0.0251	0.0081	0.0002
EXB#12	VRE46A-1i	2.0086	0.05	-0.0039	0.01	-0.0390	0.0383	-0.0102	0.0251	0.0081	0.0002

Suplementary Table 3.1C. Alder Creek Rhyolite Sanidine standard results

Sample ID	Step No	Laser Power	^{40}Ar (fA)	±1σ	^{39}Ar (fA)	±1σ	^{38}Ar (fA)	±1σ	^{37}Ar (fA)	±1σ	^{36}Ar (fA)	±1σ	^{39}Ar (x10^{-14} mol)	Ca/K	±1σ	%^{40}Ar*	^{40}Ar*/^{39}Ar	±1σ
A1																		
A1-1	1	35%	402.84	0.11	64.66	0.02	0.0147	0.0002	7.7832	3.1923	0.0781	0.0008	0.2296	0.211	0.086	94.27	5.873	0.005
A1-2	1	35%	580.66	0.16	94.37	0.03	0.0163	0.0001	6.4593	2.3070	0.0869	0.0004	0.3350	0.120	0.043	95.57	5.881	0.003
A1-3	1	35%	418.97	0.16	68.17	0.03	0.0121	0.0001	0.0728	2.5815	0.0642	0.0005	0.2420	0.002	0.066	95.47	5.868	0.004
A1-4	1	35%	383.73	0.05	62.80	0.04	0.0098	0.0001	0.2840	2.2735	0.0521	0.0007	0.2230	0.008	0.063	95.98	5.865	0.005
A1-5	1	35%	728.19	0.20	103.35	0.03	0.0819	0.0002	1.9564	1.3876	0.4361	0.0013	0.3669	0.033	0.023	82.30	5.799	0.004
A2																		
A2-1	1	35%	484.14	0.08	77.33	0.05	0.0192	0.0002	7.8366	5.1123	0.1023	0.0011	0.2745	0.177	0.116	93.75	5.870	0.006
A2-2	1	35%	517.64	0.11	82.12	0.05	0.0256	0.0002	13.0580	4.3486	0.1362	0.0008	0.2915	0.278	0.093	92.22	5.814	0.005
A2-3	1	35%	841.28	0.09	114.26	0.04	0.1097	0.0009	-3.2302	-6.2394	0.5839	0.0047	0.4056	-0.049	-0.096	79.49	5.853	0.012
A2-1	1	35%	484.14	0.08	77.33	0.05	0.0192	0.0002	7.8366	5.1123	0.1023	0.0011	0.2745	0.177	0.116	93.75	5.870	0.006
A2-2	1	35%	517.64	0.11	82.12	0.05	0.0256	0.0002	13.0580	4.3486	0.1362	0.0008	0.2915	0.278	0.093	92.22	5.814	0.005
A2-3	1	35%	841.28	0.09	114.26	0.04	0.1097	0.0009	-3.2302	-6.2394	0.5839	0.0047	0.4056	-0.049	-0.096	79.49	5.853	0.012
A2-4	1	35%	601.87	0.09	98.88	0.09	0.0151	0.0002	-5.0718	-3.8528	0.0802	0.0010	0.3510	-0.090	-0.068	96.06	5.847	0.006
A2-5	1	35%	649.18	0.08	107.33	0.06	0.0227	0.0002	17.5891	5.7909	0.1207	0.0010	0.3810	0.287	0.094	94.50	5.716	0.004
A2-6	1	35%	572.14	0.14	83.61	0.03	0.0520	0.0001	-1.6563	-4.4624	0.2766	0.0006	0.2968	-0.035	-0.093	85.71	5.865	0.003
A2-7	1	35%	411.45	0.09	67.25	0.04	0.0109	0.0001	-4.9928	-6.1649	0.0581	0.0007	0.2387	-0.130	-0.160	95.82	5.863	0.005
A2-8	1	35%	587.57	0.05	78.95	0.05	0.0951	0.0002	25.6756	7.0498	0.5061	0.0012	0.2803	0.569	0.156	74.55	5.548	0.006

Heating steps in red are rejected.

Suplementary Table 3.1D. Inverse Isochron

Aliquant no.	steps	steps included	$^{39}Ar/^{40}Ar$	error %	$^{36}Ar/^{40}Ar$	error %	R	$^{40}Ar/^{36}Ar$	error %	MSWD	$^{40}Ar/^{39}Ar$	error (%)	Age (ka)
VRE20-1a	1		0.01557	0.07742	0.00327	0.07061	0.22410						
VRE20-1b	2	x	0.01747	0.04743	0.00327	0.08644	0.45102						
VRE20-1c	3	x	0.02010	0.09049	0.00326	0.12691	0.23546						
VRE20-1d	4	x	0.01917	0.06039	0.00327	0.11423	0.42275						
VRE20-1e	5	x	0.01609	0.08994	0.00329	0.10682	0.38732	296.6	1.7	1.2	1.62	0.32	349 ± 68 (2σ)
VRE20-1f	6	x	0.01310	0.06273	0.00330	0.08085	0.17746						
VRE20-1g	7		0.01243	0.06687	0.00329	0.14302	0.11388						
VRE20-1h	8		0.01062	0.11965	0.00329	0.05989	0.17097						
VRE20-1i	9		0.00888	0.26211	0.00327	0.10089	0.03404						
VRE46A-1a	1	x	0.03804	0.04830	0.00313	0.10839	0.13926						
VRE46A-1b	2	x	0.04107	0.06440	0.00312	0.09748	0.19516						
VRE46A-1c	3	x	0.03561	0.06312	0.00318	0.14046	0.09487						
VRE46A-1d	4	x	0.02806	0.09086	0.00322	0.20180	0.04587						
VRE46A-1e	5	x	0.02018	0.11545	0.00328	0.09003	0.09246	295.6	3.0 (95%CI)	35	1.85	0.38 (95% CI)	374 ± 76 (2σ)
VRE46A-1f	6	x	0.01215	0.14037	0.00333	0.11343	0.08599						
VRE46A-1g	7	x	0.00985	0.12127	0.00332	0.12611	0.05885						
VRE46A-1h	8	x	0.00980	0.22484	0.00330	0.12914	0.02700						
VRE46A-1i	9	x	0.01043	0.21016	0.00329	0.10850	0.05372						

Suplementary Figure 3.1.Ca/K spectrum.

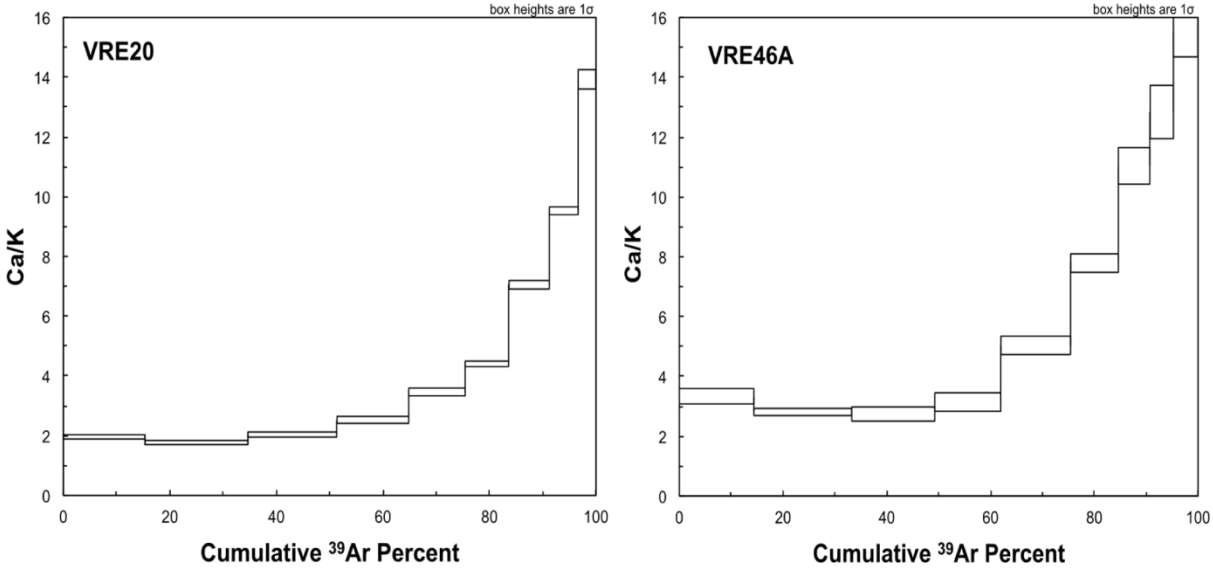

Chapter 4:

Localised magmatic constraints on continental back-arc volcanism in southern Mendoza, Argentina: The Santa Maria volcano

Venera R. Espanon [a,b], Allan R. Chivas[a], Simon P. Turner[c], Leslie P.J. Kinsley[d] and Anthony Dosseto[a,b]

[a] *GeoQuest Research Centre, School of Earth & Environmental Sciences, University of Wollongong, NSW 2522, Australia.*

[b] *Wollongong Isotope Geochronology Laboratory, School of Earth & Environmental Sciences, University of Wollongong, NSW 2522, Australia.*

[c] *GEMOC, Department of Earth and Planetary Sciences, Macquarie University, Sydney, NSW 2109, Australia.*

[d] *Research School of Earth Sciences, The Australian National University, Canberra, ACT 0200, Australia.*

Allan R. Chivas: toschi@uow.edu.au

Simon P. Turner: sturner@els.mq.edu.au

Leslie J. Kinsley: leslie.kinsley@anu.edu.au

Anthony Dosseto: tonyd@uow.edu.au

Abstract

Payún Matrú volcanic field (PMVF) constitutes part of the continental back-arc in central west Argentina. This volcanic field has been the focus of several regional investigations; however, geochemical analysis on recent volcanoes (<10 ka) at a volcano based-scale, has not been conducted. The Santa Maria volcanic cone and corresponding basaltic flow constitutes one of the most recent eruptions from the PMVF and it is geographically isolated from other recent basaltic flows and volcanic cones. Therefore, this volcano provides an appropriate setting to conduct a detailed geochemical analysis on a local-scale. We present results from major- and trace- element analysis as well as ^{238}U-^{230}Th-^{226}Ra disequilibria in order to determine the melting conditions below this volcano. The geochemical evidence suggests that the Santa Maria magmatic source has a composition similar to the local ocean island basalt (OIB), with some lower crustal assimilation and not influenced by subduction processes, agreeing with previous studies from the area.

U-series analyses, suggest a differentiation trend in the magmatic chamber, which modified the ^{266}Ra-^{230}Th disequilibrium, however it is not able to explain the original ^{226}Ra excess prior to differentiation. The high ^{226}Ra excess in the rocks from the Santa Maria volcano is better explained by partial melting at intermediate pressure such as lithospheric mantle depth. Due to the short half-life of ^{226}Ra (1600 years) and the high excess, which will reach secular equilibrium in approximately 5 half-lives, we estimated fast magma ascent rates in the order of 20 to 40 m/a likely to be achieved by a channelized flow. Agreeing with a dynamic melting model adjusted to an intermediate pressure, which best resemble the activity ratios observed in this volcano. Based on the location at which partial melting is inferred to occur, and the previous geophysical investigations we suggest that magma with an OIB-like composition is ponded below the continental crust.

4.1. Introduction

Continental back-arc volcanism refers to regions behind the main volcanic arc front of a continental-oceanic collision. These regions are generally associated with areas where the subducting slab is located greater depth than in the volcanic arc front, and therefore less likely to be influenced by fluids released through metasomatism (Schmidt and Poli, 1998). The volcanism in the Payún Matrú volcanic field in southern Mendoza, Argentina is associated with the previously described setting. This volcanic field the is associated with an enriched mantle similar to an Ocean Island Basalt-type (OIB), (Jacques et al., 2013, Søager et al., 2013, Burd et al., 2014; Chapter 2).

The chemical composition of continental back-arc basalts may be controlled by several processes such as lower continental crust contamination (Søager et al., 2013, Chapter 2), slab partial melts (Sigmarsson et al., 2002, Jacques et al., 2013) and the continental lithospheric mantle (Varekamp et al., 2010). This heterogeneity has been previously identified in several continental back-arcs, such as in the Loncopue graben (Figure 4.1) by Varekamp et al. (2010) and in the Payenia Basaltic Province by Søager et al. (2013), Jacques et al. (2013) and Chapter 2. In order to avoid confusion among lava flows with different heterogeneities, in this volcanically dense basaltic province, an isolated cinder cone and its corresponding basaltic flow have been chosen for the current investigation. The purpose of this investigation is to i) determine the processes contributing to the heterogeneity of this isolated volcano (Santa Maria) and to apply these findings to the Payún Matrú volcanic field, and ii) to determine the possible melting conditions for this basaltic flow using isotopes of the U-series decay chain.

4.2. Geographical Setting

The Payún Matrú volcanic field (PMVF) is part of the Payenia Basaltic Province (PBP, Figure 4.1; Appendix B) described by Polanski (1954). The Payenia Basaltic Province is the northernmost continental back-arc field of the Andean Southern Volcanic Zone (SVZ, comprising the volcanic arc between 33°S and 46°S). The southern Mendoza and northern Neuquén volcanism represent the largest Quaternary continental back-arc in the SVZ (Figure 4.1) (Bermudez and Delpino, 1989; Kay et al., 1994,2006a,b; Pasquarè et al., 2008; Bertotto et al., 2009; Germa et al., 2010; Søager et al., 2013; Kay et al., 2013; Chapter 2). Holocene volcanism is only evident in the Payún Matrú volcanic field (Germa et al., 2010, Espanon et al., 2014a, Marchetti et al., 2014). This volcanic field is located approximately 450 km from the Peru-Chile trench and does not display a subduction-related geochemical signature (Chapter 2). The Payún Matrú volcanic field has intraplate signatures associated with an enriched up-welling mantle similar to an OIB (Germa et al., 2010, Jacques et al., 2013, Søager et al., 2013, Chapter 2). Much of the continental back-arc volcanism from 36°S to 46°S shows characteristics of an enriched mantle; however, some volcanic fields such as the Loncopue area, Neuquén (Varekamp et al., 2010) and the Llancanelo volcanic field (Chapter 2) have minor arc signatures.

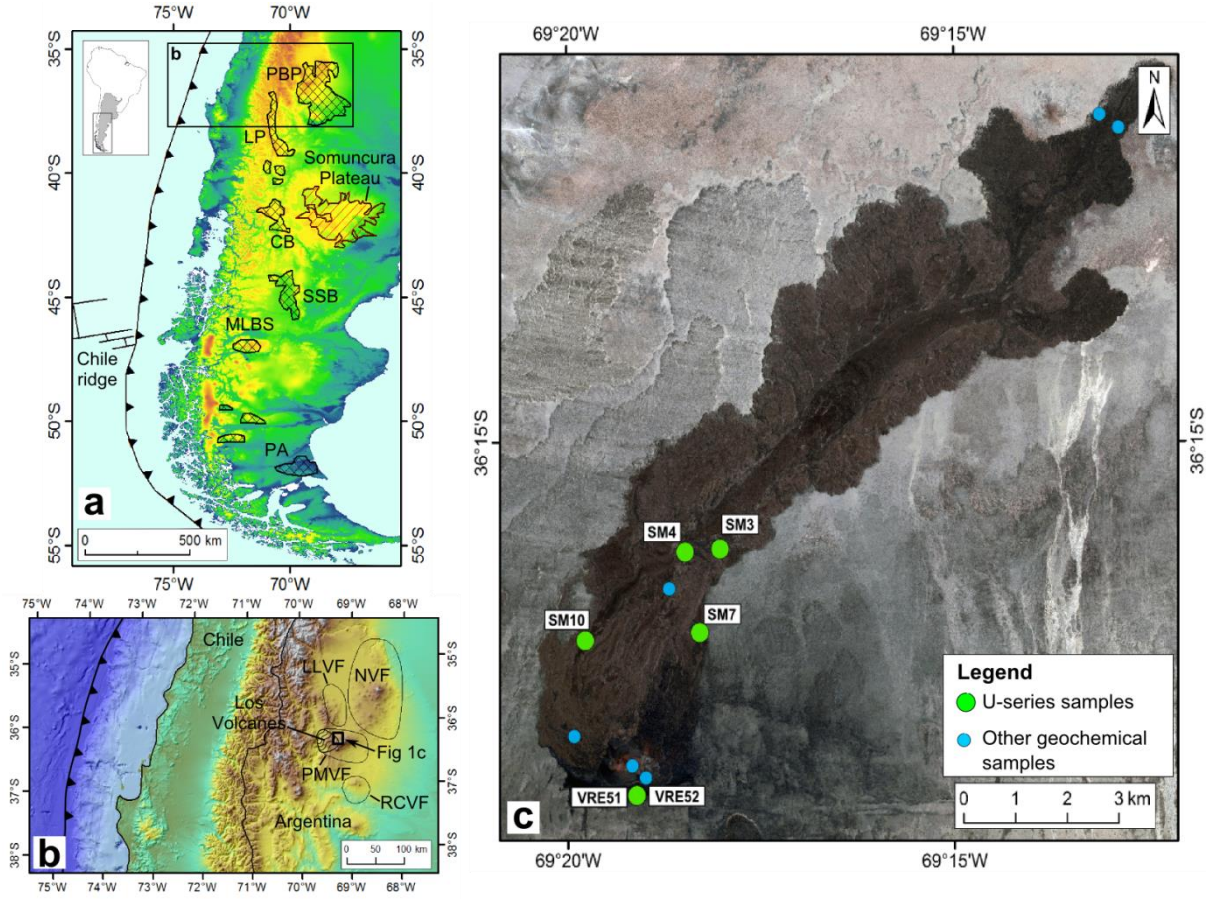

Figure 4.1. Location of the Payenia Basaltic Province, Payún Matrú volcanic field and the Santa Maria volcano. **a**) Location of the Quaternary back-arc volcanic fields in Patagonia (modified after Kay et al., 2007). Payenia Basaltic Province (PBP), Loncopue (LP), Crater basalt (CB), Sierra de San Bernardo (SSB), Meseta del Lago Buenos Aires (MLBS) and Pali Aike (PA). The Somuncura Plateau is the only Neogene Patagonian basaltic field shown. Note that to the north of the Chile Ridge the volcanic zone is named the Southern Volcanic Zone (SVZ), while south of the ridge it is the Austral Volcanic Zone (AVZ). **b**) Detail of the Payenia Basaltic Province showing the main four volcanic fields, the Llancanelo (LLVF), Nevado (NVF), Payún Matrú (PMVF) and Río Colorado (RCVF) volcanic fields. Note the location of the trench in relation to the PMVF which contains the Santa Maria volcano. **c**) Santa Maria volcano and corresponding basaltic flow with sample locations. Green dots indicate samples used for geochemistry as well as for U-series disequilibria and blue dots indicate samples used for geochemistry only. Note that samples VRE51 and VRE52 share the same location as the two samples were taken from within couple metres but from different material. Sample VRE 51 is a basaltic bomb while VRE52 is from a basaltic flow. Base images from Gtopo 30 (Global 30 Arc-Second Elevation Data Set), GEBCO 08 grid and Landsat 7.

The Santa Maria cinder cone and its associated basaltic a'a flow are located on the central northern part of the Payún Matrú volcanic field (Figure 4.1) and to the north-west of the Payún Matrú caldera. This cinder cone and flow correspond to the younger part of the Payún Matrú volcanic field, which is located to the west of the Payún Matrú caldera and is part of Los Volcanes area (Figure 4.1) (Germa et al., 2010). A reliable age for the Santa Maria volcano, has not been determined and the only available ages come from a basaltic flow and bomb, using surface exposure dating (based on cosmogenic ^{3}He and ^{21}Ne; Espanon et al., 2014a). The

calculated ages are <10 ka; however, the associated errors are large as the cosmogenic isotopic abundance is low. The Santa Maria volcano was last active during the Holocene as the volcanic products did not have sufficient time to accumulate enough cosmogenic isotope (Espanon et al., 2014a). F Morphological and morphometric studies of this volcano suggest that it is young (Inbar and Risso, 2001). The available geochemical data from the Santa Maria volcano are restricted to a single sample taken from the Santa Maria flow to the west its volcanic cone, which is classified as a trachy-basalt (Søager et al., 2013).

4.3. Methods

A total of thirteen samples were collected from the Santa Maria volcano and flow. Most of the samples are basalts collected from the Santa Maria flow (nine samples) (Figure 4.1 and Table 4.1). Three samples are scoria collected from, the main Santa Maria cone (SM8), from a small scoria cone on the eastern flank of the main cone (SM12) and from a linear vent on the north-west side of the main cone (SM9). One basaltic bomb sample VRE51 was analysed from the Santa Maria volcano bomb field (Figure 4.2 and Table 4.1).

Samples were cleaned and crushed using a Cr-Ni rock crusher N.V. TEMA at the School of Earth and Environmental Sciences, University of Wollongong. The rock powder was mixed with a flux (a mixture of 35.3% lithium tetraborate and 64.7% lithium metaborate) and fused in order to produce a glass disc for each sample. The glass discs were analysed for major elements using a Spectro Xepos energy dispersive polarization X-ray spectrometer at the School of Earth and Environmental Sciences at the University of Wollongong. The accuracy of the measurement was monitored using a natural standard (dolerite) W-2 (n=2) (Gladney and Roelandts, 1988), with a relative deviation from the recommended values of <3% for all major elements. Loss on ignition was measured using approximately 1 g of powder sample in a furnace at 1050°C, for two hours.

Trace elemental analysis for two samples, VRE51 and VRE52 were performed using X-ray fluorescence. Samples were pressed into a pellet using a PVF binder. The pellets were analysed using the spectrometer mentioned. The remaining of the samples were analysed for trace elements by laser ablation inductively-coupled plasma mass spectrometry (LA ICP-MS) at the Research School of Earth Sciences, Australian National University. The laser employed was an Excimer laser (ArF 193 nm) 50mJ, 5Hz at a scan rate of 10 microns per second and a spot diameter of 105 µm. The aerosols released were immediately analysed on an Agilent 7200 quadrupole ICP-MS. The samples were analysed under the same conditions with standard NIST612 (n=6) (GeoReM reference material; Jochum et al., 2011) and data were calibrated according to this standard. BCR-2 (n=6) (USGS, Wilson, 1997) a natural rock standard was used to monitor the accuracy. The relative deviation from accepted concentrations for BCR-2 was less than 7% for all the elements analysed.

Uranium-series isotopes were analysed on six samples from the Santa Maria basaltic flow and one sample (PY-4) from another area within the Payún Matrú volcanic field, in order to have a uranium-series analogue from the same volcanic field. Sample preparation was done at the Wollongong Isotope Geochronology Laboratory, University of Wollongong. Approximately 0.3 g and 0.02 g of ^{228}Ra and ^{229}Th-^{236}U tracer solutions, respectively, were added to 0.6-1.4 g of ground sample prior to digestion. Samples were digested in 1.5 ml 12M HCl, 0.5 ml 16M HNO_3, 2 ml 12M $HClO_4$ and 2 ml 28M HF at 130°C for 12 hours. Samples were then re-dissolved in a H_3BO_3-saturated solution of 6M HCl and boric acid and left to react for several hours at 120°C in order to dissolve any insoluble fluorides (Koornneef et al., 2010). After evaporation of the H_3BO_3-saturated solution, the samples were re-dissolved in 7.5M HNO_3. Uranium, Th and Ra were then separated using a series of solid-liquid chromatography columns packed with ion exchange resins. The U-Th and Ra separation procedure was modified from Luo et al. (1997) and Claude-Ivanaj et al. (1998), respectively. The first column was packed with 0.1ml of Eichrom pre-filter® resin in order to prevent any organic components passing through, overlain by 0.5 ml (except sample SM4 and VRE51 for which 0.75 ml was used) of EichromTRU resin. This first column was used to separate the Th and U from the matrix. The second column was packed with 8 ml of Bio-Rad AG50-WX8 cationic resin, onto which the matrix eluted from the first column was loaded. This column was used as a first purification of Ra and Ba from the matrix. The third column was packed with 1 ml of AG50-WX8 resin and used to purify the Ra-Ba fraction from the matrix. The fourth column was packed with 150µl of Eichrom Ln-Spec® resin to further purify the Ra-Ba fraction; the fifth column was packed with 150µl of Eichrom Sr-Spec® resin to separate Ra from Ba. The final Ra fraction was loaded on a Re filament in Ta oxide and analysed on a Thermo Finnigan Triton® Thermal Ionization Mass Spectrometry (TIMS) at GEMOC, Department of Earth and Planetary Sciences, Macquarie University. U and Th concentrations were measured on a Thermo Neptune Plus® multi-collector ICP-MS at the Research School of Earth Sciences, Australian National University. The procedure blank was <2 fg for Ra, while for Th it was 78 ± 12 pg and for U, 43 ± 3 pg. The two ^{226}Ra standards, used are within 1% of the recommended value (433 fg/g). Three individual aliquots of BCR-2 rock standard were digested and used throughout the separation procedure and analysis to assess the accuracy. The Th and U concentrations were within 1% error of the published values (Wilson, 1997), while Ra was 20% lower than previous published values (Koornneef et al., 2010, Reubi et al., 2014). The (^{230}Th/^{232}Th) and (^{234}U/^{238}U) activity ratios (brackets denote activity ratio) were within 1.5% of previously published values, while (^{230}Th/^{238}U) and (^{238}U/^{232}Th) were within 5.5% of previous published values (Sims et al., 2008, Reubi et al., 2014). In the case of (^{226}Ra/^{230}Th), the measured value was 18% lower than the recommended value for BCR-2 (Koornneef et al., 2010, Reubi et al., 2014). It is important to consider that BCR-2 has not been widely used as quality control standard among U-series publications presenting U, Th and Ra disequilibria except for the work by Koornneef et al. (2010) and Reubi et al. (2014). The BCR-2 standard has low (^{226}Ra/^{230}Th), while the samples have values >1, implying that the

measured values are probably minimal. Thus, despite poor accuracy, the lavas exhibit Ra-excess, and we focus on trying to explain this excess.

4.4. Results

4.4.1. Geomorphic description of the Santa Maria cone and flow

Santa Maria is a monogenetic volcano with a well-preserved scoria cone breached to the north-west. The main cone is composed of two craters and one small scoria cone on the southeastern side of the main cone. This volcano is located at 1940 masl and rises 140 m above the surrounding topography. The basaltic flow extends for 16.5 km from the cone in a north-easterly direction with a topographic slope of 1.97% covering an area of 42.4 km^2 with a volume of 0.94 km^3 (calculated using the method described in Chapter 3). The Santa Maria cone has high slope angles (>30°) which are related to young volcanic activity, as generally, the angle decreases with time due to erosion (Inbar and Risso, 2001). Furthermore, the scoria ejected has been preserved in place on the southern and northeastern side of the cone, the basaltic bombs ejected have also been preserved and deposited on the southern side of the cone. The bomb size ranges from a few centimetres to almost a metre, most have a near-spherical shape, while there are some examples of spindle, bread-crust and ribbon bombs (Figure 4.2). The main cone has several spatter ramparts (Figure 4.2e) which suggest an eruption event similar to a volcanic fountain, while on the northwestern side of the cone there is a linear vent (Figure 2e) which is currently covered by red scoria. These effusion points, have been previously interpreted as the migration of the eruptive vent when the system was active (Risso et al., 2006).

On the top of the cone, a clay rich area with lighter colour is likely to be the remnants of a fumarole (Figure 4.2). The morphology of the Santa Maria volcano suggest that the eruption had a Hawaiian style, which then developed into a Strombolian style in order to produce the scoria and basaltic bomb field. The different colours within the Santa Maria flow (Figure 4.1) represent several generations of basaltic flow, with the darker one being typical of an a'a flow (Figure 4.2c). A'a is the dominant lava type, however, there are some structures such as lava ridges and tube-like structures (Figure 4.2b; approximately where sample SM3 was collected Figure 4.1c), suggesting that at some stage the lava was less viscous.

Figure 4.2. Field images of the Santa Maria volcanic cone, flow and pyroclastic material. a) View of Santa Maria main cone and flow. Note the high angle of the main cone with a breached crater to the NW. b) Inner part of the Santa Maria flow close to sample site SM3 (Figure 4.1c). Person for scale. c) Inner part of the flow presenting the typical aa style of the flow. d) Upper part of the main Santa Maria cone. Note the light colours possibly indicating an extinct fumarole. e) View from the inner part of the main crater to the NW showing part of the collapsed ramparts. In the background, one of the eruption points is present as a fissure. f) Ribbon-type pyroclastic bomb. g) Spindle pyroclastic bomb. h) Bread-crust pyroclastic bomb.

4.4.2. Petrography of the Santa Maria flow

The basalts from Santa Maria are vesicular and the dominant texture is porphyritic. However, some samples have a seriate or less commonly a glomeroporphyritic texture. The most abundant phenocrysts are plagioclase and olivine, with low abundance of clinopyroxene microcrysts. Most of the olivine phenocrysts have euhedral to subhedral crystal shape; while samples SM10 and SMT3 present skeletal olivine and sample VRE51 has a single anhedral olivine. The plagioclase phenocrysts are mainly euhedral, however some of them are sieved. The groundmass is mainly plagioclase and olivine with some interstitial glass. Alteration is not evident and phenocryst boundaries are sharp. Most plagioclase phenocrysts show typical multiple twinning however some show oscillatory zoning.

4.4.3. Major- and trace-element results

Major element concentrations, show a narrow range of values. The MgO concentration ranges from 5.94 to 6.69 wt % with only sample SM8 (scoria) being more differentiated with a higher SiO_2, and lower MgO, Al_2O_3, TiO_2 and Na_2O contents. In a total alkalis versus silica diagram (Le Bas et al., 1986), all samples are within the alkaline trachy-basalt field (Figure 4.3) with an alkali content greater than 5 wt %. The three scoria samples SM8, SM9 and SM12 have lower alkali content and are classified as basalts.

Rare Earth Element (REE) normalised to chondrites (Boynton, 1984) show a smooth pattern with enrichment in light rare earth elements (LREE) relative to heavy rare earth elements (HREE) (Figure 4.4a). In this diagram, samples show patterns between those of an average ocean island basalt composition end-member (Sun and McDonough, 1989) and an average lower continental crust composition (LCC) (Rudnick and Gao, 2003). The Santa Maria samples have the highest La/Yb ratios of all the samples from Payún Matrú volcanic field (Chapter 2) ranging from 9.31 to 10.94 with an average value of 9.94. Trace element content for the Santa Maria samples and an average arc composition were normalised to primitive mantle composition in order to compare the composition of Santa Maria lava to that of the volcanic arc (McDonough and Sun, 1995) (Figure 4.4). The Santa Maria volcano shows enrichment in highly incompatible elements (Cs, Rb, Ba, Th, U) while they do not show any Nb, Ta or Ti negative anomaly generally associated with subduction-related magmatism. Furthermore, the composition of Santa Maria samples and an average lower continental crust composition were normalised to an average OIB composition (Sun and McDonough, 1989).

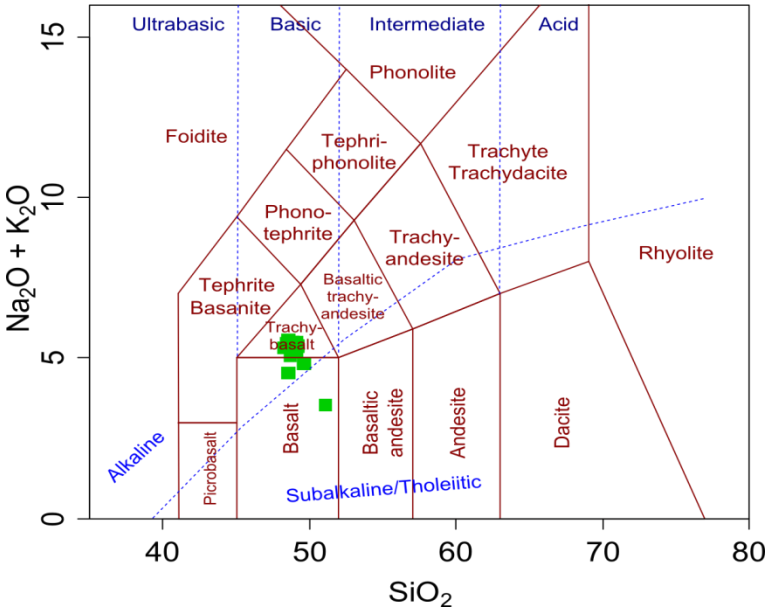

Figure 4.3. Total alkalies versus silica diagram (Le Bas et al., 1986). All the Santa Maria samples are alkaline with the majority of the samples being classified as trachy-basalts. The only sample that has very low alkali content is SM8, which corresponds to basaltic scoria from the upper part of the Santa Maria cone.

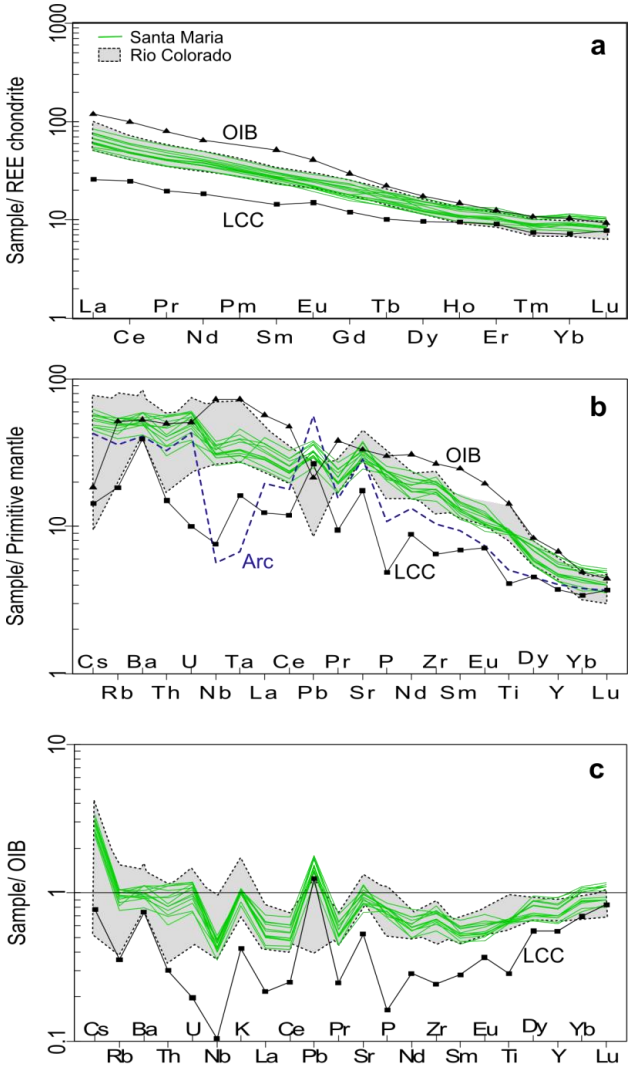

Figure 4.4 Normalised trace-element diagrams. a) Rare Earth Element (REE) concentrations normalised to chondrites (Boynton, 1984). b) Sample concentration normalised to primitive mantle values from McDonough and Sun (1995). c) Sample concentrations normalised to OIB value from Sun and McDonough (1989). The average lower continental crust (LCC) is from Rudnick and Gao (2003). The Río Colorado field represents the local intraplate end-member with an OIB-like composition from Søager et al. (2013). The arc end-member is an average from the Andean volcanic arc with <53 SiO_2 wt % between 35°S and 38°S (Lopez-Escobar et al., 1977, Tormey et al., 1991, Ferguson et al., 1992, Tormey et al., 1995, Costa and Singer, 2002, Jacques et al., 2013).

Table 4.1. Major- and trace-element concentrations for the Santa Maria volcano.

Sample	SM3	SM4	SM6	SM7	SM8	SM9
Material	Basalt	Basalt	Basalt	Basalt	Scoria	Scoria
Latitude	-36.2669	-36.2674	-36.2732	-36.2802	-36.3013	-36.2966
Longitude	-69.3005	-69.3080	-69.3114	-69.3049	-69.3195	-69.3320
Elevation (MASL)	1634	1635	1664	1660	1939	1793
SiO_2	48.84	49.16	49.04	48.30	51.01	48.52
TiO_2	1.92	1.81	1.80	1.88	1.77	1.83
Al_2O_3	17.55	16.99	17.03	17.10	16.29	17.50
Fe_2O_3	10.19	10.48	10.55	10.81	14.56	10.46
MnO	0.14	0.15	0.15	0.15	0.14	0.14
MgO	5.94	6.54	6.50	6.66	3.92	6.64
CaO	9.42	9.03	8.94	9.31	8.18	9.93
Na_2O	4.02	3.90	3.96	3.88	2.28	3.34
K_2O	1.48	1.48	1.53	1.43	1.26	1.19
P_2O_5	0.49	0.45	0.49	0.49	0.47	0.42
V	236	228	225	233	225	238
Cr	206	231	209	208	190	241
Ni	96.0	94.7	89.3	94.1	47.7	103
Cu	49.50	45.2	45.5	48.0	60.9	46.4
Zn	51.7	54.2	54.3	54.9	44.9	52.7
Ga	20.0	20.4	19.7	20.0	19.6	19.5
Rb	28.0	28.9	30.0	26.6	25.4	23.6
Sr	640	563	565	584	487	605
Y	20.3	20.3	20.4	19.6	18.3	18.0
Zr	185	187	187	172	178	155
Nb	20.7	20.2	20.4	19.2	19.2	16.9
Cs	1.03	1.10	1.14	0.99	0.99	0.94
Ba	343	329	330	321	393	277
Sc	25.7	25.5	25.0	25.5	26.0	26.9
La	18.9	18.4	19.1	18.4	16.4	15.6
Ce	39.5	38.1	39.7	38.5	35.1	33.0
Pr	5.07	4.91	5.05	5.00	4.33	4.27
Nd	22.5	21.4	22.6	21.5	19.1	19.2
Sm	5.27	5.30	5.10	5.17	4.71	4.51
Eu	1.64	1.59	1.61	1.58	1.42	1.51
Gd	4.57	4.64	4.66	4.45	4.03	4.22
Tb	0.74	0.91	0.73	0.70	0.65	0.64
Dy	4.11	4.11	3.98	3.96	3.68	3.63
Ho	0.79	0.80	0.78	0.76	0.69	0.68
Er	2.12	2.13	2.19	2.07	1.91	1.86
Tm	0.29	0.30	0.29	0.28	0.28	0.26
Yb	1.90	1.97	1.88	1.84	1.70	1.61
Lu	0.27	0.28	0.27	0.27	0.24	0.25
Hf	4.28	4.36	4.37	3.98	4.19	3.64
Ta	1.23	1.21	1.22	1.11	1.13	1.01
Pb	4.37	4.53	4.57	4.41	4.93	3.76
Th	3.24	2.42	3.70	3.04	3.36	2.77
U	0.97	0.75	1.07	0.93	1.12	0.77

The major elements are in wt % and the trace elements are in ppm. Errors are <3 % and <6.7 %, respectively.

Table 4.1. cont.

Sample	SM10	SM12	SM13	SMT3	SMT4	VRE51	VRE52
Material	Basalt	Scoria	Basalt	Basalt	Basalt	Basaltic bomb	Basalt
Latitude	-36.2814	-36.3032	-36.2948	-36.2002	-36.1981	-36.3060	-36.3060
Longitude	-69.3296	-69.3165	-69.3186	-69.2145	-69.2186	-69.3185	-69.3185
Elevation (MASL)	1723	1848	1774	1534	1517	1811	1811
SiO_2	49.17	49.53	48.67	48.46	48.52	48.96	49.09
TiO_2	1.81	1.91	1.91	1.86	1.84	1.85	1.81
Al_2O_3	16.88	17.48	17.17	16.74	16.95	17.26	17.17
Fe_2O_3	10.55	10.80	10.80	11.16	10.84	10.62	10.63
MnO	0.15	0.15	0.15	0.16	0.16	0.16	0.16
MgO	6.69	6.25	6.54	6.58	6.50	6.29	6.29
CaO	8.94	8.51	9.24	9.10	9.08	9.15	9.14
Na_2O	3.88	3.37	3.62	3.91	4.02	3.65	3.72
K_2O	1.47	1.43	1.46	1.54	1.55	1.51	1.48
P_2O_5	0.46	0.44	0.43	0.48	0.49	0.53	0.48
V	225	233	249	225	231	212	214
Cr	239	187	197	218	213	158	165
Ni	104	80.4	95.1	96.0	92.6	67.5	67.5
Cu	48.9	34.7	40.5	44.1	49.4	45.7	48.1
Zn	56.6	56.3	58.8	58.7	58.2	90.3	91.5
Ga	19.6	21.0	21.0	20.0	20.5	21.4	20.7
Rb	29.6	32.4	30.7	31.2	32.3	32.5	32.7
Sr	548	734	749	617	661	687	647
Y	19.8	22.6	22.8	23.9	24.5	26.9	27.0
Zr	180	228	213	202	212	208	204
Nb	19.9	24.7	23.5	22.0	23.1	22.8	21.8
Cs	1.14	1.31	1.23	1.19	1.20	N/A	N/A
Ba	319	390	389	345	362	351	335
Sc	24.9	27.3	27.6	25.6	25.5	21.9	21.9
La	18.6	21.1	20.6	22.7	23.7	26.2	23.5
Ce	38.5	43.2	42.8	46.6	48.4	54.7	48.5
Pr	4.90	5.48	5.50	5.85	6.14	6.92	6.21
Nd	21.4	23.6	24.0	25.0	26.4	29.8	26.5
Sm	4.94	5.39	5.69	5.85	5.96	6.52	5.96
Eu	1.54	1.77	1.82	1.83	1.88	2.14	1.93
Gd	4.35	5.11	5.24	5.44	5.83	6.63	6.03
Tb	0.70	0.81	0.85	0.88	0.91	0.90	0.82
Dy	3.87	4.57	4.64	4.91	4.97	5.35	4.94
Ho	0.75	0.92	0.88	0.96	0.96	0.97	0.90
Er	2.15	2.46	2.40	2.58	2.62	2.80	2.61
Tm	0.29	0.34	0.33	0.35	0.35	0.35	0.33
Yb	1.91	2.16	2.21	2.26	2.32	2.39	2.26
Lu	0.27	0.33	0.31	0.34	0.33	0.35	0.33
Hf	4.20	5.52	5.18	4.95	5.07	N/A	N/A
Ta	1.16	1.55	1.44	1.38	1.45	1	1.7
Pb	4.81	5.37	4.92	4.74	5.45	5.7	5.6
Th	3.77	4.45	4.13	4.43	4.58	3.24	2.82
U	1.17	1.21	1.10	1.17	1.19	1.00	0.87

4.4.4. U-series isotopes

The results from the U-series analysis indicate that Santa Maria lavas show restricted Ra concentrations, from 393 to 431 fg/g (Table 4.2). The Th and U contents range from 2.42 to 3.77 ppm and 0.75 to 1.17 ppm, respectively. Sample PY-4, corresponding to a basaltic bomb from Pampas Negras (a location within the Payún Matrú volcanic field), has lower Ra, Th and U concentrations (269 fg/g 1.64 and 0.5 ppm respectively). The (^{230}Th/^{232}Th) and (^{238}U/^{232}Th) activity ratios have a restricted range from 0.92 to 0.95 and from 0.91 to 0.94, respectively (Table 4.2). These values are typical of intraplate volcanism (such as ocean island basalts; OIB) or mid-ocean ridge basalts, which tend to show a shift to the left of the equiline in a (^{238}U/^{232}Th) vs (^{230}Th/^{232}Th) diagram (Figure 4.6; Lundstrom, 2003), while convergent margins generally show a shift to the right of the equiline as a ^{238}U excess is associated with fluid addition from dehydration of the subducting slab (Turner et al., 2003). The (^{230}Th/^{238}U) ratios for our samples range from 0.98 to 1.02, close to secular equilibrium (Table 4.2). The (^{234}U/^{238}U) ratios also show little deviation from secular equilibrium except for sample SM7 that shows ^{234}U/^{238}U of 1.034 ± 0.006 (Table 4.2). A deviation of (^{234}U/^{238}U) from secular equilibrium can be indicative of low-temperature sample alteration; however, petrographic observations suggest that the sample is unaltered as neither secondary mineralisation nor alteration was detected. The (^{226}Ra/^{230}Th) activity ratios range from 1.11 to 1.58 (Table 4.2), which is similar to the range observed in intraplate settings (such as OIB ≤ 1.7; based on values from Hawaii and the Canary Islands from Sims et al., 1999 and Lundstrom et al., 2003, respectively). The (^{226}Ra/^{230}Th) from the Santa Maria samples are positively correlated with Nb/U, Rb/Th, Ba/Th, Nb/Th and Zr/U while it is negatively correlated with Th (Figure 4.6), with sample SM10 having the highest Th content and the lowest activity ratio. The measured activity ratios represent the minimum values as the eruption ages are unknown. Therefore, the following discussion is not focused on range of values measured, but rather in accounting for the origin of the ^{226}Ra excess.

Table 4.2. U-Th-Ra disequilibria for Santa Maria volcano and Pampas Negras (PY-4).

Sample	[Ra] (fg/g)	(^{230}Th/^{232}Th)[a]	(^{238}U/^{232}Th)[b]	(^{230}Th/^{238}U)[c]	(^{234}U/^{238}U)[d]	(^{226}Ra/^{230}Th)[e]
SM3	422	0.929	0.907	1.024	1.004	1.260
SM4	393	0.928	0.943	0.984	1.009	1.578
SM7	409	0.946	0.932	1.015	1.034	1.282
SM10	431	0.925	0.938	0.986	1.013	1.115
VRE51	411	0.927	0.941	0.985	1.007	1.224
VRE52	410	0.920	0.942	0.977	1.011	1.422
PY-4	268	1.027	0.930	1.104	1.013	1.438

[a] Based on λ_{230}= 9.158 x 10^{-6} yr^{-1} and λ_{232}= 4.948 x 10^{-11} yr^{-1} , errors range from 0.1% to 0.4%
[b] Based on λ_{238}= 1.551 x 10^{-10} yr^{-1}, errors range from 0.5% to 1.8%
[c] Errors range from 0.5% to 1.8%
[d] Based on λ_{234}= 2.826 x 10^{-6}, errors range from 0.2% to 0.6%
[e] Based on λ_{226}= 4.332 x 10^{-4}, errors range 0.3% to 2.7% (SM4)

4.5. Discussion

4.5.1. Geochemistry of the Santa Maria Volcano

The Santa Maria volcano has been investigated in the context of its geochemistry in order to better understand the processes that have contributed in forming this young (<8 ka) basaltic flow. The geochemistry of its lavas indicates that they are enriched in the most incompatible elements and its composition is intermediate to that of average OIB and LCC (Figure 4.4). Furthermore, the composition of Santa Maria lavas is similar to that of the local intraplate field (Figure 4.5b, c, d, and e) represented by the OIB-like Río Colorado volcanic field (Søager et al., 2013). The samples have high contents of High Field Strength Elements (HFSE) comparable to that described in Chapter 2, for Los Volcanes group. Furthermore, the intermediate composition of the samples to that of Río Colorado and an average LCC suggest characteristics of intraplate magmatism with possible lower crust assimilation in order to reduce the Nb and Ta and increase Pb (Figure 4.5b, d, e). Assimilation of LCC has been previously suggested to be involved at the Payún Matrú volcanic field (Søager et al., 2013, Chapter 2), including a high LCC assimilation in the Nevado volcanic field (Søager et al., 2013). However, the topic of lower continental crust assimilation is uncertain, as most of the signatures between lower continental crust and the volcanic arc are similar. Therefore, it is here proposed that the source can be affected by some lower crustal assimilation; however, a slight influence from the volcanic arc cannot be fully ruled out.

4.5.2. U-series

The general geochemistry of Santa Maria volcanic rocks suggests an intraplate signature modified by lower crustal assimilation as determined in Section 4.5.1. In Section 4.4.4, we have established that activity ratios are characteristic of intraplate volcanism, in agreement with trace-element compositions. In addition, samples are also characterised by ^{226}Ra excess. This excess can have several potential origins, which are reviewed in the following section.

4.5.2.1. Hydrothermal alteration and crustal assimilation

Hydrothermal activity can produce radioactive disequilibrium. This generally involves the addition of fluid-mobile U to the magma, resulting in ($^{238}U/^{232}Th$) and ($^{230}Th/^{238}U$) activity ratios being negatively correlated (Villemant et al., 1996). This negative correlation should be accompanied by petrographic observations of glass in the matrix and a decrease in arsenic between the host lava and enclaves of altered glass (Villemant et al., 1996). Villemant et al. (1996) proposed that ^{238}U-^{230}Th disequilibrium in lavas from the Lesser Antilles could be accounted for, by either magma mixing or interaction with hydrothermal fluids. In our case, the Santa Maria rocks are characterised by only small ^{238}U-^{230}Th disequilibrium and restricted ranges for ($^{230}Th/^{232}Th$), ($^{238}U/^{232}Th$), ($^{230}Th/^{238}U$) (Figure 4.6 a,b) and Th/U ratios. Thus, it is unlikely that hydrothermal activity plays a significant role in the U-series isotope composition of these lavas. This is supported by petrographic observations, which do not indicate hydrothermal

alteration, as there are no secondary phases present, on the rim of phenocrysts. In addition, low SO_3 concentrations further support the lack of significant hydrothermal activity.

Upper crust assimilation results in low to negligible U-series isotopic disequilibrium (Berlo et al., 2004); nevertheless, it is here briefly examined. Upper crust assimilation should incur in an increase in $^{87}Sr/^{86}Sr$ ratios in the magma. Santa Maria lavas show a restricted range of low $^{87}Sr/^{86}Sr$ values (0.703861 to 0.703867) arguing for little to no upper crust assimilation. Accordingly, hydrothermal alteration and upper crust assimilation are likely to be minor processes among the Santa Maria rocks.

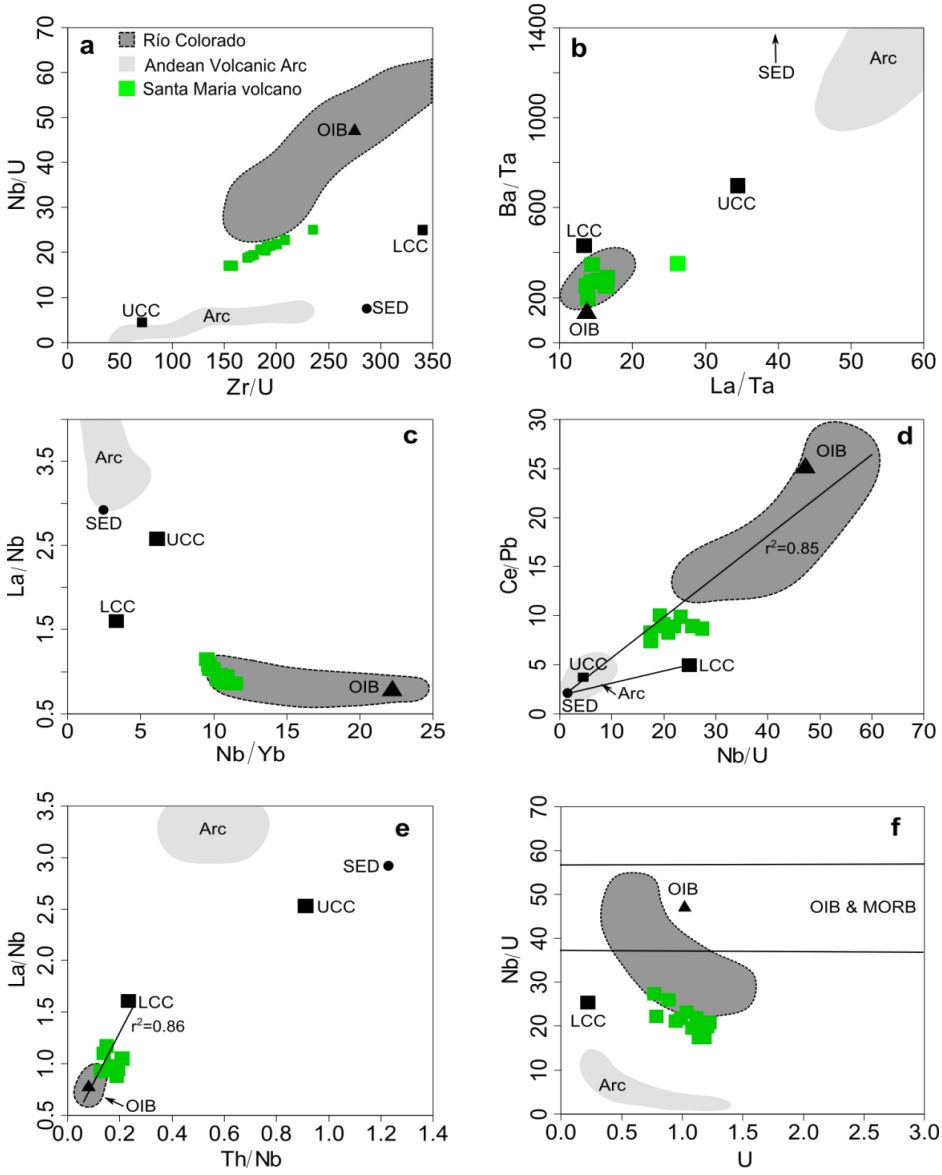

Figure 4.5. Trace-element ratios. a) Zr/U vs Nb/U, b) La/Ta vs Ba/Ta, c) Nb/Yb vs La/Nb, d) Nb/U vs Ce/Pb, e) Th/Nb vs La/Nb and f) Nb/U vs U concentration (ppm). The ocean island basalt (OIB) composition is from Sun and McDonough (1989). The upper (UCC) and lower continental crust (LCC) compositions are from Rudnick and Gao (2003). The sediment (SED) end-member is from Jacques et al., 2013. The OIB and MORB ranges in (f) are from Hofmann et al. (1986). Same reference for the average arc value and Río Colorado field as in Figure 4.4.

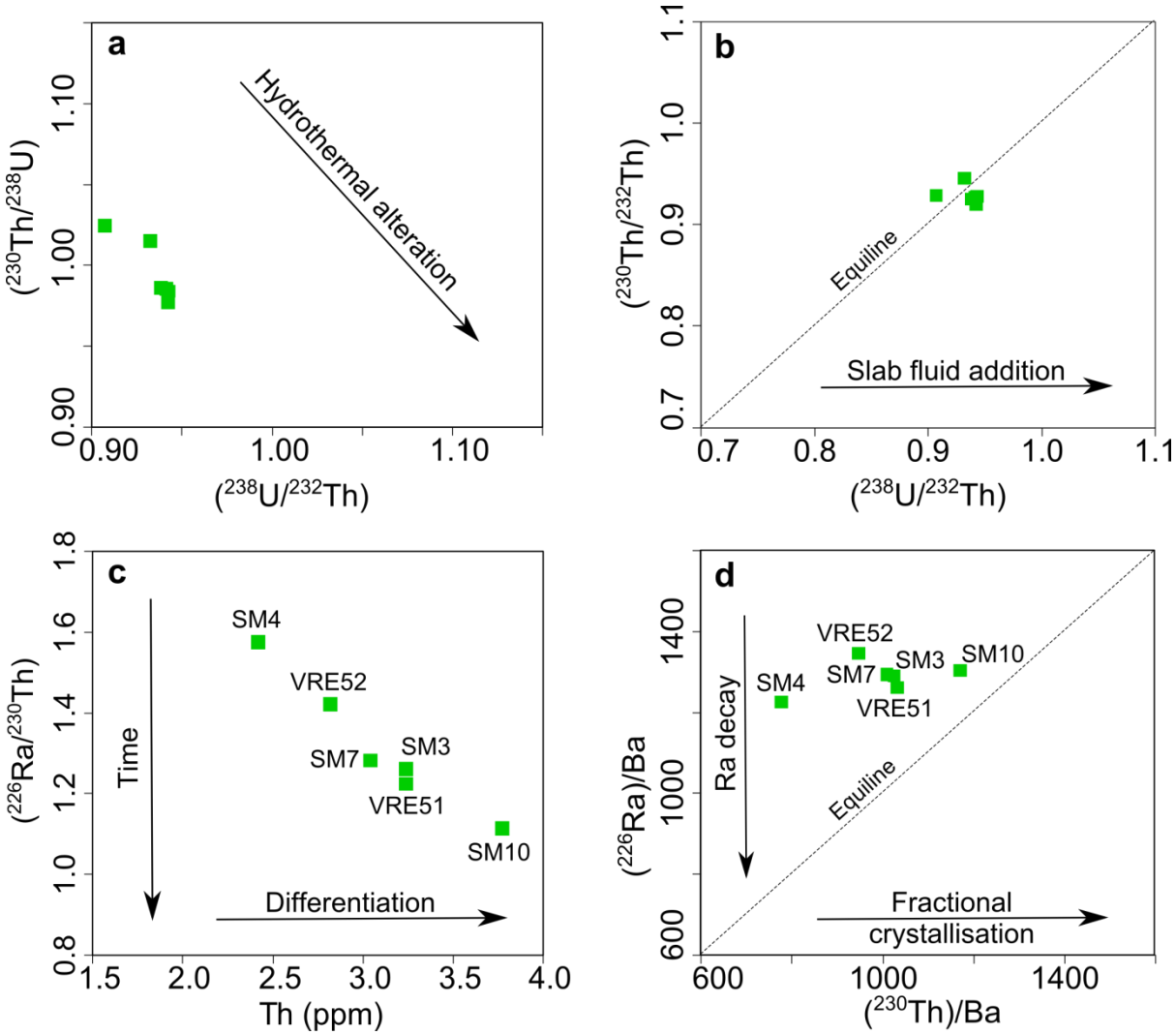

Figure 4.6. U-Th-Ra disequilibria. a) ($^{238}U/^{232}Th$) vs ($^{230}Th/^{238}U$); b) ($^{238}U/^{232}Th$) vs ($^{230}Th/^{232}Th$); c) Th (ppm) vs ($^{226}Ra/^{230}Th$) and d) (^{230}Th)/ Ba vs (^{226}Ra)/Ba (in dpa/g). The equiline, represents secular equilibrium between the parent and the daughter isotope. The arrows indicate the effects of different processes on lavas. Differentiation represents the change in composition while fractional crystallisation is a process to create differentiation. Note that the ^{226}Ra excess has not been corrected for the decay since eruption, as eruption ages are unknown.

4.5.2.2. Magma chamber differentiation

Uranium, Th and Ra are strongly incompatible therefore, accumulation of mafic minerals such as olivine is not capable of affecting the ($^{226}Ra/^{230}Th$), ($^{230}Th/^{232}Th$), ($^{238}U/^{232}Th$) and ($^{230}Th/^{238}U$) ratios. For instance, Vigier et al. (1999) showed that as much as 30% of plagioclase accumulation results in only a slight decrease in ($^{226}Ra/^{230}Th$).

The Santa Maria volcanic rocks have a common magmatic source as indicated from the consistent ($^{230}Th/^{232}Th$) and $^{87}Sr/^{86}Sr$ ratios values (proxy from Vigier et al., 1999). Sample PY-4 (from Pampas Negras) from a different area within the Payún Matrú volcanic field, as expected, has different isotopic ratios (Table 4.2), suggesting a different magmatic source;

therefore, it is not further considered. The negative correlation between ($^{226}Ra/^{230}Th$) ratios and Th concentrations characterises a differentiation trend suggesting that these rocks are genetically related (Figure 4.6c). Furthermore, negative correlations between Nb/U and U concentrations (Figure 4.5f) and between Nb/Th and Th concentrations also suggest a co-genetic origin. The negative correlation inferred for several elemental ratios starts with sample SM4 having the lowest Th and U and concludes with sample SM10 (Figure 4.5a and 4.6c, d) also agreeing with a differentiation in the magma chamber. The horizontal trend in Figure 4.6d is best explained by differentiation over timescales shorter than a few thousand years, such that the ^{226}Ra excess is preserved (Vigier et al., 1999). While differentiation has modified the ^{226}Ra excess, the most primitive magma displays the largest excess, suggesting a deep origin for the Ra-Th disequilibrium.

4.5.2.3. Slab dehydration

At convergent margins, ^{226}Ra excess is generally associated with dehydration of the subducting slab. However, the inferred depth of the subducting slab beneath the Payún Matrú volcanic field is approximately 220 km (Tassara et al., 2006) and ^{226}Ra excesses are not observed in volcanic rocks where the depth of the slab is greater than 110 km (Turner et al., 2003). Therefore, it is unlikely that the ^{226}Ra excess observed in the Santa Maria volcanic rocks is related to slab dehydration. Furthermore, slab dehydration generally also yields ^{238}U excess, which is not observed here (Figure 4.6b). Finally, alkali basalts erupted in this part of the continental back-arc have been previously described as intraplate (Pasquarè et al., 2008, Bertotto et al., 2009, Germa et al., 2010, Hernando et al., 2012, Jacques et al., 2013, Søager et al., 2013) showing negligible arc signatures (Chapter 2). According to the evidence presented here, it is improbable that the ^{226}Ra excess is related to fluids released from the subducting Nazca plate.

4.5.2.4. Deep magmatic processes

Since the ^{226}Ra excess is produced before differentiation in the crust (Section 4.5.2.2) and it is unlikely to be associated with fluid addition (Section 4.5.2.3), the remaining consideration is that, it is produced during partial melting. The partial melting region has been hypothesised to be at intermediate pressure (approximately less than 3 GPa) based on results from the current contribution and previous geophysical investigations (Gilbert et al., 2006; Burd et al., 2014). Partial melting at approximately less than 3GPa is inferred from small enrichment in ^{232}Th and ^{238}U (Bourdon and Sims, 2003), high K content, and the presence of a proposed thermal anomaly underneath the back-arc at 36°S (~40 km depth) intruding basaltic material into the lower crust (Gilbert et al., 2006). Furthermore, a recent magnetotelluric study in the Payenia Basaltic Province, has proposed that there is magma accumulation below the crust (Burd et al., 2014) which also supports the presence of a magmatic source at intermediate pressures. Furthermore, in a melting model proposed by Søager et al. (2013), similar melting pressures are proposed for the Payún Matrú volcanic field. At these pressures, minerals such as garnet are stable and they are likely to be present during partial melting as also suggested by the REE

spider plot. Furthermore, the La/Yb ration from the Santa Maria are the high (ranging from 9.3 to 10.9), similar signatures in combination with low Yb have been associate with equilibration in the presence of garnet (Kay et al., 2005). It is here inferred that partial melting in the presence if garnet produced the ^{226}Ra excess. U-series isotope and geophysical data suggest that the source of the Santa Maria magma may be located in the lithospheric mantle at depth of approximately 40 km.

In Section 4.5.1, it was inferred that the Santa Maria volcanic rocks exhibit geochemical similarities with an OIB magmatic source. In typical OIB settings, the ($^{226}Ra/^{230}Th$) ratios are relatively low, and attributed to ^{226}Ra decay during ascent through or in the magma chamber (Bourdon and Sim, 2003). The ($^{226}Ra/^{230}Th$) ratios for Santa Maria are only slightly greater than those observed in Hawaii (Sims et al., 1999), which is remarkable considering that the Santa Maria magmas had to traverse a much thicker crust. In addition, it is hypothesised that the magma resided in the magmatic chamber for a short time in order to preserve the high ^{226}Ra excess. Resulting in high magma travel rates which have been estimated to be in the order of 20 - 40 m/a and possibly higher, based on the melts located below the continental crust (40 km) and the high ^{226}Ra excess associated with a short time scale in the range of 2000 to 1000 years, respectively. These fast ascent rates are comparable to previous estimates of 10 -100 m/a in continental settings such as in the Southern volcanic Zone in South America (Sigmarsson et al., 2002). Fast melt transport is better explained by channel flow rather than porous flow. The previously inferred source location in the lithospheric mantle agrees with the channel flow as the brittle lithosphere facilitates channel formation (Kelemen et al., 1997).

4.5.2.5. Partial melting model

The inferred deep magmatic conditions have been used in order to model the magma production under Santa Maria, for this, we used U-series isotopes. We investigate dynamic and chromatographic melting models, to determine which conditions of partial melting best reproduce our data. As shown above, partial melting is likely to occur at intermediate pressures (less than3 GPa) and partition coefficients were chosen accordingly (Table 4.3). The degree of partial melting and the upwelling velocity were taken to be 2% and 5 cm/a, respectively, based on the partial melting range (2 to 5%) proposed by Søager et al. (2013) for the same region and in low mantle upwelling velocities from Sims et al. (1999). Furthermore, Kay et al. (2013) inferred similar pressure and partial melting conditions for the Auca Mahuida volcanic field, in the southern Payenia Basaltic Province. Whether by using partial melting values of 2% or 5%, the final modelled value was not significantly affected. Sets of activity ratios were calculated using different values of porosity: 1, 2, 3 and 4 %. The mineralogy of the source rock was taken to include up to 8% garnet. Partition coefficients were calculated for the following source-rock mineralogy using the modal inputs in Table 4.3.

Table 4.3. Mineral modes and partition coefficients used in partial melting models.

Mineral phase	modal input 1	modal input 2	D_u	D_{Th}	D_{Ra}	Reference
Olivine	56%	50%	0.000059	0.000014	1.00E-06	Stracke et al. (2006)
Orthopyroxene	12%	12%	0.0047	0.0032	1.00E-05	Stracke et al. (2006)
Clinopyroxene	30%	30%	0.018	0.021	5.00E-05	Stracke et al. (2006)
Garnet	2%	8%	0.018	0.0046	0.00E+00	Stracke et al. (2006)

D_u, D_{Th} and D_{Ra} refer to partition coefficients of U, Th and Ra, respectively.

Calculations show that the dynamic melting model yields similar composition to those observed, using mineralogical assemblage (1) or (2) (Figure 4.7). In addition, the Usercalc V2.0 software (Spiegelman, 2000) was used to model U-series isotope composition using the porous-flow melting model applying the same parameters as for the dynamic model. However, the porous-flow melting model approximates the Santa Maria measured values, only at high upwelling velocities (~20 cm/yr) and very low porosity (~0.1%), which are unrealistic. The preferred melting model that closely resembles the conditions below Santa Maria volcano is the dynamic melting of Williams and Gill (1989). Furthermore, the dynamic melting model agrees with fast ascent rates as proposed in Section 5.2.4.

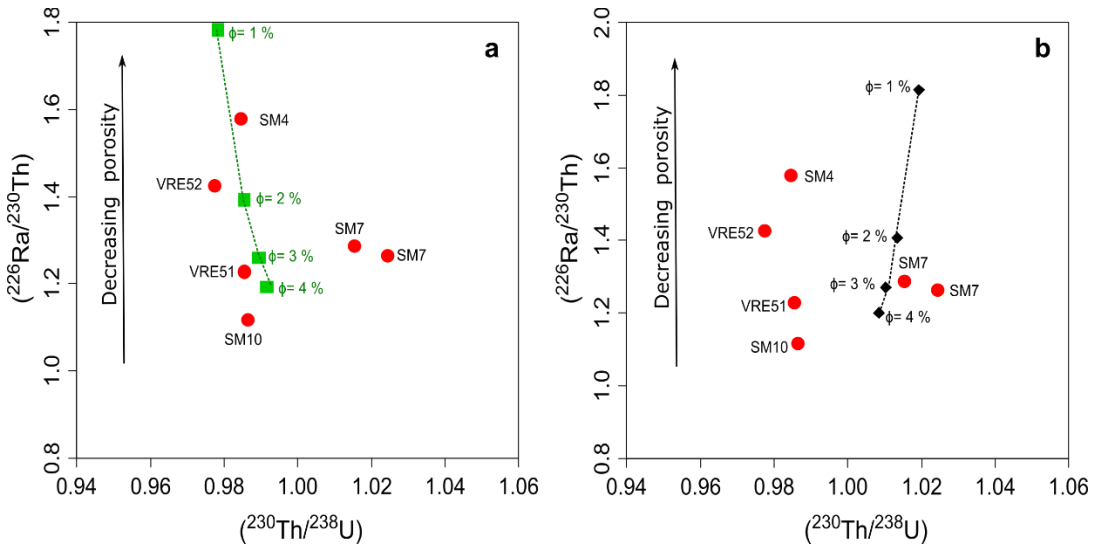

Figure 4.7. Dynamic melting model. a) Using modal input 1 (green squares) and b) Using modal input 2 (black diamonds) corresponding to olivine 56% and 50% respectively, orthopyroxene 12%, clinopyroxene 30% and garnet 2% and 8% respectively. Both were calculated using a 2% constant melting degree and 5 cm/yr constant upwelling rate. The porosity modelled ranges from 1% to 4%. The red dots are the measured U-series data from six lava samples from the Santa Maria volcano.

4.6. Conclusions

The geochemistry of the Santa Maria volcanic rocks has been used to show that the magmatic source has a composition similar to that of an OIB-like mantle, comparable to that of the Payún Matrú volcanic field. Furthermore, trace elements suggest that mantle-derived magmas are possibly affected by lower continental crust assimilation, with no contribution from slab-derived metasomatic fluids.

The lower crustal assimilation has been related with a heat source below the continental crust capable of heating the lower continental crust such as magma ponding (Figure 4.8). The melting source for the Santa Maria volcano has been located at intermediate pressures such as at lithospheric mantle depth. In order to model the U-series disequilibrium measured, a dynamic melting model was used. Considering a low degree of partial melting (2%) at intermediate pressures and a source rock containing garnet, it is possible to reproduce observed activity ratios, for porosity values between 1 and 4%.

A differentiation trend has been inferred for the magmatic chamber of the Santa Maria volcano, however, this process is not capable of accounting for the high ^{226}Ra excess. Fluid addition can neither explain the high ^{226}Ra excess over ^{230}Th, therefore it is attributed to deep magmatic processes in this case, partial melting. One of the most interesting features of the high ^{226}Ra excess is that the magma transport rate has to be fast in order to preserve ^{226}Ra excess during transit of a 40 km-thick crust. An estimate of high velocity transport rate, in the range of 20 to 40 m/a is been proposed, associated with a channelised flow.

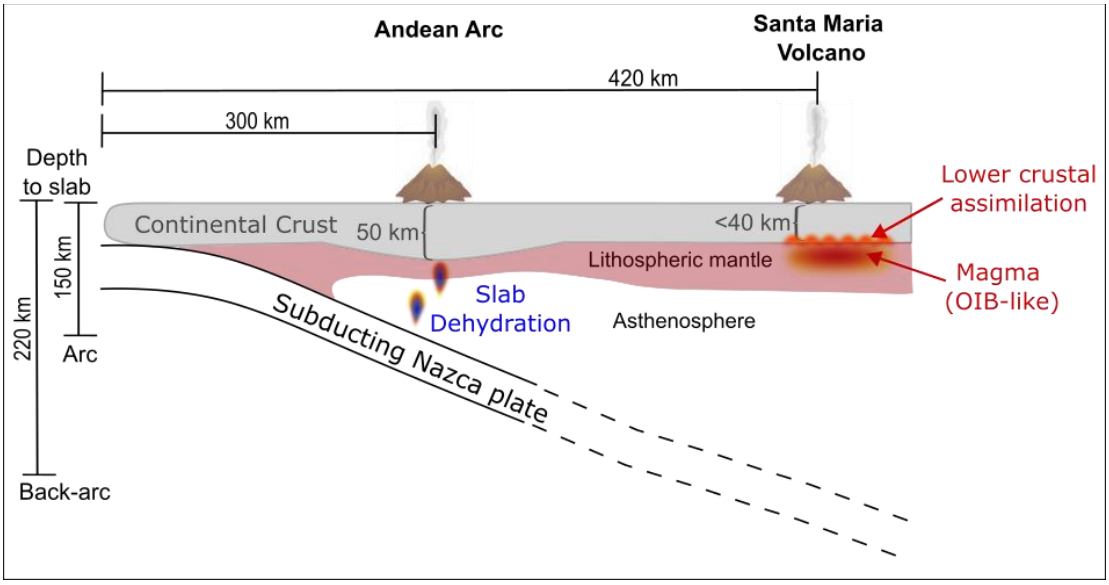

Figure 4.8. Simplified graphical representation of the magmatic source below the Santa Maria volcano including the Andean arc magmatic source for comparison. The continental back-arc is here represented by the Santa Maria volcano. Magma ponded below the continental crust has an OIB-like composition. The lithosphere-asthenosphere boundary (LAB) is located at a depth of approximately 60 km. The subducting plate is located approximately 150 km below the Andean arc and approximately 220 km below the continental back-arc. The Nazca plate subducts at 7-8 cm/yr.

Chapter 5:

Chronology of Quaternary volcanism in the continental back-arc from southern Mendoza, Argentina

Venera R. Espanon [a,b], Allan R. Chivas[a], Masahiko Honda[c], David Phillips[d], Erin L. Matchan[d] and David M. Price[a]

[a] *GeoQuest Research Centre, School of Earth & Environmental Sciences, University of Wollongong, NSW 2522, Australia.*

[b] *Wollongong Isotope Geochronology Laboratory, School of Earth & Environmental Sciences, University of Wollongong, NSW 2522, Australia*.

[c] *Research School of Earth Sciences, The Australian National University, Canberra, ACT 0200, Australia.*

[d] *School of Earth Sciences, The University of Melbourne, Parkville, VIC 3010, Australia*

Allan R. Chivas: toschi@uow.edu.au

Masahiko Honda: masahiko.honda@anu.edu.au

David Phillips: dphillip@unimelb.edu.au

Erin L. Matchan: ematchan@unimelb.edu.au

David M. Price dprice@uow.edu.au

Abstract

The Quaternary Payenia Basaltic Province (PBP) in southern Mendoza covers an area of approximately 40000 km^2 and is characterised by intraplate, Ocean Island Basalts-like (OIB-like) geochemical signatures. In the current contribution nine new radiometric ages are presented, six correspond to the late Pleistocene and three to the Holocene from a combination of surface exposure dating, $^{40}Ar/^{39}Ar$ and thermoluminescence dating methods. The surface exposure ages obtained using cosmogenic ^{3}He and ^{21}Ne are in good agreement with previous publication and confidently suggest that part of this basaltic province was active at least 4000 years ago (taking a conservative approach). The additional Quaternary ages here presented in combination with the geochemical data inferred from the previous three chapters as well as from previous publication have been used in order to reconstruct the evolution of this basaltic province.

During the Pleistocene an arc-like signature was evident in the north eastern part (Nevado volcanic field) of Payenia Basaltic Province while at the same time OIB-like volcanism was occurring in the southern part (Río Colorado volcanic field) of this basaltic province. The arc-like signature decreased during the Pleistocene as evidenced by a reduction in Ba/La and La/Ta from ~1.5 Ma to ~0.7 Ma in the Nevado volcanic field, while a similar trend is inferred for the Llancanelo volcanic field. The Holocene volcanism is restricted to the western side of the Payún Matrú volcanic field and is dominated by OIB-like signatures such as high Ta/Hf and low Ba/La and La/Ta. This contribution confirms that two different types of volcanism occurred simultaneously during the Pleistocene, arc-like in the northern part and OIB-like in the south, while the Holocene volcanism is OIB-like and is restricted to a small area.

5.1. Introduction

The volcanism in southern Mendoza, Argentina, is linked to the subducting Nazca plate to the west of South America and with a diverse slab influence (arc-like signature) recorded in the magmas erupted in the continental back-arc. It has been suggested that the sources of slab influence in the Payenia Basaltic Province (PBP) are related to mantle-wedge metasomatism by slab dehydration (Stern et al., 1990; Kay et al., 2006a; Bertotto et al., 2009), slab partial melts (Jacques et al., 2013) and/or by sediments transported by the slab (Søager et al., 2013; Chapter 2). Furthermore, it has also been proposed that some portions of this basaltic province have a negligible arc influence (Kay et al., 2004; Søager et al., 2013; Chapter 2) and that these have a typical intraplate geochemical signature, associated with asthenospheric upwelling (Kay et al., 2004; Germa et al., 2010). The geochemistry of this basaltic province is diverse and it has been broadly linked to its chronological evolution, in which, three periods have been recognised (Kay et al., 2006a and b; Kay and Copeland, 2006; Dyhr et al., 2013a). The first characterised by early Miocene volcanism showing no slab influence, corresponding to La Mantancilla, Huantraico and Cerro Fortunoso areas (Figure 5.1). The second period corresponds to the late Miocene (~8-5 Ma) Chachahuén (Figure 5.1) volcanism having arc-like signatures up to 500 km from the trench, corresponding to a period of shallow subduction (Kay et al., 2006b). Arc-like volcanism in the late Miocene has also been recognised by Dyhr et al, (2013a) in the Sierra de Palaoco (Figure 5.1). During the last period, the subducting slab returned to a steeper subducting angle (~25°) in the latest Miocene to early Pliocene and the Quaternary volcanism is mainly dominated by intermediate arc-like to intraplate and intraplate signatures.

In the last few years several publications have provided detailed chronological records confirming the age span of this basaltic province using radiometric age constrains. More than 100 new ages have been obtained in the last 8 years from the Payenia Basaltic Province; hence, providing a good overview of the geochronology and providing means to better understand the evolution of this basaltic province. Nevertheless, the temporal link with the geochemistry after the steepening of the slab is not well constrained. Furthermore, most of the radiometric ages correspond to the Pleistocene (Llambías et al., 2010), while Holocene radiometric ages are scarce, as they are difficult to resolve by conventional dating methods. We present nine new Quaternary ages from several methods including, surface exposure dating using cosmogenic ^{3}He and ^{21}Ne, ^{40}Ar/^{39}Ar, and thermoluminescence. Accordingly, the purpose of this investigation is to establish a correlation between the geochemical signatures and timescales of Quaternary volcanism in the PBP.

5.2. Geological timeframe and geographical setting

Evidence for continental back-arc volcanism is found in southern Mendoza ranging from the Miocene, especially in the Chachahuén region, to the Quaternary, such as in the Payenia Basaltic Province (PBP). The PBP constitutes the northernmost back-arc basaltic province of the Patagonian basaltic provinces, in South America. It is characterised by Quaternary basaltic

volcanism, with Miocene basaltic rocks outcropping in the Sierra de Chachahuén, La Matancilla, Sierra de Palaoco and Cerro Fortunoso areas (Figure 5.1). Pliocene volcanism appears less abundant, with some exposures in the Chachahuén area with ages of 4.7 ± 0.4 Ma (Kay et al., 2006b), in the southern Nevado volcanic field with ages of 4.03 ± 0.16 Ma and 2.83 ± 0.04 Ma (Gudnason et al., 2012; Dyhr et al., 2013b), Río Grande 2.83 ± 0.04 Ma (Dyhr et al., 2013a) and Tromen region 4.0 ± 0.4 Ma (Kay et al., 2006a). The Pliocene represents the transition period from the late Miocene shallow subduction associated with an arc-like composition to the steepening of the slab (~5 - 2.5 Ma; Kay et al., 2006a), therefore the older samples have a more clearly defined arc-like composition. During the late Pliocene, the arc influenced volcanism in the back-arc migrated from east to west, from the Nevado volcanic field (Figure 5.1) to the Río Grande valley (Dyhr et al., 2013a) which is the basis for the slab-rollback hypothesis (Folguera et al., 2009; Gudnason et al., 2012).

Abundant Quaternary volcanism has been recognised and described in the Payenia Basaltic Province (Bermudez and Delpino, 1989; Kay et al., 2004; Bertotto et al., 2009; Germa et al., 2010; Gudnason et al., 2012; Jacques et al., 2013; Søager et al., 2013; Chapter 2) with intraplate geochemical signatures with some areas showing influence from slab-related components. The chronological evolution of the PBP is from east to west with the older flows in the eastern part, mostly mid to late Pleistocene, while the western part also has Holocene volcanism. The current investigation utilises the sub-division proposed by Gudnason et al, (2012) for the Quaternary volcanism in southern Mendoza. The five volcanic fields are Nevado, Llancanelo, Northern segment, Payún Matrú and Río Colorado (Figure 5.1). The volcanic evolution of the Nevado volcanic field follows a south to north (Gudnason et al., 2012) trajectory with the older flows in the southern part of the volcanic field while the younger volcanic eruptions are in the northern area. The northern segment was active during the mid to late Pleistocene (1.16 ± 0.07 Ma to 0.054 ± 0.006 Ma, Folguera et al., 2009) and coincides with the migration of the volcanism from the southern to the northern Nevado volcanic field and then to the northern segment, having both a is similar arc-related signatures (Søager et al., 2013).

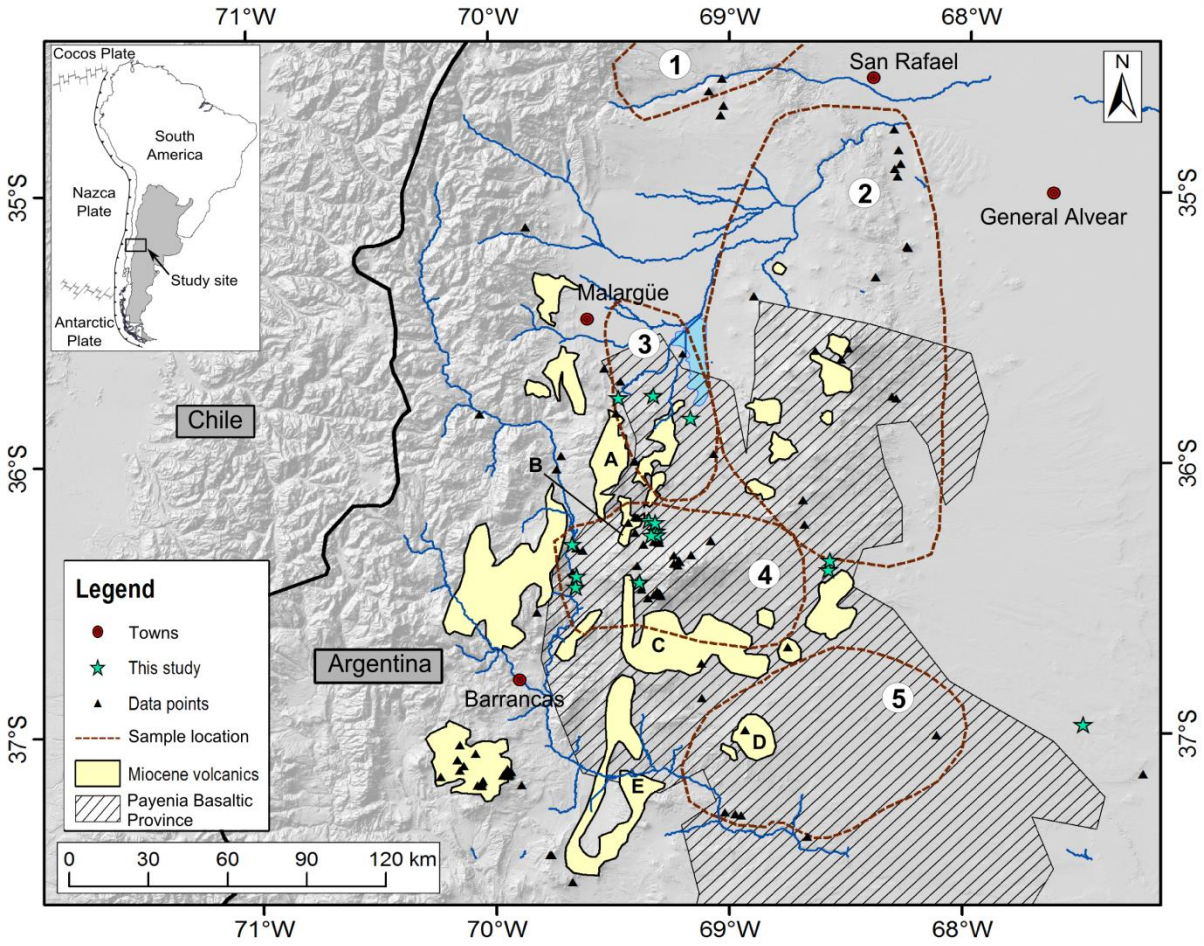

Figure 5.1. Geographical setting of the southern Mendoza continental back-arc volcanism. The striped area corresponds to the Payenia Basaltic Province (modified after Kay et al., 2007). The dashed lines correspond to volcanic fields in the back-arc, 1) Northern segment, 2) Nevado volcanic field, 3) Llancanelo volcanic field, 4) Payún Matrú volcanic field and 5) Río Colorado volcanic field (modified after Gudnason et al., 2012). The yellow areas correspond to Miocene volcanism (after Dyhr et al., 2013a), named as A) Palaoco, B) Cerro Fortunoso, C) La Matancilla, D) Sierra de Chachahuén and E) Huantraico. The black triangles are sample locations taken from several publications (Melchor and Casadío, 1999; Kay et al., 2006a; Folguera et al., 2009; Quidelleur et al., 2009; Germa et al., 2010; Gudnason et al., 2012; Dyhr et al., 2013a; Dyhr et al., 2013b; Espanon et al., 2014a; Hernando et al., 2014a; Marchetti et al., 2014; Chapter 3).

The Llancanelo volcanic field is dominated by Pleistocene volcanism (with the exception of the Miocene volcanism in the Palaoco region described by Dyhr et al., 2013a). A basaltic flow from the Trapal volcano, from the Llancanelo volcanic field has been dated to 0.395 ± 0.068 Ma (1σ) using $^{40}Ar/^{39}Ar$ (Espanon, 2010). Recently Gudnason et al. (2012) dated two basaltic flows also from the Llancanelo volcanic field using $^{40}Ar/^{39}Ar$ to 0.16 ± 0.07 Ma (2σ) and 0.28 ± 0.02 Ma (2σ). Furthermore, cosmogenic ^{21}Ne dating of a basaltic tumulus has been used to suggest that the previously mentioned volcanic field was active ~ 50 ka (Espanon et al., 2014a). The Quaternary geochronology of the Payún Matrú volcanic field is better constrained (Quidelleur et al., 2009; Germa et al., 2010; Espanon et al., 2014a; Marchetti et al., 2014) with ages ranging

from 1.716 ± 0.025 Ma (Quidelleur et al., 2009), to <2 ka (Marchetti et al., 2014). Most of the chronology of the Payún Matrú volcanic field points to semi-continuous volcanic activity from the mid Pleistocene to recent times. Holocene volcanic events in the Payenia Basaltic Province are mostly present in the Payún Matrú volcanic field with some events estimated to be younger than <2 ka; however, no reliable radiometric ages have been reported for the last 2000 years.

The Río Colorado volcanic field (RCVF) was emplaced where the Miocene Chachahuén volcanic complex was located (Figure 5.1). Nevertheless, in this contribution the Río Colorado volcanic field refers only Quaternary volcanism having a geochemical signature closely associated with ocean island basalts (OIB) (Søager et al., 2013), while the Miocene volcanism with arc-like signatures (Kay et al., 2006b) is referred to as Sierra de Chachahuén. The RCVF activity ranges from 1.54 ± 0.13 Ma to 0.34 ± 0.13 Ma (Gudnason et al., 2012).

5.3. Methods

5.3.1. Surface exposure dating

Surface exposure dating was performed on eight samples from lava flows with primary flow morphologies (Table 5.1, Figure 5.2). The method assumes that the sample is part of the original lava flow upper surface, and that since eruption, the sample has been accumulating terrestrial cosmogenic nuclides (TCN) in this case ^{3}He and ^{21}Ne by interacting with cosmic rays. As cosmogenic ^{3}He and ^{21}Ne are stable, the concentration of the cosmogenic nuclides is directly proportional to the time since exposure at the Earth's surface. The samples were carefully selected in order to prevent any cover, while the topographic shielding is negligible at all sampling sites. The orientation of each sample was recorded, and in the laboratory, samples were carefully dissected so that only the upper 5 cm of each sample was used to perform the analysis as cosmic-ray penetration decreases exponentially with depth (Lal, 1991). The material was crushed and sieved to 355 – 212 µm and to 212 – 180 µm, washed with distilled water prior to magnetic separation and the olivine-concentrate portion was purified using density separation (methylene iodide with a density of 3.33 g cm^{-3}). The final olivine separate was inspected under a binocular microscope to remove impurities such as clinopyroxene, spinel, hornblende and composite grains. Finally the olivine separates were washed ultrasonically twice in an ethanol-acetone 50:50 mixture for 15 minutes followed by a final wash with ethanol.

A portion of each olivine separate (~0.4 g) was analysed for major-element contents using a Spectro Xepos energy dispersive polarisation X-ray spectrometer at the School of Earth and Environmental Sciences at the University of Wollongong (Supplementary Table 5.1A). Li, Th and U were analysed by digesting (0.1g) of olivine separate in a HF-HNO_3 mixture and measured using an Agilent 7500cs ICP-MS at the above institution.

Table 5.1. Geographical location and dating methods used for samples collected from the Payún Matrú (PMVF) and Llancanelo volcanic fields (LLVF).

Sample	Location	Latitude °S	Longitude °W	Elevation (masl)	Dating method
VRE46	Pampas Onduladas flow, PMVF	-36.9712	-67.4923	447	SED
VRE21	Pampas Onduladas flow, PMVF	-36.3732	-68.5754	1268	SED
VRE42	S of Carapacho volcano, LLVF	-35.8487	-69.1620	1344	SED
VRE7	Cueva del Tigre, LLVF	-35.7649	-69.3196	1487	SED
VRE9	Malacara volcano, LLVF	-35.7722	-69.4659	1670	$^{40}Ar/^{39}Ar$
RG1	Río Grande, PMVF	-36.4719	-69.6500	1124	$^{40}Ar/^{39}Ar$
RG2	Río Grande, PMVF	-36.4722	-69.6502	1110	$^{40}Ar/^{39}Ar$
RG8	Río Grande, PMVF	-36.4314	-69.6461	1225	TL
RG11	Río Grande, PMVF	-36.4315	-69.6461	1228	$^{40}Ar/^{39}Ar$
VRE12	La Pasarela, PMVF	-36.3142	-69.6634	1218	SED
SM4	Santa Maria Volcano, PMVF	-36.2674	-69.3080	1635	SED
SM7	Santa Maria Volcano, PMVF	-36.2802	-69.3049	1660	SED
SM10	Santa Maria Volcano, PMVF	-36.2814	-69.3296	1723	SED
SM14	W side of Santa Maria flow, PMVF	-36.2270	-69.3393	1620	$^{40}Ar/^{39}Ar$
SM17	W side of Santa Maria flow, PMVF	-36.2357	-69.3122	1596	$^{40}Ar/^{39}Ar$
SM18	W side of Santa Maria flow, PMVF	-36.2353	-69.3133	1580	$^{40}Ar/^{39}Ar$
LV6	La Calle flow, PMVF	-36.4541	-69.3812	2224	$^{40}Ar/^{39}Ar$

Geographical coordinates WG84 datum
SED refers to Surface Exposure Dating
TL refers to Thermoluminescence

Noble gas abundance and isotopic composition were measured at the Research School of Earth Sciences at the Australian National University. Olivine separates (>2 g, except sample VRE42 crushed, Supplementary Table 5.1B) were wrapped in tin foil and loaded into a sample holder, the samples were then dropped into the tantalum furnace on-line to a VG5400 noble gas mass spectrometer. Noble gases were extracted at two step-heating temperatures of 700°C and at 1800°C. All data were corrected for isobaric interferences, analytical blanks and mass discrimination (Espanon et al., 2014a). The uncertainties correspond to a 1σ confidence level. A vacuum crushing experiment was performed on sample VRE42 using 2.2 g of olivine separate.

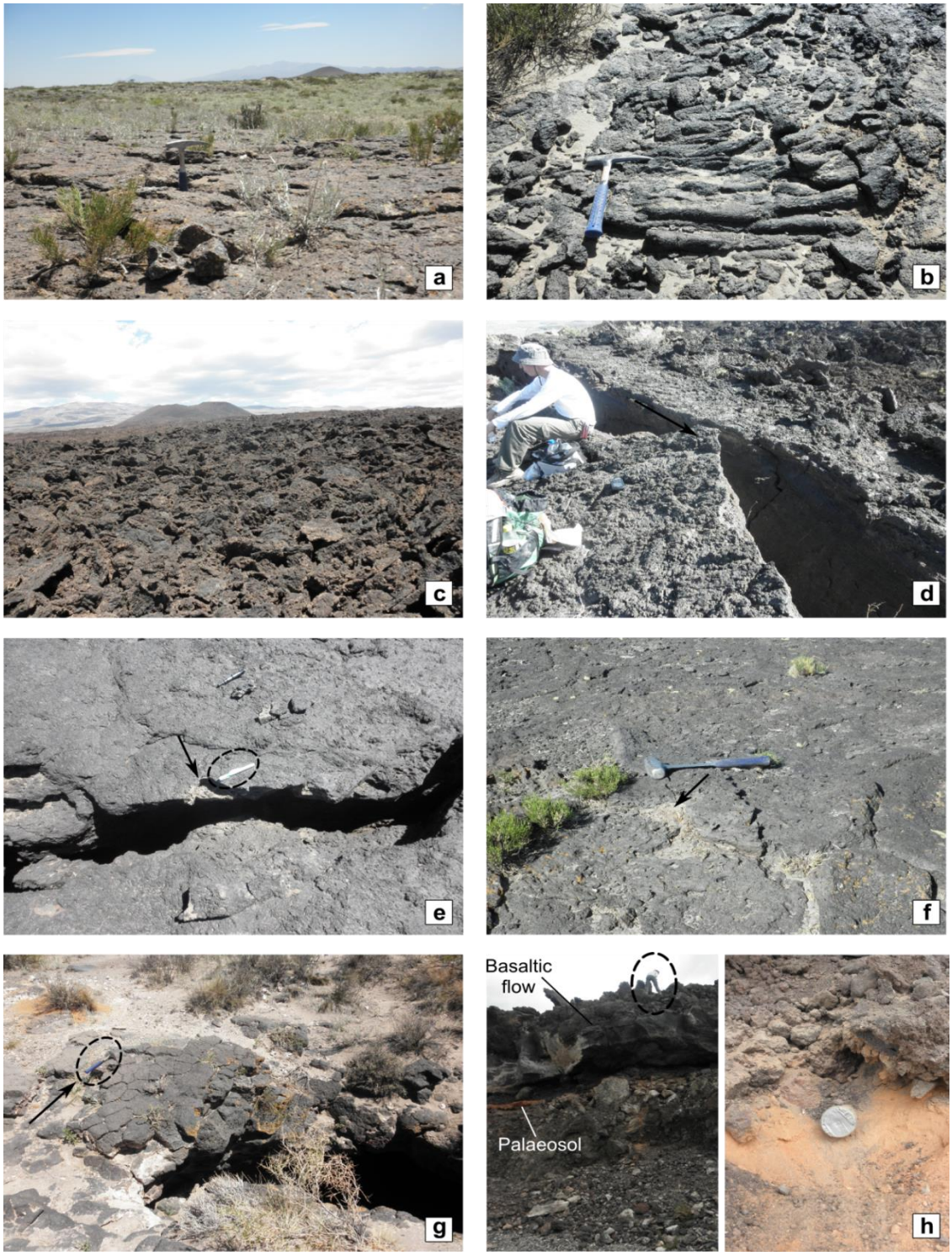

Figure 5.2. Field images of selected sampling sites. a to g are lavas with primary flow morphology. a) VRE 21 Pampas Onduladas flow; b) VRE12 La Pasarela, note the ropy surface typical of a pahoehoe flow; c) sample SM10 from the inner part of the Santa Maria flow; note this flow has a typical a'a morphology; d) sample SM7 Santa Maria flow, note person for scale; e) sample SM4 was collected from the inner part of Santa Maria flow, note pen for scale (~ 13 cm); f) sample VRE42, south of Carapacho volcano and g) sample VRE7 from the entrance to Cueva del Tigre lava tube in the Llancanelo volcanic field. Note the geological hammer (~32 cm) for scale in a), b), f) and g). h) Thermoluminescence palaeosol sampling point (RG8) and overaying basaltic flow corresponding to sample RG11.

5.3.2. $^{40}Ar/^{39}Ar$ dating

Radiometric $^{40}Ar/^{39}Ar$ dating of basaltic groundmass was performed on 8 samples from the Payún Matrú and Llancanelo volcanic fields (Supplementary Tables 5.2A to 5.2D). The samples were prepared using the procedure of Matchan and Phillips (2014). Approximately 300 g of whole-rock sample were crushed and sieved to isolate the 180-250 µm grain-size fraction. The phenocrysts were separated from the groundmass by magnetic separation and the groundmass separate was washed with 5% HNO_3, de-ionised water and acetone. The groundmass portions and a radiation flux monitor standard (Alder Creek Rhyolite sanidine, 1.186 ± 0.012 Ma (1σ); Turrin et al. (1994)) were sent to the USGS TRIGA reactor, to be irradiated at 0.5 MWH in the Cd-lined facility. After irradiation and conversion of ^{39}K to ^{39}Ar, approximatelly 100 mg of sample was loaded into a copper holder and analysed at the School of Earth Sciences at the University of Melbourne. The analysis was conducted using a multi-collector Thermo Fisher Scientific ARGUSVI mass spectrometer, connected to a gas extraction and purification line and a Photon Machines fusion 10.6 µm CO_2 laser system with a laser beam of 6 mm by 6 mm (Phillips and Matchan, 2013). The loaded samples and Alder Creek Rhyolite (ACR) sanidine standard were baked overnight at ~120°C followed by heating at low laser power ~0.2 - 0.7 W (~1% to 3%) using the laser system to remove excess argon (Matchan and Phillips, 2014). The two ACR sanidine standards were analysed by 4 and 7 heating steps respectively, at high laser power ~7.4 W (35%). The J-value which relates the production of ^{39}Ar from ^{39}K during the radiation process and is dependent on the duration of radiation, neutron flux and neutron-capture distance (McDougall and Harrison, 1999) is calculated from the known ACR sanidine standard for each sample (Supplementary Table 5.2C).

Argon was extracted from most of the samples in 6 heating steps, except sample VRE9, SM17 and SM18, increasing the laser energy from 0.7-0.9 W to 2.9 W (3% - 4% to 14% laser power). Each heating step involved 3.15 min of laser scanning, after which the gases were purified by a getter pump. Blanks were measured after every sample and yielded <11.5 fA for ^{40}Ar, corresponding to 0.14% of the measured ^{40}Ar for all samples except VRE9, for which the blank levels are high (Supplementary Table 2B). Mass discrimination was determined by automated air pipette aliquots before analysis assuming an atmospheric $^{40}Ar/^{36}Ar$ of 295.5 ± 0.5 (Nier, 1950). Correction factors used are $(^{36}Ar/^{37}Ar)_{Ca}$ = 2.7002 (± 0.0024) x 10^{-4}, $(^{39}Ar/^{37}Ar)_{Ca}$ = 6.716 (± 0.018) x 10^{-4}; $(^{40}Ar/^{39}Ar)_K$ =3.00 (± 0.93) x 10^{-4}; $(^{38}Ar/^{39}Ar)_K$ = 0.013109 (± 0.000017). The plateau age spectrum is composed of at least three contiguous heating steps, which together represent more than 50% of the total ^{39}Ar released (McDougall and Harrison, 1999). The reported ages correspond to a 95% confidence level or 2σ, unless otherwise stated.

5.3.3. Thermoluminescence dating (TL)

Sample RG8 was collected from a baked palaeosol located directly below a basaltic flow from which sample RG11 (Figure 5.2) was taken. The palaeosol sample was analysed at the thermoluminescence dating laboratory at the University of Wollongong. Using fine grained (90-

125 μm) quartz grains and assuming that they have been sufficiently heated by the basaltic flow to empty their electron traps (signal re-set). Through time the electrons traps will load again at a known rate, determined by the radiation of long-lived isotopes of uranium, thorium and potassium, hence the amount of trapped electrons resolved is directly proportional to the time since lava emplacement.

Dilute HCl was used to remove the carbonate fraction within the palaeosol, after which the fine-grain fraction was isolated. Eighteen polymineral sample aliquots of approximately 2 mg each were prepared for this sample, five of which were used to measure TL naturally accumulated since the time of traps re-set. Eight aliquots were serially and incrementally irradiated using a calibrated laboratory beta radiation source and subsequently used in the preparation of an additive TL growth curve. A further five aliquots were again serially and incrementally irradiated using a calibrated alpha radiation source and an alpha TL growth curve was constructed. The comparison of these two growth curves provides a measure of the ability of the sample to produce TL under alpha irradiation compared to that produced by beta irradiation (called "k factor"). The TL signal from each aliquot was measured by heating to 500°C at a rate of 20°C/second in a high purity nitrogen atmosphere. The TL signal emitted was measured using an EMI 9635QB photomultiplier fitted with a Corning 7-59 transmitting filter and a Chance Pilkington heat filter and recorded on an X-Y recorder. In order to correct for possible variation between the aliquots, all TL values were normalised by means of a second glow procedure following a standard irradiation (3.24 Gray).

Trace amounts of long-lived isotopes of U, Th and K provide the majority of the energy, which raises electrons to the trapped energy levels. In order to determine the annual radiation dose derived from the palaeosol and the overlying basalt it is necessary to determine the sample's content of these elements and thus compute the radiation dose they provide. The annual radiation dose is resolved by thick-source alpha counting (TSAC) and XRF. Rubidium and cosmic radiation also make minor contributions to the annual radiation dose received. The sample's rubidium content was determined by X-ray fluorescence at the School of Earth and Environmental Sciences at the University of Wollongong, and the cosmic contribution by reference to published data (Aitken, 1985). Sample moisture has a moderating effect on the radiation received but in this case was assumed to be zero.

5.4. Results

5.4.1. Surface exposure dating

Results of the helium and neon abundances and their isotopic compositions are in Supplementary Table 1B. Corrections for shielding and cover were not performed as shielding is negligible at the sampling locations and the effects of snow are not likely to have affected the cosmic ray influx as the area of the Payenia Basaltic Province is semi-arid and the annual rainfall is less than 200 mm (Inbar and Risso, 2001).

In order to determine the cosmogenic nuclide abundances, contributions from non-cosmogenic components need to be evaluated. These include contributions from *in*-situ produced radiogenic and/or nucleogenic components as well as trapped components (Mamyrin and Tolstikhin, 1984). The nucleogenic component is produced from $^{6}Li(n,\alpha)^{3}H(\beta^{-})^{3}He$ in nucleogenic ^{3}He and from $^{18}O(\alpha,n)^{21}Ne$ in nucleogenic ^{21}Ne (Niedermann, 2002). The radiogenic ^{4}He component is produced by α particles from U and Th decay, which is generally low to negligible in young samples (<500 ka) with low U and Th concentrations (Niedermann, 2002). Accordingly U, Th and Li were measured on olivine separates (Supplementary Table 1C). The trapped component can be mantle, crustal or atmospheric. In the case of helium the trapped component is generally magmatic (mantle) in origin while in the case of neon it is mainly atmospheric.

5.4.1.1. Trapped neon and helium component

In order to determine the trapped component, *in-vacuo* analyses were performed which involve crushing a portion of the olivine separate under vacuum conditions to determine the isotopic composition of the noble gases trapped in fluid inclusions. The vacuum crushing analysis of sample VRE42 did not yield a detectable amount of noble gases. Therefore, mantle $^{3}He/^{4}He$ isotope composition was not determined. For neon we assumed that the trapped component composition is indistinguishable from that of the atmosphere. This is also supported by the low temperature (700°C) fusion experiment in which the $^{21}Ne/^{20}Ne$ and $^{22}Ne/^{20}Ne$ ratios show values very close (difference with air composition is <5.5%, except sample VRE42) to the air composition of $^{21}Ne/^{20}Ne = 0.002959$ and $^{22}Ne/^{20}Ne= 0.102$ (Eberhardt et al., 1965).

The helium trapped-component was not characterised for sample VRE42, therefore in order to be able to determine the cosmogenic ^{3}He abundance in the current study, an average from previous mantle $^{3}He/^{4}He$ values from the same basaltic province were used. Marchetti et al. (2014) performed vacuum crushing analysis on basalts from the Payún Matrú volcanic field, and reported $(^{3}He/^{4}He)_{magmatic}/ (^{3}He/^{4}He)_{air}$ R/Ra values of 7.31, 7.29 and 7.68 (where $R/Ra = (^{3}He/^{4}He)_{magmatic}/ (^{3}He/^{4}He)_{air}$, and $^{3}He/^{4}He$ air = 1.4×10^{-5}). Accordingly, an average of these values, 7.43 ± 0.18 ($^{3}He/^{4}He = 1.027 \pm 0.025 \times 10^{-5}$), is used as a trapped component when calculating cosmogenic ^{3}He abundance.

5.4.1.2. In-situ produced radiogenic and nucleogenic components

Despite the low U and Th concentration in olivine separates i*n-situ* produced radiogenic ^{4}He from α decay of U and Th was calculated for all samples (Supplementary Table 5.1C). In order to calculate the radiogenic ^{4}He retained within olivine, equations from Andrews (1985) were used. The impact of radiogenic ^{4}He is more critical in samples VRE46 and VRE21 than in the rest of the samples as it constitutes 58% and 55% respectively, of the total measured ^{4}He.

In-situ produced nucleogenic ^{3}He was calculated based on equations of Andrews (1985) utilizing the Li, U and Th concentrations. The calculated *in-situ* nucleogenic ^{3}He is almost negligible (<26 at/g); hence it does not contribute to the final cosmogenic ^{3}He concentration.

The nucleogenic ^{21}Ne component was estimated using the calculated radiogenic ^{4}He content and the $^{21}Ne_{nucleogenic}/^{4}He_{radiogenic}$ production ratio of 4.5 x 10^{-8} (Yatsevich and Honda, 1997). Nucleogenic ^{21}Ne ranges from 6898 at/g to 85 at/g, which is negligible.

5.4.1.3. Cosmogenic ^{3}He and ^{21}Ne

Cosmogenic ^{3}He and ^{21}Ne were calculated from the total gas abundance extracted at 700°C and 1800°C. The cosmogenic nuclide concentration was calculated after corrections for nucleogenic, radiogenic and trapped component in the case of ^{3}He, and nucleogenic and atmospheric components in the case of ^{21}Ne. The cosmogenic ^{3}He represents more than 97% of the total ^{3}He measured in samples VRE46, VRE21 and VRE42 while it is more than 50% in samples VRE12 and VRE 7, ~10% for sample SM7 and less than 2% for samples SM4 and SM10 (Supplementary Table 5.1C). The very low abundance of cosmogenic ^{3}He in samples from the Santa Maria Volcano (SM4, SM7 and SM10) is owing to their youthfulness. Most of the ^{3}He in these samples has a magmatic origin as the $^{3}He/^{4}He$ ratios observed in these samples are close to He isotope composition assumed to be a trapped mantle component of 1.03 x 10^{-5} as reported by Marchetti et al. (2014). After the corrections (e.g. in-situ radiogenic ^{4}He), the cosmogenic ^{3}He and ^{21}Ne concentrations were calculated (Supplementary Table 5.1D). The cosmogenic isotopic abundance has been adjusted by the scaling factors of Lal (1991) and Dunai (2000) in order to compare the age difference using one of the simplest scaling factors (Lal's) in relation to a more contemporaneous and increasingly accepted scaling factor (Dunai's) (For further details of the two scaling factors see Chapter 1.5.1.3 Scaling factors)

Cosmogenic ^{21}Ne was detected in most samples, nevertheless the sample from Santa Maria volcano have a Ne isotope composition close to the atmospheric as can be seen in the total neon 3-isotope plot (Figure 5.3). Furthermore, in the Ne plot, the data for individual temperature fractions are plotted (Supplementary Figure 5.1). The Ne isotope compositions in the lower temperature fraction (700°C) are close to atmospheric values within uncertainties whereas those at the higher extraction temperature (1800°C) lie on the olivine cosmogenic line (Fenton et al., 2009) except for Santa Maria and VRE42 and VRE42 crushing samples. In the neon 3-isotope plot (Niedermann, 2002), most of the total extracted gases are, within error, on the neon cosmogenic line (except sample VRE42) (Fenton et al., 2009) (Figure 5.3). In the same isotope plot, sample VRE42 crushed has been displaced to a lower $^{22}Ne/^{20}Ne$ and $^{21}Ne/^{20}Ne$, possibly related to re-adsorption of air gas as this sample was previously crushed in vacuum and then used for fusion analysis. Furthermore, sample VRE42 is not located on the spallation line and is displaced to a higher $^{22}Ne/^{20}Ne$ possibly related to isotope fractionation of the atmospheric component or related to systematic mass bias introduced by correcting doubly charged Ar and CO_2 (Fenton and Niedermann, 2014).

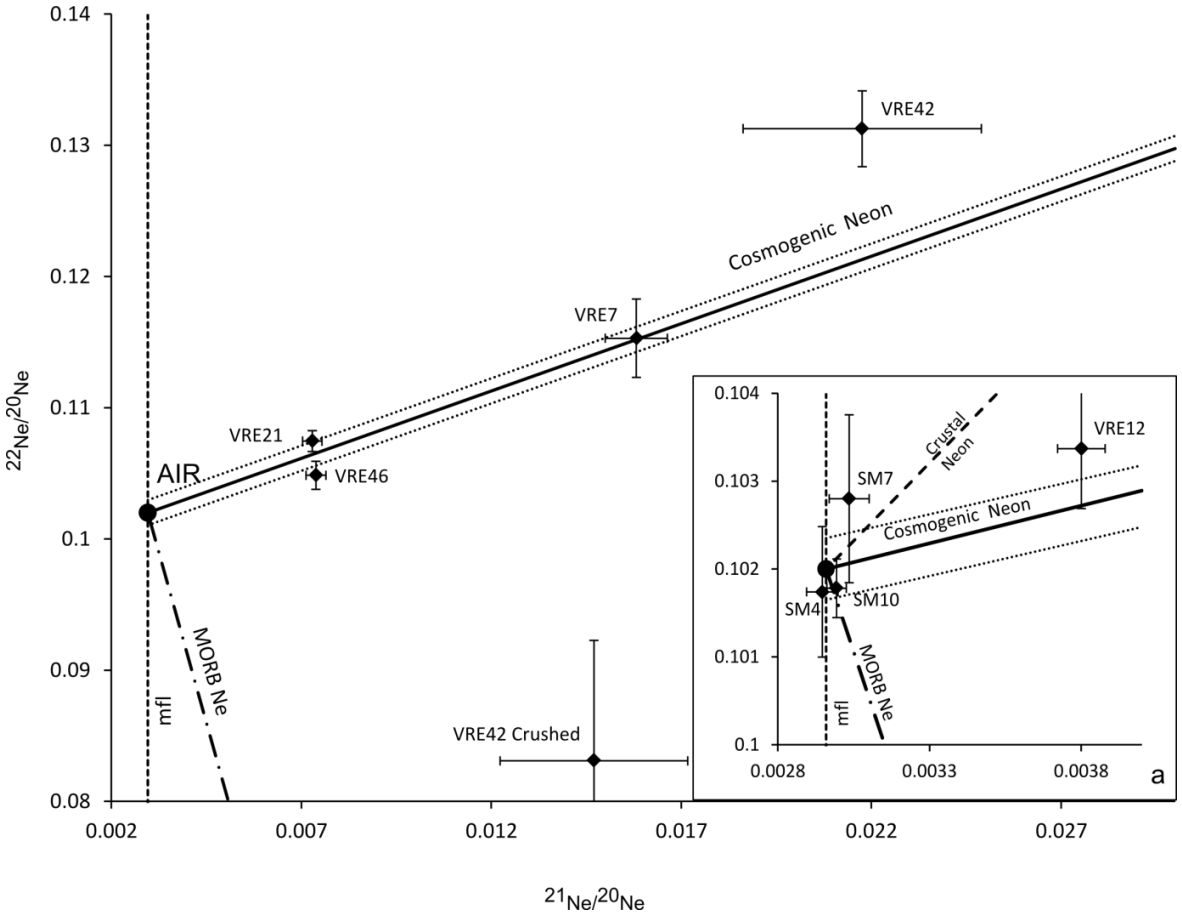

Figure 5.3. Total neon three-isotope plot from samples analysed. The cosmogenic line for olivine is from Fenton et al. (2009) and dotted line represents the error on the cosmogenic line. The atmospheric neon composition is shown as AIR from Eberhardt et al. (1965). The neon isotopic composition for MORB is from Sarda et al. (1988). The atmospheric neon mass-fractionation line (mfl) is shown on the diagram. The crustal neon line in inset b) is from Kennedy et al. (1990).

5.4.1.4. Surface exposure ages

A total of eight samples were analysed to resolve surface exposure ages from the Payún Matrú and the Llancanelo volcanic fields. Cosmogenic ^{3}He and ^{21}Ne abundances were determined for most of the samples with exception to sample SM4 from Santa Maria Volcano from which cosmogenic nuclides were not detected above background. The ages were calculated using both the Lal (1991) and Dunai (2000) scaling factors (Supplementary Table 5.1D). The calculated ages using the two scaling factors are within error however; on average (based on the actual age) using Lal's scaling factor the ages are 3.2% and 7.1% younger than Dunai's for cosmogenic ^{3}He and ^{21}Ne, respectively. The higher difference (between Lal's scaling factor and Dunai's) for cosmogenic ^{21}Ne can be attributed to the fact that cosmogenic ^{21}Ne production rate (Poreda and Cerling, 1992) originally used Lal's scaling factor. This point has previously been emphasised by Niedermann, (2002) as he suggested that the scaling factor used for samples should be consistent with the original one used for the production rate. Therefore, in the current investigation and in the following discussion only ages calculated based on the Lal (1991) scaling factor are used. The production rate used for cosmogenic ^{21}Ne is 45 ± 4 at/g/a (Poreda

and Cerling, 1992) and for cosmogenic ^{3}He is 121 ± 11 at/g/a (Gohering et al., 2010) both based on the Lal (1991) scaling factor.

The current investigation presents three new ages for the **Santa Maria** volcano although, owing to low cosmogenic ^{3}He and ^{21}Ne concentrations, the errors in the calculated exposure ages are large. Volcanic products from this volcano were previously analysed by Espanon et al. (2014a), concluding that they are Holocene as the authors could not detect, or detected very low concentrations of cosmogenic ^{3}He and ^{21}Ne; therefore their age determinations have large errors. Sample SM7 provided sufficient cosmogenic ^{3}He and ^{21}Ne to resolve an age from each nuclide (Supplementary Table 5.1D), these ages are within error and they are located on the 1:1 line in Figure 5.4, which gives some robustness to the age despite the large associated error. In the case of samples SM10 and SM4, the concentration of cosmogenic ^{3}He is very low and with large errors, therefore an age was not calculated from this nuclide, for any of these samples. The ages here inferred for the Santa Maria volcano support the first numerical age presented by Espanon et al. (2014a) and indicate that this basaltic flow was emplaced between 4000 and 300 years ago (taking into account the older age with maximum and minimum errors).

Sample VRE12 from **La Pasarela** is the only sample that does not fit the 1:1 line in Figure 5.4, therefore presenting an older cosmogenic ^{21}Ne surface exposure age than cosmogenic ^{3}He. Consequently, the age presented in Table 5.2 for this sample is not an average from both cosmogenic ^{3}He and ^{21}Ne exposure ages. The age for this sample is based on the cosmogenic ^{21}Ne exposure age as there are less corrections for this nuclide than for cosmogenic ^{3}He. Sample VRE12 yielded a cosmogenic ^{21}Ne exposure age of 55 ± 7 ka which is within error of samples from Marchetti et al. (2014), resolved using cosmogenic ^{3}He exposure dating and corresponding to the same locality and volcanic feature.

Two aliquots from sample VRE42 olivine separate (south of Carapacho) were analysed. The first is a fine grained (<180μm) aliquot, initially used for vacuum crushing analysis followed by analysing the crushed material by fusion. The second aliquot is a coarse grained (355-212 μm). Neither aliquot corresponds to the olivine cosmogenic line (Figure 5.3). Nevertheless, the two aliquots plot on the 1:1 line in Figure 5.4. Sample VRE 7 also from the Llancanelo volcanic field has a similar age to sample VRE42 and it plots on the 1:1 line. The mean age from the two aliquots and from cosmogenic ^{3}He and ^{21}Ne of this sample is 130 ± 19 ka and it constitutes the first age from the top collapse wall of the **Cueva del Tigre** lava tube (Figure 5.2g).

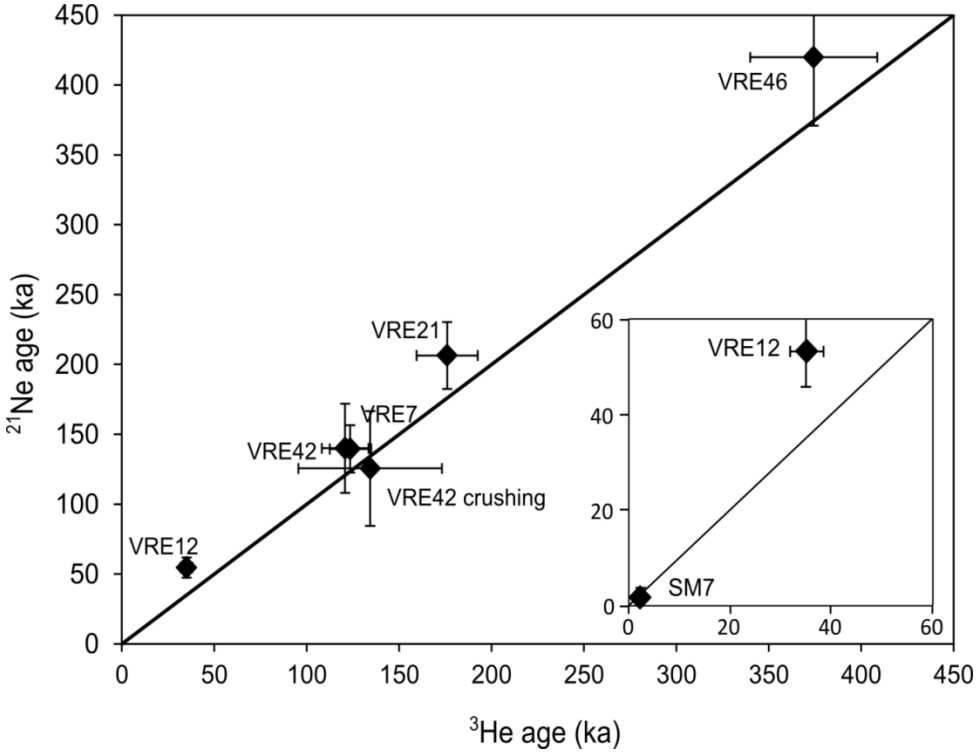

Figure 5.4. Surface exposure ages calculated from cosmogenic ^{3}He and ^{21}Ne. The 1:1 line represents cosmogenic ^{21}Ne ages which are equal to cosmogenic ^{3}He ages. The error bars correspond to the calulated error from the age at 1σ confidence level.

Sample VRE46 is from **Pampas Onduladas**. This flow has been described as the longest Quaternary flow on Earth (Pasquarè et al., 2008). This flow has been morphologically and geochonologically analysed in Chapter 3, where the flow length was calculated to 167 km and ^{40}Ar/^{39}Ar analysis were performed on two samples one from the initial part of the flow (VRE20) and another 120 km to the SE (VRE46a) close to the end of the flow. The ^{40}Ar/^{39}Ar plateau age for this flow is reported to be 372 ± 5 ka (2σ) for sample VRE20 (Chapter 3). In Chapter 3, a similar inverse isochron age for sample VRE46a is reported but with larger errors. These correspond to the first radiometric ages obtained from this long flow. The two samples here investigated from this flow correspond to similar locations and sample VRE46 was collected from the same site as sample VRE46a, therefore allowing comparison. The cosmogenic ^{3}He and ^{21}Ne exposure ages are 374 ± 34 ka and 422 ± 49 ka, respectively and the mean of the two ages was calculated to 398 ± 30 ka for sample VRE46. These two cosmogenic nuclide exposure ages are robust as the two plot on the olivine cosmogenic line (Fenton et al., 2009) in Figure 5.3 and on the 1:1 line in Figure 5.4. The new exposure age here reported for Pampas Onduladas is almost indistinguishable from the ^{40}Ar/^{39}Ar plateau age (VRE20 = 373 ± 10 ka 2σ), from the inverse isochron (VRE46a = 374 ± 76 ka 2σ) and total gas (VRE46a = 370 ± 10 ka 2σ) ages reported in Chapter 3.

Sample VRE21 also from the Pampas Onduladas flow, has noble gas abundances and compositions very similar to sample VRE46 (Supplementary Table 5.1A and 5.1B) as shown in Figure 5.3, the two samples plot on the olivine spallation line (Fenton et al., 2009) and close to each other. In addition, they both plot on the 1:1 line in Figure 5.4 but the age range is considerably different as sample VRE21 has a mean exposure age of 192 ± 14 ka while sample VRE46 is 398 ± 30 ka. One of the possible explanations for this discrepancy can be related to the choice of scaling factors which are based on elevation or atmospheric depth and since the difference in elevation is 821 m or 93 g/cm^2 (in the case of atmospheric depth), the corresponding scaling factor is 1.9 x higher in sample VRE21 than in VRE46. The scaling factor difference results in younger ages for sample VRE21 which was taken ~3 km north of sample VRE20 (analysed by $^{40}Ar/^{39}Ar$ to 373 ± 10 ka, Chapter 3), therefore the exposure age here determined for sample VRE21 is regarded as not appropriate.

5.4.2. $^{40}Ar/^{39}Ar$ dating

Results from the eight samples from the Llancanelo and Payún Matrú volcanic fields including sample step-heating, ACR standard, blank experiments and age spectra as well as inverse isochron graphs are in Supplementary Tables 5.2A to 5.2D and Supplementary Figure 5.2.

5.4.2.1. Río Grande samples

Three samples (RG2, RG11 and RG1) were analysed from the Río Grande area although, two of these samples (RG2 and RG11) correspond to a single flow that flowed from the western side of the Payún Matrú volcanic field into the Río Grande valley. These two samples did not yield a plateau age as the samples are low in K, and radiogenic ^{40}Ar was not detected within error above atmospheric Ar from sample RG11. The only age estimate for this flow comes from the fact that less than 0.05 % of the total Ar released is radiogenic in sample RG2. A poorly constrained weighted mean age on this sample is indistinguishable from zero at 2σ level, therefore it is suggested that this sample's age is approximately <10ka. The inverse isochron age was not resolved for any of these samples (Supplementary Table 5.2A and 5.2D).

Sample RG1 is from a strath terrace on the Río Grande velley located ~10 metres above sample RG2 and corresponds to an older basaltic flow. A plateau age for this sample is 317 ± 2 ka (2σ) (Supplementary Table 2A and Supplementary Figure 5.2). The Inverse isochron of this sample indicates $^{40}Ar/^{36}Ar_i$ of 292.4 ± 5.7 (2σ) which is, within error, atmospheric in composition (atmospheric $^{40}Ar/^{36}Ar$ = 295.5 ± 0.5, at 2σ, (Nier, 1950). The associated inverse isochron age is 328 ± 19 ka (2σ) and the total-gas age is 318 ± 10 ka (2σ). The three ages are within error and give robustness to the plateau age, which is regarded as the accepted age for this sample. Furthermore, the plateau age is in good agreement with an $^{40}Ar/^{39}Ar$ plateau age reported of 320 ± 50 ka (Gudnason et al., 2012) from a terrace approximately 6 km north of sample RG1 and also part of the Río Grande valley. In the same area a K-Ar age was determined to be 233 ± 11 ka (1σ) (Germa et al., 2010).

5.4.2.2. La Calle flow and western side of Santa Maria volcano

The single sample (LV6, La Calle flow) analysed from **Los Volcanes**, sample LV6 did not produce any reliable results as radiogenic ^{40}Ar was not resolved, therefore an inverse isochron or a total-gas age were not determined. Based on the lack of radiogenic ^{40}Ar in this sample we estimate that it is very young, possibly <10 ka.

The 3 samples analysed from the western side of Santa Maria volcano did not produce a reliable plateau age. The apparent age from the individual step-heating for samples SM14 and SM18 (Supplementary Figure 5.2), increase with temperature possibly reflecting extraneous ^{40}Ar in these samples. The addition of extraneous ^{40}Ar, is generally described as excess or inherited ^{40}Ar, consequently the $^{40}Ar/^{36}Ar$ tends to increase (McDougall and Harrison, 1999), deviating from the atmospheric composition (295.5 ± 0.5, at 2σ, Nier 1950). This is shown in sample SM14 as the $^{40}Ar/^{36}Ar_i$ is high with a value of 306.5 ± 9.4 ka (2σ).

Radiogenic ^{40}Ar was not detected for sample SM17, thereby indicating that it is very young possibly <10ka. For samples SM14 and SM18 the radiogenic ^{40}Ar is less than 1.2% and 0.8 % respectively and an inverse isochron age was not constrained from these samples. An approximate age estimate for samples SM14 and SM18 can be derived by using the first heating-step apparent age, as a maximum age as it is likely to be the step least affected by extraneous ^{40}Ar. However, this is a crude estimate, from which we propose these samples are possibly between 0 and 30 ka at the 2σ uncertainty level.

5.4.2.3. Malacara volcano

This sample (VRE9) is the only one analysed from the Llancanelo volcanic field, and constitutes the first attempt to numerically date a basaltic flow from the Malacara volcano. A plateau age could not be resolved from this sample, nevertheless we can estimate that the apparent ages from the first two step-heating, are close approximations to the actual age of the flow, as these two heating steps constitute more than 70% of the total radiogenic ^{40}Ar released. However, in order to construct a plateau age three contiguous heating steps are commonly needed (McDougall and Harrison, 1999), which is not the case here as in the 3rd step the radiogenic ^{40}Ar was exhausted resulting in younger apparent ages (Supplementary Figure 5.2). The inverse isochron indicates that $^{40}Ar/^{36}Ar_i$ is lower than atmospheric at the 2σ level and the associated age is 167.4 ± 4.3 ka (2σ) while the total release Ar age is 137.6 ± 3.6 ka (2σ). The inverse isochron age is here treated as a conservative maximum age estimate.

5.4.3. Thermoluminescence dating

The palaeosol (RG8) located directly below the basaltic flow from which sample RG11 was collected, has a minimum age of 5880 ± 450 a and a maximum age of 7040 ± 530 a, both at 1σ uncertainly level (Supplementary Table 5.3). The minimum age is based on the assumption that all the gamma radiation dose to the palaeosol is derived from the palaeosol itself. The maximum

age is based on the assumption that all the gamma radiation dose comes from the overlying basaltic flow. The true age at the time when the palaeosol was baked should be closer to the lower limit as most environmental dose is generated by the palaeosol itself. Nevertheless, due to the low relative difference between the maximum and minimum ages we take a conservative approach and propose the maximum age as the age of basaltic flow emplacement. In any case, the maximum and the minimum age fit well with the previous, albeit crude, estimated age for sample RG11 and RG2 (<10 ka) from the same basaltic flow.

5.5. Discussion

5.5.1. Quaternary chronology of the Payenia Basaltic Province

Nine new radiometric ages that span the past 500 ka have been presented for the Payún Matrú and Llancanelo volcanic fields. Furthermore, seven maximum-age estimates have been proposed. The oldest age inferred is 398 ± 30 ka (1σ) (Table 5.2) for sample VRE46 from near the terminal-part of the long (>167 km) Pampas Onduladas flow. This age inferred from surface exposure dating is in good agreement with an $^{40}Ar/^{39}Ar$ age of 373 ± 10 ka (2σ) (Chapter 3) for the same flow. Both ages constitute the first radiometric ages to be reported for this flow and they agree with a previous estimate to be younger than 400 ka based on a K/Ar age from a stratigraphically lower basaltic flow (Melchor and Casadio, 1999). Sample VRE21, also from the Pampas Onduladas flow, did not yield a comparable age despite having similar noble gas concentration and isotopic composition (Supplementary Table 5.1B). The issue here identified is possibly related to the scaling factors (Lal 1991; Dunai 2000) (Supplementary Table 5.1D), as both are mainly based on cosmic-ray intensities and their elevation dependence, either expressed as elevation (Lal, 1991) or as atmospheric depth (Dunai, 2000). The problem with scaling factors is beyond the scope of this work; nevertheless it highlights the importance of using a multi-proxy approach in order to fully assess the results. The surface exposure age obtained from sample VRE21 will not be further discussed due to the large discrepancy with sample VRE46 and with previous $^{40}Ar/^{39}Ar$ ages from the same flow.

A sample collected from a strath terrace ~10 m higher and ~ 900 m to the north west of the current Río Grande course, yielded an $^{40}Ar/^{39}Ar$ age of 316 ± 2.4 ka (2σ) in agreement with an age reported by Gudnason et al. (2012) of 320 ± 50 ka (2σ). Sample VRE12 from a ropy lava surface close to La Pasarela is within error of ages reported by Marchetti et al. (2014) for the same flow. Other samples analysed from the Payún Matrú volcanic field are Holocene, however the associated errors are relatively large. Of significance are the two ages reported for Santa Maria volcano, as the ages inferred for SM7 (using cosmogenic ^{3}He and ^{21}Ne) and for SM10 (using cosmogenic ^{21}Ne) are within error of each other. They are also within the age range proposed by Espanon et al. (2014a). The strong association of the three analysed samples (SM4, SM7 and SM10) from the Santa Maria volcano with atmospheric neon (Figure 5.3) and the lack of cosmogenic nuclides in sample SM4, are interpreted as a function of the young age of this volcano. The evidence presented suggests that it was active in the last 4000 years.

Three samples were analysed from the Llancanelo volcanic field and have ages younger than 170 ka (Table 5.2). Two of the three ages were resolved for this volcanic field based on surface exposure dating and they agree with an $^{40}Ar/^{39}Ar$ age determination of 160 ± 70 ka (2σ) from Gudnason et al. (2012) from Cerro Jarilloso on the western side of Llancanelo Lake (Figure 5.1). The single sample (VRE9) from this volcanic field analysed for $^{40}Ar/^{39}Ar$ did not produced a plateau age hence we estimate that it is younger than 167 ka. This evidence suggests that the Llancanelo volcanic field was active between 200 ka and 100 ka (possibly later), especially in the area west of the Llancanelo Lake.

5.5.2. Correlation of tectonic changes with basalt geochemistry

The Quaternary volcanism in the Payenia Volcanic Province is geochemically diverse as previously suggested (Søager et al., 2013; Chapter 2) while a chronological northward migration has been identified by Gudnason et al. (2012). Volcanism in the Payenia Basaltic Province progressed from arc-like signatures in the Chachahuén region (Figure 5.1) related to shallow subduction in the late Miocene (Kay et al., 2006a) towards the Nevado volcanic field in the Pliocene to early Pleistocene. The volcanic evolution of the Nevado volcanic field suggests that the slab was present below this volcanic field in the early Pleistocene and that the back-arc volcanism migrated to the north-west (Gudnason et al., 2012). This is also suggested using geochemical distribution maps (Chapter 2) (Figure 5.5), where La/Nb, Th/Nb and Ba/Nb are higher, as typical for the Andean arc related basalts, in the northern part of the nevado volcanic field than in the southern part of the same volcanic field. In addition, this Pleistocene volcanic field has Ba/La higher than 20 (Figure 5.6 a, b) which is interpreted as related to arc signatures (based on Kay et al., 2006a). The Ba/La values from this volcanic field decrease with age (Figure 5.6a, b). The Andean arc-like signatures in the northern part (Llancanelo and northern segment, Figure 5.1 and 5.5) have been previously recognised by Søager et al. (2013) and in Chapter 2. Using the Pleistocene chronology from this contribution as well as from previous publications and the geochemical data available, we can constrain that the arc-like signature corresponds mainly to the last 0.5 Ma in the Llancanelo volcanic field and the northern segment while the northern part of the Nevado volcanic field had this signatures since ~1.5 Ma (Figure 5.5 and 5.6). The trend observed in the interpolation maps to the north-west is related to slab roll back, as was previously suggested based on the migration of volcanism from E of 69°W from approximately 2.83 Ma to 0.5 Ma followed by a westward shift westof 69°W in the last 0.5 Ma (Gudnason et al., 2012).

The southern part of the Nevado volcanic field was active around 1 Ma to 1.5 Ma, with transitional volcanism, as geochemical ratios are intermediate between arc-like ratios (northern segment and northern Nevado volcanic field) and intraplate volcanism (Río Colorado and Payún Matrú volcanic fields). Furthermore, the interpolation maps suggest that different volcanism was occurring at the Nevado and the Río Colorado volcanic fields during the same time (Figure 5.5 and 5.6). The Ba/Nb interpolation map (Figure 5.5c) shows high ratios in the northern part of the

Nevado volcanic field around 1.5 Ma which is related to an Andean arc signature, while at the same time, basalts with a low Ba/Nb ratio associated with an intraplate setting were erupting in the Río Colorado volcanic field and the Tromen region. This is observed with almost all the interpolation maps while the trend is reversed for Nb/U as this ratio is high in intraplate related basalts and it is low in arc-like basalts. Furthermore, in Figure 5.6, a single sample from the Río Colorado volcanic field (sample 126232 Søager et al., 2013) with and age of 1.54 Ma (Gudnason et al., 2012) has a composition typical of intraplate basalts with an OIB-like signature while a sample from Nevado volcanic field (sample 123956, Søager et al., 2013) with a similar age of 1.58 Ma has an arc-like signature (Figure 5.6). Therefore, suggesting that different processes were occurring at the same time during the Pleistocene in different areas of Payenia Basaltic Province.

The intraplate basalts in the Río Colorado region and the Payún Matrú volcanic field are associated with an ocean island basalt-like (OIB-like) setting (Kay et al., 2006b; Germa et al., 2010; Søager et al., 2013; Chapter 2) with minimal to negligible subducting slab input (Jacques et al., 2013; Søager et al., 2013; Chapter 2). The majority of the samples from the Payún Matrú volcanic field have a composition similar to that of the local OIB, which is here represented by the Río Colorado basalts from Søager et al. 2013, (Figure 5.6c). The geochemical signature in the southern part of the Payenia Basaltic Province can be traced to the early Miocene (Kay et al., 2006a) (Figure 5.6 a, c), with this OIB-like signature changing to and arc-like signature during the late Miocene as observed in Figure 5.6a and c with samples from this period plotting within the Quaternary Andean-arc basaltic field.

The OIB-like signatures during the Quaternary in the southern part of the Payenia Basaltic Province, especially in the Río Colorado volcanic field, have been present from at least the early Pleistocene (~2 Ma) until approximately 0.5 Ma, probably suggesting its relation to a rising asthenospheric structure. Furthermore, and despite the relatively scarce geochemical data available for Holocene volcanics, we can suggest that the basalts erupted during this period have also an OIB-like geochemistry (Figure 5.6c) extending the influence of the rising asthenospheric or a plume-like structure to the last 10000 years. A plume-like structure was previously recognised based on geophysical studies performed in the Payún Matrú volcanic field (Burd et al., 2008). Recently, this plume-like structure has been inferred to be decapitated, resulting in magma ponded below the continental crust (Burd et al., 2014; Chapter 4).The Pleistocene volcanism in the Payenia Basaltic Province is diverse as it has arc-like signatures in the northern part while intraplate OIB-like signatures were determined in its the southern part. Nevertheless, we regard the Holocene volcanism has having a restricted distribution as it is strictly related to OIB-like signatures and intraplate type of volcanism.

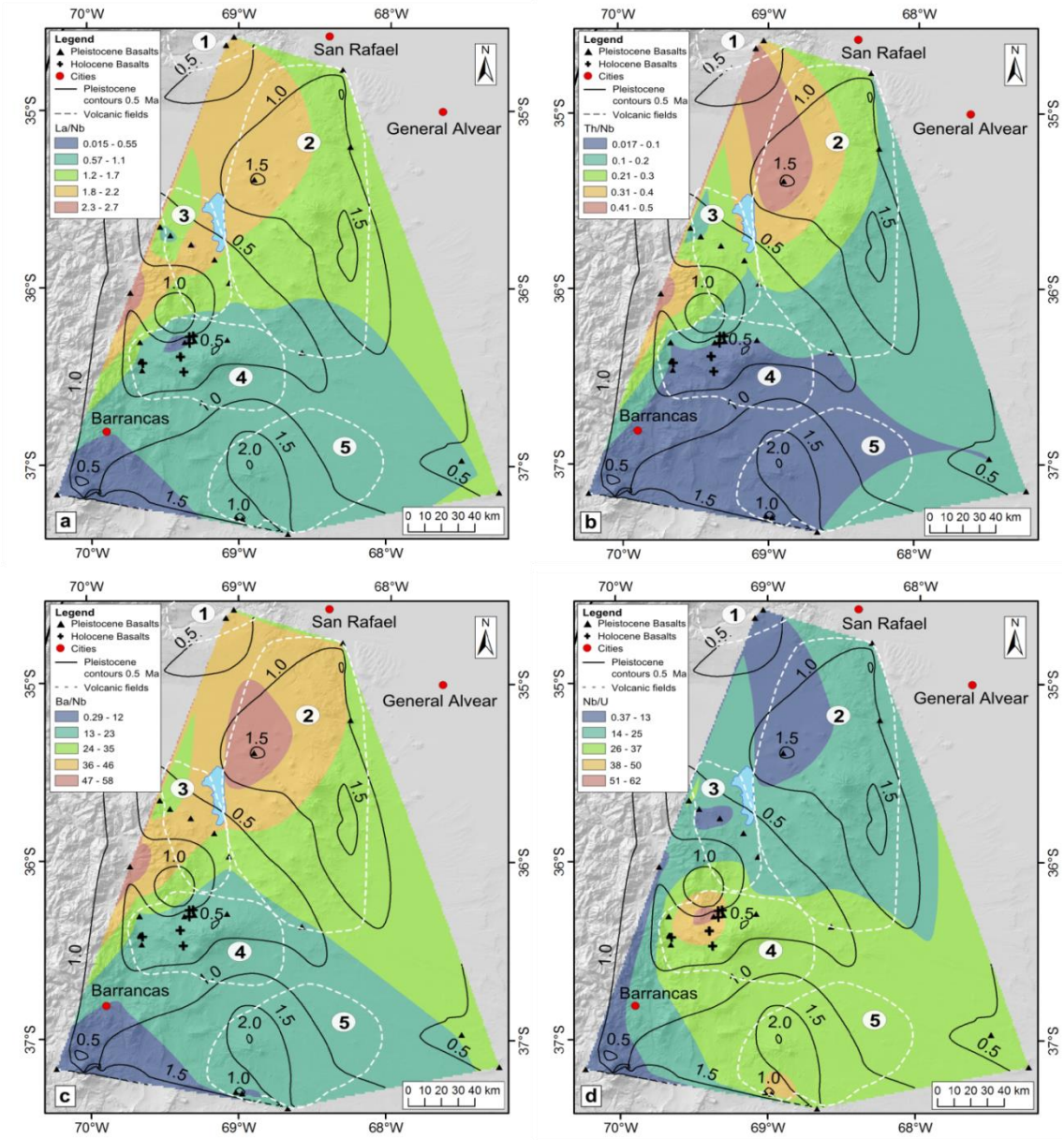

Figure 5.5. Maps of interpolatated geochemial ratios from Pleistocene samples in the Payenia Basaltic Province. a) La/Nb, b) Th/Nb, c) Ba/Nb and d) Nb/U. The procedure used to produce these maps is described in Chapter 2 and based on 27 Pleistocene lavas from the current investigation as well as previously published lavas with <53 wt % SiO_2 (Melchor and Casadío, 1999; Kay et al., 2006a; Germa et al., 2010; Gudnason et al., 2012; Søager et al., 2013; Espanon et al., 2014a; Chapter 3; Chapter 2). The dotted lines correspond to volcanic fields in the back-arc, 1) Northern Segment, 2) Nevado volcanic field, 3) Llancanelo volcanic field, 4) Payún Matrú volcanic field and 5) Río Colorado volcanic field (modified after Gudnason et al., 2012). Note that the position of analysed Holocene lavas have been plotted for reference but that the geochemical data from these young samples have not been included in the interpolation.

Table 5.2. Geochronological results from samples analysed from the Payún Matrú and Llancanelo volcanic fields.

Location	Sample	Age (ka)	Comment
Pampas Onduladas	VRE46	**398 ± 30**	Age based on an average from cosmogenic ^{3}He and ^{21}Ne, based on Lal (1991) scaling factor
Pampas Onduladas	VRE21	**192 ± 14**	Same as above
South of Carapacho volcano	VRE42	**130 ± 19**	Same as above and based on a weighted mean from two aliquots (Supplementary Table 1D)
Cueva del Tigre	VRE7	**132 ± 10**	Age based on an average from cosmogenic ^{3}He and ^{21}Ne, based on Lal (1991) scaling factor
Malacara Volcano	VRE9	<167	Based on total argon gas released, this is an estimated age. The first two heating steps point to a similar age.
Río Grande	RG1	**316 ± 2.4**	^{40}Ar/^{39}Ar plateau age
Río Grande	RG2	<10	Radiogenic ^{40}Ar was low for these samples, <0.05% of total ^{40}Ar, constraining a poor weighted mean indistinguishable from zero at 2σ. Possibly Holocene
Río Grande	RG8	**7.04 ± 0.53**	Age based on thermoluminescence dating from a palaeosol located directly below the RG11 basaltic flow.
Río Grande	RG11	<10	Radiogenic ^{40}Ar was not resolved for this sample. Possibly Holocene
La Pasarela	VRE12	**55 ± 7**	Age based on cosmogenic ^{21}Ne nuclide abundance and based on Lal (1991) scaling factor
Santa Maria volcano	SM4	-	No surface exposure age was resolved for this sample due to negligible cosmogenic nuclide concentration
Santa Maria volcano	SM7	**2.02 ± 1.03**	Age based on an average from cosmogenic ^{3}He and ^{21}Ne based on Lal (1991) scaling factor
Santa Maria volcano	SM10	**1.73 ± 1.61**	Age based on cosmogenic ^{21}Ne nuclide abundance and based on Lal (1991) scaling factor
W side of Santa Maria volcano	SM14	0-30	Based on the apparent age of the first heating step as a maximum age estimate
W side of Santa Maria volcano	SM17	<10	Radiogenic ^{40}Ar was not resolved for this sample. Possibly Holocene
W side of Santa Maria volcano	SM18	0-30	Based on the apparent age of the first heating step as a maximum age estimate
La Calle flow	LV6	<10	Radiogenic ^{40}Ar was not resolved for this sample. Possibly Holocene

Ages in boldface type are robust ages constrained from this study, except SM7 and SM10 which have large associated errors, related to the low cosmogenic nuclide concentration

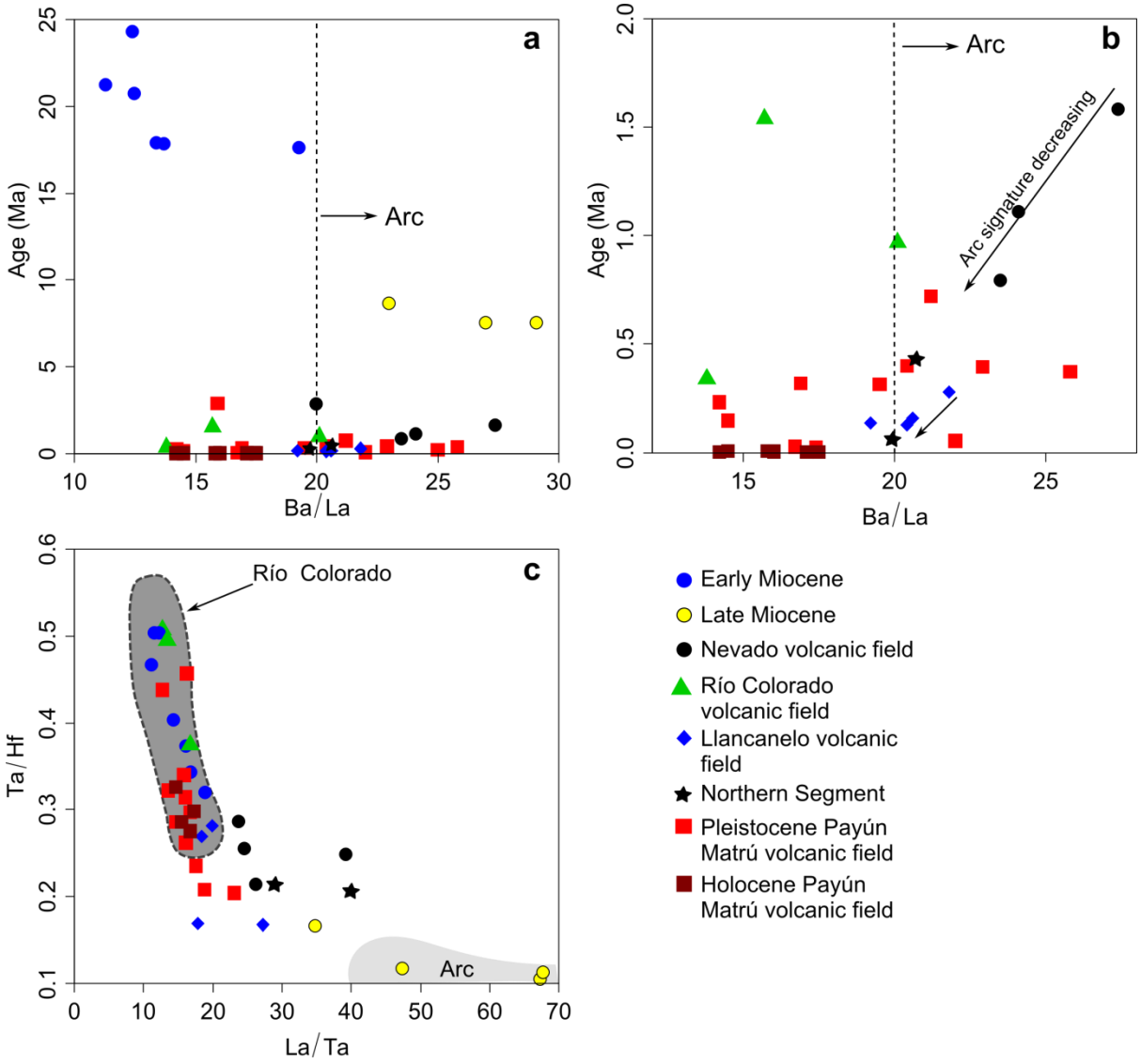

Figure 5.6. Geochemial and geochronological correplation of volcanic rocks from the Payenia Basaltic Province. a) Ba/La vs age (Ma) from early Miocene to Holocene. b) Ba/La vs age (Ma) for Quaternary volcanic rocks. The Ba/La line is from Kay et al. (2006a). c) La/Ta vs Ta/Hf including the Río Colorado volcanic field (Río Colorado field is from Søager et al., 2013 represent the local intraplate component with an Ocean Island basalt-like composition) and the arc (Arc field from Chapter 2). Data points for these plots are from this contrubution and previous publications (Kay et al., 2006a; Germa et al., 2010; Gudnason et al., 2012; Dyhr et al., 2013a; Dyhr et al., 2013b; Søager et al., 2013; Espanon et al., 2014a; Chapter 3; Chapter 2).

5.6. Conclusions

In the current investigation, nine new ages from a range of dating methods are presented for the Payenia Basaltic Province. Seven surface-exposure ages using cosmogenic ^{3}He and ^{21}Ne range from <400 ka to <4 ka. The younger range has large errors due to the relative low abundance of cosmogenic nuclide; nevertheless, the ages are in good agreement and suggest that the Santa Maria volcano was active in the last 4000 years. The oldest sample dated using cosmogenic nuclides yielded a combined age of 398 ± 30 ka from the long (>167 km) Pampas

Onduladas flow, which is in good agreement with a previous $^{40}Ar/^{39}Ar$ age of 372 ± 5 ka(2σ) (Chapter 2). Furthermore, cosmogenic nuclide abundances were analysed from a second sample from the same long flow. Although the two samples have very similar noble gas abundances and compositions, the age difference between the two samples is ~200 ka. We propose that the age discrepancy between samples of the same flow can be related to problems with the scaling factor as the elevation difference between the two samples is approximately 800 m. This issue requires attention in the future investigations as surface exposure dating has not been tested on long flows (>100 km).

An $^{40}Ar/^{39}Ar$ age of 316 ± 2.4 ka has been resolved for a basaltic flow in the vicinity of Río Grande while the rest of the samples analysed using this method did not produce reliable ages possibly related to the youthfulness of the samples analysed. Furthermore, an age of 7.04 ± 0.53 ka has been inferred for a basaltic flow filling part of the Río Grande valley (~7 km in length). This age was derived using thermoluminescence dating of a palaeosol directly below the basaltic flow. The three Holocene ages presented here contribute to the scarce numerical chronology that exists from this basaltic province for the last 10000 years. Other ages are from the late Pleistocene agreeing with the suggestion that volcanic activity peaked during this time (Gudnason et al., 2012).

The geochemical evolution of the Payenia Basaltic Province suggests that it was diverse during the Pleistocene, as arc-like signatures such as high Ba/La, Th/Nb, Ba/Nb and La/Nb are registered at approximately 1.5 Ma in the northern Nevado volcanic field while at the same time in the Río Colorado volcanic field, basalts with an ocean island basalt-like composition were erupting. The arc-like signature in the Nevado volcanic field decreased in a northwesterly direction as suggested by Gudnason et al. (2012) and it is confirmed here by the interpolation maps. A similar decreasing trend was inferred for the Llancanelo volcanic field while for the Payún Matrú volcanic field no trend has been inferred. The Holocene volcanism analysed here corresponds only to the Payún Matrú volcanic field and has a composition similar to that of the local-intraplate.

Supplementary Tables 5.1A to 1D. Surface exposure dating

Supplementary Table 5.1A. Major-element XRF analyses of olivine separates

	VRE46	VRE21	VRE42	VRE12	VRE7	SM4	SM7	SM10
SiO_2	38.24	38.23	37.84	38.38	38.36	35.70	38.45	38.60
TiO_2	0.16	0.16	0.08	0.14	0.08	0.14	0.09	0.19
Al_2O_3	0.78	0.89	0.63	1.03	0.82	0.78	0.58	1.32
FeO	21.59	21.12	20.54	18.80	18.96	18.58	19.00	18.79
MnO	0.25	0.26	0.25	0.23	0.22	0.23	0.23	0.23
MgO	38.35	38.46	39.55	39.91	40.66	37.67	40.78	38.69
CaO	0.63	0.68	0.49	0.74	0.49	0.57	0.54	0.98
K_2O	0.06	0.06	0.02	0.05	0.02	0.07	0.04	0.11
P_2O_5	0.03	0.03	0.01	0.03	0.01	0.03	0.02	0.04
Na_2O	0.20	0.20	0.15	0.18	0.15	0.14	0.17	0.31
Total	100.27	100.08	99.55	99.48	99.76	93.90	99.89	99.26
Fo content[a]	76	76	77	79	79	78	79	79

[a] forsterite content (atomic Mg/(Mg+Fe)) of olivine separates was calculated from the Mg and Fe contents.

Supplementary Table 5.1B. Results of helium and neon isotopic analysis from Llancanelo and Payún Matrú volcanic fields. Noble gas concentrations expressed in cm^3 STP/g.

Sample	Sample mass (g)	Grain Size (µm)	Temperature (°C)	^{4}He (10^{-9})	^{20}Ne (10^{-11})	$^{3}He/^{4}He$ (10^{-5})	$^{21}Ne/^{20}Ne$ (10^{-3})	$^{22}Ne/^{20}Ne$ (10^{-1})
VRE46	2.17	355-212 µm	700	3.062 ± 0.036	10.45 ± 0.65	19.63 ± 0.29	3.086 ± 0.098	1.017 ± 0.015
			1800	5.776 ± 0.054	9.40 ± 0.60	29.11 ± 0.41	12.17 ± 0.33	1.083 ± 0.015
			Total	8.838 ± 0.065	19.85 ± 0.88	25.83 ± 0.29	7.385 ± 0.26	1.049 ± 0.011
VRE21	2.17	355-212 µm	700	2.258 ± 0.080	9.26 ± 0.58	22.27 ± 0.85	2.836 ± 0.067	1.016 ± 0.012
			1800	5.6721 ± 0.084	9.59 ± 0.56	26.73 ± 0.46	11.59 ± 0.33	1.132 ± 0.0090
			Total	7.93 ± 0.12	18.85 ± 0.81	25.46 ± 0.41	7.29 ± 0.25	1.0745 ± 0.0080
VRE42	2.21	355-212 µm	700	20.52 ± 0.049	1.0 ± 0.30	99.16 ± 23.39	2.27 ± 0.76	1.146 ± 0.057
			1800	4.190 ± 0.100	2.12 ± 0.26	30.12 ± 0.78	30.98 ± 3.48	1.391 ± 0.021
			Total	4.39 ± 0.11	3.12 ± 0.40	33.34 ± 1.51	21.76 ± 3.14	1.313 ± 0.029
VRE42 (crushed)[a]	0.8	<180 µm	700	38.44 ± 21.91	1.35 ± 0.47	150.8 ± 84.6	1.52 ± 0.49	0.82 ± 0.13
			1800	2.588 ± 0.22	3.12 ± 0.94	39.83 ± 3.25	20.41 ± 2.36	0.83 ± 0.18
			Total	2.973 ± 0.31	4.47 ± 1.05	54.18 ± 13.40	14.70 ± 2.47	0.83 ± 0.091
VRE12	2.17	355-212 µm	700	1.1403 ± 0.0061	17.43 ± 0.88	5.298 ± 0.45	3.063 ± 0.060	1.0196 ± 0.0077
			1800	31.58 ± 0.15	8.17 ± 0.53	2.057 ± 0.030	5.38 ± 0.17	1.064 ± 0.013
			Total	32.72 ± 0.15	25.60 ± 1.02	2.170 ± 0.033	3.801 ± 0.079	1.0337 ± 0.0068
VRE7	2.15	212-180 µm	700	2.626 ± 0.044	2.89 ± 0.22	12.31 ± 0.25	3.11 ± 0.19	0.988 ± 0.037
			1800	28.22 ± 0.15	2.27 ± 0.16	5.680 ± 0.067	31.99 ± 0.77	1.362 ± 0.043
			Total	30.84 ± 0.15	5.16 ± 0.27	6.244 ± 0.066	15.82 ± 0.82	1.153 ± 0.030
SM4	2.24	355-212µm	700	2.601 ± 0.030	19.28 ± 0.88	1.381 ± 0.15	2.873 ± 0.057	1.0140 ± 0.0068
			1800	32.6 ± 0.16	3.77 ± 0.24	0.996 ± 0.022	3.32 ± 0.12	1.035 ± 0.029
			Total	35.18 ± 0.16	23.06 ± 0.91	1.024 ± 0.023	2.947 ± 0.052	1.0174 ± 0.0074
SM7	2.084	355-212 µm	700	2.914 ± 0.053	12.72 ± 0.59	1.396 ± 0.15	2.977 ± 0.064	1.0221 ± 0.0092
			1800	20.44 ± 0.11	3.17 ± 0.21	1.104 ± 0.043	3.27 ± 0.21	1.052 ± 0.031
			Total	23.35 ± 0.12	15.88 ± 0.63	1.140 ± 0.042	3.035 ± 0.066	1.0280 ± 0.0095
SM10	3.77	355-180 µm	700	3.461 ± 0.031	21.42 ± 0.96	0.97 ± 0.15	2.968 ± 0.028	1.0043 ± 0.0036
			1800	18.14 ± 0.10	6.83 ± 0.34	1.044 ± 0.026	3.20 ± 0.77	1.0602 ± 0.0074
			Total	21.60 ± 0.11	28.25 ± 1.024	1.032 ± 0.033	2.994 ± 0.032	1.0178 ± 0.0033

[a] Sample previously crushed under vacuum conditions

Supplementary Table 5.1C. Predicted nucleogenic ^{3}He and radiogenic ^{4}He components from olivine, based on Li, Th and U concentrations and using equations from Andrews (1985)

Sample	Li (ppm)	Th (ppm)	U (ppm)	Predicted nucleogenic ^{3}He (at/g)[a]	Predicted radiogenic ^{4}He (10^{9} at/g)[b]	Measured total ^{4}He (10^{9}at/g)	Radiogenic ^{4}He in total measured (%)	Mantle ^{4}He in total measured ^{4}He (%)[c]	Mantle ^{3}He in total measured ^{3}He (%)[d]	Cosmogenic ^{3}He (10^{5}at/g) after nucleogenic and radiogenic corrections[e]	Cosmogenic ^{3}He in total measured ^{3}He (%)[f]
VRE46	0.220	0.132	0.054	26.2	138	238	58.0	42	1.7	603.2	98.3
VRE21	0.198	0.089	0.051	23.7	117	213	54.9	45	1.8	532.6	98.2
VRE42	0.130	0.012	0.023	2.0	8	118	6.8	93	2.9	282.5	97.1
VRE42 (Crushed)	0.130	0.012	0.023	2.0	8	79.9	10.0	90	1.7	425.5	98.3
VRE12	0.125	0.067	0.030	1.7	15	879	1.7	98	46.5	102.0	53.5
VRE7	0.118	0.052	0.015	0.8	9	829	1.1	99	16.3	433.4	83.7
SM4	0.135	0.183	0.057	0.3	3	945	0.3	100	99.9	0.067	0.1
SM7	0.117	0.078	0.034	0.2	2	628	0.3	100	89.8	7.277	10.2
SM10	0.132	0.219	0.068	0.4	4	581	0.7	99	98.8	0.699	1.2

[a] Nucleogenic ^{3}He calculated from Li, U and Th concentrations using a maximum age of 500 ka for samples VRE46 and VRE21, 100 ka for samples VRE42, VRE12 and VRE7 and 10 ka for samples SM4, SM7 and SM10; based on the equations of Andrews (1985).

[b] Radiogenic ^{4}He calculated from U and Th concentrations of the olivine separate and whole-rock based on the equations of Andrews (1985)

[c] Assuming that, total ^{4}He = ^{4}He mantle + ^{4}He radiogenic, the percentage represents the amount of mantle ^{4}He after subtracting radiogenic ^{4}He from total measured ^{4}He

[d] Assuming that mantle ^{3}He = (^{4}He mantle %) * (total ^{4}He) * $(^{3}He/^{4}He)_{magmatic}$. Where $(^{3}He/^{4}He)$magmatic is = $(1.027 \pm 0.025) \times 10^{-5}$ corresponding to an average local value otained by vacuum crushing from Marchetti et al., 2014

[e] Calculated after nucleogenic and radiogenic correction at sea level and high latitude (SLHL).

[f] Based on cosmogenic ^{3}He = (total ^{3}He) - (mantle ^{3}He) - (predicted nucleogenic ^{3}He).

Supplementary Table 5.1D. Cosmogenic ^{3}He and ^{21}Ne concentrations and corresponding exposure ages

Sample	Lal (1991)					Dunai (2000)					$^{21}Ne_c/^{3}He_c$
	Scaling factor[a]	Cosmogenic ^{3}He (10^{6}at/g)[b]	Cosmogenic ^{21}Ne (10^{6} at/g)[b]	^{3}He age (ka)[c]	^{21}Ne age (ka)[d]	Scaling factor[a]	Cosmogenic ^{3}He (10^{6} at/g)[b]	Cosmogenic ^{21}Ne (10^{6}at/g)[b]	^{3}He age (ka)[c]	^{21}Ne age (ka)[d]	
VRE46	1.33	45.3 ± 0.69	17.7 ± 1.3	374 ± 34	422 ± 49	1.20	50.5 ± 0.68	19.8 ± 1.5	401 ± 45	470 ± 54	0.391 ± 0.029
VRE21	2.50	21.3 ± 0.47	8.77 ± 0.64	176 ± 17	208 ± 22	2.32	23.0 ± 0.51	9.47 ± 0.69	182 ± 21	225 ± 26	0.412 ± 0.031
VRE42	2.62	14.6 ± 0.78	6.03 ± 1.3	121 ± 13	140 ± 32	2.42	15.8 ± 0.84	6.51 ± 1.4	125 ± 15	151 ± 34	0.412 ± 0.090
VRE42 Crushed	2.62	16.3 ± 4.4	6.64 ± 2.3	134 ± 39	125 ± 54	2.42	17.6 ± 4.80	7.18 ± 2.4	139 ± 41	136 ± 58	0.332 ± 0.129
VRE12	2.41	4.24 ± 0.13	2.41 ± 0.59	35 ± 3	55 ± 7	2.22	4.59 ± 0.14	2.60 ± 0.27	36 ± 4	59 ± 8	0.568 ± 0.06
VRE7	2.90	14.9 ± 0.21	6.15 ± 0.51	124 ± 11	140 ± 17	2.70	16.1 ± 0.22	6.61 ± 0.54	127 ± 14	150 ± 18	0.411 ± 0.034
SM4	3.26	0.0021 ± 0.070	-	-	-	3.07	0.0022 ± 0.0744	-	-	-	-
SM7	3.32	2.19 ± 0.081	0.0979 ± 0.0849	1.81 ± 0.69	2.23 ± 1.94	3.13	0.232 ± 0.086	0.104 ± 0.090	1.84 ± 0.71	2.36 ± 2.06	0.447 ± 0.421
SM10	3.47	0.020 ± 0.056	0.0763 ± 0.0704	-	1.73 ± 1.61	3.28	0.0213 ± 0.059	0.0807 ± 0.0744	-	1.84 ± 1.70	3.79 ± 11.1

(-) no data available. Sample SM4 was measured by step heating fusion; however its isotopic ratios is similar to the atmospheric neon composition

[a] Scaling factor calculated using CosmoCalc 2.2 (Vermeesch, 2007), based on Lal (1991) and Dunai (2000)

[b] Final cosmogenic ^{3}He and ^{21}Ne abundance corrected according to scaling factor

[c] Exposure ages calculated using the Gohering et al. (2010) production of 121 ± 11 (at/g/a) using the Lal (1991) scaling factor and 126 ± 14 (at/g/a) using the Dunai (2000) scaling factor

[d] Exposure ages calculated using the Poreda and Cerling (1992) production of 45 ± 4 (at/g/a) for both scaling factors.

Supplementary Figure 5.1. Total neon three-isotope plot, showing the isotopic compositions for different heating steps

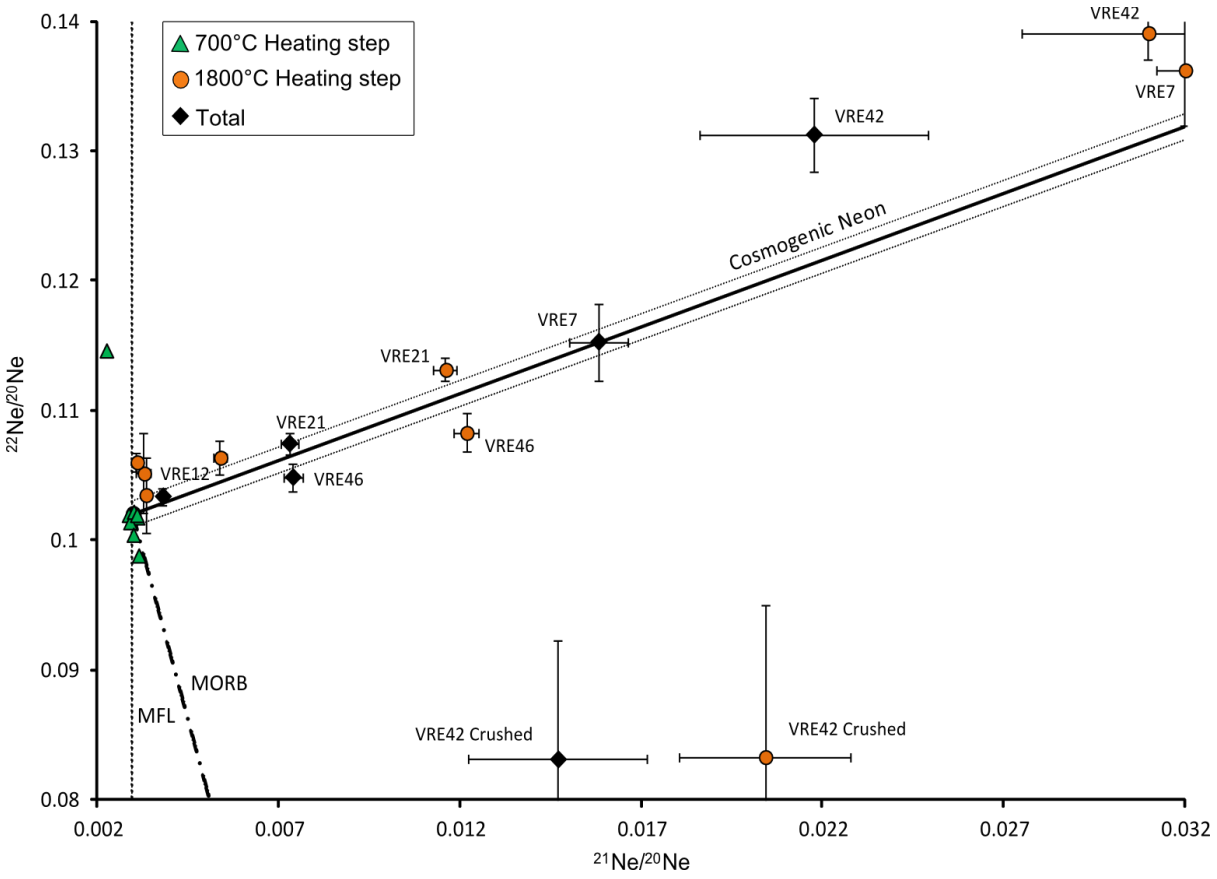

Supplementary Tables 5.2A to 2D. $^{40}Ar/^{39}Ar$

Table 2A: ARGUSVI $^{40}Ar/^{39}Ar$ Analytical Results (UM#57)

Sample ID	Step No	Laser Power	^{40}Ar (fA)	±1σ	^{39}Ar (fA)	±1σ	^{38}Ar (fA)	±1σ	^{37}Ar (fA)	±1σ	^{36}Ar (fA)	±1σ	^{39}Ar (x10^{-14} mol)	Ca/K	±1σ	$\%^{40}Ar^*$	$^{40}Ar^*/^{39}Ar$	±1σ	Cum.% ^{39}Ar	Age (ka)	±1σ
VRE9-1																					
1a	1	4%	1,176.43	0.45	166.10	0.03	0.6709	0.0004	330.0	3.2	3.5710	0.0023	0.5897	3.477	0.034	10.30	0.73	0.00	43.06	147.5	1.0
1b	2	6%	955.64	0.14	120.82	0.11	0.5543	0.0008	260.7	1.9	2.9502	0.0044	0.4289	3.776	0.028	8.77	0.69	0.01	74.39	140.3	2.2
1c	3	8%	645.98	0.17	56.09	0.03	0.3879	0.0005	183.7	6.7	2.0648	0.0025	0.1991	5.730	0.208	5.55	0.64	0.01	88.93	129.2	2.7
1d	4	10%	453.90	0.17	26.16	0.03	0.2795	0.0003	165.5	4.1	1.4877	0.0016	0.0929	11.075	0.275	3.15	0.55	0.02	95.71	110.4	3.8
1e	5	14%	431.70	0.09	16.54	0.03	0.2699	0.0003	195.9	5.6	1.4364	0.0017	0.0587	20.734	0.598	1.68	0.44	0.03	100.00	88.6	6.2
			3,663.65	**0.54**	**385.71**	**0.12**					**11.5101**	**0.0060**		**40Ar*± 1σ:**	**262.42**	**1.86**	**0.68**	**0.02**	**Total-gas age:**	**137.6**	**3.6**
RG-1-1																					
1a	1	3%	740.32	0.51	105.76	0.07	0.3663	0.0006	95.5	5.7	1.9497	0.0029	0.3754	1.580	0.095	22.18	1.55	0.01	14.60	313.9	1.9
1b	2	4%	840.54	0.68	151.85	0.17	0.3794	0.0009	141.3	6.3	2.0194	0.0049	0.5391	1.629	0.072	29.00	1.61	0.01	35.56	324.6	2.2
1c	3	6%	1,144.16	1.37	210.35	0.31	0.5182	0.0013	215.5	6.1	2.7580	0.0068	0.7467	1.793	0.051	28.77	1.56	0.01	64.60	316.4	2.4
1d	4	8%	769.11	0.78	132.35	0.13	0.3570	0.0004	190.9	4.4	1.9000	0.0024	0.4698	2.524	0.059	27.00	1.57	0.01	82.88	317.3	1.6
1e	5	10%	504.56	0.26	73.49	0.04	0.2473	0.0006	160.2	5.1	1.3165	0.0034	0.2609	3.816	0.121	22.90	1.57	0.01	93.02	317.9	2.9
1f	6	14%	477.39	0.26	50.56	0.03	0.2539	0.0006	215.9	4.5	1.3513	0.0030	0.1795	7.472	0.157	16.35	1.54	0.02	100.00	312.3	3.7
			4,476.08	**1.83**	**724.35**	**0.39**					**11.2950**	**0.0102**		**40Ar*± 1σ:**	**1,138.40**	**3.54**	**1.57**	**0.05**	**Total-gas age:**	**317.8**	**10.4**
RG-2-1																					
1a	1	4%	2,769.20	0.89	224.87	0.08	1.7610	0.0015	298.8	6.9	9.3734	0.0079	0.7983	2.326	0.053	0.00	0.00	0.00	42.83	N/A	N/A
1b	2	5%	1,434.26	0.44	115.63	0.08	0.9095	0.0012	170.3	6.4	4.8413	0.0065	0.4105	2.577	0.097	0.26	0.03	0.02	64.85	6.4	3.5
1c	3	6%	941.26	0.49	73.65	0.03	0.5972	0.0009	134.7	5.7	3.1787	0.0045	0.2615	3.200	0.136	0.21	0.03	0.02	78.87	5.4	3.9
1d	4	8%	954.68	0.21	63.71	0.07	0.6063	0.0007	195.3	8.6	3.2274	0.0037	0.2262	5.365	0.236	0.10	0.02	0.02	91.01	3.1	3.6
1e	5	10%	600.20	0.20	29.72	0.03	0.3807	0.0005	168.0	5.9	2.0264	0.0027	0.1055	9.894	0.350	0.24	0.05	0.03	96.67	9.6	5.6
1f	6	14.0%	556.24	0.19	17.51	0.03	0.3548	0.0008	205.4	6.6	1.8886	0.0042	0.0621	20.529	0.663	0.00	0.00	0.00	100.00	N/A	N/A
			7,255.85	**1.16**	**525.09**	**0.15**					**24.5357**	**0.0128**		**40Ar*± 1σ:**	**5.54**	**3.96**	**0.01**	**0.01**	**Total-gas age:**	**2.1**	**1.5**

SM14-1																				
1a	1	3.0%	1,373.27	1.92	72.94	0.05	0.8752	0.0009	105.2	9.4	4.6585	0.0048	0.2589	2.524	0.224	0.00	0.00	0.00	20.27	N/A	N/A
1b	2	5.0%	2,825.03	1.61	171.22	0.11	1.8083	0.0019	257.1	10.3	9.6252	0.0102	0.6078	2.628	0.106	0.00	0.00	0.00	67.84	N/A	N/A
1c	3	8.0%	2,115.99	0.93	115.72	0.07	1.3436	0.0012	228.8	6.4	7.1519	0.0065	0.4108	3.460	0.097	0.12	0.02	0.02	100.00	4.6	3.7
SM14-2																				
2a	1	3.00%	3,630.91	3.92	170.84	0.27	2.3054	0.0048	270.2	9.5	12.2713	0.0253	0.6065	2.768	0.097	0.13	0.03	0.05	30.00	5.6	10.0
2b	2	4.00%	2,635.15	1.48	138.45	0.15	1.6714	0.0043	236.4	13.6	8.8964	0.0230	0.4915	2.988	0.171	0.24	0.05	0.05	54.31	9.2	10.2
2c	3	6.00%	2,754.25	2.09	146.95	0.10	1.7412	0.0018	259.1	10.7	9.2679	0.0096	0.5217	3.086	0.128	0.57	0.11	0.02	80.12	21.5	4.9
2d	4	8.00%	1,624.83	0.88	65.61	0.05	1.0230	0.0010	181.7	9.5	5.4454	0.0055	0.2329	4.848	0.253	0.97	0.24	0.03	91.64	48.5	5.7
2e	5	10.00%	566.08	0.33	21.76	0.04	0.3557	0.0006	74.27	11.5	1.8931	0.0031	0.0773	5.970	0.925	1.18	0.31	0.05	95.46	62.0	9.1
2f	6	14.00%	712.19	0.34	25.86	0.02	0.4488	0.0007	132.1	9.0	2.3887	0.0036	0.0918	8.939	0.607	0.89	0.24	0.04	100.00	49.5	8.7
			11,923.40	**4.79**	**569.48**	**0.33**					**40.1629**	**0.0363**		**40Ar*± 1σ:**	**55.26**	**11.74**	**0.10**	**0.02**	**Total-gas age:**	**19.7**	**4.2**
SM17																				
1a	1	3.0%	2,184.35	0.70	82.34	0.05	1.3998	0.0020	171.2	8.9	7.4508	0.0104	0.2923	3.638	0.190	0.00	0.00	0.00	21.92	N/A	N/A
1b	2	4.0%	2,531.37	1.80	107.58	0.12	1.6208	0.0018	231.5	9.5	8.6270	0.0096	0.3819	3.765	0.155	0.00	0.00	0.00	50.57	N/A	N/A
1c	3	6.0%	3,082.06	0.59	114.32	0.05	1.9797	0.0028	274.0	8.2	10.5378	0.0148	0.4058	4.194	0.126	0.00	0.00	0.00	81.00	N/A	N/A
1d	4	10.0%	2,798.83	1.04	71.35	0.02	1.7924	0.0027	346.0	10.5	9.5408	0.0144	0.2533	8.487	0.256	0.00	0.00	0.00	100.00	N/A	N/A
SM18-1																				
1a	1	3.0%	1,586.59	0.54	60.88	0.07	1.0061	0.0012	172.1	10.9	5.3555	0.0066	0.2161	4.948	0.314	0.25	0.07	0.03	20.86	13.4	6.8
1b	2	4.0%	1,946.42	0.68	74.07	0.04	1.2333	0.0011	219.6	11.1	6.5649	0.0057	0.2629	5.189	0.263	0.33	0.09	0.02	46.23	17.8	4.9
1c	3	5.0%	1,604.70	0.64	53.57	0.04	1.0121	0.0009	172.7	10.2	5.3873	0.0050	0.1902	5.644	0.334	0.79	0.24	0.03	64.58	48.3	6.1
1d	4	6.0%	1,247.49	0.24	35.89	0.03	0.7889	0.0010	146.7	9.5	4.1992	0.0054	0.1274	7.151	0.463	0.53	0.18	0.04	76.88	37.5	9.1
1e	5	8.0%	1,374.09	0.60	36.32	0.04	0.8702	0.0012	221.3	6.6	4.6321	0.0064	0.1289	10.665	0.316	0.39	0.15	0.05	89.32	29.7	11.1
1f	6	10.0%	883.55	0.28	19.49	0.04	0.5582	0.0008	187.8	6.1	2.9710	0.0043	0.0692	16.859	0.550	0.64	0.29	0.07	100.00	58.7	13.6
1g	7	14.0%	738.31	0.23	11.67	0.02	0.4703	0.0009	201.5	5.8	2.5031	0.0045	0.0414	30.201	0.868	0.00	0.00	0.00	N/A	N/A	N/A
			9,381.15	**1.31**	**291.90**	**0.11**					**31.6130**	**0.0145**		**40Ar*± 1σ:**	**39.51**	**4.48**	**0.14**	**0.02**	**Total gas-age:**	**27.5**	**3.2**

LV6-1																					
1a	1	3.0%	760.52	0.20	83.52	0.06	0.4845	0.0012	164.9	7.7	2.5792	0.0062	0.2965	3.456	0.162	0.00	0.00	0.00	24.92	N/A	N/A
1b	2	4.0%	971.52	0.31	100.67	0.04	0.6192	0.0005	231.8	12.1	3.2960	0.0029	0.3574	4.030	0.211	0.00	0.00	0.00	54.96	N/A	N/A
1c	3	6.0%	1,227.94	0.36	96.18	0.07	0.7852	0.0016	308.5	9.6	4.1795	0.0084	0.3414	5.614	0.175	0.00	0.00	0.00	83.65	N/A	N/A
1d	4	8.0%	761.03	0.30	34.34	0.03	0.4862	0.0009	233.0	11.2	2.5881	0.0049	0.1219	11.874	0.570	0.00	0.00	0.00	93.90	N/A	N/A
1e	5	10.0%	526.94	0.26	13.12	0.04	0.3365	0.0006	210.1	14.0	1.7912	0.0032	0.0466	28.015	1.873	0.00	0.00	0.00	97.82	N/A	N/A
1f	6	14.0%	518.29	0.26	7.32	0.03	0.3313	0.0009	261.2	15.3	1.7633	0.0047	0.0260	62.431	3.667	0.00	0.00	0.00	100.00	N/A	N/A
RG11-1																					
1a	1	3.00%	794.14	0.15	70.92	0.02	0.5054	0.0007	170.3	10.3	2.6903	0.0037	0.2518	4.204	0.254	0.00	0.00	0.00	16.42	N/A	N/A
1b	1	4.00%	1,009.36	0.42	96.06	0.12	0.6468	0.0013	233.3	12.3	3.4430	0.0068	0.3410	4.251	0.225	0.00	0.00	0.00	38.67	N/A	N/A
1c	1	6.00%	1,518.17	0.27	122.67	0.15	0.9754	0.0006	321.0	8.7	5.1921	0.0031	0.4355	4.579	0.124	0.00	0.00	0.00	67.08	N/A	N/A
1d	1	8.00%	1,162.30	0.33	65.85	0.04	0.7433	0.0013	210.2	12.8	3.9566	0.0068	0.2338	5.587	0.341	0.00	0.00	0.00	82.33	N/A	N/A
1e	1	10.00%	932.20	0.22	36.44	0.02	0.5960	0.0004	187.4	11.1	3.1725	0.0023	0.1294	8.998	0.533	0.00	0.00	0.00	90.77	N/A	N/A
1f	1	14.00%	1,601.59	0.67	26.67	0.02	1.0180	0.0013	241.9	10.7	5.4187	0.0069	0.0947	15.878	0.703	0.00	0.00	0.00	96.94	N/A	N/A
1g	1	18.00%	654.23	0.20	9.50	0.03	0.4189	0.0006	137.3	13.0	2.2296	0.0032	0.0337	25.276	2.390	0.00	0.00	0.00	99.14	N/A	N/A
1h	1	22.00%	321.58	0.12	3.70	0.01	0.2046	0.0004	83.74	12.8	1.0893	0.0020	0.0131	39.661	6.076	0.00	0.00	0.00	100.00	N/A	N/A

Weight of sample VRE9 = 99.2 mg, J-value = $(112.076 \pm 0.088)x10^{-6}$
Weight of sample RG1 = 101.5mg, J-value = $(112.097 \pm 0.090)x10^{-6}$
Weight of sample RG2 =100.9 mg, J-value = $(112.157 \pm 0.116)x10^{-6}$
Weight of sample SM14 = 76.2 mg, J-value = $(112.279 \pm 0.168)x10^{-6}$
Weight of sample SM14 = 103.5 mg, J-value = $(112.279 \pm 0.168)x10^{-6}$
Weight of sample SM17 = 100.6 mg, J-value = $(112.330 \pm 0.206)x10^{-6}$
Weight of sample SM18 = 102.8 mg, J-value = $(112.432 \pm 0.281)x10^{-6}$
Weight of sample LV6 = 103.8 mg, J-value = $(112.728 \pm 0.282)x10^{-6}$
Weight of sample RG11 = 103.8 mg, J-value = $(112.323 \pm 0.283)x10^{-6}$

1. Errors are one sigma uncertainties and exclude uncertainties in the J-value.
2. Data are corrected for mass spectrometer backgrounds, discrimination and radioactive decay.
3. Corrections: $(^{36}Ar/^{37}Ar)_{Ca} = 2.7002\ (\pm 0.0024) \times 10^{-4}$, $(^{39}Ar/^{37}Ar)_{Ca} = 6.716\ (\pm 0.018) \times 10^{-4}$; $(^{40}Ar/^{39}Ar)_{K} = 3.00\ (\pm 0.93) \times 10^{-4}$; $(^{38}Ar/^{39}Ar)_{K} = 0.013109\ (\pm 0.000017)$
4. J-value is based on an age of 1.186 ± 0.006 Ma for AC sanidine (Turrin et al., 1994).

Table 5.2B. ARGUS VI blanks (UM#57)

Blank Data	Sample ID	^{40}Ar (fA)	±1σ	^{39}Ar (fA)	±1σ	^{38}Ar (fA)	±1σ	^{37}Ar (fA)	±1σ	^{36}Ar (fA)	±1σ
EXB#14	VRE9-1a	1176.4806	0.45	166.0091	0.03	3.0133	0.0339	1.7362	0.0167	3.6602	0.0023
EXB#14	VRE9-1b	955.6748	0.14	120.7678	0.11	2.2219	0.0447	1.3713	0.0102	3.0207	0.0044
EXB#17	VRE9-1c	645.9948	0.17	56.1082	0.03	1.1840	0.0446	0.9653	0.0351	2.1144	0.0025
EXB#17	VRE9-1d	453.9086	0.17	26.2217	0.03	0.6578	0.0408	0.8699	0.0215	1.5324	0.0016
EXB#18	VRE9-1e	431.7028	0.09	16.6384	0.03	0.4807	0.0325	1.0291	0.0296	1.4893	0.0017
EXB#25	RG-1-1a	1.4140	0.10	0.0405	0.03	-0.0082	0.0272	0.0012	0.0105	0.0065	0.0003
EXB#25	RG-1-1b	1.4140	0.10	0.0405	0.03	-0.0082	0.0272	0.0012	0.0105	0.0065	0.0003
EXB#26	RG-1-1c	3.0888	0.48	0.1205	0.01	-0.0079	0.0133	-0.0407	0.0173	0.0128	0.0012
EXB#26	RG-1-1d	3.0888	0.48	0.1205	0.01	-0.0079	0.0133	-0.0407	0.0173	0.0128	0.0012
EXB#27	RG-1-1e	2.2182	0.25	0.1220	0.02	-0.0268	0.0148	0.0073	0.0065	0.0109	0.0005
EXB#27	RG-1-1f	2.2182	0.25	0.1220	0.02	-0.0268	0.0148	0.0073	0.0065	0.0109	0.0005
EXB#21	RG-2-1a	1.1088	0.03	0.0122	0.02	-0.0566	0.0266	-0.0085	0.0160	0.0053	0.0001
EXB#21	RG-2-1b	1.1088	0.03	0.0122	0.02	-0.0566	0.0266	-0.0085	0.0160	0.0053	0.0001
EXB#23	RG-2-1c	2.0255	0.10	0.0795	0.02	-0.0131	0.0242	-0.0034	0.0222	0.0077	0.0005
EXB#23	RG-2-1d	2.0255	0.10	0.0795	0.02	-0.0131	0.0242	-0.0034	0.0222	0.0077	0.0005
EXB#24	RG-2-1e	2.9618	0.19	0.1209	0.03	0.0187	0.0274	-0.0238	0.0228	0.0103	0.0009
EXB#24	RG-2-1f	2.9618	0.19	0.1209	0.03	0.0187	0.0274	-0.0238	0.0228	0.0103	0.0009
EXB#41	SM14-2a	0.9936	0.02	-0.0254	0.02	-0.0828	0.0235	-0.0287	0.0188	0.0054	0.0003
EXB#41	SM14-2b	0.9936	0.02	-0.0254	0.02	-0.0828	0.0235	-0.0287	0.0188	0.0054	0.0003
EXB#41	SM14-2c	0.9936	0.02	-0.0254	0.02	-0.0828	0.0235	-0.0287	0.0188	0.0054	0.0003
EXB#42	SM14-2d	3.2210	0.33	0.0784	0.02	-0.0504	0.0138	-0.0230	0.0221	0.0129	0.0005
EXB#42	SM14-2e	3.2210	0.33	0.0784	0.02	-0.0504	0.0138	-0.0230	0.0221	0.0129	0.0005
EXB#42	SM14-2f	3.2210	0.33	0.0784	0.02	-0.0504	0.0138	-0.0230	0.0221	0.0129	0.0005
EXB#33	SM17-1a	1.2810	0.07	0.0345	0.01	-0.0484	0.0250	-0.0056	0.0213	0.0060	0.0002
EXB#33	SM17-1b	1.2810	0.07	0.0345	0.01	-0.0484	0.0250	-0.0056	0.0213	0.0060	0.0002
EXB#33	SM17-1c	1.2810	0.07	0.0345	0.01	-0.0484	0.0250	-0.0056	0.0213	0.0060	0.0002
EXB#33	SM17-1d	1.2810	0.07	0.0345	0.01	-0.0484	0.0250	-0.0056	0.0213	0.0060	0.0002
EXB#29	SM18-1a	0.7991	0.01	-0.0077	0.02	-0.0446	0.0268	-0.0467	0.0325	0.0046	0.0001
EXB#29	SM18-1b	0.7991	0.01	-0.0077	0.02	-0.0446	0.0268	-0.0467	0.0325	0.0046	0.0001
EXB#30	SM18-1c	1.0541	0.04	0.0037	0.01	-0.0675	0.0269	-0.0464	0.0292	0.0056	0.0002
EXB#30	SM18-1d	1.0541	0.04	0.0037	0.01	-0.0675	0.0269	-0.0464	0.0292	0.0056	0.0002
EXB#31	SM18-1e	2.1070	0.16	0.0282	0.02	-0.0465	0.0104	-0.0502	0.0168	0.0100	0.0003
EXB#31	SM18-1f	2.1070	0.16	0.0282	0.02	-0.0465	0.0104	-0.0502	0.0168	0.0100	0.0003
EXB#32	SM18-1g	1.6303	0.16	0.0432	0.01	-0.0727	0.0245	0.0117	0.0068	0.0078	0.0005
EXB#35	LV6-1a	0.7669	0.01	0.0269	0.03	-0.0856	0.0183	-0.0372	0.0191	0.0045	0.0001
EXB#35	LV6-1b	0.7669	0.01	0.0269	0.03	-0.0856	0.0183	-0.0372	0.0191	0.0045	0.0001
EXB#35	LV6-1c	0.7669	0.01	0.0269	0.03	-0.0856	0.0183	-0.0372	0.0191	0.0045	0.0001
EXB#36	LV6-1d	2.2841	0.26	0.0924	0.03	-0.0283	0.0147	-0.0350	0.0316	0.0100	0.0007
EXB#36	LV6-1e	2.2841	0.26	0.0924	0.03	-0.0283	0.0147	-0.0350	0.0316	0.0100	0.0007
EXB#36	LV6-1f	2.2841	0.26	0.0924	0.03	-0.0283	0.0147	-0.0350	0.0316	0.0100	0.0007
EXB#37	RG11-1a	1.6037	0.03	0.0470	0.02	-0.0291	0.0256	-0.0192	0.0173	0.0066	0.0005
EXB#37	RG11-1b	1.6037	0.03	0.0470	0.02	-0.0291	0.0256	-0.0192	0.0173	0.0066	0.0005
EXB#37	RG11-1c	1.6037	0.03	0.0470	0.02	-0.0291	0.0256	-0.0192	0.0173	0.0066	0.0005
EXB#38	RG11-1d	11.5518	0.16	0.2393	0.01	0.0087	0.0100	0.0579	0.0291	0.0398	0.0009
EXB#39	RG11-1e	4.0435	0.11	0.1703	0.01	-0.0492	0.0280	0.0005	0.0303	0.0132	0.0011
EXB#39	RG11-1f	4.0435	0.11	0.1703	0.01	-0.0492	0.0280	0.0005	0.0303	0.0132	0.0011
EXB#39	RG11-1g	4.0435	0.11	0.1703	0.01	-0.0492	0.0280	0.0005	0.0303	0.0132	0.0011
EXB#39	RG11-1h	4.0435	0.11	0.1703	0.01	-0.0492	0.0280	0.0005	0.0303	0.0132	0.0011

Supplementary Table 5.2C. ARGUSVI $^{40}Ar/^{39}Ar$ analytical results for AC sanidine flux monitor (UM#57)

Sample ID	Step No	Laser Power	^{40}Ar (fA)	±1σ	^{39}Ar (fA)	±1σ	^{38}Ar (fA)	±1σ	^{37}Ar (fA)	±1σ	^{36}Ar (fA)	±1σ	^{39}Ar ($x10^{-14}$ mol)	Ca/K	±1σ	$\%^{40}Ar^*$	$^{40}Ar^*/^{39}Ar$	±1σ
A1																		
A1-1	1	35%	402.84	0.11	64.66	0.02	0.0147	0.0002	7.7832	3.1923	0.0781	0.0008	0.2296	0.211	0.086	94.27	5.873	0.005
A1-2	1	35%	580.66	0.16	94.37	0.03	0.0163	0.0001	6.4593	2.3070	0.0869	0.0004	0.3350	0.120	0.043	95.57	5.881	0.003
A1-3	1	35%	418.97	0.16	68.17	0.03	0.0121	0.0001	0.0728	2.5815	0.0642	0.0005	0.2420	0.002	0.066	95.47	5.868	0.004
A1-4	1	35%	383.73	0.05	62.80	0.04	0.0098	0.0001	0.2840	2.2735	0.0521	0.0007	0.2230	0.008	0.063	95.98	5.865	0.005
A1-5	1	35%	728.19	0.20	103.35	0.03	0.0819	0.0002	1.9564	1.3876	0.4361	0.0013	0.3669	0.033	0.023	82.30	5.799	0.004
A2																		
A2-1	1	35%	484.14	0.08	77.33	0.05	0.0192	0.0002	7.8366	5.1123	0.1023	0.0011	0.2745	0.177	0.116	93.75	5.870	0.006
A2-2	1	35%	517.64	0.11	82.12	0.05	0.0256	0.0002	13.0580	4.3486	0.1362	0.0008	0.2915	0.278	0.093	92.22	5.814	0.005
A2-3	1	35%	841.28	0.09	114.26	0.04	0.1097	0.0009	-3.2302	-6.2394	0.5839	0.0047	0.4056	-0.049	-0.096	79.49	5.853	0.012
A2-1	1	35%	484.14	0.08	77.33	0.05	0.0192	0.0002	7.8366	5.1123	0.1023	0.0011	0.2745	0.177	0.116	93.75	5.870	0.006
A2-2	1	35%	517.64	0.11	82.12	0.05	0.0256	0.0002	13.0580	4.3486	0.1362	0.0008	0.2915	0.278	0.093	92.22	5.814	0.005
A2-3	1	35%	841.28	0.09	114.26	0.04	0.1097	0.0009	-3.2302	-6.2394	0.5839	0.0047	0.4056	-0.049	-0.096	79.49	5.853	0.012
A2-4	1	35%	601.87	0.09	98.88	0.09	0.0151	0.0002	-5.0718	-3.8528	0.0802	0.0010	0.3510	-0.090	-0.068	96.06	5.847	0.006
A2-5	1	35%	649.18	0.08	107.33	0.06	0.0227	0.0002	17.5891	5.7909	0.1207	0.0010	0.3810	0.287	0.094	94.50	5.716	0.004
A2-6	1	35%	572.14	0.14	83.61	0.03	0.0520	0.0001	-1.6563	-4.4624	0.2766	0.0006	0.2968	-0.035	-0.093	85.71	5.865	0.003
A2-7	1	35%	411.45	0.09	67.25	0.04	0.0109	0.0001	-4.9928	-6.1649	0.0581	0.0007	0.2387	-0.130	-0.160	95.82	5.863	0.005
A2-8	1	35%	587.57	0.05	78.95	0.05	0.0951	0.0002	25.6756	7.0498	0.5061	0.0012	0.2803	0.569	0.156	74.55	5.548	0.006
A3																		
A3-1	1	35%	638.60	0.12	95.79	0.05	0.0611	0.0002	2.0484	2.8743	0.3250	0.0008	0.3401	0.037	0.053	84.96	5.664	0.004
A3-2	1	35%	403.32	0.09	67.40	0.02	0.0058	0.0001	-7.0138	-3.8773	0.0308	0.0005	0.2393	-0.182	-0.101	97.74	5.849	0.003
A3-3	1	35%	622.82	0.13	104.68	0.05	0.0051	0.0001	13.2278	4.6838	0.0273	0.0007	0.3716	0.221	0.078	98.70	5.873	0.003
A3-4	1	35%	502.40	0.11	81.18	0.03	0.0171	0.0001	2.4806	4.5604	0.0908	0.0004	0.2882	0.053	0.098	94.66	5.859	0.003
A3-5	1	35%	536.50	0.18	83.87	0.04	0.0301	0.0002	-16.8519	-7.1107	0.1602	0.0009	0.2978	-0.352	-0.148	91.17	5.832	0.005
A3-6	1	35%	405.72	0.06	65.78	0.04	0.0135	0.0001	-9.3360	-4.5215	0.0716	0.0004	0.2335	-0.248	-0.120	94.78	5.846	0.004

A4																	
A4-1	1	35%	364.93	0.09	37.75	0.01	0.0963	0.0001	-5.1050	-7.6553	0.5128	0.0007	0.1340	-0.237	-0.355	58.48	5.653	0.006
A4-2	1	35%	404.87	0.02	66.21	0.04	0.0122	0.0001	-9.8695	-7.0615	0.0650	0.0006	0.2350	-0.261	-0.187	95.25	5.825	0.005
A4-3	1	35.%	1,089.65	0.28	102.17	0.03	0.3127	0.0004	7.2552	8.9951	1.6644	0.0021	0.3627	0.124	0.154	54.86	5.851	0.007
A4-4	1	35%	459.88	0.12	75.90	0.04	0.0096	0.0001	11.9126	8.4051	0.0509	0.0005	0.2695	0.275	0.194	96.73	5.861	0.004
A4-5	1	35%	550.15	0.16	89.14	0.07	0.0177	0.0001	13.8400	2.9704	0.0940	0.0003	0.3164	0.272	0.058	94.95	5.860	0.005
A4-6	1	35%	592.16	0.30	89.09	0.06	0.0529	0.0001	20.0054	4.3078	0.2817	0.0008	0.3163	0.393	0.085	85.94	5.712	0.006
A5																		
A5-1	1	35%	693.05	0.16	107.98	0.04	0.0433	0.0001	8.2121	7.0260	0.2305	0.0007	0.3833	0.133	0.114	90.17	5.787	0.003
A5-2	1	35%	473.48	0.16	75.29	0.07	0.0216	0.0001	1.5079	6.2922	0.1151	0.0005	0.2673	0.035	0.146	92.81	5.837	0.006
A5-3	1	35%	495.06	0.06	74.71	0.06	0.0389	0.0003	2.9321	4.4753	0.2072	0.0015	0.2652	0.069	0.105	87.63	5.807	0.007
A5-4	1	35%	801.46	0.16	116.39	0.06	0.0774	0.0005	6.1381	6.2173	0.4118	0.0025	0.4132	0.092	0.093	84.81	5.841	0.007
A5-5	1	35%	363.17	0.08	58.39	0.04	0.0159	0.0001	6.9280	9.9032	0.0847	0.0008	0.2073	0.208	0.297	93.10	5.791	0.006
A5-6	1	35%	273.34	0.10	41.39	0.05	0.0259	0.0001	20.2285	7.0083	0.1378	0.0008	0.1469	0.855	0.296	85.10	5.620	0.008

1. Errors are one sigma uncertainties and exclude uncertainties in the J-value.

2. Data are corrected for mass spectrometer backgrounds, discrimination and radioactive decay.

3. Corrections: $(^{36}Ar/^{37}Ar)_{Ca} = 2.7002\ (\pm 0.0024) \times 10^{-4}$, $(^{39}Ar/^{37}Ar)_{Ca} = 6.716\ (\pm 0.018) \times 10^{-4}$; $(^{40}Ar/^{39}Ar)_{K} = 3.00\ (\pm 0.93) \times 10^{-4}$; $(^{38}Ar/^{39}Ar)_{K} = 0.013109\ (\pm 0.000017)$

Supplementary Table 5.2D. Summary of results from $^{40}Ar/^{39}Ar$ analysis

Location	Sample	Plateau age				
		^{39}Ar (%)	steps used	Age ± 2σ (ka)	MSWD	
Río Grande	RG1	64.40	4 of 6	317 ± 2	0.56	

		Inverse isochron age			Total-gas age
		$^{40}Ar/^{36}Ar_i$	MSWD	Age ± 2σ (ka)	Age ± 2σ (ka)
Río Grande	RG1	292.4 ± 5.7	2.5	328 ± 19	318 ±10
Río Grande	RG2	295.4 ± 1.5	2	N/R	2.1 ± 1.5
W side of Santa Maria flow	SM14	306.5 ± 9.4	2.5	N/R	20 ± 4
W side of Santa Maria flow	SM18	288.2 ± 23.25	5.8	N/R	28 ± 3
Malacara Volcano	VRE9	290.7 ± 0.68	1.8	168 ± 4.3	138 ± 3.6

N/R refers to not resolved

Supplementary Figure 5.2. $^{40}Ar/^{39}Ar$ spectra results and inverse isochrons. Plateau steps are in red and rejected steps are in blue.

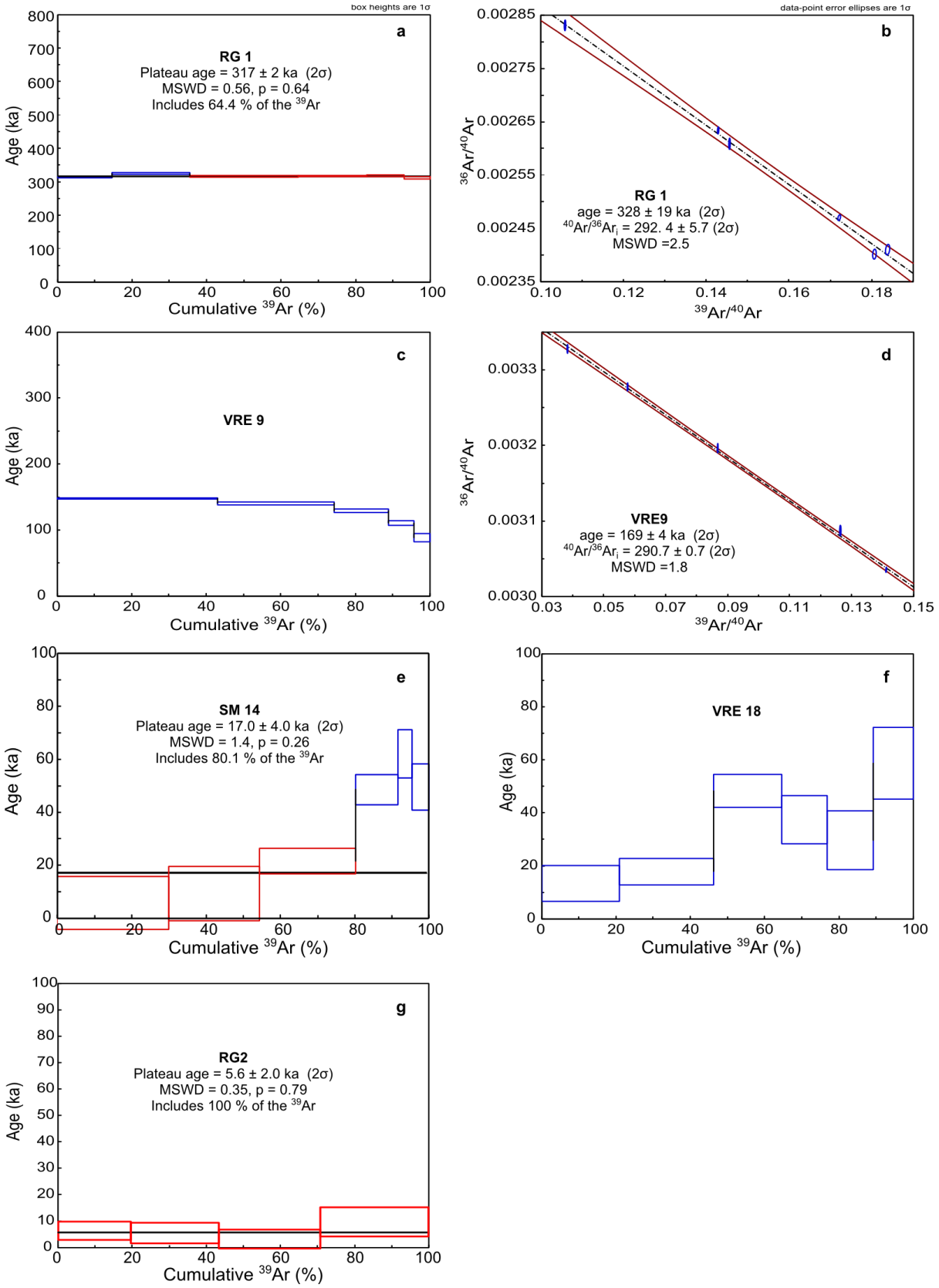

Supplementary Table 5.3. Thermoluminescence dating parameters and results

Specimen No.	**W4670pal**	**W4670bas**
Reference	Minimum age	Maximum age
Plateau region (°C)	275 - 425	275 - 425
Analysis temperature (°C)	350	350
Palaeodose (Gray)	20.9 ± 1.6	20.9 ± 1.6
K content (% by XRF)	1.45 ± 0.05	1.00 ± 0.05
Rb content (ppm by XRF)	68 ± 10	18 ± 5
Moisture content (weight %)	0	0
k coefficient alpha/beta efficiency	0.059 ± 0.010	0.059 ± 0.010
Specific activity (Bq/kg U+Th)	60.3 ± 1.5	15.6 ± 0.4
Cosmic contribution (µGy/a assumed)	75 ± 25	75 ± 25
Annual radiation dose (µGy/a)	3556 ± 88	2972 ± 81
TL Age (years BP)	**5880 ± 450**	**7040 ± 530**

Chapter 6

Synthesis

Global perspective

The alkaline volcanism occurring in central west Argentina can be classified geographically as retroarc as it is located behind the Andean volcanic arc with low degree of extension. However, the geochemical signatures suggest an intraplate setting in parts slightly modified by subduction to the west. The lack of clear characterisation of basaltic volcanism occurring behind a continental volcanic arc, has been previously proposed for the High Lava Plains in the north-west United States (Jordan, 2001). The understanding of continental back-arc volcanism constitutes one of the principal aims of the current investigation. According to the findings from this contribution, the continental back-arc in central west Argentina is characterised by alkali basaltic volcanism (Chapter 2 and 4) and a low degree of partial melting (Chapter 4) with minor influence from subduction-related components (Chapter 2). These broad findings are also relevant to similar settings outside the Patagonian back-arc fields, such as in the High Lava Plains in the western USA (Jordan, 2001; Till et al., 2013), the Eastern Mexican Volcanic Belt, (Carrasco-Núñez et al., 2005), the Auckland volcanic field in New Zealand (McGee et al., 2013) and the Behind the Volcanic Front lavas in eastern Nicaragua (Janoušek et al., 2010).

One of the volcanic products commonly associated with back-arc settings is the production of tholeiite lavas such as in the case of the High Lava Plains in the western USA, where this type of lava, is the most abundant and is associated with an extensional tectonic setting. The Eastern Mexican Volcanic Belt also shows tectonic extension (Márquez et al., 1999), while in other places like the Auckland volcanic field and the Behind the Volcanic Front lavas, tectonic extension has not been reported. In the case of the Llancanelo and Payún Matrú volcanic fields low degree extension since the Pliocene, has been inferred (Kay et al. 2006a). Tectonic extension results in crustal thinning, therefore the lithosphere becomes thinner and the asthenosphere shallower. In all the continental back-arc settings previously mentioned, the continental crust is thinner than 40 km and in some cases such as the High Lava Plains in Oregon USA the lithosphere-asthenospheric boundary is located at approximately at 40-60 km depth (Till et al., 2013). In the Western USA, the back-arc basalts are predominantly sourced by a depleted upper mantle similar to a Mid-ocean ridge basalt source, with low influence from an enriched mantle similar to Ocean Island Basalt (OIB; Jordan, 2001). The High Lava Plains suite is the most depleted having the lowest enrichment in immobile elements such as Nb and Zr, and the highest Ba enrichment, while the Auckland volcanic field is the most enriched, with the highest content of immobile elements and lowest Ba content (Figure 6.1). Other continental back-arcs are located between these two extremes except three samples from the Behind the Volcanic Front in Nicaragua (Samples NC15, NC16 and NC17) for which subduction-related signatures were described (Janoušek et al., 2010). Accordingly, all the continental back-arc

basalts have some subduction-related signature, which could range from minimal to negligible such as in the Auckland volcanic field or the Behind the Volcanic Front lavas to elevated such as in the case of the High Lava Plains and samples NC15, NC16 and NC17 from the Nicaraguan back-arc. The Llancanelo and the Payún Matrú volcanic fields share a similar diversity as in the Eastern Mexican Volcanic Belt, between the high and low subduction influenced limits (Figure 6.1).

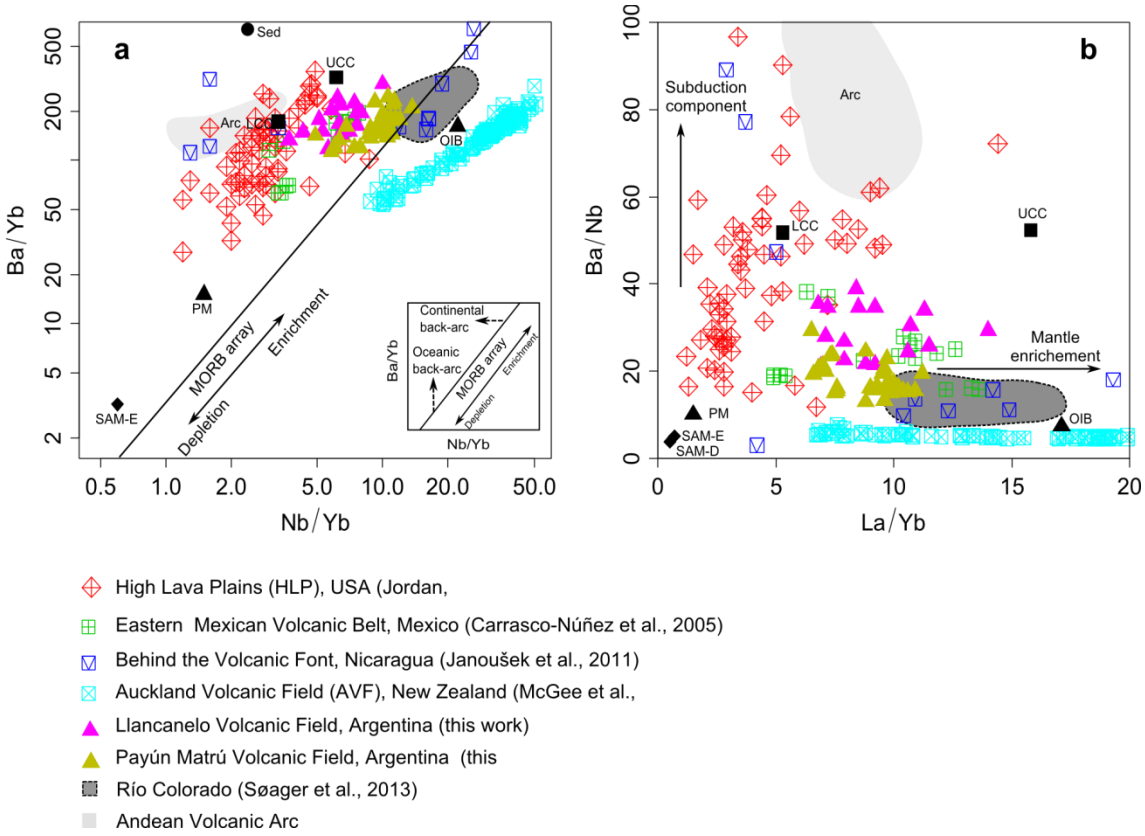

Figure 6.1. Trace-element ratio diagrams of continental back-arc settings. a) log Nb/Yb (proxy for mantle fertility) vs log Ba/Yb (proxy for shallow subduction component. b) La/Yb vs Ba/Nb, (La/Yb proxy for mantle enrichment), Ba/Nb (proxy for total subduction component). Both diagrams have been modified from Pearce et al., 2005. The data correspond to basalts from continental back-arc fields. The Andean volcanic arc field utilises data from samples with SiO_2 ranging from 50.9 to 53.0 wt % from the Andean arc between 35°S and 38°S (Costa and Singer, 2002; Ferguson et al., 1992; Jacques et al., 2013; Lopez-Escobar et al., 1977; Tormey et al., 1991; 1995). The dark grey field corresponds to the Río Colorado volcanic field (data from Søager et al., 2013) and represents the local ocean island basalt (OIB) end-member for the Argentina data. Compositions for the upper continental crust (UCC) and the lower continental crust (LCC) are from Rudnick and Gao (2003). Composition for the OIB is from Sun and McDonough (1989) while the primordial mantle (PM) composition is from McDonough and Sun, (1995). Values for sediment from the subducting Nazca plate (SED), South Atlantic Mid-ocean ridge basalt enriched (SAM-E) and depleted (SAM-D) are from Jacques et al. (2013). The data trend for the Oceanic back-arc (inset, panel a) is from Pearce et al. (2005) based on the Marianas back-arc basin.

The composition of continental back-arc volcanism in central west Argentina suggest a complex setting, as it has been not only slightly influenced by the Nazca plate subducting to the west of

the continent, but also by an upwelling mantle having a composition similar to that of OIB (Chapter 2). Most of the continental back-arc settings have some association with an enriched mantle component and an opposite trend with subduction is observed, in which the High Lava Plains represents the most depleted while the Auckland volcanic field is the most enriched. Accordingly the enriched mantle source (Chapter 2) for the southern Mendoza back-arc will be compared with the most enriched type of lavas erupted from a continental back-arc such as the Auckland volcanic field, in the northern island of New Zealand. The Auckland volcanic field is comparatively smaller and younger than the Payenia Basaltic Province and is classified as intraplate, while the region has prior episodes of obduction and subduction-related magmatism (McGee et al., 2013). The intraplate volcanism in New Zealand has been related to a fertile garnet peridotite source with some regions of eclogite (McGee et al., 2013). A similar type of source has been previously proposed for the OIB-like volcanism in the Payenia Basaltic Province (Søager and Holm, 2013). The mantle peridotite that interacted with eclogite melts has not been thoroughly described. However, it has been suggested that it is fertile (Søager and Holm, 2013) therefore, assuming that it should be similar to a garnet-bearing peridotite which is stable at a depth of more than 80 km. However, in the Llancanelo and Payún Matrú volcanic fields the garnet signature is not strong (Chapter 2) and especially, in the Payún Matrú volcanic field, the modelling indicates that the amount of garnet in the source is small (Chapter 4). Melting in the presence of garnet results in ^{230}Th excess and increased radiogenic Pb (McGee et al., 2013) which is not the case for the Payún Matrú volcanic field as ^{230}Th/^{238}U is close to secular equilibrium (Chapter 4) and radiogenic Pb is relatively low (Jacques et al., 2013; Søager and Holm, 2013). Therefore, the magmatic source for the southern Mendoza continental back-arc is likely to be shallower in order to produce a weak garnet signature. In any case, the magmatic source for the Payún Matrú volcanic field is not strictly garnet- or spinel-bearing peridotite, but is located closer to the garnet stability boundary (Chapter 4).

Placing the magmatic source at a shallower depth raises the question of the possibility of lithospheric mantle involvement. Nevertheless, the involvement of the lithospheric mantle in the basalts erupted in the Payún Matrú and Llancanelo volcanic fields is questioned by some authors (Søager et al., 2013; Søager and Holm, 2013; Hernando et al., 2014a) and proposed by others (Jacques et al., 2013) in the Payenia Basaltic Province and in Patagonian volcanic fields (Varekamp et al., 2010; Massaferro et al., 2014). The effect of the lithospheric mantle in the basalts is difficult to assess in this setting where lower continental crust assimilation has been suggested (Chapter 2). In this study, the influence of the lithospheric mantle is neither accepted nor rejected. However, it will be desirable to utilise different isotopic systems, which could differentiate the lower continental crust from the lithospheric mantle and possibly U-Th disequilibria not only in the Holocene lavas but on the Pleistocene Llancanelo volcanic field.

In conclusion, the continental back-arc is more enriched in inmobile elements relative to fluid-mobile elements than in oceanic back-arcs. Therefore, the continental back-arc has an oblique trend from the MORB array in the Nb/Yb vs Ba/Yb (Figure 6.1a, modified after Pearce et al.,

2005) between the arc front and the intraplate end-member (similar to OIB), while the oceanic back-arc has a vertical trend towards the arc front from the MORB array mostly associated with the depleted end. Continental back-arc settings can be described in general as areas where mainly alkali volcanism occurs behind the volcanic front on continental lithosphere with a few percent partial melting and displaying a weak arc signature. In addition, being in a continental setting, the magmatic source could be affected by continental crust assimilation and lithospheric partial melts, while the proportional slab influence can vary.

Local Perspective

This investigation also highlights the importance of a multi–proxy approach in which geochemistry and geochronology are utilised. Accordingly, it has been determined that the geochemistry during the Pleistocene varies significantly between the southern and northern part of the Payenia Basaltic Province (Chapter 5). The alkali volcanism in the last 10 ka have signatures that suggest a strong intraplate signature (similar to OIB) from a shallower source as inferred from U-series, possibly modified by lower continental crust assimilation (Chapters 4 and 5). Moreover, this investigation proposes a change in basaltic flow morphology with time. On one hand, the Pampas Onduladas flow has a typical pahoehoe character, dated to 373 ± 10 ka constituting the first radiometric age of this exceptional long flow of almost 170 km (Chapter 3). On the other hand, the most recent eruptions dated to 1.9 ± 1.0 ka and 1.7 ± 1.6 ka from Santa Maria have a strict a'a character and flow lengths an order of magnitude smaller (Chapter 4 and 5). The change in morphology not only shows a variation in the viscosity and temperature, but also in the geochemistry of the basalts erupted with time. For example the subduction signature was stronger approximately 1.5 Ma ago, especially in the Nevado volcanic field, decreasing towards the late Pleistocene, while the Holocene volcanism does not show subduction-related magmatism.

The Quaternary volcanism of the Payenia Basaltic Province suggests that its activity started possibly in the Nevado volcanic field, with subduction-related signatures, while the Río Colorado volcanic field has ocean island basalt (OIB)-like signatures (Figure 6.2) during the same period. Approximately 1.5 Ma ago, the subduction-related signature migrated from the northern Nevado Volcanic field in a north-west direction. The subduction related volcanism in the Nevado volcanic field continued until 790 ka (Gudnason et al., 2012) while the OIB-like signatures (also called intraplate signature in Chapter 2) in the Río Colorado volcanic field prevailed until approximately 340 ka (Gudnason et al., 2012; Figure 6.2). The Llancanelo volcanic field has followed the migration trend observed in Nevado volcanic field in the last million years; however, the arc-related geochemical signature is slightly weaker (Chapter 5). The subduction signature migration trend can be associated with an inferred roll-back effect (Kay and Copeland, 2006) of the subducting slab towards the trench, therefore allowing the asthenosphere to ascend.

The arc-like signatures in the Llancanelo volcanic field prevailed until the latest Pleistocene and possibly up to 50 ka ago. The latter age corresponds to the last active period in this volcanic

field. The volcanic activity in the Payún Matrú volcanic field peaked from approximately 500 ka and decrease towards the late Holocene (Figure 6.2). Some of the older basaltic flows from this volcanic field are the Pampas Onduladas (Chapter 3) and the Río Grande (Chapter 5) flows displaying geochemistry signatures of an OIB-like source, but with a possible lower continental crust assimilation especially in the Pampas Onduladas basalts (Chapter 2). Nevertheless, the oldest activity in the Payún Matrú volcanic field has been recently placed at 700 ka, based on a pre-caldera trachyte (Hernando et al., 2014a). The youngest volcanic activity in the Payenia Basaltic Province is concentrated on the western side of the Payún Matrú volcanic field and has been dated to 1.7 ± 1.6 ka and 1.9 ± 1.0 (Chapter 5) corresponding to the Santa Maria volcano representing the latest activity in this volcanic field and in the Payenia Basaltic Province (Figure 6.2).

The Holocene volcanism has geochemical signatures strongly resembling the local OIB source, which is taken as the Río Colorado volcanic field (Chapter 4). Magma ascent rates were estimated to be high in the Holocene Santa Maria volcano (Chapter 4), which is consistent with a thin crust (~40km). In addition, it is proposed that weak subduction signatures are evident in the Llancanelo volcanic field, while, no subduction signatures have been described for the Payún Matrú volcanic field. The magmatic source for the Payún Matrú volcanic field is relatively shallow; hence, the pressure has been estimated to be intermediate. The shallow source hypothesis can be expanded to other areas of the Payenia Basaltic Province; nevertheless, further isotopic analysis, is needed from other volcanic fields. One of the questions that remains is whether this basaltic province and especially the Llancanelo and the Payún Matrú volcanic fields could be active in the near future. Based on the dynamics of the two volcanic fields and the extended periods of activity in combination with the range of components that have contributed to modify the geochemistry of these basalts and the recent activity in the last 2 ka, it is reasonably to think that this area could produce further eruptions possibly of a Hawaiian style.

	Volcanic Field			
Period	Río Colorado	Nevado	Llancanelo	Payún Matrú
2.6 – 1Ma	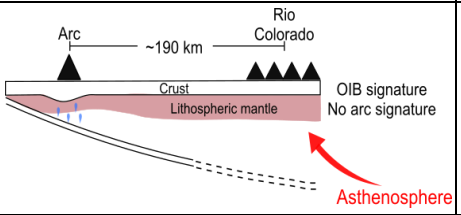	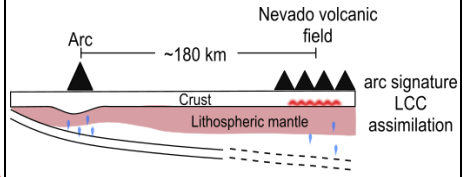	?	?
1 – 0.5 Ma	Same as above	Northern Nevado Volcanic field same as above 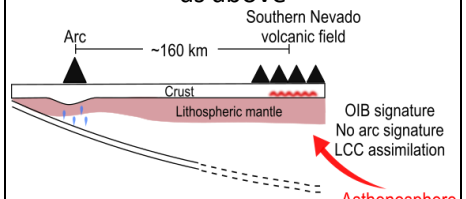	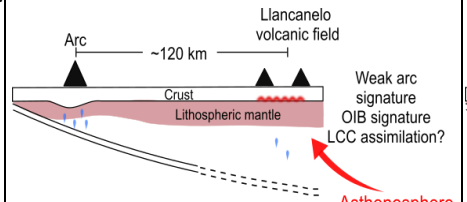	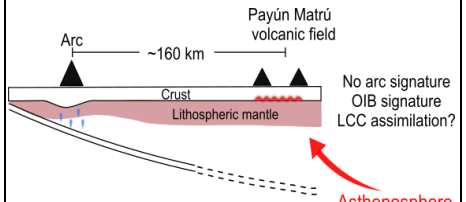
0.5 – 0.01 Ma	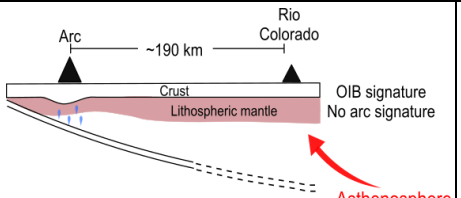	?	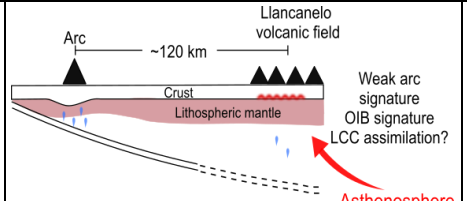	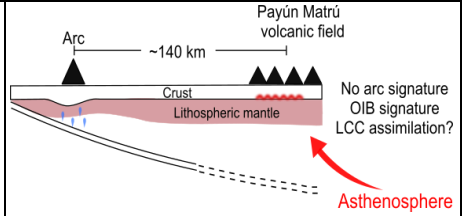
< 0.01 Ma	No activity recorded	No activity recorded	No activity recorded	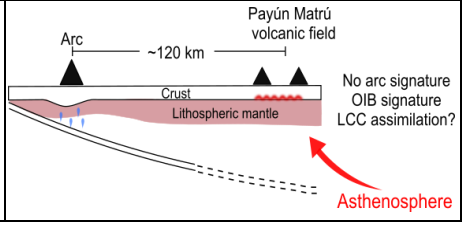

Figure 6.2. Conceptualisation of the volcanic activity in the Payenia Basaltic Province. Note, the distance to the subducting slab is only illustrative and the slab influence or arc signature does not precisely represent slab dehydration in the back-arc volcanic fields. The number of volcanic cones shown in the back-arc is proportional to the interpreted intensity of volcanic activity.

Recommendations for future studies

- The presence of a plume-like upwelling mantle body can be assessed using a multi-proxy approach combining geophysical, geochronological and geochemical data. To determine areas of mantle upwelling, the geospatial distribution maps can provide a practical tool as they illustrate areas of high or low trace-element ratios suggesting areas of mantle anomalies. Some of the remaining questions related to the Payenia Basaltic Province are, for example, whether the lithospheric mantle has played a role in the lavas erupted or not. In order to assess the influence from the lithospheric mantle a combination of isotopic systems should be used among Quaternary lavas of this basaltic province. For example Pb isotopes have been analysed in the Payún Matrú volcanic field and only several samples (<5) have been analysed from the Llancanelo volcanic field. Analysing the Pb isotopes of the rocks not only from Llancanelo volcanic field but also from the Payún Matrú volcanic field can contribute to understand if these rocks are depleted or enriched in radiogenic Pb. According to the available data from Pb isotopes (Jacques et al., 2013; Søager and Holm, 2013) from the two volcanic fields, their composition is similar to that of the south Atlantic and Pacific Mid-ocean ridge basalt at a lower radiogenic Pb. However, the inferred lithospheric mantle composition in the New Zealand intraplate setting, for example, has also a composition with low radiogenic Pb. Thus, again raising again the issue of the lithospheric mantle and its impact (or not) on the magmas erupted. In addition, Hf and oxygen isotopes have only been employed by Jacques et al. (2013), who attributed the isotopic signatures, to the sub-continental lithospheric mantle. The contribution of the lithospheric mantle topic in this setting is contentious at this stage; however; with further analysis of isotopic systems such as those mentioned, in addition to Os and further U-series investigations, the matter may be clarified.

- Noble-gas analysis conducted on fluid inclusions, will contribute to understand the composition of the mantle below the Payenia Basaltic Province. It will also be desirable to analyse mantle xenoliths, which are scarce. However, some mantle xenoliths have been reported from the basalts on the eastern side of the Payún Matrú volcanic field (Bertotto, 2000). Nevertheless, no oxygen-isotope analyses have been reported, which can contribute to better understand the mantle composition in this region. In addition, oxygen-isotope analysis from mantle-derived minerals such as olivine can contribute to determine if there is crustal contamination. In relation to this subject, it was previously mentioned (Chapter 2) that the crustal isotopic composition in the Payenia Basaltic Province is unknown.

- The chronology of the Payenia Basaltic Province is relatively well known and several eruptive periods have been identified. Nevertheless, do those periods represent periods of maximum volcanic activity or are they just a function of the rocks available and the

dating method? Currently, early Pleistocene ages are not abundant and are restricted to the Nevado and the Río Colorado volcanic fields. The available Holocene dates are also limited and with large errors as dating basalts <10 ka is challenging by conventional methods. Furthermore, the Payenia Basaltic Province has the potential for new dating methods such as in the case of the Portezuelo ignimbrite which has not yet been dated and it obscures part of the history of the Payún Matrú caldera and the landscape it buried.

References

Aitken, M. J., 1985. Thermoluminescence Dating. Academic Press, London

Aitken, M., 1990. Science-based dating in archaeology, Longman, London.

Aldrich, L. T., Nier, A. O., 1948. Argon 40 in potassium minerals. Physical Review, 74, 876.

Allen, J. C., Boettcher, A. L., 1983. The stability of amphibole in andesite and basalt at high pressures. American Mineralogist, 68, 307-314.

Allkofer, O. C., Grieder, P. K. F., 1984. Cosmic rays on earth. Physics Data, 25-1. Fachinformationszentrum, Karlsruhe.

Andrews, J., 1985. The isotopic composition of radiogenic helium and its use to study groundwater movement in confined aquifers. Chemical Geology, 49, 339-351.

Ayers, J. C., Dittmer, S. K., Layne, G. D., 1997. Partitioning of elements between peridotite and H_2O at 2.0–3.0 GPa and 900–1100° C, and application to models of subduction zone processes. Earth and Planetary Science Letters, 150, 381-398.

Balco, G., Shuster, D. L., 2009. Production rate of cosmogenic ^{21}Ne in quartz estimated from ^{10}Be, ^{26}Al, and ^{21}Ne concentrations in slowly eroding Antarctic bedrock surfaces. Earth and Planetary Science Letters, 281, 48-58.

Ballentine, C. J., Burnard, P. G., 2002. Production, release and transport of noble gases in the continental crust. In: Porcelli, D., Ballentine, C. J., Wieler, R., (eds.), Noble Gases in Geochemistry and Cosmochemistry, Reviews in Mineralogy and Geochemistry 47: 481-538.

Barberi, F., Coltelli, M., Ferrara, G., Inocenti, F., Navarro, J. M., Santacroce, R., 1988. Plio-Quaternary volcanism in Ecuador. Geological Magazine, 125, p. 1-14.

Barragan, R., Geist, D., Hall, M., Larson, P., Kurz, M., 1998. Subduction controls on the compositions of lavas from the Ecuadorian Andes. Earth and Planetary Science Letters, 154, 153-166.

Berlo, K., Turner, S., Blundy, J., Hawkesworth, C., 2004. The extent of U-series disequilibria produced during partial melting of the lower crust with implications for the formation of the Mount St. Helens dacites. Contributions to Mineralogy and Petrology, 148, 122-130.

Bermudez, A., Delpino, D., 1989. La Provincia Basaltica Andino Cuyana (35-37°L.S.). Revista de la Asociación Geológica Argentina, XLIV, 35-55.

Bertotto, G. W., 1997. Estudio volcanológico y petrográfico de los conos basálticos cerros del Nido, Escorial y Agua Poca. Departamentos Puelén y Chicalcó, sector occidental de la provincia de La Pampa. Trabajo Final de Licenciatura (inédito), Universidad Nacional de La Pampa.

Bertotto, G. W., 2000. Cerro Agua Poca, un cono basáltico cuaternario portador de xenolitos ultramáficos, en el oeste de la provincia de La Pampa, Argentina. Revista de la Asociación Geológica Argentina, 55 (1/2), 59-71.

Bertotto, G. W., Cingolani, C., Bjerg, E., 2009. Geochemical variations in Cenozoic back-arc basalts at the border of La Pampa and Mendoza provinces, Argentina. Journal of South American Earth Sciences, 28, 360-373.

Blard, P. H., Farley, K. A., 2008. The influence of radiogenic ^{4}He on cosmogenic ^{3}He determinations in volcanic olivine and pyroxene. Earth and Planetary Science Letters, 276, 20-29.

Blundy, J., Wood, B., 2003. Mineral-melt partitioning of uranium, thorium and their daughters. Reviews in Mineralogy and Geochemistry, 52, 59-123.

Bottinga, Y., Weill, D. F., 1972. The viscosity of magmatic silicate liquids; a model calculation. American Journal of Science, 272, 438-475.

Bourdon, B., Turner, S., Henderson, G. M., Lundstrom, C. C., 2003. Introduction to U-series Geochemistry. In: Bourdon, B., Henderson, G.M., Lundstrom, C.C., Turner, S., (eds.) Uranium-Series Geochemistry. Reviews in Mineralogy and Geochemistry 52: 1-21.

Bourdon, B., Sims, K., 2003. U-series Constrains on Intraplate Basaltic Magmatism. In: Bourdon, B., Henderson, G.M., Lundstrom, C.C., Turner, S., (eds.) Uranium-Series Geochemistry. Reviews in Mineralogy and Geochemistry 52: 215-254.

Bowring, S. A., Williams, I. S., 1999. Priscoan (4.00 - 4.03 Ga) orthogneisses from northwestern Canada. Contributions to Mineralogy and Petrology, 134, 3-16.

Boynton, W. V., 1984. Cosmochemistry of the rare earth elements: meteoric studies. Rare earth element geochemistry, 63-114.

Bruno, L. A., Baur, H., Graf, T., Schlüchter, C., Signer, P., Wieler, R., 1997. Dating of Sirius Group tillites in the Antarctic Dry valleys with cosmogenic ^{3}He and ^{21}Ne, Earth and Planetary Science Letters, 147, 37-54.

Burd A., Booker J. R., Pomposiello M. C., Favetto A., Larsen J., Giordanengo G., Orozco-Bernal, L., 2008. Electrical conductivity beneath the Payún Matrú Volcanic Field in the Andean back-arc of Argentina near 36.5°S: Insights into the magma source. 7th International Symposium on Andean Geodynamics (ISAG). Nice.

Burd, A. I., Booker, J. R., Mackie, R., Favetto, A., Pomposiello, M. C., 2014. Three-dimensional electrical conductivity in the mantle beneath the Payún Matrú Volcanic Field in the Andean backarc of Argentina near 36.5°S: evidence for decapitation of a mantle plume by resurgent upper mantle shear during slab steepening. Geophysical Journal international, 198, 812-827.

Cande, S., Leslie, R. B., 1986. Late Cenozoic tectonics of the Southern Chile Trench. Journal of Geophysical Research, 91, 471-496.

Carrasco-Núñez, G., Righter, K., Chesley, J., Siebert, L., Aranda-Gómez, J., 2005. Contemporaneous eruption of calc-alkaline and alkaline lavas in a continental arc (Eastern Mexican Volcanic Belt): chemically heterogeneous but isotopically homogeneous source. Contributions to Mineralogy and Petrology, 150, 423-440.

Cassata, W. S., Singer, B. S., Cassidy, J., 2008. Laschamp and Mono Lake geomagnetic excursions recorded in New Zealand. Earth and Planetary Science Letters, 268, 76-88.

Cashman, K., Soule, S., Mackey, B., Deligne, N., Deardorff, N., Dietterich, H., 2013. How lava flows: New insights from applications of lidar technologies to lava flow studies. Geosphere, 9, 1664-1680.

Cembrano, J., Hervé, F., Lavenu, A., 1996. The Liquiñe Ofqui fault zone: a long-lived intra-arc fault system in southern Chile. Tectonophysics, 259, 55-66.

Cerling, T. E., Craig, H., 1994. Cosmogenic ^{3}He production rates from 39°N to 46°N latitude, western USA and France. Geochimica et Cosmochimica Acta 58, 249-255.

Claude-Ivanaj, C., Bourdon, B., Allègre, C. J., 1998. Ra–Th–Sr isotope systematics in Grande Comore Island: a case study of plume–lithosphere interaction. Earth and Planetary Science Letters, 164, 99-117.

Condomines, M., Gauthier, P.-J., Sigmarsson, O., 2003. Timescales of Magma Chamber Processes and Dating of Young Volcanic Rocks. In: Bourdon, B., Henderson, G.M., Lundstrom, C.C., Turner, S., (eds.) Uranium-Series Geochemistry. Reviews in Mineralogy and Geochemistry 52: 125-174.

Costa, F., Singer, B., 2002. Evolution of Holocene dacite and compositionally zoned magma, Volcán San Pedro, Southern Volcanic Zone, Chile. Journal of Petrology, 43, 1571-1593.

Davis, R., Schaeffer, O. A., 1955. Chlorine-36 in nature, Annals of the New York Academy of Sciences, 62, 105-122.

De Ignacio, C., López, I., Oyarzun, R., Márquez, A., 2001. The northern Patagonia Somuncura plateau basalts: a product of slab-induced, shallow asthenospheric upwelling? Terra Nova, 13, 117-121.

DeMets, C., Gordon, R. G., Argus, D. F., Stein, S., 1990. Current plate motion. Geophysical Journal International, 101, 425 - 478.

Desilets, D., Zreda, M., 2003. Spatial and temporal distribution of secondary cosmic-ray nucleon intensities and applications to in situ cosmogenic dating. Earth and Planetary Science Letters, 206, 21-42.

Dosseto, A., Bourdon, B., Joron, J.-L., Durpre, B. 2003. U-Th-Pa-Ra study of the Kamchatka arc: New constraints on the genesis of arc lavas. Geochimica et Cosmochimica Acta, 67, 2857-2877.

Dosseto, A., Turner, S., 2011. Magma cooling and differentiation - Uranium-series isotopes. In: Dosseto, A., Turner, S., Van Orman, J.A., (eds.) Timescales of Magmatic Processes: From Core to Atmosphere. Singapore: Wiley-Blackwell.

Dosseto, A., Turner, S., Costa, F., Van Orman, J. A., 2011. Introduction to the timescales of magmatic processes. In: Dosseto, A., Turner, S. & Van Orman, J. A. (eds.) Timescales of Magmatic Processes, From Core to Atmosphere. Singapore: Wiley-Blackwell.

Dunai, T., 2000. Scaling factors for production rates of in situ produced cosmogenic nuclides: a critical reevaluation, Earth and Planetary Science Letters, 176, 157-169.

Dunai, T., 2001. Influence of secular variation of the geomagnetic field on production rates of in-situ produced cosmogenic nuclides, Earth and Planeary Science Letters, 193, 197–212.

Dunai, T., 2010. Cosmogenic Nuclides: Principles, Concepts and Applications in the Earth Surface Sciences, Cambridge, New York.

Dyhr, C. T., Holm, P. M., Llambías, E. J., 2013a. Geochemical constraints on the relationship between the Miocene–Pliocene volcanism and tectonics in the Palaoco and Fortunoso volcanic fields, Mendoza Region, Argentina: New insights from ^{40}Ar/^{39}Ar dating, Sr–Nd–Pb isotopes and trace elements. Journal of Volcanology and Geothermal Research, 266, 50-68.

Dyhr, C. T., Holm, P. M., Llambías, E. J., Scherstén, A., 2013b. Subduction controls on Miocene back-arc lavas from Sierra de Huantraico and La Matancilla and new $^{40}Ar/^{39}Ar$ dating from the Mendoza Region, Argentina. Lithos, 179, 67-83.

Eberhardt, P., Eugster, O., Marti, K., 1965. A redetermination of the isotopic composition of atmospheric neon. Zeitschrift Naturforschung Teil A, 20, 623.

Eby, N., 1990. The A-type granitoids: A review of their occurence and chemical charcteristics and speculations on their petrogenesis. Lithos, 26, 115-134.

Ernst, W. 1975. Systematics of large-scale tectonics and age progressions in Alpine and Circum-Pacific blueschist belts. Tectonophysics, 26, 229-246.

Espanon, V. R., 2010. Cosmogenic ^{21}Ne and ^{3}He dating and geochemistry of young basaltic lavas from southern Mendoza, Argentina. BSc Honours Thesis, University of Wollongong.

Espanon, V. R., Honda, M., Chivas, A. R., 2014a. Cosmogenic ^{3}He and ^{21}Ne surface exposure dating of young basalts from Southern Mendoza, Argentina. Quaternary Geochronology, 19, 76-86. (also as Appendix C of this thesis)

Espanon, V. R., Chivas, A. R., Kinsley, L. P. J., Dosseto, A., 2014b. Geochemical variations in the Quaternary Andean back-arc volcanism, southern Mendoza, Argentina. Lithos, 208–209, 251-264.(also as Chapter 2 of this thesis and Appendix D)

Espanon, V. R., Chivas, A. R., Phillips, D., Matchan, E. L., Dosseto, A., in-press. Geochronological, morphometric and geochemical constraints on the Pampas Onduladas long basaltic flow (Payún Matrú Volcanic Field, Mendoza, Argentina). Journal of Volcanology and Geothermal Research. (also as Chapter 3 of this thesis)

Fenton, C. R., Niedermann, S., Goethals, M. M., Schneider, B., Wijbrans, J., 2009. Evaluation of cosmogenic ^{3}He and ^{21}Ne production rates in olivine and pyroxene from two Pleistocene basalt flows, western Grand Canyon, AZ, USA. Quaternary Geochronology, 4, 475–492.

Fenton, C. R., Niedermann, S., 2014. Surface exposure dating of young basalts (1–200 ka) in the San Francisco volcanic field (Arizona, USA) using cosmogenic ^{3}He and ^{21}Ne. Quaternary Geochronology, 19, 87-105.

Ferguson, K. M., Dungan, M. A., Davidson, J. P., Colucci, M. T., 1992. The Tatara–San Pedro volcano, 36 °S, Chile: A chemically variable, dominantly mafic magmatic system. Journal of Petrology, 33, 1-43.

Folguera, A., Naranjo, J. A., Orihashi, Y., Sumino, H., Nagao, K., Polanco, E., Ramos, V. A., 2009. Retroarc volcanism in the northern San Rafael Block (34°–35°30′S), southern Central Andes: Occurrence, age, and tectonic setting. Journal of Volcanology and Geothermal Research, 186, 169–185.

Folguera, A., Ortis, D., Spagnuolo, M., Rojas Vera, E., Litvak, V., Sagripanti, L., Ramos, M. E., Ramos, V. A., 2011. A review of Late Cretaceous to Quaternary palaeogeography of the southern Andes. Biological Journal of the Linnean Society, 103, 250–268.

Gerlach, D. C., Frey, F. A., Moreno-Roa, H., Lopez-Escobar, L., 1988. Recent volcanism in the Puyehue-Cordon Caulle region, Southern Andes, Chile (40.5°S): petrogenesis of evolved lavas. Journal of Petrology, 29, 333-382.

Germa, A., Quidelleur, X., Gillot, P. Y., Tchilinguirian, P., 2010. Volcanic evolution of the back-arc Pleistocene Payun Matru volcanic field (Argentina). Journal of South American Earth Sciences, 29, 717-730.

Gilbert, H., Beck, S., Zandt, G., 2006. Lithospheric and upper mantle structure of central Chile and Argentina. Geophysical Journal International, 165, 383-398.

Gill, J., Condomines, M., 1992. Short-lived radioactivity and magma genesis. Science, 257, 1368-1376.

Gladney, E. S., Roelandts, I., 1988. 1987 Compilation of Elemental Concentration Data for USGS BIR-1, DNC-1, and W-2. Geostandards Newsletter, 12, 63-118.

Glodny, J., Echtler, H., Figueroa, O., Franz, G., Gräfe, K., Kemnitz, H., Kramer, W., Krawczyk, C., Lohrmann, J., Lucassen, F., Melnick, D., Rosenau, M., Seifert, W., 2006. Long-Term Geological Evolution and Mass-Flow balance of the South-Central Andes. In: Oncken, O., Chong, G., Franz, G., Gise, P., Götze, H.-J., Ramos, V.A., Strecker, M.R., Wigger, P., (eds.) The Andes, Active subduction orogeny. Germany: Springer.

Goethals, M., Hetzel, R., Niedermann, S., Wittmann, H., Fenton, C.R., Kubik, R.W., Christl, M., Von Blanckenburg, F., 2009. An improved experimental determination of cosmogenic $^{10}Be/^{21}Ne$ and $^{26}Al/^{21}Ne$ production ratios in quartz. Earth and Planetary Science Letters, 284, 187-198.

Gohering, B. M., Kurz, M. D., Balco, G., Schaefer, J. M., Licciardi, J. M., Lifton, N., 2010. A reevaluation of in situ cosmogenic ^{3}He production rates. Quaternary Geochronology, 5, 410-418.

Goldschmidt, V. M., 1933. Grundlagen der quantitatiren Geochemie; Fortschr. Mineralogie, Kristallographie, Petrographie, 17, 112-156.

Goncharov, V., 1964. Dynamics of Channel Flow, 317 pp., translated from Russian by Israel Program Sci. Transl., US Dep. of Commer., Off. of Tech. Serv., Washington, DC.

Gosse, J. C., Phillips, F. M., 2001. Terrestrial in situ cosmogenic nuclides: theory and application. Quaternary Science Reviews. 20, 1475-1560.

Graham, D. W., 2002. Noble gas isotopic geochemistry of mid-ocean ridge and ocean island basalts: characterization of mantle source reservoirs. Reviews in Mineralogy and Geochemistry, 47, 247–318.

Groeber, P., 1946. Observaciones geológicas a lo largo del meridiano 70. Asociación Geológica Argentina, Serie C reimpresiones, 1, Buenos Aires, 5-174.

Grosse, A., 1934. An unknown radioactivity. Journal of the American Chemical Society, 56, 1922-1924.

Gudnason, J., Holm, P. M., Søager, N., Llambías, E. J., 2012. Geochronology of the late Pliocene to Recent volcanic activity in the Payenia back-arc volcanic province, Mendoza Argentina. Journal of South American Earth Sciences, 37, 191-201.

Haller, M., 2000. Crater basalt: a back-arc postglacial volcanic event in northwestern Patagonia. Profil 18, 33.

Halldorsson, S. A., Oskarsson, N., Gronvold, K., Sigurdsson, G., Sverrisdottir, G., Steinthorsson, S. 2008. Isotopic-heterogeneity of the Thjorsa lava-implications for mantle

sources and crustal processes within the Eastern Rift Zone, Iceland. Chemical Geology, 255, 305-316.

Harris, S. L., 2000. Archeology and Volcanism. In: Sigurdsson, H. (ed.) Encyclopaedia of Volcanoes. United States of America: Academic Press.

Hernando I. R., Llambías E. J, González P. D., Sato K., 2012. Volcanic stratigraphy and evidence of magma mixing in the Quaternary Payún Matrú volcano, Andean backarc in western Argentina. Andean Geology, 39, 158-179.

Hernando, I. R., Aragón, E., Frei, R., González, P. D., Spakman, W., 2014a. Constraints on the origin and evolution of magmas in the Payún Matrú Volcanic Field, Quaternary Andean back-arc of western Argentina. Journal of Petrology, 55, 209-239.

Hernando, I. R., Franzese, J. R., Llambías, E. J., Petrinovic, I. A., 2014b. Vent distribution in the Quaternary Payún Matrú Volcanic Field, western Argentina: Its relation to tectonics and crustal structures. Tectonophysics, 622, 122-134.

Herron, E. M., Cande, S. C., Hall, B. R., 1981. An active spreading center collides with a subduction zone, a geophysical survey of the Chile margin triple junction. Geological Society of America Memories, 154, 683-701.

Hervé, F., Munizaga, F., Parada, M., Brook, M., Pankhurst, R., Snelling, N., Drake, R., 1988. Granitoids of the Coast Range of central Chile: geochronology and geologic setting. Journal of South American Earth Sciences, 1, 185-194.

Hofmann, A. W., Jochum, K. P., Seufert, M., White, W. M., 1986. Nb and Pb in oceanic basalts: new constraints on mantle evolution. Earth and Planetary Science Letters, 79, 33-45.

Hon, K., Kauahikaua, J., Denlinger, R., Mackay, K., 1994. Emplacement and inflation of pahoehoe sheet flows: observations and measurements of active lava flows on Kilauea Volcano, Hawaii. Geological Society of America Bulletin, 106, 351-370.

Inbar, M., Risso, C., 2001. A morphological and morphometric analysis of high density cinder cone volcanic field - Payun Matru, south-central Andes, Argentina. Zeitschrift fur Geomorphologie, 45, 321-343.

Ivy-Ochs, S., Kober, F., Alfimov, V., Kubik, P.W., Synal, H.-A., 2007. Cosmogenic ^{10}Be, ^{21}Ne and ^{36}Cl in sanidine and quartz from Chilean ignimbrites. Nuclear Instruments and Methods in Physics Research B 259, 588–594.

Ivy-Ochs, S., Kober, F., 2008. Surface exposure dating with cosmogenic nuclides. Eiszeitalter und Gegenwart, 57, 179-209.

Jacques, G., Hoernle, K., Gill, J., Hauff, F., Wehrmann, H., Garbe-Schönberg, D., Van Den Bogaard, P., Bindeman, I., Lara, L. E., 2013. Across-arc geochemical variations in the Southern Volcanic Zone, Chile (34.5-38.0°S): Constrains on mantle wedge and slab input compositions. Geochimica et Cosmochimica Acta, 123, 218-243.

James, D. E. 1981. The combined use of oxygen and radiogenic isotopes as indicators of crustal contamination. Annual Review of Earth and Planetary Sciences, 9, 311.

Janoušek, V., Farrow, C., Erban, V., 2006. Interpretation of whole-rock geochemical data in igneous geochemistry: introducing Geochemical Data Toolkit (GCDkit). Journal of Petrology, 47**,** 1255-1259.

Janoušek, V., Erbana, V., Holubb, F. V., Magnaa, T., Bellond, H., Mlčocha, B., Wiecherte, U., Rappricha, V., 2010. Geochemistry and genesis of behind-arc basaltic lavas from eastern Nicaragua. Journal of Volcanology and Geothermal Research, 192, 232-256.

Jeffreys, H ., 1925. The flow of water in an inclined channel of rectangular section. Philosophical Magazine, 49, 793-807.

Jochum, K. P., Weis, U., Stoll, B., Kuzmin, D., Yang, Q., Raczek, I., Jacob, D. E., Stracke, A., Birbaum, K., Frick, D. A., 2011. Determination of reference values for NIST SRM 610–617 glasses following ISO guidelines. Geostandards and Geoanalytical Research, 35, 397-429.

Jordan, T. E., Burns, W. M., Veiga, P., Pángaro, F., Copeland, P., Kelley K., Mpodozis, C., 2001. Extension and basin formation in the southern Andes caused by increased convergence rate: A mid-Ceneozoic trigger for the Andes. Tectonics, 20, 308-324.

Jordan, B. T. 2001. Basaltic volcanism and tectonics of the High Lava Plains, southeastern Oregon. PhD thesis, Oregon State University, 218 pp.

Kay, S. M., Ramos, V. A., Mpodozis, C., Sruoga, S., 1989. Late Paleozoic to Jurassic silicic magmatism at the Gondwana margin: Analogy to the Middle Proterozoic in North America? Geology, 17, 324-328.

Kay, S. M., Coira, B., Viramonte, J., 1994. Young mafic back arc volcanic rocks as indicators of continental lithospheric delamination beneath the Argentine Puna plateau, central Andes. Journal of Geophysical Research: Solid Earth (1978–2012), 99, 24323-24339.

Kay, S. M., Gorring, M., Ramos, V. A., 2004. Magmatic sources, setting and causes of Eocene to Recent Patagonian plateau magmatism (36°S to 52°S latitude). Revista de la Asociación Geológica Argentina, 59, 556-568.

Kay, S. M., Godoy, E., Kurtz, A., 2005. Episodic arc migration, crustal thickening, subduction erosion, and magmatism in the south-central Andes. Geological Society of America Bulletin, 117, 67-88

Kay, S. M., Burns, W. M., Copeland, P., Mancilla, O., 2006a. Upper Cretaceous to Holocene magmatism and evidence for transient Miocene shallowing of the Andean subduction zone under the northern Neuquén Basin. In Kay, S.M., Ramos, V.A., (eds.) Evolution of an Andean Margin: A Tectonic and Magmatic View from the Andes to the Neuquén Basin (35°-39°S lat), 407, 19-60.

Kay, S. M., Mancilla, O., Copeland, P., 2006b. Evolution of the late Miocene Chachahuen volcanic complex at 37°S over a transient shallow subduction zone under the Neuquen Andes. Geological Society of America, Special Papers, 407, 215-246.

Kay, S. M., Copeland, P., 2006. Early to middle Miocene backarc magmas of the Neuquén Basin: Geochemical consequences of slab shallowing and the westward drift of South America. Geological Society of America Special Papers, 407, 185-213.

Kay, S. M., Ardolino, A. A., Gorring, M. L., Ramos V. A. 2007. The Somuncura large igneous province in Patagonia: interaction of a transient mantle thermal anomaly with a subducting slab. Journal of Petrology, 48, 43-77.

Kay, S. M., Jones, H. A., Kay, R. W., 2013. Origin of Tertiary to Recent EM- and subduction-like chemical and isotopic signatures in Auca Mahuida region (37°–38° S) and other Patagonian plateau lavas. Contributions to Mineralogy and Petrology, 166, 165-192.

Kelemen, P. B., Hirth, G., Shimizu, N., Spiegelman, M., Dick, H. J., 1997. A review of melt migration processes in the adiabatically upwelling mantle beneath oceanic spreading ridges. Philosophical Transactions of the Royal Society of London. Series A: Mathematical, Physical and Engineering Sciences, 355, 283-318.

Kendrick, E., Bevis, M., Smalley, R. J., Brooks, B., Barriga, R., Lauría, E., Fortes, L. P. S., 2003. The Nazca-South America Euler vector and its rate of change. Journal of South American Earth Sciences, 16, 125-131.

Kennedy, B. M., Hiyagon, H., Reynolds, J.H., 1990. Crustal neon: a striking uniformity. Earth and Planetary Science Letters, 98, 277-286.

Kessel, R., Schmidt, M. W., Ulmer, P., Pettke, T., 2005. Trace element signature of subduction-zone fluids, melts and supercritical liquids at 120-180 km depth. Nature, 437, 724-727.

Keszthelyi, L., Pieri, D. C., 1993. Emplacement of the 75-km-long Carrizozo lava flow field, south-central New Mexico. Journal of Volcanology and Geothermal Research, 59, 59-75.

Keszthelyi, L., Self, S., 1998. Some physical requirements for the emplacement of long basaltic lava flows. Journal of Geophysical Research: Solid Earth (1978–2012), 103, 27447-27464.

Kober, F., Ivy-Ochs, S., Leya, I., Baur, H., Magna, T., Wieler, R., Kubik, P. W., 2005. In situ cosmogenic ^{10}Be and ^{21}Ne in sanidine and in situ cosmogenic ^{3}He in Fe–Ti-oxide minerals. Earth and Planetary Science Letters, 236, 404-418.

Koornneef, J. M., Stracke, A., Aciego, S., Reubi, O., Bourdon, B., 2010. A new method for U–Th–Pa–Ra separation and accurate measurement of ^{234}U–^{230}Th–^{231}Pa–^{226}Ra disequilibria in volcanic rocks by MC-ICPMS. Chemical Geology, 277, 30-41.

Kurz, M. D., 1986. In situ production of terrestrial cosmogenic helium and some applications to geochronology, Geochimica et Cosmochimica Acta, 50, 2855-2862.

Kurz, M. D., Colodner, D., Trull, T. W., Moore, R. B., O'brien, K., 1990: Cosmic ray exposure dating with in-situ produced cosmogenic 3He: results from young Hawaian lava flows. Earth and Planetary Science Letters, 97, 177-189.

Lal, D., Peters, B., 1967. Cosmic Ray Produced Radioactivity on the Earth. In: Sitte, K. (ed.) Kosmische Strahlung II / Cosmic Rays II. Springer Berlin Heidelberg.

Lal, D., 1988. In situ-produced cosmogenic isotopes in terrestrial rocks. Annual Review of Earth and Planetary Sciences, 16, 355-388.

Lal, D., 1991. Cosmic ray labeling of erosion surfaces: in situ nuclide production rates and erosion models, Earth and Planetary Science Letters, 104, 424-439.

Le Bas, M. J., Le Maitre, R. W., Streckeisen, A., Zanettin, B., 1986. A chemical classification of volcanic rocks based on the total alkali–silica diagram. Journal of Petrology, 27, 745-750.

Libby, W., Anderson, E. C., Arnold, J. R., 1949. Age determination by radiocarbon content: world-wide essay of natural radiocarbon. Science, 109, 227-228.

Licciardi, J. M., Kurz, M. D., Clark, P. U., Brook E. J., 1999. Calibration of cosmogenic ^{3}He production rates from Holocene lava flows in Oregon, USA, and effects of the Earth's magnetic field. Earth and Planetary Science Letters, 17, 261-271.

Lifton, N., Bieber, J. W., Clem, J. M., Duldig, M. L., Evenson, P., Humble, J. E., Pyle, R., 2005. Addressing solar modulation and long-term uncertainties in scaling secondary cosmic rays for in situ cosmogenic nuclide applications. Earth and Planetary Science Letters, 239, 140-161.

Lipman, P. W., Banks, N. G., 1987. Aa Flow Dynamics, Mauna Loa 1984, U.S. Geological Survey Professional Paper, vol. 1350: 1527-1567.

Llambías, E. J., 1966. Geología y petrología del volcán Payún Matrú. Acta Geológica Lilloana 8, 65-315.

Llambías, E. J., 2008. Geología de los cuerpos ígneos Buenos Aires, Argentina, Associacion Geológica Argentina.

Llambías, E. J., 2009. Volcanes; nacimiento, estructura, dinámica, Vazquez Mazzini Buenos Aires, Argentina.

Llambías, E. J., Bertotto, G., Risso, C., Hernando, I., 2010. El volcanismo Cuaternario en el retroarco de Payenia: Una revisión. Revista de la Asociación Geológica Argentina, 67, 278-300.

Lopez-Escobar, L., Frey, F. A., Vergara, M., 1977. Andesites and high-alumina basalts from the central-south Chile high Andes: Geochemical evidence bearing on their petrogenesis. Contributions to Mineralogy and Petrology, 63, 199-228.

Ludwig, K. R. 2012. User's Manual for Isoplot 3.75. A Geochronological Toolkit for Microsoft Excel. Special Publication No. 5. Berkeley Geochronology Center, Berkeley, California. p 75.

Lugmair, G. W., Marti, K., 1978. Lunar initial $^{143}Nd/^{144}Nd$: Differential evolution of the lunar crust and mantle. Earth and Planetary Science Letters, 39, 349-357.

Lundstrom, C. C., 2003. Uranium-series disequilibria in mid-ocean ridge basalts: observations and models of basalt genesis. Reviews in Mineralogy and Geochemistry, 52, 175-214.

Lundstrom, C. C., Hoernle, K., Gill, J., 2003. U-series disequilibria in volcanic rocks from the Canary Islands: Plume versus lithospheric melting. Geochimica et Cosmochimica Acta, 67, 4153-4177.

Luo, X., Rehkämper, M., Lee, D.-C., Halliday, A. N., 1997. High precision $^{230}Th/^{232}Th$ and $^{234}U/^{238}U$ measurements using energyfiltered ICP magnetic sector multiple collector mass spectrometry. International Journal of Mass Spectrometry and Ion Processes, 171, 105-117.

Mamyrin, B. A., Tolstikhin, L., 1984. Helium isotopes in nature, Amsterdam, Elsevier.

Marchetti, D., Hynek, S., Cerling, T., 2014. Cosmogenic ^{3}He exposure ages of basalt flows in the northwestern Payún Matru volcanic field, Mendoza Province, Argentina. Quaternary Geochronology, 19, 67-75.

Márquez, A., Oyarzun, R., Doblas, M., Verma, S. P., 1999. Alkalic (ocean-island basalt type) and calc-alkalic volcanism in the Mexican volcanic belt: A case for plume-related magmatism and propagating rifting at an active margin? Geology, 27, 51-54

Masarik, J., 2002. Numerical simulation of in situ production of cosmogenic nuclides. Geochimica et Cosmochimica Acta, 66, A491.

Massaferro, G. I., Haller, M. J., D'orazio, M., Alric, V. I., 2006. Sub-recent volcanism in Northern Patagonia: A tectonomagmatic approach. Journal of Volcanology and Geothermal Research, 155, 227-243.

Massaferro, G. I., Haller, M. J., Dostal, J., Pécskay, Z., Prez, H., Meister, C., Alric, V., 2014. Possible sources for monogenetic Pliocene–Quaternary basaltic volcanism in northern Patagonia. Journal of South American Earth Sciences, 55, 29-42.

Matchan, E. L., Phillips, D., 2014. High precision multi-collector $^{40}Ar/^{39}Ar$ dating of young basalts: Mount Rouse volcano (SE Australia) revisited. Quaternary Geochronology, 22, 57-64.

McDonough, W. F., Sun, S.-S., 1995. The composition of the Earth. Chemical Geology, 120, 223-253.

McDougall, I., Harrison, T. M., 1999. Geochronology and Thermochronology by the $^{40}Ar/^{39}Ar$ Method, Oxford University Press.

McGee, L. E., Smith, I. E. M., Millet, M.-A., Handley, H. K., Lindsay, J. M., 2013. Asthenospheric control of melting processes in a monogenetic basaltic system: a case study of the Auckland Volcanic Field, New Zealand. Journal of Petrology, 54, 2125-2153.

McKenzie, D., 1985. ^{230}Th- ^{238}U disequilibrium and the melting processes beneath ridge axes. Earth and Planetary Science Letters, 72, 149-157.

Melchor, R., Casadío, S., 1999. Hoja Geológica 3766-III La Reforma, provincia de La Pampa. Buenos Aires.

Mellaart, J., 1967. Catul Huyuk: A Neolithic town in Anatolia. McGraw- Hill.

Méndez, V., Zanettini, J. C., Zappettini, E. O. 1995. Geología y metalogénesis del Orógeno andino central, República Argentina, Secretaría de Minería de la Nación, Dirección Nacional del Servicio Geológico.

Merrihue, C., 1965. Trace-element determinations and potassium-argon dating by mass spectroscopy of neutron-irradiated samples. Transactions American Geophysical Union, 46, 125.

Merrihue, C., Turner, G., 1966. Potassium-argon dating by activation with fast neutrons. Journal of Geophysical Research, 71, 2852-2857.

Mitchell, J., 1968. The argon-40/argon-39 method for potassium-argon age determination. Geochimica et Cosmochimica Acta, 32, 781-790.

Moffat, I., 2013. Spatially resolved strontium isotope micro-analysis of lower and middle Palaeolithic fauna from archaeological sites in Israel and southern France, PhD thesis, The Australian National University. 1127 pp.

Mpodozis, C., Allmendinger, R. W., 1993. Extensional tectonics, Cretaceous Andes, northern Chile (27°S). Geological Society of America Bulletin, 105, 1462-1477.

Muñoz, J., Stern, C. R., 1988. The quaternary volcanic belt of the southern continental margin of South America: Transverse structural and petrochemical variations across the segment between 38°S and 39°S. Journal of South American Earth Sciences, 1, 147-161.

Muñoz, J., Stern, C. R., Bermúdez, A., Delpino, D., Dobbs, M. F., Frey, F. A., 1989. El volcanismo Plio-Cuaternario a través de los 34°-39°S de los Andes. Revista de la Asociación Geológica Argentina, 44, 270-186.

Narciso, V., Santamaría, G., Zanettini, J. 2001. Hoja Geológica 3769-I, Barrancas. Provincias de Mendoza y Neuquén. Instituto de Geología y Recursos Minerales, Servicio Geológico Minero Argentino, Boletín, 253.

Narciso, V., Zanettini, J., Sepulveda, E., 2001. Hoja Geológica 3769-II, Agua Escondida. Provincias de Mendoza y La Pampa. Instituto de Geología y Recursos Minerales, Servicio Geológico Minero Argentino, Boletín, 300.

National Institute of Standards and Technology, 2007. Certificate of Analysis, standard reference material 987, Strontium carbonate. Gaithersburg, Maryland, USA.

Nemeth, K., Haller, M., Martin, C., Risso, C., Massaferro, G. 2008. Morphology of lava tumuli from Mendoza (Argentina), Patagonia (Argentina), and Al-Haruj (Libya). Zeitschrift für Geomorphologie, 52, 181-194.

Neumann, W., Huster, E., 1976. Discussion of the ^{87}Rb half-life determined by absolute counting. Earth and Planetary Science Letters, 33, 277-288.

Niedermann, S., Graf, T., Marti, K., 1993. Mass spectrometric identification of cosmic-ray-produced neon in terrestrial rocks with multiple neon components. Earth and Planetary Science Letters, 118, 65-73.

Niedermann, S., 2000. The ^{21}Ne production rate in quartz revisited. Earth and Planetary Science Letters, 183, 361-364.

Niedermann, S., 2002. Cosmic-Ray-Produced Noble Gases in Terrestrial Rocks: Dating Tools for Surface Processes. In: Porcelli, D., Ballentine, C.J., Wieler, R., (eds.) Noble Gases in Geochemistry and Cosmochemistry. Reviews in Mineralogy and Geochemistry 47: 731-784.

Nier, A. O., 1950. A redetermination of the relative abundances of the isotopes of carbon, nitrogen, oxygen, argon, and potassium. Physical Review, 77, 789.

Nullo, F., Stephens, G., Combina, A. M., Dimieri, L., Baldauf, P., Bouza, P., 2005. Hoja Geológica 3569-III, Malargüe. Provincia de Mendoza. Instituto de Geología y Recursos Minerales, Servicio Geológico Minero Argentino, Boletín, 346.

Núñez, E., 1976. Descripción geológica de la Hoja 31e Chical-Có, provincias de Mendoza y La Pampa. Servicio Nacional Geológico Minero, Informe Inédito. Buenos Aires.

Ostera, H., Dalpeña, C., 2003. Environmental isotopes and geochemistry of Bañado Carilauquen, Mendoza, Argentina. 4th South American Symposium on Isotope Geology, Short Papers, 2003 Salvador. 461-464.

Pasquarè, G., Bistacchi, A., Mottana, A., 2005. Gigantic individual lava flows in the Andean foothills near Malargue (Mendoza, Argentina). Rendiconti Fis. Acc. Lincei 16, 127-135.

Pasquaré, G., Bistacchi, A., Francalanci, L., Bertotto, G., Boari, E., Massironi, M., Rossotti, A., 2008. Very long pahoehoe inflated basaltic lava flows in the Payenia Volcanic Province (Mendoza and La Pampa, Argentina). Revista de la Asociación Geológica Argentina, 63, 131-149.

Pearce, J. A., Stern, R. J., Bloomer, S. H., Fryer, P., 2005. Geochemical mapping of the Mariana arc-basin system: Implications for the nature and distribution of subduction components. Geochemistry, Geophysics, Geosystems, 6, Q07006.

Pearce, J. A., 2008. Geochemical fingerprinting of oceanic basalts with applications to ophiolite classification and the search for Archean oceanic crust. Lithos, 100, 14-48.

Phillips, D., Matchan, E. L., 2013. Ultra-high precision $^{40}Ar/^{39}Ar$ ages for Fish Canyon Tuff and Alder Creek Rhyolite sanidine: New dating standards required? Geochimica et Cosmochimica Acta, 121, 229-239.

Pinkerton, H., Stevenson, R., 1992. Methods of determining the rheological properties of lavas from their physico-chemical properties. Journal of Volcanology and Geothermal Research, 53, 47-66.

Pinkerton, H., Wilson, L., 1994. Factors controlling the lengths of channel-fed lava flows. Bulletin of Volcanology, 56, 108-120.

Polanski, J., 1954. Rasgos geomorfológicos del territorio de la provincia de Mendoza. Instituto de Investigaciones Económicas y Tecnológicas, Cuadernos de Estudio e Investigación, 4, 10. Mendoza.

Poreda, R., Cerling, T., 1992. Cosmogenic neon in recent lavas from the western United States. Geophysical Rearch Letters, 19, 1863-1866.

Powell, C. F., Fowler, P. H., Perkins, D. H., 1959. The Study of Elementary Particles by the Photographic Method, London: Pergamon.

Quidelleur, X., Carlut, J., Tchilinguirian, P., Germa, A., Gillot, P. Y., 2009. Paleomagnetic directions from mid-latitude sites in the southern hemisphere (Argentina): Contribution to time averaged field models. Physics of the Earth and Planetary Interiors, 172, 199-209.

Ramos, V.A. 1978. Estructura. En Geologia y Recursos Naturales de Neuquen. 7°Congreso Geologico Argentino, Relatorio: 99-118.

Ramos, V. A., 1988. Late Proterozoic-early Paleozoic of South America: a collisional history. Episodes, 11, 168-174.

Ramos, V. A., Folguera, A., 2011. Payenia volcanic province in the Southern Andes: An appraisal of an exceptional Quaternary tectonic setting. Journal of Volcanology and Geothermal Research, 201, 53-64.

Renne, P., Sharp, W., Deino, A., Orsi, G., Civetta, L., 1997. $^{40}Ar/^{39}Ar$ dating into the historical realm: calibration against Pliny the Younger. Science, 277, 1279-1280.

Reubi, O., Sims, K., Bourdon, B., 2014. ^{238}U-^{230}Th equilibrium in arc magmas and implications for the time scales of mantle metasomatism. Earth and Planetary Science Letters, 391, 146-158.

Reynolds, A. J., 1974. Turbulent flow in Engineering, New York, John Wiley.

Risso, C., Nemeth, K., Marti, U., 2006. Proposed geosites on Pliocene to Recent pyroclastic cone fields in Mendoza, Argentina. Zeitschrift der Deutschen Gesellschaft für Geowissenschaften, 157, 477-490.

Risso, C., Németh, K., Combina, A. M., Nullo, F., Drosina, M., 2008. The role of phreatomagmatism in a Plio-Pleistocene high-density scoria cone field: Llancanelo Volcanic Field (Mendoza), Argentina. Journal of Volcanology and Geothermal Research, 169, 61-86.

Rivalenti, G., Mazzucchelli, M., Laurora, A., Ciuffi, S. I. A., Zanetti, A., Vannucci, R. Cingolani, C., 2004. The backarc mantle lithosphere in Patagonia, South America. Journal of South American Earth Sciences, 17, 121-152.

Rodriguez, E., Morris, C. S., Belz, J. E. 2006. A global assessment of the SRTM performance. Photogrammetric Engineering and Remote Sensing, 72, 249-260.

Rudnick, R., Gao, S., 2003. Composition of the continental crust. Treatise on Geochemistry, 3, 1-64.

Sarda, P., Staudacher, T., Allègre, C. J., 1988. Neon isotopes in submarine basalts. Earth Planetary Science Letters, 91, 73-88.

Schäfer, J. M., Ivy-Ochs, S., Wieler, R., Leya, I., Baur, H., Denton, G. H. & Schüchter, C., 1999. Cosmogenic noble gas studies in the oldest landscape on earth: surface exposure ages of the Dry Valleys, Antarctica. Earth and Planetary Science Letters, 167, 214-226.

Schmidt, M. W., Poli, S., 1998. Experimentally based water budgets for dehydrating slabs and consequences for arc magma generation. Earth and Planetary Science Letters, 163, 361-379.

Schmincke, H.-U., 2006. Volcanism. Springer.

Sepulveda, E., Bermudez, A., Bordonaro, O., Delpino, D., 2007. Hoja Geológica 3569-IV, Embalse El Nihuil. Provincias de Mendoza. Instituto de Geología y Recursos Minerales, Servicio Geológico Minero Argentino, Boletín, 268.

Sigmarsson, O., Martin, H., Knowles, J., 1998. Melting of a subducting oceanic crust from U-Th disequilibria in austral Andean lavas. Nature, 394, 566-569.

Sigmarsson, O., Chmeleff, J., Morris, J., Lopez-Escobar, L., 2002. Origin of ^{226}Ra-^{230}Th disequilibria in arc lavas from southern Chile and implications for magma transfer time. Earth and Planetary Science Letters, 196, 189-196.

Sigurdsson, H., 2000. Encyclopaedia of Volcanoes. Academic Press.

Simpson, J., Fagot, W., 1953. Properties of the low energy nucleonic component at large atmospheric depths. Physical Review, 90, 1068.

Sims, K., Depaolo, D., Murrell, M., Baldridge, W., Goldstein, S., Clague, D., Jull, M., 1999. Porosity of the melting zone and variations in the solid mantle upwelling rate beneath Hawaii: inferences from ^{238}U-^{230}Th-^{226}Ra and ^{235}U-^{231}Pa disequilibria. Geochimica et Cosmochimica Acta, 63, 4119-4138.

Sims, K., Gill, J. B., Dosseto, A., Hoffmann, D. L., Lundstrom, C. C., Williams, R. W., Ball, L., Tollstrup, D., Turner, S., Prytulak, J., Glessner, J. J. G., Standish, J. J., Elliott, T., 2008. An Inter-Laboratory Assessment of the Thorium Isotopic Composition of Synthetic and Rock Reference Materials. Geostandards and Geoanalytical Research, 32, 65-91.

Singer, B.S., Pringle, M.S. 1996. Age and duration of the Matuyama-Brunhes geomagnetic polarity reversal from $^{40}Ar/^{39}Ar$ incremental heating analyses of lavas. Earth and Planetary Science Letters, 139, 47-61.

Sisson, T. W., Grove, T. L., 1993. Experimental investigations of the role of H_2O in calc-alkaline differentiation and subduction zone magmatism. Contributions to Mineralogy and Petrology, 113, 143-166.

Skewes, M. A., Stern, C. R., 1979. Petrology and geochemistry of alkali basalts and ultramafic inclusions from the Pali-Aike volcanic fields in southern Chile and the origin of the Patagonian plateau lavas. Journal of Volcanology and Geothermal Research, 6, 3-25.

Smith, M. J., Rose, J., Gousie, M. B., 2009. The Cookie Cutter: A method for obtaining a quantitative 3D description of glacial bedforms. Geomorphology, 108, 209-218.

Søager, N., Holm, P. M., Llambías, E.J., 2013. Payenia volcanic province, southern Mendoza, Argentina: OIB mantle upwelling in a backarc environment. Chemical Geology, 349, 36-53.

Søager, N., Holm, P. M., 2013. Melt–peridotite reactions in upwelling eclogite bodies: Constraints from EM1-type alkaline basalts in Payenia, Argentina. Chemical Geology, 360, 204-219.

Spiegelman, M., Elliott, T. 1993. Consequences of melt transport for uranium series disequilibrium in young lavas. Earth and Planetary Science Letters, 118, 1-20.

Spiegelman, M., 2000. UserCalc: A Web-based uranium series calculator for magma migration problems. Geochemistry, Geophysics, Geosystems, 1, 1016.

Steiger, R. H., Jäger, E., 1977. Subcommission on geochronology: convention on the use of decay constants in geo-and cosmochronology. Earth and Planetary Science Letters, 36, 359-362.

Stephenson, P., Burch-Johnston, A., Stanton, D., Whitehead, P., 1998. Three long lava flows in north Queensland. Journal of Geophysical Research: Solid Earth, 103, 27359-27370.

Stern, C. R., Frey, F. A., Futa, K., Zartman, R. E., Peng, Z., Kyser, T. K., 1990. Trace-elements and Sr, Nd, Pb and O isotopic composition of Pliocene and Quaternary alkali basalts of the Patagonian Plateau lavas of southernmost South America. Contributions to Mineralogy and Petrology, 104, 294-308.

Stern, C. R., 2004. Active Andean volcanism: its geologic and tectonic setting. Revista Geológica de Chile, 31, 161-206.

Stone, J. O. 2000. Air pressure and cosmogenic isotope production. Journal of Geophysical Research: Solid Earth, 105, 23753-23759.

Stracke, A., Bourdon, B., Mckenzie, D., 2006. Melt extraction in the Earth's mantle: Constrains from U-Th-Pa-Ra studies in oceanic basalts. Earth and Planetary Science Letters, 244, 97-112.

Sun, S.-S., McDonough, W. F., 1989. Chemical and isotopic systematics of oceanic basalts: implications for mantle composition and processes. Geological Society, London, Special Publications, 42, 313-345.

Tassara, A., Götze, H.-J., Schmidt, S., Hackney, R., 2006. Three-dimensional density model of the Nazca plate and the Andean continental margin. Journal of Geophysical Research: Solid Earth, 111, B09404.

Taylor, S. R., 1992. Solar system evolution. Cambridge University Press, Cambridge UK.

Tazieff, H. 1977. An exceptional eruption: Mt. Niragongo, Jan. 10th, 1977. Bulletin of Volcanology, 40, 189-200.

Thorpe, R. S. 1984. The tectonic setting of active Andean volcanism. In Andean magmatism: Chemical and Isotopic Constraints. Shiva Geological Series, Shiva Publications, Nantwich, U.K., p. 4-8.

Till, C. B., Grove, T. L., Carlson, R. W., Donnelly-Nolan, J. M., Fouch, M. J., Wagner, L. S., Hart, W. K., 2013. Depths and temperatures of< 10.5 Ma mantle melting and the lithosphere-asthenosphere boundary below southern Oregon and northern California. Geochemistry, Geophysics, Geosystems, 14, 864-879.

Tormey, D. R., Hickey-Vargas, R., Frey, F. A., López-Escobar, L., 1991. Recent lavas from the Andean volcanic front (33 to 42°S); interpretations of along-arc compositional variations. Andean magmatism and its tectonic setting: Geological Society of America Special Paper, 265, 57-77.

Tormey, D. R., Frey, F. A., Lopez-Escobar, L., 1995. Geochemistry of the active Azufre-Planchon-Peteroa Volcanic Complex, Chile (35°15'S): Evidence for multiple sources and processes in a cordilleran arc magmatic system. Journal of Petrology, 36, 265-298.

Turner, S., Bourdon, B., Hawkesworth, C., Evans, P., 2000. ^{226}Ra-^{230}Th evidence for multiple dehydration events, rapid melt ascent and the time scales of differentiation beneath the Tonga-Kermadec island arc. Earth and Planetary Science Letters, 179, 581-593.

Turner, S., Bourdon, B., Gill, J., 2003. Insights into magma genesis at convergent margins from U-series isotopes. In: Bourdon, B., Henderson, G. M., Lundstrom, C. C. & Turner, S. (eds.) Uranium-Series Geochemistry. Reviews in Mineralogy and Geochemistry 52: 255-315.

Turner, S., Bourdon, B., 2011. Melt Transport from the Mantle to the Crust – Uranium-Series Isotopes. In: Dosseto, A., Turner, S., Van Orman, J.A., (eds.) Timescales of Magmatic Processes: From Core to Atmosphere. Singapore: Wiley-Blackwell.

Turrin, B. D., Donnelly-Nolan, J. M., Hearn , B. C., 1994. ^{40}Ar/^{39}Ar ages from the rhyolite of Alder Creek, California: Age of the Cobb Mountain Normal-Polarity Subchron revisited. Geology, 22, 251-254.

Varekamp, J., Hesse, A., Mandeville, C., 2010. Back-arc basalts from the Loncoupe graben (Province of Neuquen, Argentina). Journal of Volcanology and Geothermal Research, 197, 313-328.

Vergani, G. D., Tankard, A. J., Belotti, H. J., Welsink, H. J., 1995. Tectonic evolution and paleogeography of the Neuquén Basin, Argentina. In: Tankard A.J., Suárez R. & Welsink H. J. (eds.) Petroleum basins of South America. The American Association of Petroleum Geologists, 383-402.

Vermeesch, P., 2007. CosmoCalc: An Excel add-in for cosmogenic nuclide calculations. Geochemistry, Geophysics, Geosystems, 8, 8.

Vigier, N., Bourdon, B., Joron, J., Allègre, C., 1999. U-decay series and trace element systematics in the 1978 eruption of Ardoukoba, Asal rift: timescale of magma crystallization. Earth and Planetary Science Letters, 174, 81-98.

Villemant, B., Bourdon, B., Komorowski, J.-C., 1996. U-series disequilibrium in arc magmas induced by water-magma interaction. Earth and Planetary Science Letters, 140, 259-267.

Vilmundardottir, E. G., 1977. Tungnarhraun, Orustofnun geologic report, Rep. OS ROD 7702, 156 pp., Reykjavik.

Walker, G. P., 1973. Length of lava flows. Philosophical Transactions of the Royal Society A 274, 107-118.

Walker, J. A., 1981. Petrogenesis of Lavas from Cinder Cone Fields behind the Volcanic Front of Central America. The Journal of Geology, 89, 721-739.

Walker, M., 2005. Quaternary Dating Methods, John Wiley & Sons.

Williams, H., McBirney, A., 1979. Volcanology. San Francisco, Freeman, Cooper and Company.

Williams, R. W., Gill, J. B., 1989. Effects of partial melting on the uranium decay series. Geochimica et Cosmochimica Acta, 53, 1607-1619.

Willner, A. P., Glodny, J., Gerya, T. V., Godoy, E., Massonne, H. J., 2004. A counterclockwise PTt-path of high-pressure/low-temperature rocks from the Coastal Cordillera accretionary complex of south-central Chile: constraints for the earliest stage of subduction mass flow. Lithos, 75, 283-310.

Wilson, S. A., 1997. The collection, preparation and testing of USGS reference material BCR-2, Columbia River, Basalt: Geological Survey Open-File report 98 xxx.

Yatsevich, I., Honda, M. 1997. Production of nucleogenic neon in the Earth from natural radioactive decay. Journal of Geophysical Research, 102, 10291-10298.

Appendix A: Co-authors contributions for chapters 2 to 5 (the contributions are presented in percentage according to the different tacks performed throughout the investigation)

Chapter 2: "Geochemical variations in the Quaternary Andean back-arc volcanism, southern Mendoza, Argentina"

	Espanon, V.R.	Chivas, A.R.	Kinsley, L.P.J.	Dosseto, A.
Field work	50%	50%		
Sample Preparation	100%			
Sample analysis	70%		10%	20%
Data interpretation	70%	15%		15%
Figures and tables	100%			
Writing	90%			10%
Proof read and discussions	60%	15%		25%

Chapter 3: "Geochronological, morphometric and geochemical constraints on the Pampas Onduladas long basaltic flow (Payún Matrú Volcanic Field, Mendoza, Argentina)"

	Espanon, V.R.	Chivas, A.R.	Phillips, D	Matchan, E.L.	Dosseto, A.
Field work	50%	50%			
Sample Preparation	100%				
Sample analysis	70%		5%	25%	
Data interpretation	80%	10%			10%
Figures and tables	100%				
Writing	85%		5%	5%	5%
Proof read and discussions	40%	20%	10%	10%	20%

Chapter 4: "Localised magmatic constrains on continental back-arc volcanism in southern Mendoza, Argentina: The Santa Maria volcano"

	Espanon, V.R.	Chivas, A.R.	Turner, S.P.	Dosseto, A.	Kinsley, L.P.J.
Field work	100%				
Sample Preparation	85%			15%	
Sample analysis	70%		5%	20%	5%
Data interpretation	70%			30%	
Figures and tables	100%				
Writing	100%				
Proof read and discussions	60%	10%		30%	

Chapter 5: "Chronology of Quaternary volcanism in the continental back-arc from southern Mendoza, Argentina"

	Espanon, V.R.	Chivas, A.R.	Honda, M.	Phillips, D	Matchan, E.L.	Price D.M.
Field work	50%	50%				
Sample Preparation	90%					10%
Sample analysis	30%		30%	5%	25%	10%
Data interpretation	70%				20%	10%
Figures and tables	100%					
Writing	90%					10%
Proof read and discussions	65%	25%	5%			5%

Full name, affiliations and position

Espanon, Venera R.:

GeoQuEST Research Centre, School of Earth & Environmental Sciences, University of Wollongong, NSW 2522, Australia.

Wollongong Isotope Geochronology Laboratory, School of Earth & Environmental Sciences, University of Wollongong, NSW 2522, Australia.

Position: PhD candidate

Chivas, Allan R.:

GeoQuEST Research Centre, School of Earth & Environmental Sciences, University of Wollongong, NSW 2522, Australia.

Position: Professor in geochemistry

Dosseto, Anthony:

GeoQuEST Research Centre, School of Earth & Environmental Sciences, University of Wollongong, NSW 2522, Australia.

Wollongong Isotope Geochronology Laboratory, School of Earth & Environmental Sciences, University of Wollongong, NSW 2522, Australia.

Position: Senior lecturer in geochemistry

Kinsley, Leslie P.J.:

Research School of Earth Sciences, The Australian National University, Canberra, ACT 0200, Australia.

Position: Technician - Marine Biogeochemistry

Phillips, David:

School of Earth Sciences, The University of Melbourne, Parkville, VIC 3010, Australia.

Position: Professor in geochemistry and geochronology

Matchan, Erin, L.:

School of Earth Sciences, The University of Melbourne, Parkville, VIC 3010, Australia.

Position: Academic in noble gas geochemistry

Turner, Simon, P.:

GEMOC, Department of Earth and Planetary Sciences, Macquarie University, Sydney, NSW 2109, Australia.

Position: Professor in geochemistry and geochronology

Honda, Masahiko:

Research School of Earth Sciences, The Australian National University, Canberra, ACT 0200, Australia.

Position: Senior Fellow in noble gas geochemistry

Price, David, M.:

GeoQuest Research Centre, School of Earth & Environmental Sciences, University of Wollongong, NSW 2522, Australia

Position: Visiting honour fellow in thermochronology

Appendix B: Geological maps of the northern and central part of the Payenia Basaltic Province.

Figure 1. Overview of the Northern and central part of Payenia Basaltic Province, including the approximate area of subsequent Figures 2 to 5.

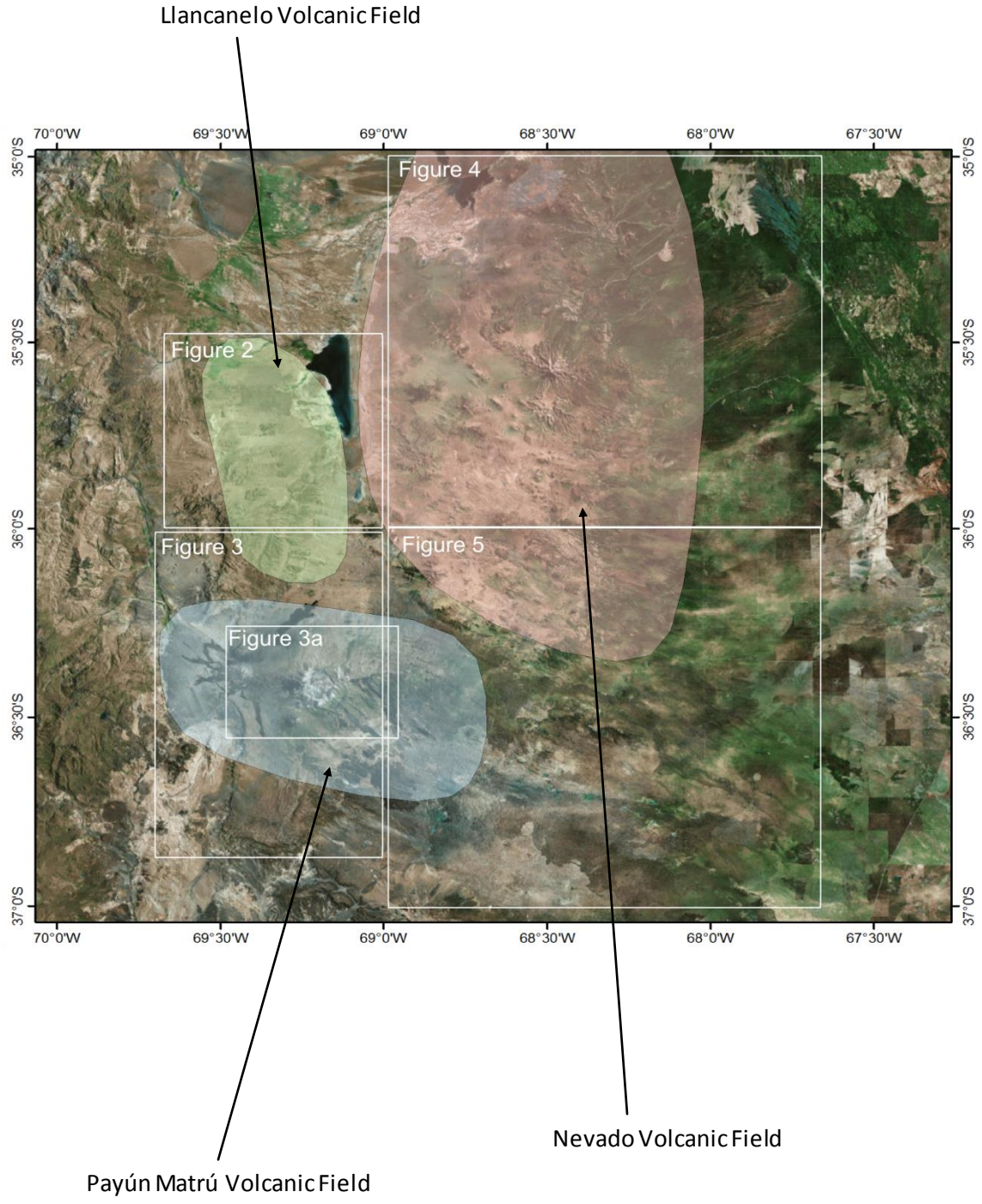

Figure 2. Geological map of part of the Llancanelo Volcanic Field. From Nullo et al. (2005)

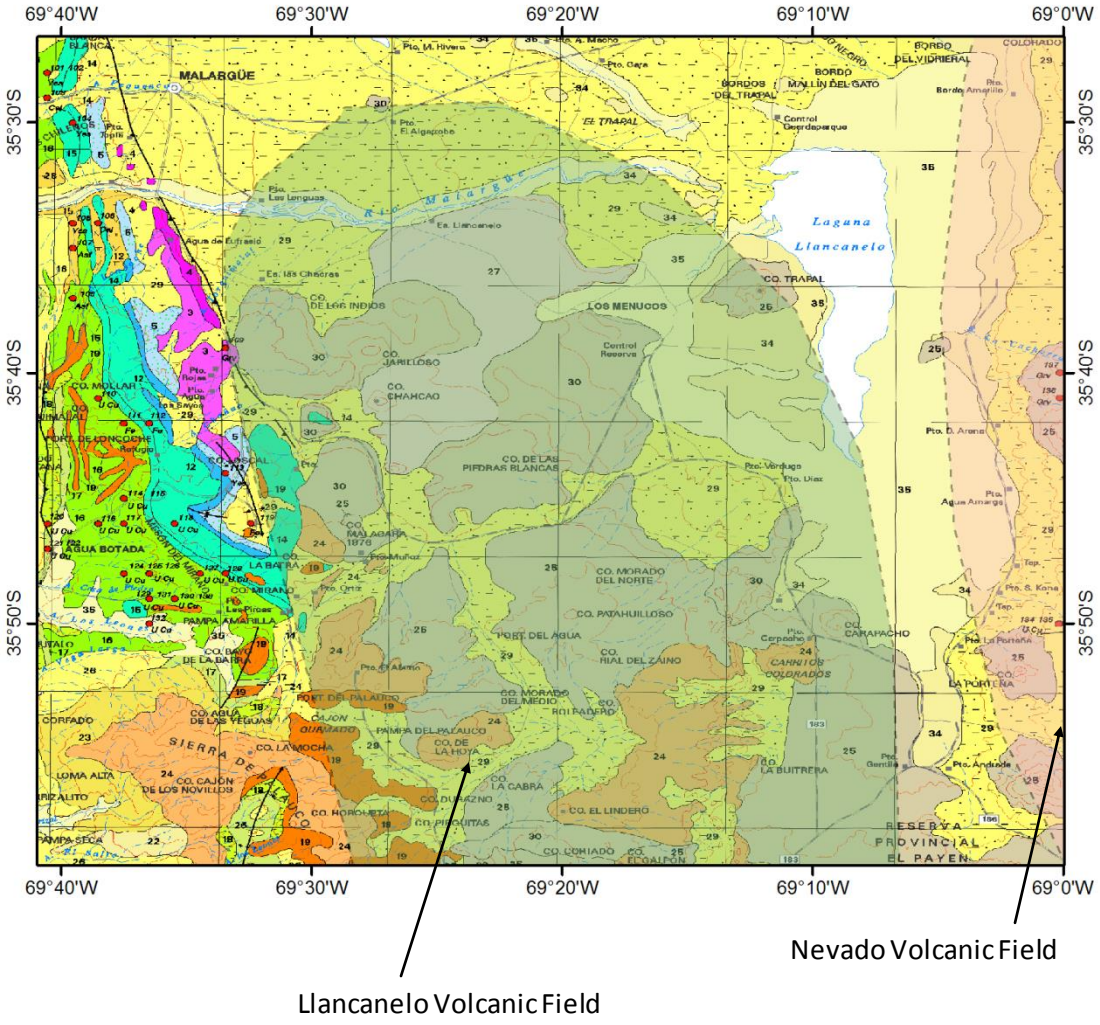

Legend

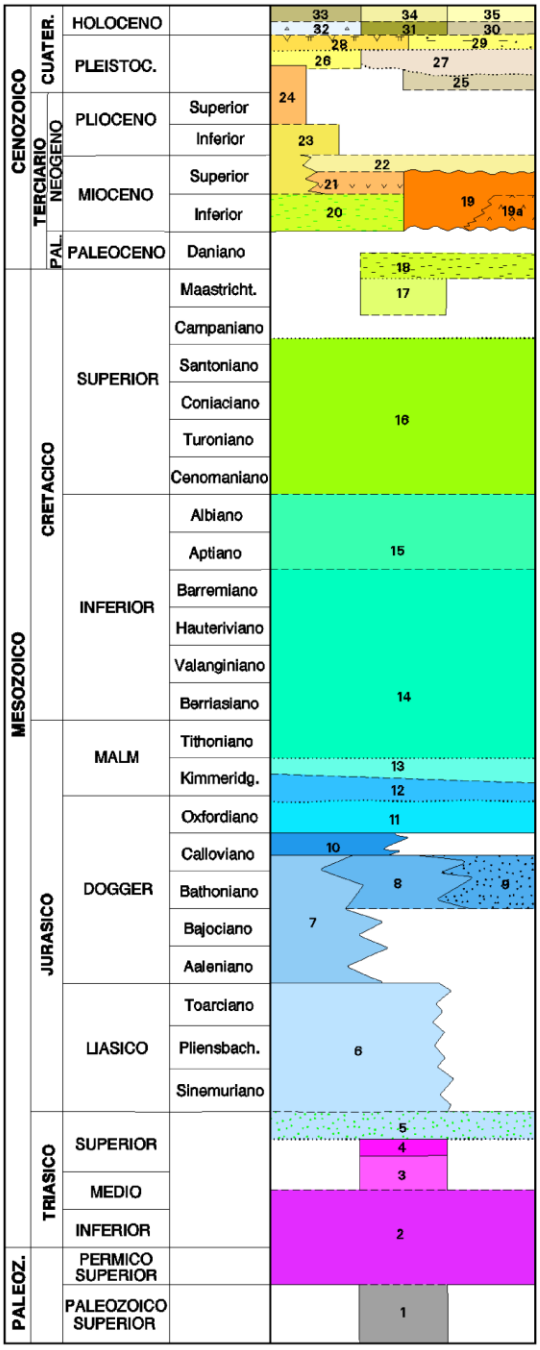

35 DEPÓSITOS ALUVIALES. Bloques, gravas, arenas, limos.
34 DEPÓSITOS EÓLICOS. Arenas finas a muy finas.
33 FORMACIÓN TROMEN. Basaltos olivínicos.
32 DEPÓSITOS MORÉNICOS. Bloques, gravas, arenas.
31 BASALTO PETEROA. Basaltos olivínicos, tobas.
30 BASALTO CERRO CAMPANARIO. Basaltos olivínicos.
29 DEPÓSITOS DE LA LLANURA PEDEMONTANA. Arenas, limos, arcillas.
28 FORMACIÓN LOMA SECA. Ignimbritas, tobas.
27 FORMACIÓN EL PUENTE. Basaltos olivínicos.
26 DEPÓSITOS DEL SEGUNDO NIVEL DE AGRADACION. Fanglomerados, conglomerados, areniscas.
25 FORMACIÓN CHAPÚA. Basaltos olivínicos.
24 FORMACIÓN COYOCHO SUPERIOR. Basaltos olivínicos.
23 DEPÓSITOS DEL PRIMER NIVEL DE AGRADACIÓN. Conglomerados, areniscas.
22 FORMACIÓN PINCHEIRA. Tobas, conglomerados, aglomerados volcánicos, areniscas.
21 FORMACIÓN COYOCHO INFERIOR. Basaltos olivínicos, brechas.
20 FORMACIÓN AGUA DE LA PIEDRA. Conglomerados, areniscas.
19 CICLO ERUPTIVO HUINCÁN. Andesitas, basaltos, basandesitas, dacitas.
19a Cuerpos Porfíricos.
18 FORMACIONES PIRCALA Y COIHUECO. Areniscas, limolitas, margas, arcilitas, yeso.
17 GRUPO MALARGÜE. Areniscas, limolitas, calizas, evaporitas.
16 FORMACIÓN DIAMANTE. Areniscas, conglomerados, limolitas, tufitas.
15 FORMACIÓN HUITRÍN. Yeso,calizas, limolitas, areniscas.
14 GRUPO MENDOZA. Pelitas, pelitas calcáreas, limolitas, areniscas finas, calizas y coquinas.
13 FORMACIÓN TORDILLO. Areniscas, conglomerados.
12 FORMACIÓN AUQUILCO. Yeso, calizas.
11 FORMACIÓN LA MANGA. Calizas, limolitas calcáreas, yeso.
10 FORMACIÓN TÁBANOS. Yeso, calizas, pelitas.
9 FORMACIÓN CALABOZO. Calizas, limolitas, dolomitas, brechas calcáreas.
8 FORMACIÓN LAJAS. Areniscas calcáreas, conglomerados.
7 FORMACIÓN TRES ESQUINAS. Areniscas, limolitas, lutitas, lutitas calcáreas.
6 FORMACIÓN PUESTO ARAYA. Areniscas, conglomerados.
5 FORMACIÓN REMOREDO. Areniscas, tufitas.
4 GRANITO Y PÓRFIDOS DEL CHIHUIDO. Granitos, pórfidos graníticos.
3 GRUPO TRONQUIMALAL. Conglomerados, areniscas.
2 GRUPO CHOIYOI. Volcanitas ácidas y mesosilícicas.
1 FORMACIÓN ARROYO MENDINO. Esquistos biotíticos oscuros.

Figure 3. Geological map of the western part of Payún Matrú Volcanic Field. From Narciso et al. (2001)

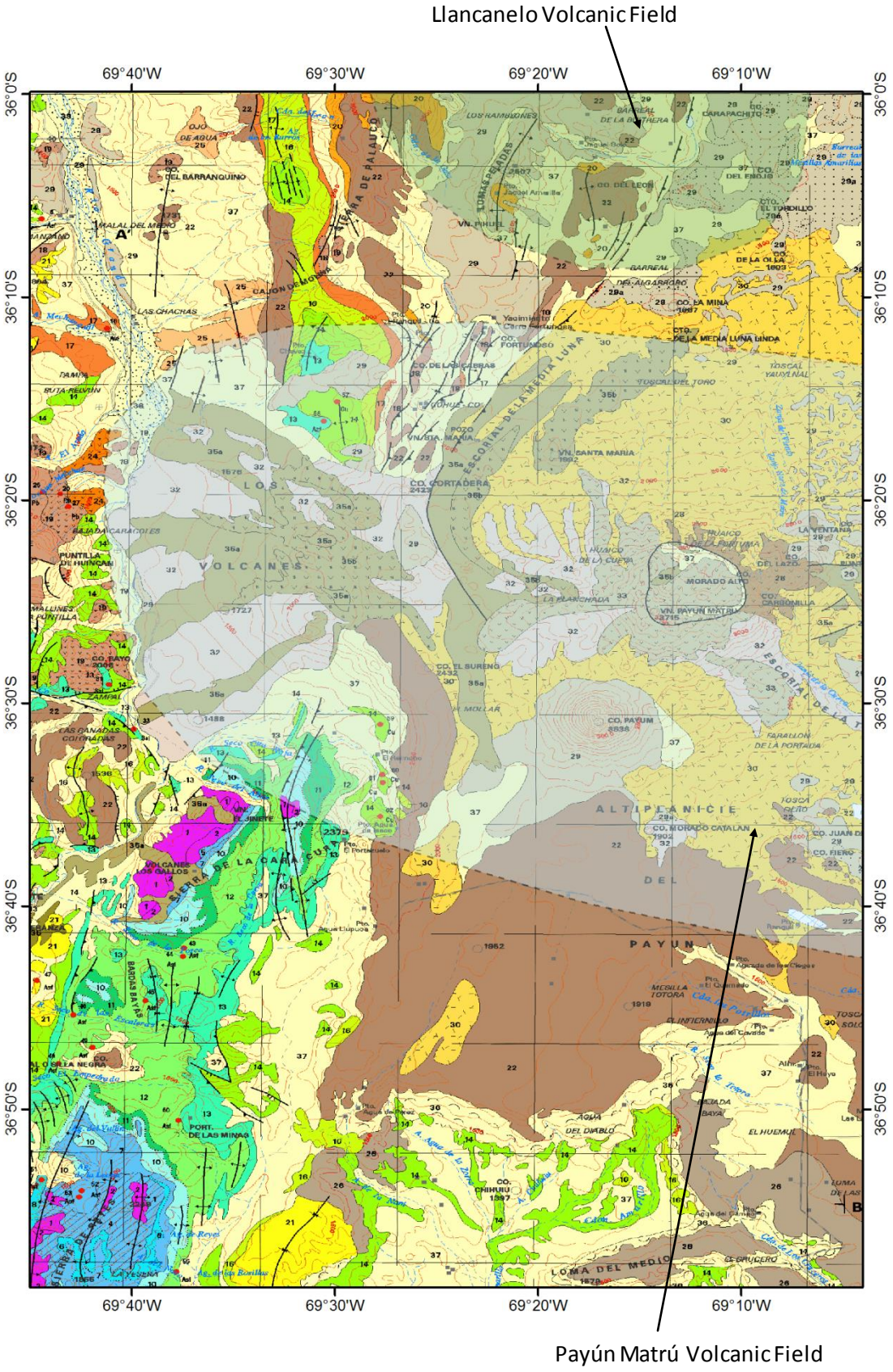

Legend

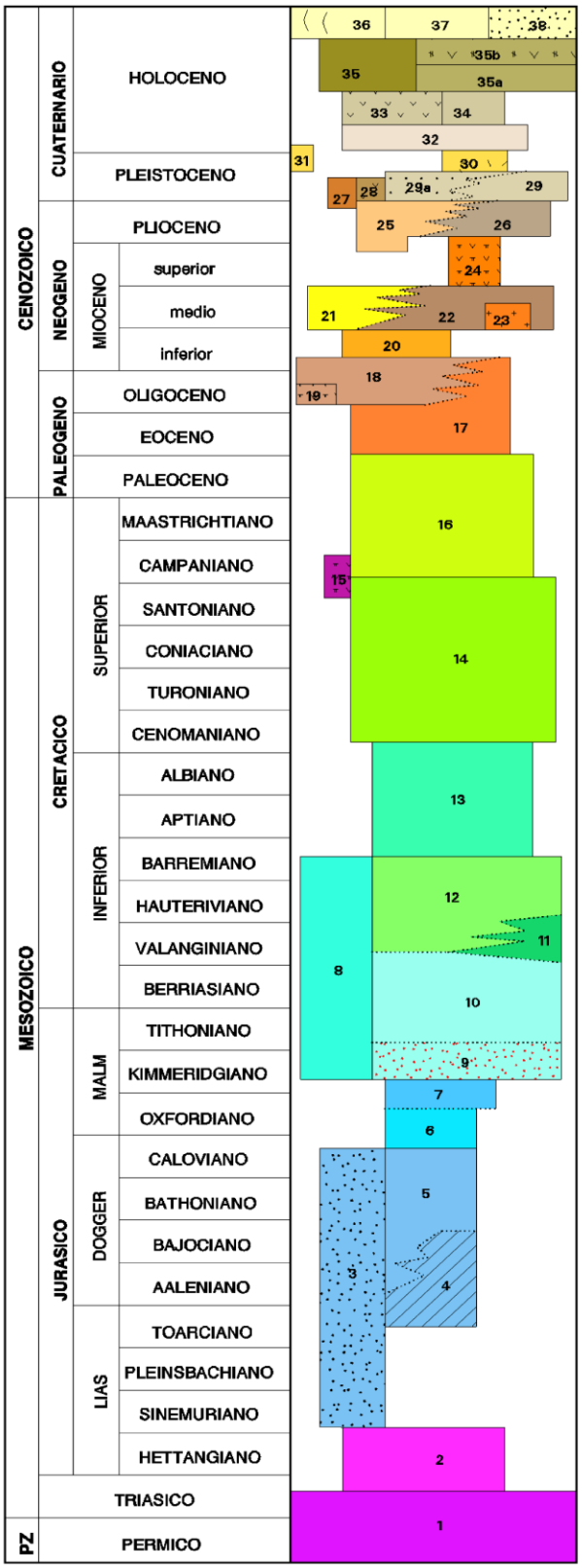

38 DEPOSITOS ALUVIALES RECIENTES: Gravas, arenas y limos.
37 DEPOSITOS ALUVIALES Y COLUVIALES: Gravas,arenas y limos.
36 DEPOSITOS DE REMOCION EN MASA: Gravas, arenas y limos.
35 Fm TROMEN: Basaltos olivínicos.
35b Fm TROMEN superior.
35a Fm TROMEN inferior.
34 ANDESITAS MATRU: Traquitas, andesitas y traquiandesitas.
33 Fm PLANCHADA: Traquitas, hialotraquitas y pumicitas.
32 Fm EL PUENTE: Basaltos piroxénicos - olivínicos y aglomerados basálticos.
31 RIOLITA CERRO DOMO: Riolitas.
30 Fm EL PORTEZUELO: Ignimbritas y tobas.
29 Fm CHAPUA: Basaltos olivínicos.
29a Fm CHAPUA semicubierta.
28 Fm PAYUN MATRU: Traquitas, traquiandesitas y andesitas.
27 VOLCANITAS PLIO - PLEISTOCENAS: Andesitas, Basandesitas, tobas y aglomerados.
26 Fm COYOCHO: Basaltos olivínicos.
25 Fm LETELIER:(continental) Areniscas arcillosas, yesíferas y calcáreos oolíticos.
24 Fm HUINCAN: Andesitas Horblendíferas y piroclástitas.
23 Grupo DOMUYO: Granitos, granodioritas, tonalitas, adamelitas y dacitas.
22 Grupo PALAUCO:Basaltos olivínicos y basandesitas,brechas aglomerados, basálticos y tobas.
21 Fm TRISTEZA:(continental) Conglomerados y areniscas.
20 LOMA FIERA: Conglomerados, aglomerados, brechas, areniscas tobáceas
19 Fm COLLIPILLI: Andesitas anfibolicas,dioritas y dacitas.
18 GRUPO MOLLE: Coladas andesitas, brechas y aglomerados, andesitas anfibolicas,dioritas y dacitas.
17 Fm AGUA DE LA PIEDRA: (continental) Conglomerados, areniscas y pelitas rojas. Basaltos olivínicos y tobas.
16 GRUPO MALARGUE:(marino y continental) Areniscas y pelitas calcáreas, calizas esqueléticas y conglomerados. Areniscas y limoarcilitas.
15 Fm PELAN: Andesitas, pórfiros dioríticos y microdioritas
14 GRUPO NEUQUEN: (continental)Conglomerados, areniscas y limoarcilitas.
13 GRUPO RAYOSO: (continental y marino) Clásticos rojos, calizas y evaporitas.
12 Fm AGRIO: (marino) Calizas y arcilitas calcáreas.
11 Fm CHACHAO: (marino) Calizas esqueléticas.
10 Fm VACA MUERTA: (marino) Pelitas negras y calizas.
9 Fm TORDILLO: (continental) Conglomerados, areniscas y limoarcilitas.
8 GRUPO MENDOZA: (marino) Pelitas calcáreas, calizas y calizas esqueléticas.
7 Fm AUQUILCO: (marino) Evaporitas, boundstone y limoarcilitas rojas.
6 Fm LA MANGA: (marino) Calizas esqueléticas y brechosas.
5 Fm LAJAS: (marino) Conglomerados y areniscas esqueléticas
4 Fm LOS MOLLES:(marino) Areniscas Calcáreas y pelitas oscuras.
3 GRUPO CUYO: (marino mixto) Areniscas calcáreas, vaques y pelitas.
2 Fm REMOREDO: (continental) Conglomerados, areniscas y tobas.
1 GRUPO CHOIYOI: (continental) Volcanitas mesosilíceas, tobas areniscas.

Figure 3a. Detailed geological map of part of the Payún Matrú Volcanic Field. From Hernando et al., 2012

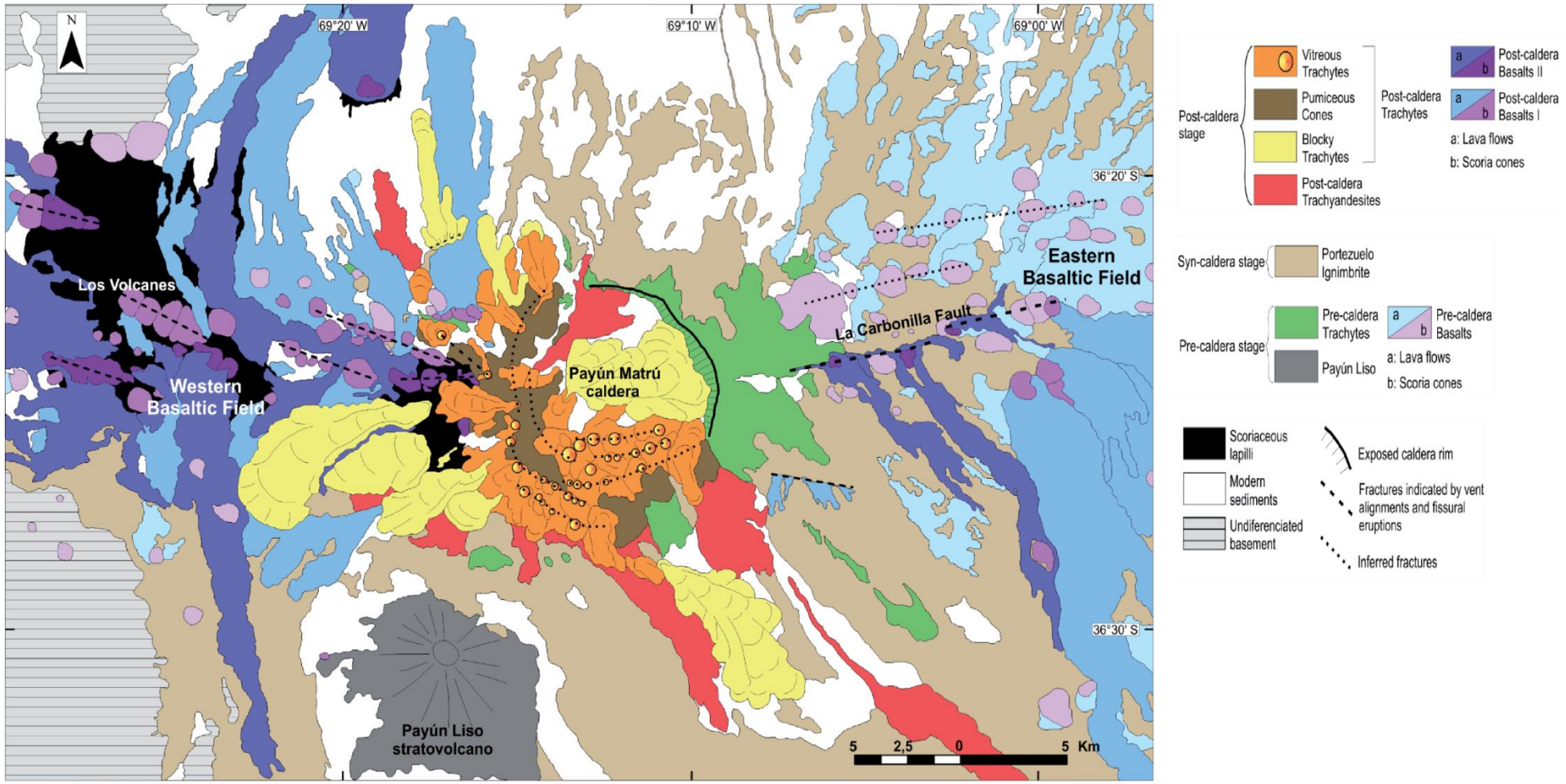

Figure 4. Geological map of part of the Nevado Volcanic Field. From Sepúlveda et al. (2007)

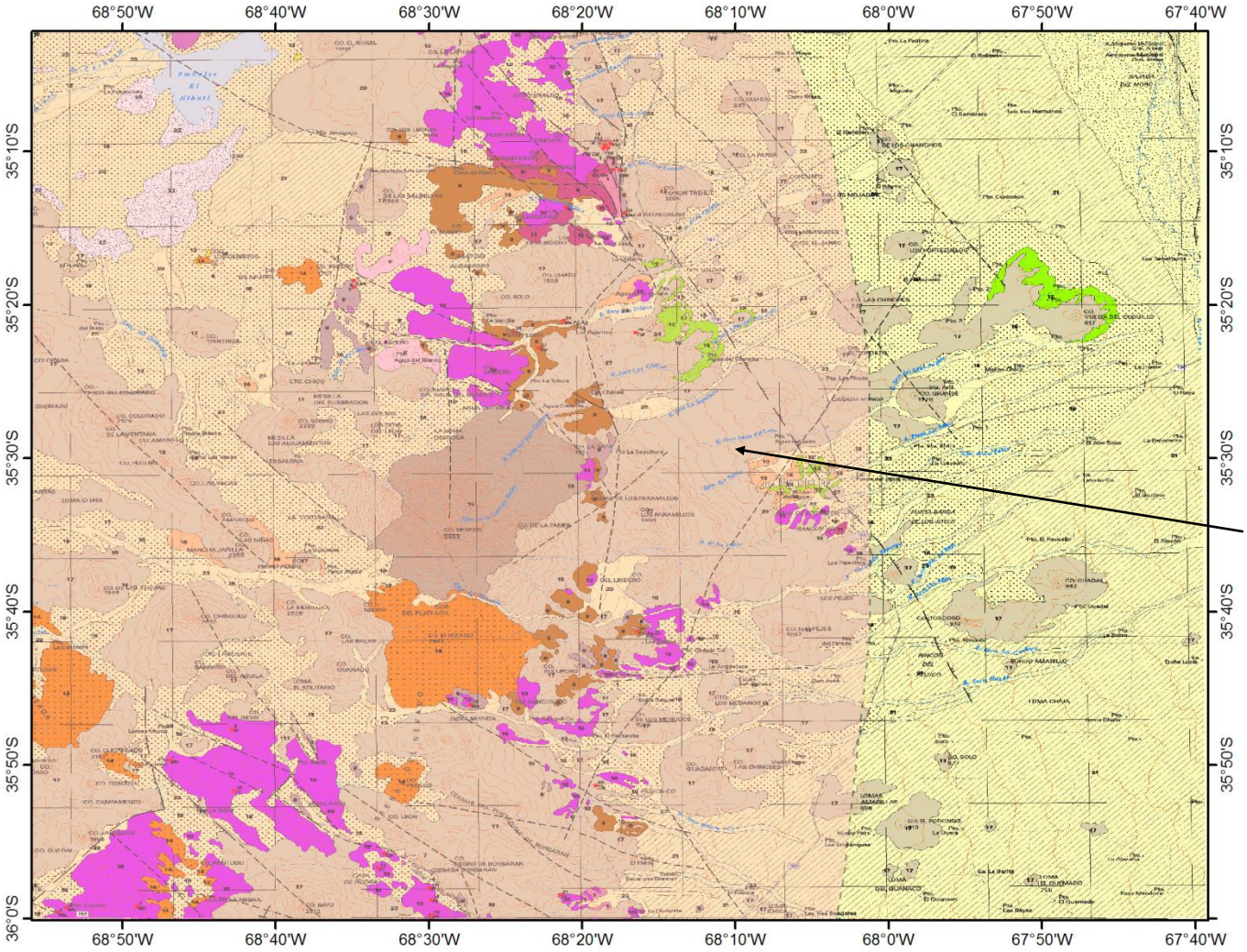

Legend

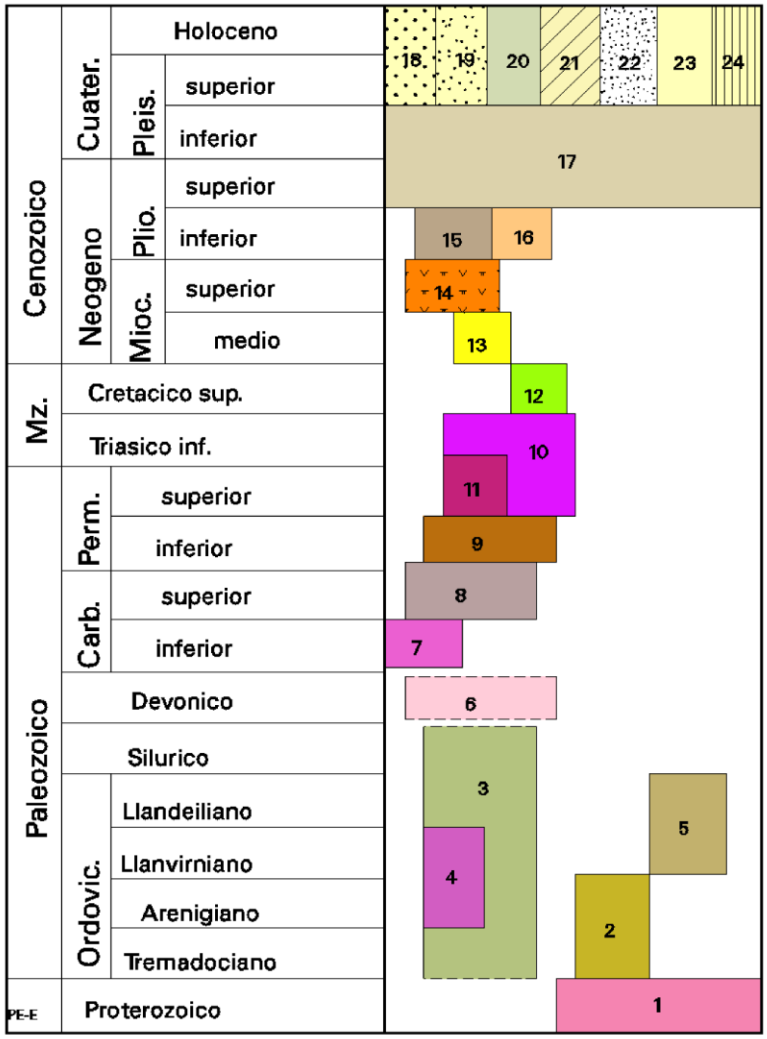

24 FORMACION DEL POZO AZUL. Turbas,conglomerados finos,arenas, limos y tobas.
23 DEPOSITOS ALUVIALES ENCAUSADOS. Gravas, arenas y limos.
22 DEPOSITOS SALITROSOS DE PLAYAS. Arenas finas, y sedimentos pelíticos salitrosos.
21 DEPOSITOS EOLICOS DE MEDANOS ACTIVOS. Arenas y limos.
20 DEPOSITOS EOLICOS DE MEDANOS VEGETADOS. Arenas y limos.
19 DEPOSITOS DE LA LLANURA ALUVIAL DEL RIO ATUEL. Aglomerados, gravas gruesas y limos.
18 DEPOSITOS ALUVIALES PEDEMONTANOS. Aglomerados, arenas y limos.
17 GRUPO CHAPUA. Basaltos, tobas y aglomerados volcánicos de composición basáltica.
16 FORMACION CAJON DE MAYO (continental). Conglomerados brechoides, gravas, arenas y limos.
15 FORMACION NEVADO. Basaltos, tobas, brechas, diques y aglomerados volcánicos de composición andesítica, dacítica y riolítica.
14 FORMACION CORTADERA. Basaltos, tobas, brechas y aglomerados volcánicos de composición andesítica, dacítica y riolítica.
13 FORMACION AISOL (continental). Areniscas, limolitas, arcilitas y tobas.
12 FORMACION PUNTA DEL AGUA (continental). Areniscas, conglomerados, limolitas y arcilitas.
11 FORMACION QUEBRADA DEL PIMIENTO. Volcanitas e hipabisales básicos.
10 SUBGRUPO CERRO CARRIZALITO. Volcanitas ácidas a mesosilícicas e hipabisales.
9 SUBGRUPO COCHICO. Volcanitas, hipabisales y sedimentitas.
8 FORMACION EL IMPERIAL (mixto). Cuarcitas, areniscas, lutitas y limolitas.
7 FORMACION PIEDRAS DE AFILAR. Granitos y granodioritas.
6 FORMACION RIO SECO DE LOS CASTAÑOS (marino). Ortocuarcitas, areniscas, grauvacas, limolitas y lutitas.
5 FORMACION LINDERO (marino). Grainstones, calcarenitas, cuarcitas, areniscas y limolitas.
4 GABRO LOMA ALTA. Gabros.
3 FORMACION LA HORQUETA (marino). Metacuarcitas, filitas y esquistos.
2 FORMACION PONON TREHUE (marino). Calizas y dolomías.
1 FORMACION CERRO LA VENTANA. Metamorfitas, plutonitas y filonianas.

Figure 5. Geological map of part of the eastern part of the Payún Matrú Volcanic Field. From Narciso et al. (2001)

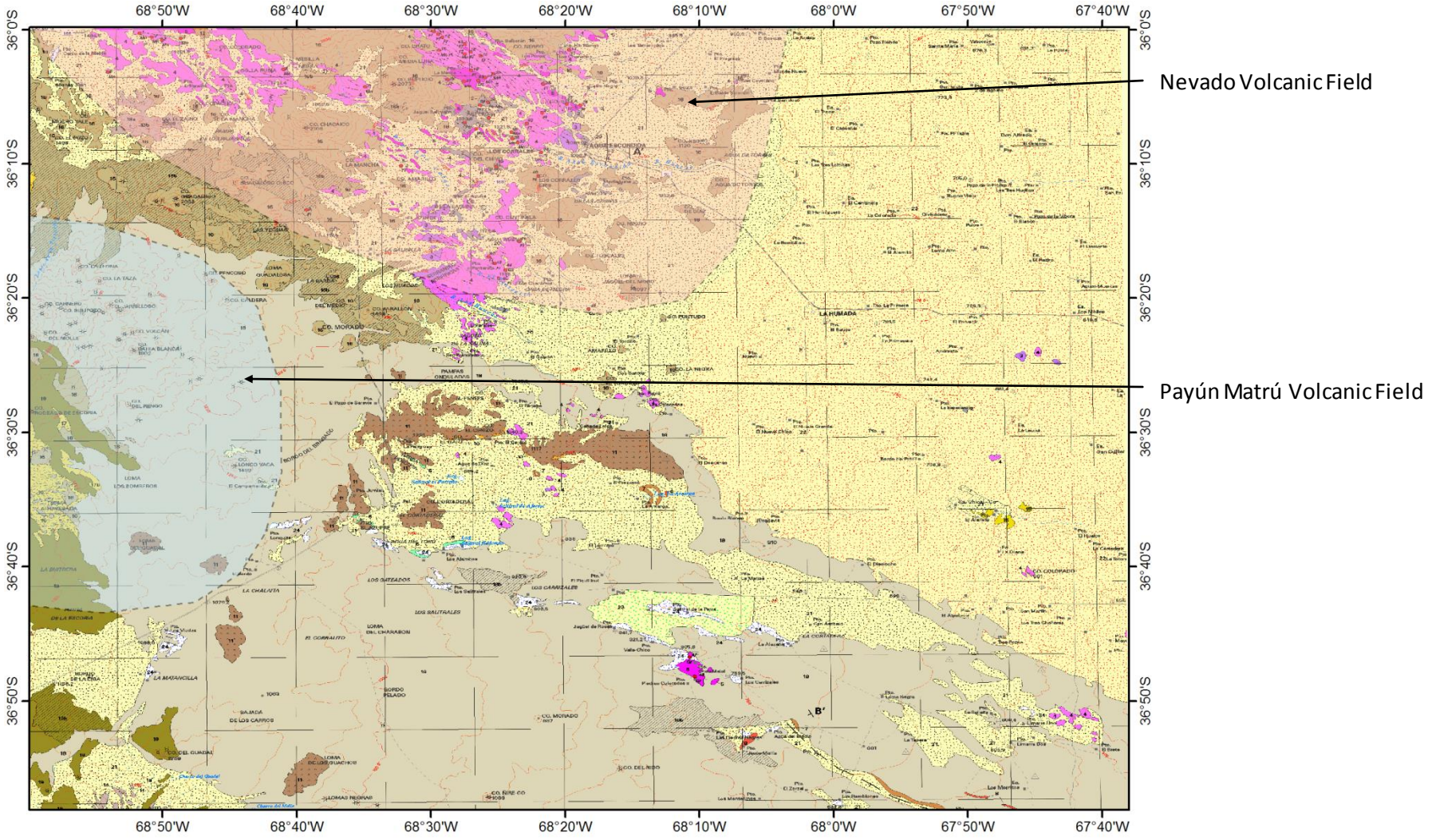

Legend

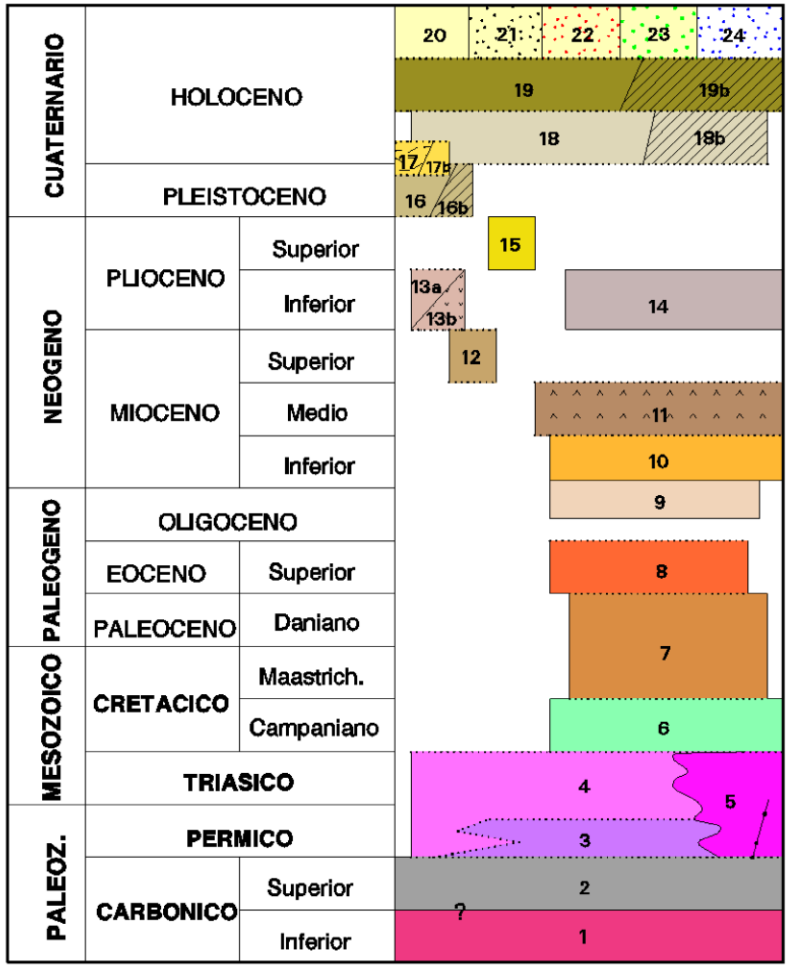

24 Depósitos de Evaporitas (continental). Cloruros, sulfatos y carbonatos.
23 Depósitos de Médanos (éolico). Arenas.
22 Depósitos de campos de arena (éolico). Arenas y limos.
21 Depósitos Aluvio-Coluviales (continental). Arenas y limos.
20 Depósitos Aluviales (continental). Gravas, arenas y limos.
19 Fm. Tromen 19b) semicubierto. Basalto olivínico.
18 Fm. El Puente 18b) semicubierto. Basalto olivínico.
17 Fm. El Portezuelo 17b) semicubierto. Ignimbritas y tobas.
16 Fm. Chapúa 16b) semicubierto. Basalto olivínico.
15 Fm. Cerro Azul (continental). Arenisca, pelitas y calizas.
14 Fm. Chachahuen. Andesitas hornblendíferas, basaltos y brechas.
13 Fm. El Zaino. Andesitas hornblendíferas a)Mb. El Zaino - b)Mb. Chiguas
12 Fm. Cortadera. Volcanitas andesíticas, dacíticas y riolíticas.
11 Grupo Palauco. Basalto olivínico.
10 Fm. Puesto Barros (continental). Areniscas tobáceas.
9 Fm. La Parva. Basalto.
8 Fm. Vaca Mahuida (marino). Grainstone, areniscas y pelitas.
7 Fm. Roca (marino). Rudstone, Grainstone, areniscas y pelitas.
6 Fm. Loncoche (marino). Arenisca, granistone, calizas y pelitas.
5 Grupo El Portillo. Diques, intrusivos graníticos y riolíticos.
4 Fm. Choique Mahuida. Lavas, tobas, ignimbritas y brechas riolíticas.
3 Fm. Agua de los Burros. Dacitas, traquiandesitas, tobas e ignimbritas.
2 Fm. Agua Escondida (marino). Areniscas, pelitas y vaques.
1 Fm. Piedra de Afilar. Granito.

Appendix C: Cosmogenic ^{3}He and ^{21}Ne surface exposure dating of young basalts from Southern Mendoza, Argentina. *Quaternary Geochronology*, 19, 76-86.

Appendix C is a publisher version of the following article that removed as copyright reason: Espanon, V. R., Honda, M. & Chivas, A. R. (2014). Cosmogenic 3He and 21Ne surface exposure dating of young basalts from Southern Mendoza, Argentina. *Quaternary Geochronology*, 19 76-86. doi:10.1016/j.quageo.2013.09.002

Appendix D: Geochemical variations in the Quaternary Andean back-arc volcanism, southern Mendoza, Argentina. *Lithos*, 208–209, 251-264.

Appendix D is a publisher version of the following article that removed as copyright reason:

Espanon, V. R., Chivas, A. R., Kinsley, L. P. J. & Dosseto, A. (2014). Geochemical variations in the Quaternary Andean back-arc volcanism, southern Mendoza, Argentina. *Lithos*, 208-209 251-264.

doi:10.1016/j.lithos.2014.09.010

Appendix E: Geochronological, morphometric and geochemical constraints on the Pampas Onduladas long basaltic flow (Payún Matrú Volcanic Field, Mendoza, Argentina). *Journal of Volcanology and Geothermal Research*, 289, 114-129.

Appendix E is a publisher version of the following article that remove as copyright reason:
Espanon, V. R., Chivas, A. R., Phillips, D., Matchan, E. L. & Dosseto, A. (2014). Geochronological, morphometric and geochemical constraints on the Pampas Onduladas long basaltic flow (Payún Matrú Volcanic Field, Mendoza, Argentina). *Journal of Volcanology and Geothermal Research*, 289 114-129.
doi:10.1016/j.jvolgeores.2014.10.018